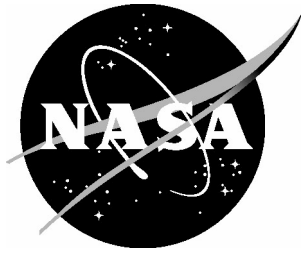


NASA/CR-2005-213919



Sensing and Active Flow Control for Advanced BWB Propulsion-Airframe Integration Concepts

*John Fleming, Jason Anderson, Wing Ng, and Neal Harrison
Techsburg, Blacksburg, Virginia*

September 2005

The NASA STI Program Office . . . in Profile

Since its founding, NASA has been dedicated to the advancement of aeronautics and space science. The NASA Scientific and Technical Information (STI) Program Office plays a key part in helping NASA maintain this important role.

The NASA STI Program Office is operated by Langley Research Center, the lead center for NASA's scientific and technical information. The NASA STI Program Office provides access to the NASA STI Database, the largest collection of aeronautical and space science STI in the world. The Program Office is also NASA's institutional mechanism for disseminating the results of its research and development activities. These results are published by NASA in the NASA STI Report Series, which includes the following report types:

- **TECHNICAL PUBLICATION.** Reports of completed research or a major significant phase of research that present the results of NASA programs and include extensive data or theoretical analysis. Includes compilations of significant scientific and technical data and information deemed to be of continuing reference value. NASA counterpart of peer-reviewed formal professional papers, but having less stringent limitations on manuscript length and extent of graphic presentations.
- **TECHNICAL MEMORANDUM.** Scientific and technical findings that are preliminary or of specialized interest, e.g., quick release reports, working papers, and bibliographies that contain minimal annotation. Does not contain extensive analysis.
- **CONTRACTOR REPORT.** Scientific and technical findings by NASA-sponsored contractors and grantees.

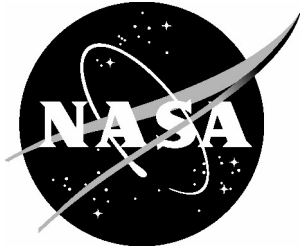
- **CONFERENCE PUBLICATION.** Collected papers from scientific and technical conferences, symposia, seminars, or other meetings sponsored or co-sponsored by NASA.
- **SPECIAL PUBLICATION.** Scientific, technical, or historical information from NASA programs, projects, and missions, often concerned with subjects having substantial public interest.
- **TECHNICAL TRANSLATION.** English-language translations of foreign scientific and technical material pertinent to NASA's mission.

Specialized services that complement the STI Program Office's diverse offerings include creating custom thesauri, building customized databases, organizing and publishing research results ... even providing videos.

For more information about the NASA STI Program Office, see the following:

- Access the NASA STI Program Home Page at <http://www.sti.nasa.gov>
- E-mail your question via the Internet to help@sti.nasa.gov
- Fax your question to the NASA STI Help Desk at (301) 621-0134
- Phone the NASA STI Help Desk at (301) 621-0390
- Write to:
NASA STI Help Desk
NASA Center for AeroSpace Information
7121 Standard Drive
Hanover, MD 21076-1320

NASA/CR-2005-213919



Sensing and Active Flow Control for Advanced BWB Propulsion-Airframe Integration Concepts

*John Fleming, Jason Anderson, Wing Ng, and Neal Harrison
Techsburg, Blacksburg, Virginia*

National Aeronautics and
Space Administration

Langley Research Center
Hampton, Virginia 23681-2199

Prepared for Langley Research Center
under Contract NAS1-03066

September 2005

Acknowledgments

This work was supported by NASA Langley under the Ultra Efficient Engine Technology (UEET) initiative, contract NAS1-03066. The contracting office's technical representative on the program at NASA was Ms. Susan A. Gorton.

Available from:

NASA Center for AeroSpace Information (CASI)
7121 Standard Drive
Hanover, MD 21076-1320
(301) 621-0390

National Technical Information Service (NTIS)
5285 Port Royal Road
Springfield, VA 22161-2171
(703) 605-6000

Abstract

The use of serpentine boundary layer ingesting (BLI) diffusers offers a significant benefit to the performance of Blended Wing Body aircraft. However, the inherent diffuser geometry combined with a thick ingested boundary layer creates strong secondary flows that lead to severe flow distortion at the engine face, increasing the possibility of engine surge and high cycle fatigue failures of fan and compressor rotor blades. This study investigated the use of enabling active flow control methods to reduce engine-face distortion.

An ejector-pump based system of fluidic actuators was used to directly manage the diffuser secondary flows. This system was modeled computationally using a novel boundary condition jet modeling method, and tested in the Techsburg ejector-driven wind tunnel facility. The tunnel test section used for this experiment was designed, built, and tested as a validation tool for the computational methods. This process resulted in the creation of a unique system capable of efficiently investigating and testing the fundamental mechanisms of flow control in BLI serpentine diffusers at a minimum of time and expense.

Results of the computational and wind tunnel analysis confirmed the large potential benefit of adopting fluidic actuators to control flow distortion in serpentine BLI inlets. Computational analysis showed a maximum 71% reduction in flow distortion at the engine face through the use of the Pyramid 1 (SP1) ejector scheme, and a 68% reduction using the circumferential ejector (FSCIR) scheme. Experimental results showed that the computational analysis slightly over-predicts flow distortion. However, the trends are accurately predicted despite slight variances in freestream Mach number between runs and a slightly lower tested altitude.

The effects of fluidic flow control actuators can, however, be deceptive. Despite dramatic decreases in engine face total pressure distortion, large-scale vortices can induce high flow swirl that can result in local stalling of compressor blades. This can lead to reduced engine performance and the increased possibility of compressor surge or stall. Computational analyses have highlighted the importance of maintaining jet separation and individuality, as the coalescence of multiple jets can result in low total pressure distortion at the expense of increased flow swirl.

As a final technical objective, a method to non-intrusively estimate inlet flow distortion using signals from an array of wall-imbedded microphones mounted in the BLI serpentine inlet. The integrated level of coherent content of the microphone array was calculated as a means to estimate the integral turbulent length scales in the flow field at the exit-plane of the inlet duct. These estimated length scales from the microphone array measurements were linearly superimposed to yield an estimator of inlet total pressure distortion at the simulated engine fan-face with an accuracy of 97% with respect to traditional methods of distortion assessment. This non-intrusive sensing technique offers the potential to close the loop of a feedback active flow control system to manage inlet flow distortions.



Table of Contents

Abstract.....	iii
Table of Contents.....	v
List of Figures.....	viii
List of Tables.....	xi
Chapter 1: Significance of Blended Wing-Body BLI Diffusing Inlets.....	1
1.1: BLI Serpentine Diffusers and Distortion.....	1
1.2: Research Motivation and Objective.....	2
1.3: Solution Plan.....	3
1.3.1: The Ejector Pump and Flow Control.....	3
1.3.2: Distortion Descriptors.....	3
1.4: Study Approach.....	5
Chapter 2: Computational Analysis.....	6
2.1.1: Computational Domain.....	6
2.1.2: Computational Grid.....	7
2.2: Flow Control CFD Grid Design.....	7
2.3: Computational Fluid Dynamics.....	8
2.3.1: Boundary Conditions.....	8
2.3.2: Jet Modeling and Hole Geometry.....	9
2.3.3: The Spalart-Allmaras Turbulence Model.....	10
2.4: Solution Convergence.....	10
2.5: Baseline Configuration.....	11
2.5.1: External Boundary Layer Characteristics.....	11
2.5.2: Baseline Solution Results.....	14
2.5.3: Baseline Flow Swirl.....	17
2.5.4: Baseline Flow Distortion Mechanisms.....	17
2.6: Flow Control Design Strategy.....	18
2.7: Blowing Configurations.....	20
2.7.1: Circumferential Blowing.....	20
2.7.2: Axial Blowing.....	21
2.7.3: Pyramid Blowing.....	21
2.7.4: Reverse Pyramid Blowing.....	22
2.8: Suction Configurations.....	22
2.9: Modeling the Ejector Pump.....	23
2.9.1: Ejector Pump Implementation Considerations.....	23
2.9.2: Blowing and Suction Configuration Selection.....	23
Flow Control Results Summary.....	24
2.9.3: Flow Control Results.....	25
2.10: Flow Control Visualization.....	28
2.11: Strake.....	33

2.12: Strake Computational Results.....	34
Chapter 3: Experimental Validation	35
3.1: Facility Overview	35
3.1.1: Boundary Layer Growth Region.....	36
3.1.2: Inlet test Section.....	37
3.1.3: Flow Control Inserts	38
3.1.4: Distortion Rake.....	39
3.1.5: Pressure Drop Screens	40
3.1.6: Flow Control: Blowing.....	40
3.1.7: Flow Control – Suction.....	41
3.2: Wind Tunnel Instrumentation.....	42
3.2.1: Pressure Transducers and Data Acquisition	43
3.3: Wind Tunnel CFD	44
3.4: Experimental Results	45
3.4.1: Ingested Boundary Layer Profile.....	45
3.4.2: Diffuser Wall Centerline Pressures.....	46
3.4.3: Baseline Distortion Contours.....	46
3.4.4: Shortcomings of DC(60).....	47
DC(60) Distortion Results – Reverse Pyramid Flow Control	49
3.4.5: DC(60) Distortion Results – Circumferential Flow Control	52
3.4.6: Strake	56
3.4.7: Effect of Strake on Flow Control.....	57
Chapter 4: Non-intrusive Flow Distortion Sensor Development.....	59
4.1: Technical Objectives of Sensing Approach.....	59
4.2: Theory of Wall-Pressure Fluctuations	59
4.3: Microphone Installation and Calibration.....	61
4.3.1: Sensor Specifications.....	61
4.3.2: Sensor Installation.....	62
4.3.3: Sensor Locations.....	63
4.3.4: Sensor Calibration.....	64
4.4: Test Matrix and Data Acquisition.....	65
4.5: Experimental Distortion Estimator Development.....	66
4.5.1: Preliminary Data and Observations	66
4.5.2: Circumferential Array Correlation Approach.....	72
4.6: Proposed Closed-Loop Implementation	81
4.7: Non-Intrusive Distortion Sensor Conclusions	82
Chapter 5: Future Potential Commercial Applications.....	83
Chapter 6: Conclusions	84
Bibliography	86
Appendix A: Distortion Descriptors	88
DC(60) and SC(60).....	88

SAE-ARP1420.....	90
Circumferential Distortion Extent.....	90
Circumferential Distortion Intensity.....	90
Circumferential Distortion Extent: Multiple per Revolution.....	91
Radial Distortion Intensity.....	91
Average Distortion Intensity: DPCP.....	92
Inlet Pressure Recovery	92
Appendix B: Geometry.....	94
Appendix C: Grid Resolution Study.....	97
Appendix D: Impact of Diffuser Mass Flow on AIP Distortion.....	101
Appendix E: Flow Control Axial Location.....	103
Appendix F: Flow Control Spanwise Spacing.....	104
Appendix G: Complete CFD Results.....	107
Baseline ARP1420 Distortion Parameter Results.....	107
Flow Control Case Descriptions.....	108
Flow Control ARP1420 Distortion Results	110
Flow Control Solution Contours.....	112
Flow Control Distortion Results.....	116
Appendix H: Calculations and Uncertainty	121
Appendix I: Wind Tunnel Adaptation of CFD Grid.....	126
Appendix J: Wind Tunnel Flow Quality.....	128
Axial Pressure Gradient.....	128
Spanwise Pressure Gradient.....	129
Diffuser Static Pressure Profile.....	130
Appendix K: ADPAC	131

List of Figures

Figure 1-1: BWB Aircraft with a BLI Serpentine Inlet	1
Figure 1-2: Serpentine BLI Inlets and Distortion	2
Figure 1-3: Ejector Pump Principle	3
Figure 1-4: DC(60) Distortion Rake	4
Figure 2-1: Extent of Computational Domain	6
Figure 2-2: 30% Boundary Layer Ingestion	6
Figure 2-3: Block Topology of Computational Domain.....	7
Figure 2-4: Mesh Detail Near Jet Location.....	8
Figure 2-5: Jet Boundary Condition Modeling.....	10
Figure 2-6: Solution Convergence.....	11
Figure 2-7: Boundary Layer Growth	12
Figure 2-8: Boundary Layer Velocity Profiles (Baseline).....	13
Figure 2-9: Diffuser Total Pressure Contours – Baseline.....	14
Figure 2-10: Diffuser Wall Static Pressure Contours – Baseline	14
Figure 2-11: Centerline Velocity Contours – Baseline.....	15
Figure 2-12: Comparative Baseline Solutions (NASA).....	16
Figure 2-13: AIP Total Pressure Contours - Baseline	17
Figure 2-14: Baseline AIP Streamwise Vorticity Contours.....	17
Figure 2-15: Flow distortion mechanisms	18
Figure 2-16: Streamlines Depicting Horseshoe/Junction Vortices.....	18
Figure 2-17: Flow Effector Location Rationale.....	19
Figure 2-18: Nominal blowing jet configuration.....	19
Figure 2-19: Circumferential Blowing.....	20
Figure 2-20: Axial Blowing.....	21
Figure 2-21: Pyramid Blowing	21
Figure 2-22: Reverse Pyramid blowing.....	22
Figure 2-23: Lip and Floor Suction	22
Figure 2-24: Cases Modeled Using Ejector Pump.....	23
Figure 2-25: Sample Ejector Pump Models.....	24
Figure 2-26: DC(60)pt Distortion Parameter Results	25
Figure 2-27: DC(60)q Distortion Parameter Results	26
Figure 2-28: DPCPavg Distortion Parameter Results.....	27
Figure 2-29: SC(60) Swirl Distortion Parameter Results with Streamwise Vorticity Contours ..	27
Figure 2-30: Total Pressure Recovery Results.....	28
Figure 2-31: Conventional Blowing and Ejector Pump Total Pressure Contour Comparison	29
Figure 2-32: Streamwise Vorticity Contours.....	31
Figure 2-33: Boundary Layer Streamlines.....	32
Figure 2-34: Jet Flow Streamlines – Circumferential Ejector (FSCIR)	32
Figure 2-35: Jet Flow Streamlines - Pyramid 1 Ejector (SP1).....	33
Figure 2-36: Strake Geometry	33
Figure 2-37: Strake Effects	34
Figure 3-1: Techsburg Ejector-Pump Wind Tunnel Facility.....	35
Figure 3-2: Ejector-Pump Tunnel Section	36

Figure 3-3: Boundary Layer Growth Region.....	37
Figure 3-4: Inlet Test Section	37
Figure 3-5: Flow Control Inserts.....	38
Figure 3-6: Six-Arm Total Pressure Distortion Rake	39
Figure 3-7: Pressure Drop Section.....	40
Figure 3-8: Flow Control - Blowing Apparatus.....	41
Figure 3-9: Flow Control - Suction Apparatus	42
Figure 3-10: Boundary Layer Rake	42
Figure 3-11: Inlet Instrumentation.....	43
Figure 3-12: Data Acquisition System.....	44
Figure 3-13: Wind Tunnel Mach Number Contours.....	44
Figure 3-14: Wind Tunnel Ingested Boundary Layer Velocity Profile	45
Figure 3-15: Comparison of CFD and measured Pressure Coefficients for upper and lower surfaces of diffuser on the axial center line	46
Figure 3-16: Baseline Solution distortion Contours (No flow control)	47
Figure 3-17: Effect of Rake on Distortion	48
Figure 3-18: AIP Static Pressure Contours.....	48
Figure 3-19: DC(60)q Experimental Distortion Results - Reverse Pyramid Blowing	49
Figure 3-20: DC(60)pt Experimental Distortion Results - Reverse Pyramid Blowing	50
Figure 3-21: Pressure Recovery Experimental Results - Reverse Pyramid Blowing.....	51
Figure 3-22: Reverse Pyramid Blowing Total Pressure Contours.....	52
Figure 3-23: DC(60)q Experimental Distortion Results - Circumferential Blowing	53
Figure 3-24: DC(60)pt Experimental Distortion Results - Circumferential Blowing	54
Figure 3-25: Inlet Pressure Recovery Experimental Results - Circumferential Blowing.....	55
Figure 3-26: Circumferential Blowing Total Pressure Contours	56
Figure 3-27: Experimental Results – Effect of Strake	57
Figure 3-28: DC(60)q Experimental Distortion Results with Strake.....	58
Figure 3-29: DC(60)pt Experimental Distortion Results with Strake	58
Figure 4-1: Wall-imbedded microphone installation technique	62
Figure 4-2: Wall-imbedded microphone installation locations in the test inlet.....	63
Figure 4-3: Dynamics that affect microphone pressure measurement.....	64
Figure 4-4: Microphone calibration technique	65
Figure 4-5: AIP flow field characteristics indicated by the AIP circumferential microphone array measurements.....	70
Figure 4-6: Detection of flow field changes by AIP circumferential microphone array due to 0.98% flow control.....	71
Figure 4-7: Detection of further flow field changes by AIP circumferential microphone array due to 1.87% flow control.....	72
Figure 4-8: CAC approach microphone approach.....	73
Figure 4-9: Two-point coherence with the microphone at location B10-B	76
Figure 4-10: Estimated length scales versus DC(60) considering only the frequency band of 1000-2000 Hz.....	77
Figure 4-11: DC(60) versus the DC(60) estimator determined from the correlations from only the 1000-2000 Hz bandwidth.....	79
Figure 4-12: Estimated length scales versus DC(60) considering only the frequency band of 1000-5000 Hz.....	80

Figure 4-13: DC(60) versus the DC(60) estimator determined from the correlations from only the 1000-5000 Hz bandwidth.....	80
Figure 4-14: Proposed flow distortion control system with microphone feedback sensors	81
Figure 4-15: Illustration of LMS adaptive filter technique to determine the correlated content between two microphone signals in real-time	82
Figure A.0-1: DC(60) Distortion Rake	88
Figure A.0-2: Ring Circumferential Distortion Extent (One-per-Revolution)	90
Figure A.0-3: Ring Circumferential Distortion Extent (Multiple-per-Revolution)	91
Figure A.0-4: Radial Distortion	92
Figure B.0-1: NASA/Boeing BLI Inlet Configuration 'A'	94
Figure B.0-2: NASA Configuration 'A' Diffuser Geometry	95
Figure B.0-3: NASA/Boeing Configuration 'A' Dimensions.....	96
Figure C.0-1: Grid Resolution Study - Baseline Total Pressure Distribution.....	97
Figure C.0-2: Grid Resolution Study - Baseline DC(60) Convergence.....	98
Figure C.0-3: Grid Resolution Study - Baseline DPCPavg Convergence	99
Figure C.0-4: Grid Resolution Study - Baseline Circumferential Distortion Intensity	100
Figure C.0-5: Grid Resolution Study - Baseline Radial Distortion Intensity	100
Figure D.0-1: Effect of Variation in AIP Mass Flow	101
Figure D.0-2: Baseline Comparative Mass Flow Solutions.....	102
Figure E.0-1: Flow Control Axial Location.....	103
Figure E.0-2: Effect of Axial Jet Location - Total Pressure Contours.....	104
Figure F.0-1: Spanwise Jet Configurations.....	105
Figure F.0-2: Effect of Jet Circumferential Spacing.....	105
Figure F.0-3: AIP Streamwise Vorticity - Effect of Spanwise Jet Spacing.....	106
Figure G.0-1: Circumferential Distortion Intensity – Baseline	107
Figure G.0-2: Radial Distortion Intensity – Baseline	108
Figure G.0-3: ARP1420 Circumferential Distortion Intensity (Selected Cases).....	110
Figure G.0-4: ARP1420 Radial Distortion Intensity	111
Figure G.0-5: DC(60)pt Distortion Parameter Results	117
Figure G.0-6: DC(60)q Distortion Parameter Results	117
Figure G.0-7: DPCPavg Distortion Parameter Results.....	118
Figure G.0-8: SC(60) Swirl Distortion Parameter Results	119
Figure G.0-9: Total Pressure Recovery Results.....	120
Figure H.0-1: Overview of measurements.....	121
Figure H.0-2: AIP measurement locations.....	123
Figure I.0-1: Wind Tunnel Grid Modification.....	126
Figure I.0-2: AIP Grid Modification.....	127
Figure J.0-1: Wind Tunnel Axial Pressure Gradient	128
Figure J.0-2: Wind Tunnel Transverse Pressure Gradient.....	129
Figure J.0-3: Baseline Diffuser Centerline Static Pressure.....	130

List of Tables

Table 2-1: Comparison of distortion reduction parameters for select cases.....	29
Table 4-1: Microphone data set configurations	66
Table H.0-1: Summary of Transducers and Data Acquisition.....	122
Table H.0-2: Transducer Uncertainties ($\delta(x)$)	124
Table H.0-3: System Metric Uncertainty Based on Transducer Error.....	125
Table H.0-4: Distortion Uncertainty Based on Assumption Error	125

Nomenclature

p_t – total pressure
 q – dynamic pressure
 ρ - density
 u – flow velocity
 M – Mach number
 Re – Reynolds Number
 μ - fluid viscosity
 ν - kinematic viscosity
 p – static pressure
 \dot{m} – mass flow
 A – area
 γ - ratio of specific heats
 T – temperature
 R - Universal Gas constant
 δ - boundary layer thickness
 δ^* - boundary layer displacement thickness
 θ - boundary layer momentum thickness
 H – Boundary layer shape function
 C_f – skin friction coefficient
DC(60) – Circumferential Distortion Coefficient
SC(60) – Swirl Distortion Coefficient
AIP – Aerodynamic Interface Plane
CFD – Computational Fluid Dynamics
BWB – Blended Wing-Body
BLI – Boundary Layer Ingesting/Ingestion
RANS – Reynolds Averaged Navier Stokes
SLA – Stereo-lithography
UAV – Uninhabited Air Vehicles
S-A – Spalart-Allmaras Turbulence Model
AFC – Active Flow Control
PFC – Passive Flow Control

Subscripts

t - total conditions
 ∞ - freestream conditions
 i – at duct inlet

Chapter 1: Significance of Blended Wing-Body BLI Diffusing Inlets

The NASA/Boeing Blended Wing Body aircraft of Figure 1-1 is a flying-wing concept capable of significant performance benefits over the conventional tube-and-wing construction. Of particular interest is the incorporation of serpentine engine inlet diffusers coupled with significant amounts of boundary layer ingestion. If adopted, this configuration promises to have a large advantage over aircraft constructed using a more conventional design. In order to realize the large potential benefits, it will first be necessary to overcome the primary difficulty with serpentine BLI inlets, namely engine-face flow distortion.

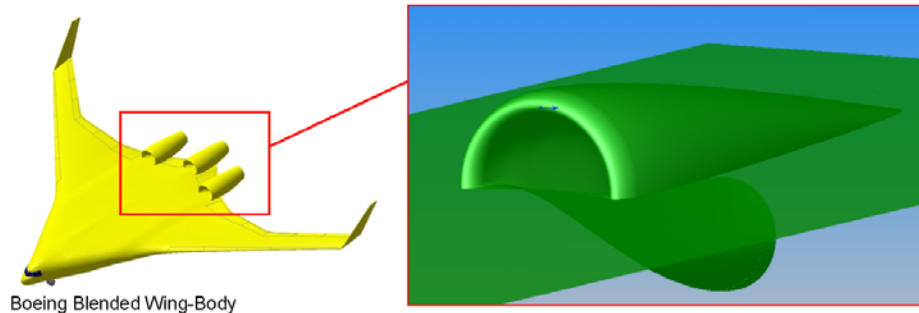


Figure 1-1: BWB Aircraft with a BLI Serpentine Inlet

1.1: BLI Serpentine Diffusers and Distortion

Distortion is created in these types of diffusers through several different mechanisms. The primary mechanism of flow distortion in serpentine inlets is due to the creation of flow swirl. Swirl represents the non-axial or cross-flow velocities present in the flow, and is especially prominent in serpentine ducts due to their physical curvature. More specifically, swirl develops in these types of ducts due to the centrifugal forces associated with turning the flow through curves in the diffuser. As the flow passes through the first bend of a serpentine diffuser, a centrifugal pressure gradient proportional to $\rho u^2/R$ exerts a force on the fluid¹. As a result, greater force is exerted on the fluid at the outside of the bend and a strong transverse pressure gradient is created across the duct. This gradient drives the flow on the outside of the turn in towards the inside turn, establishing a secondary flow field. The secondary flows have the effect of driving the low-momentum boundary layer fluid from the periphery of the duct towards the inside turn. This fluid then collects on the inside of the turn forming an area of total pressure deficit.

Boundary layer ingestion provides an additional complication to the creation of flow distortion. If the boundary layer is ingested into the diffuser, it can cause a large increase in engine-face distortion by supplying areas of low momentum flow from the boundary layer to the diffuser inlet; flows that are easily influenced by the strong pressure gradients present in the diffuser.

In addition, the interaction of vorticity present in the boundary layer with the nacelle-body junction can cause the formation of a junction (or horseshoe) vortex. This vortex has the same sense of rotation as the secondary flows formed by the centrifugal forces, and thus increases the severity of the flow distortion at the AIP. The combined effect are highlighted in Figure 1-2.

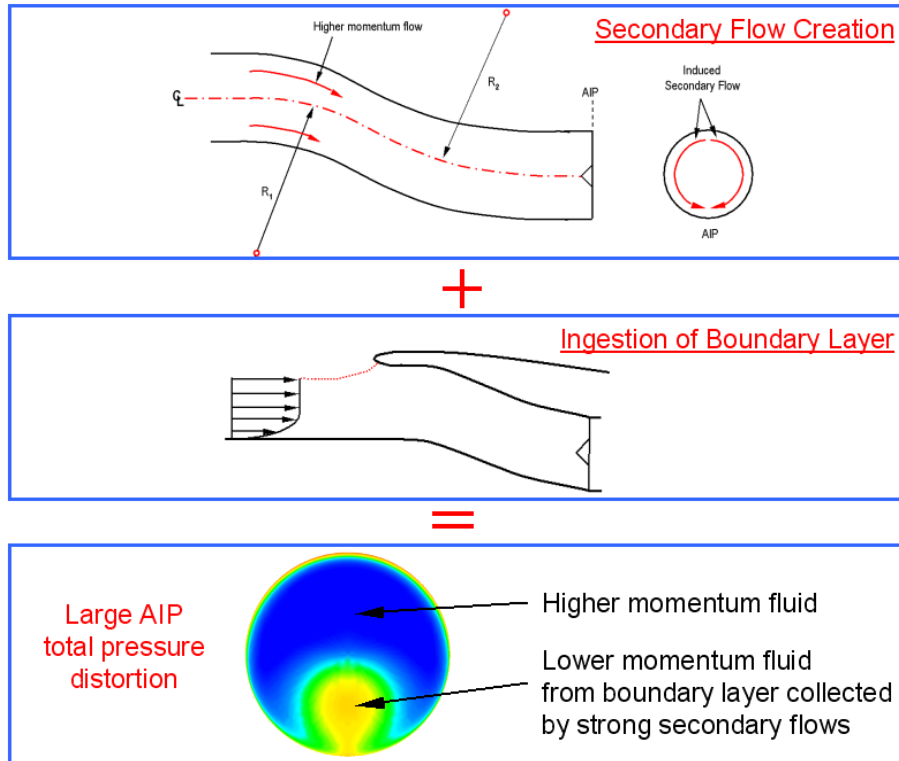


Figure 1-2: Serpentine BLI Inlets and Distortion

Due to the severe physical curvature of serpentine inlets, the flow has a tendency to separate in areas of strong adverse pressure gradients, as well as induce strong secondary flows throughout the duct. Increased total pressure losses, as well as severe flow distortion at the engine-fan interface are characteristic of these types of systems. This trend is only increased in severity when coupled with designs that incorporate high levels of boundary layer ingestion. By introducing low momentum fluid to the inside turn of a serpentine duct, the severity of the cross-flow pressure gradients is increased. The high-momentum fluid from the outside turn collects the boundary layer fluid at the bottom of the duct creating a substantial circumferential total pressure distortion.

1.2: Research Motivation and Objective

In order to realize the substantial performance benefits of serpentine BLI diffusers, this study investigated the use of ejector-based active flow control methods to reduce AIP flow distortion.

1.3: Solution Plan

In order to maximize the possible effectiveness of active flow control jets, an ejector pump system of fluidic jets will be investigated as a means of boosting the system performance. A variety of jet configurations will be examined with the goal of determining the driving parameters of jet effectiveness in reducing AIP distortion in serpentine BLI inlets. This system will be modeled using a boundary condition jet modeling technique. Results from the computational studies will be validated in the Techsburg ejector-driven wind tunnel facility.

Some key identifying elements of the study will now be defined.

1.3.1: The Ejector Pump and Flow Control

In order to increase jet effectiveness, the ejector pump utilizes a high-pressure motive jet to entrain additional air mass into a core jet. The motive jet creates an area of locally lower static pressure behind the jet. When this area is connected to a plenum chamber of higher static pressure, fluid is entrained into the jet according to the Venturi effect. Thus, air from a higher static pressure is drawn into the low-pressure region created by the jet and entrained into the jet core flow. By locating the plenum chamber under the surface of a moving body, fluid from the flow boundary layer can be drawn into the plenum chamber, providing a measure of boundary layer suction.

The effectiveness of the ejector pump is also aided by taking advantage of existing pressure gradients. By locating the suction in areas of locally high pressure, and the jets in areas of lower pressure, a natural pressure gradient is established and additional system effectiveness is obtained. When aided by existing pressure gradients, motive to suction mass flow ratios of 1:1 can be realistic performance expectations.² Thus, the ejector-pump approach can yield blowing mass flow rates of up to 2% of the total duct mass flow at the bleed expenditure of only 1% of the total mass flow while simultaneously providing 1% of mass in flow suction.

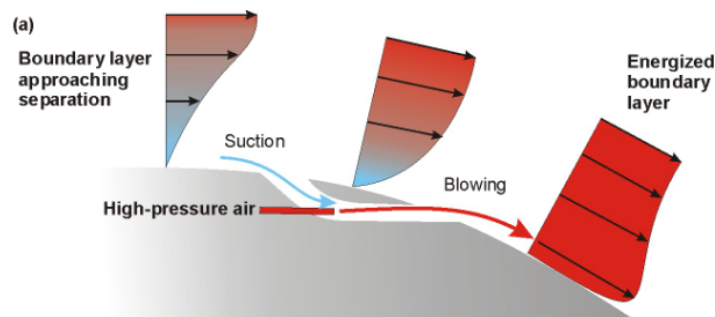


Figure 1-3: Ejector Pump Principle

1.3.2: Distortion Descriptors

In order to characterize the flow at the AIP, several descriptors are available that characterize the various elements of distortion. The primary of these descriptors are the DC(60) parameters¹. These examine the flow distortion based upon measurements obtained from a six-arm distortion rake that measures total pressures in 60° sections. Each arm has five probe measurement locations that are located such that they each represent an equal area-averaged

section of the 60° wedge, as shown in Figure 1-4. Values from this rake are then examined to determine the flow distortion at the AIP.

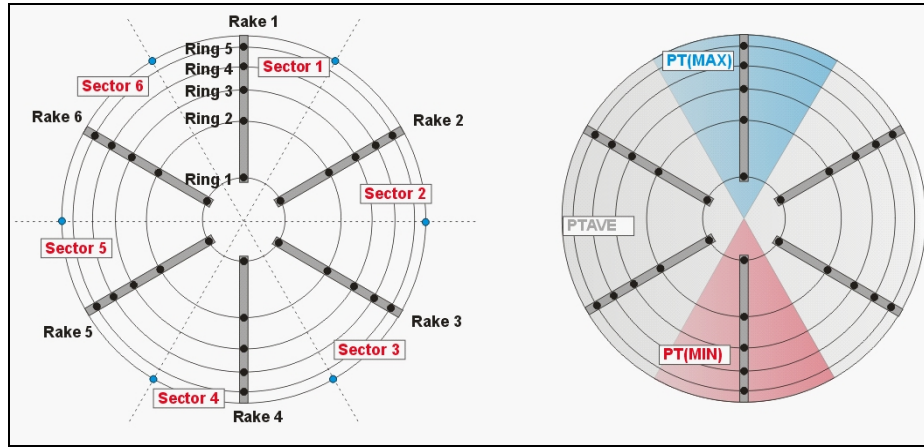


Figure 1-4: DC(60) Distortion Rake

The DC(60)pt value is used as a general flow health monitoring parameter by determining the ‘worst’ case for a 60° sector of the flow.

$$DC(60)_{PT} = \frac{PT_{MAX} - PT_{MIN}}{PT_{AVE}} \quad (2-1)$$

The DC(60)q parameter is the most common of the DC(60) parameters and examines the ratio of the difference between the average and minimum total pressure sectors and the face dynamic pressure. This parameter highlights the average flow distortion and compares it to dynamic pressure; this can roughly serve as a non-dimensionalization by the flow kinetic energy, which is related to distortion severity.

$$DC(60)_q = \frac{PT_{AVE} - PT_{MIN}}{q_{AVE}} \quad (2-2)$$

The flow at the AIP can also be characterized by examining the magnitude of the secondary flow or swirl velocities.³ The SC(60) parameter provides a measure of the severity of the secondary flows and characterizes the non-axial flow that could lead to a stalling of the compressor blades.

$$SC(60) = \frac{V_{CF_MAX} - V_{CF_MIN}}{V_{AVE}} \quad (2-3)$$

Another typical duct flow descriptor is the inlet pressure recovery. This parameter characterizes the efficiency of the diffuser to convert kinetic energy to pressure energy.

$$PR = \frac{AIP \text{ Total pressure}}{Freestream \text{ Total pressure}} \quad (2-4)$$

Additional distortion descriptors used in this study are based upon standards proposed by SAE-ARP1420.⁴ The parameters use the standard distortion rake to characterize circumferential, radial, and average (DPCPavg) distortion intensity. These parameters are more complicated to calculate, but can provide a more detailed analysis of the flow distortion.

For a more complete description of all distortion parameters used in this analysis, please refer to Appendix A.

1.4: Study Approach

This study will focus on the computational design and experimental validation of fluidic vortex generators for the purpose of reducing flow distortion in BLI serpentine inlets. The inlet aerodynamic effects of using the ejector-pump concept to augment the thrust from the fluidic vortex generators will also be analyzed.

The computational analysis will be based upon investigation that utilizes a novel jet modeling technique in order to analyze multiple jet configurations and investigate the fundamental mechanisms of fluidic vortex generating jet effectiveness.

Results will be verified experimentally at flight Mach number (~ 0.85) for selected configurations to verify the validity of the approach. The Techsburg wind tunnel will be used to simulate the low pressure, high subsonic Mach number cruise conditions typical of the BWB. This is accomplished by using an ejector-pump based system, which offers significant advantage over systems that utilize cryogenic helium in order to obtain the desired simulated flight condition -- a feature that adds complexity and cost to the system.

Finally, Techsburg will experimentally develop a non-intrusive technique to estimate the total pressure metric $DC(60)$ using an array of wall-imbedded microphones.

Chapter 2: Computational Analysis

The computational analysis focused on the evaluation of the vortex generator flow control configuration in several stages. First, baseline flow distortion was analyzed in order to provide a benchmark result for comparison with accepted data. In the second phase, the flow control was analyzed using a novel boundary condition for jet modeling that allowed for rapid analysis of jet performance and fundamental flow investigations.

Flow Domain and Mesh Generation

2.1.1: Computational Domain

The computational domain was created to simulate one half of a center-mounted engine in a BWB configuration as represented in Figure 2-1. The computational domain was required to simulate both duct capture and a portion of the bypass flow. The precise inlet geometry for this study was defined by NASA configuration 'A'. (Geometry details are outlined in detail in Appendix B.)

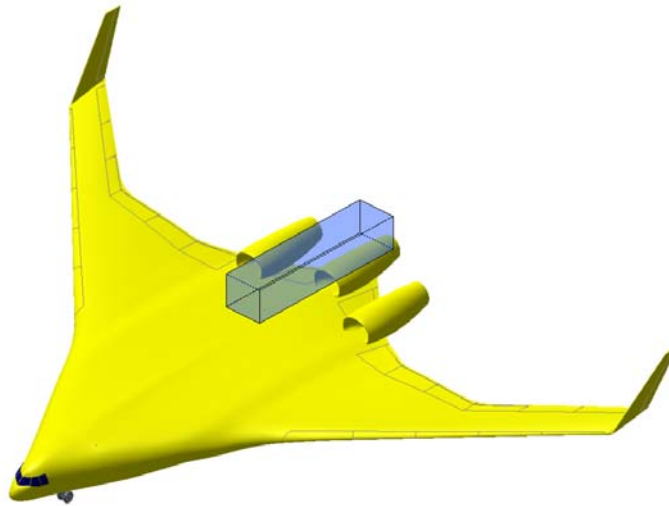


Figure 2-1: Extent of Computational Domain

In order to simulate the BWB flight condition, the domain had to simulate the appropriate boundary layer thickness and Mach number consistent with this type of installation. The design requirement for the simulation is depicted in Figure 2-2: an ingested boundary layer thickness of approximately 30% of the total inlet height at a freestream Mach number of $M = 0.85$.

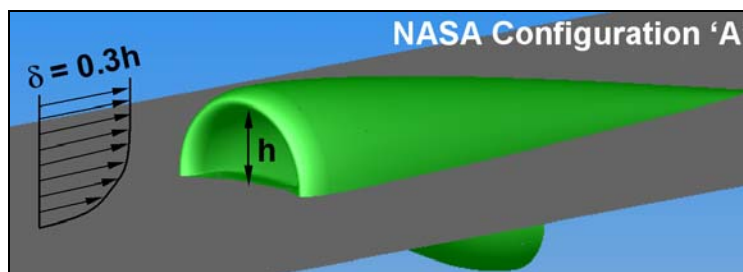


Figure 2-2: 30% Boundary Layer Ingestion

2.1.2: Computational Grid

The domain grid for the analysis was created using the mesh generator Gridgen V.14. The general mesh topology is based upon a multiple-block structured grid. In addition, the mesh was created to be compatible with the multi-grid solving capability of ADPAC (discussed in Section 3.3). The completed grid consisted of 10 blocks and a total mesh size of ~ 2.7 million nodes. Near wall spacing was created with a nominal $y^+ \approx 1$ in order to fully capture the boundary layer. General grid topology is shown in Figure 2-3.

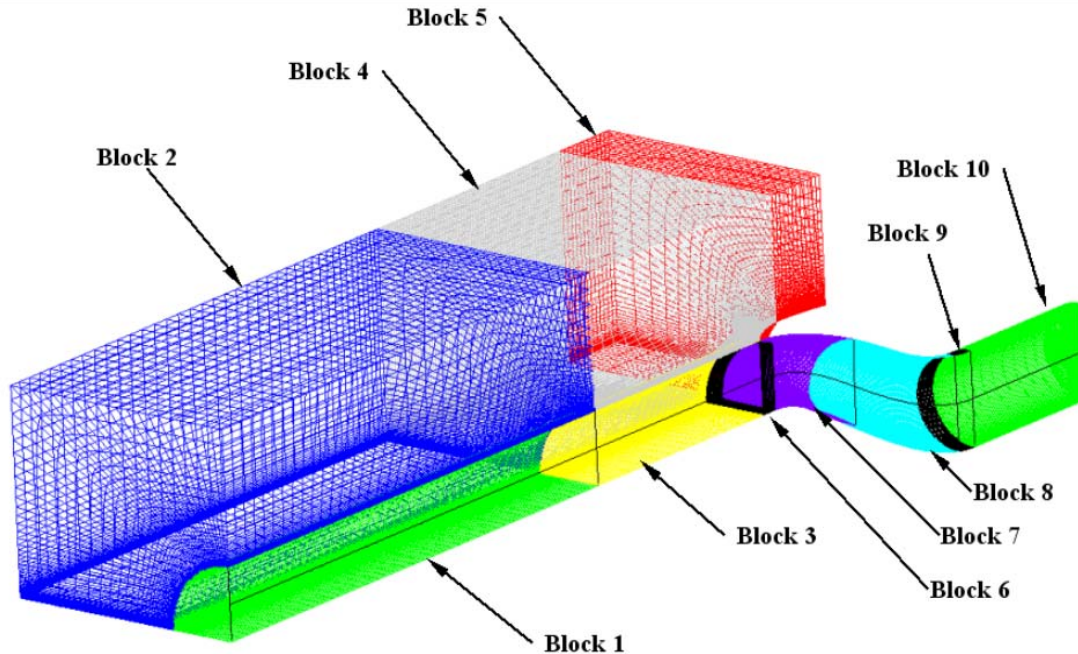


Figure 2-3: Block Topology of Computational Domain

Blocks 1-4 were used to ‘grow’ the boundary layer to the desired 30% thickness, and simulate the freestream flow. Block 5 diverts the bypass air around the external engine nacelle. Blocks 6-9 represent the inside of the diffuser. Block 10 was added to the end of the diffuser so that boundary conditions were not imposed directly at the AIP, which could have influenced the measured distortion values.

2.2: Flow Control CFD Grid Design

In order to better model the vortex generating jets, the internal duct grid was designed with a high cell density in the axial direction in regions where the flow control would be applied. This enabled more realistic hole sizes and geometries to be modeled, since more control over the sizing of the blowing or suction “hole” size was possible with increased cell density. Figure 2-4 gives a detailed look at the inlet mesh, showing the cell density in close detail. Increased block cell density allowed for higher-fidelity modeling of the local flow field; downstream block cell densities were also increased to capture the increased flow complexity resulting from flow control.

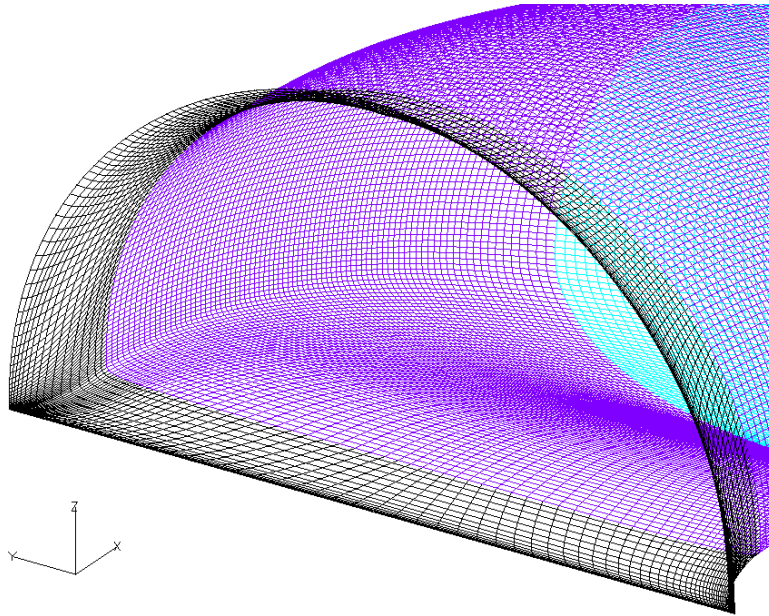


Figure 2-4: Mesh Detail Near Jet Location

2.3: Computational Fluid Dynamics

The CFD solution solver used in this investigation was ADPAC (Advanced Ducted Propfan Analysis Code), which was created by the Allison Engine Company in cooperation with NASA Langley.⁵ The code utilizes a finite volume formulation to solve the Reynolds-Averaged Navier-Stokes (RANS) equations. For a more detailed description, refer to Appendix K.

2.3.1: Boundary Conditions

As noted earlier, the computational domain is intended to simulate the aft portion of a center engine installation on a Blended Wing-Body aircraft. Thus, the boundary conditions must be specified in order to simulate this condition as closely as possible.

The inboard and outboard boundaries were both modeled using a mirror condition (inviscid wall) in order to simulate the symmetry associated with a centerline engine installation. By modeling half of the inlet, the total computational grid size was decreased. All boundaries coinciding with aircraft surfaces were modeled using a viscous wall condition, while the fore and aft boundaries were used to control the total mass flow and velocity through the block consistent with cruise performance at 39,000 ft. Flow conditions are given below, and are meant to be representative of a BWB aircraft at cruise conditions:

- Freestream Mach Number $M_\infty = 0.85$
- Design AIP Mach Number $M \approx 0.5$ (average)
- Altitude 39,000 ft
- Reference total pressure $p_t = 664.58 \text{ lb/ft}^2$
- Reference total temperature $T_t = 447.26 \text{ }^\circ\text{R}$
- AIP mass flux $= mc/A_{\text{AIP}} = 30.8 \text{ lbm/s / ft}^2$ (corrected mass flow / per unit area)
- Mass flow coefficient $= C\dot{m} = 0.635$
- AIP mass flow $= 0.672 \text{ lbm/s}$ (uncorrected).

These conditions were used to set up the CFD analysis. The mass flow specified above was scaled from Boeing design data for a typical engine mass flow requirement. In the design case, this would yield a nominal Mach number of ~ 0.5 at the AIP. This mass flow is typically related to sea level conditions as a reference:

$$\dot{m}_c = \dot{m}_{actual} \left(\frac{\sqrt{T_{0\infty} / T_{ref}}}{P_{0\infty} / P_{ref}} \right). \quad (3-1)$$

In order to be able to compare CFD results from different sources with different geometries, additional mass flow-related parameters are specified. The AIP mass flux is useful to compare inlets of different physical size⁶, and was calculated according to:

$$mc / A_{AIP} = \frac{\dot{m}_c}{A_{AIP}}. \quad (3-2)$$

The mass flow coefficient parameter can be used to compare mass flow rates for different flow properties and conditions, as well as different sized inlets⁷:

$$C_{\dot{m}} = \frac{\dot{m}_{actual}}{\rho_{\infty} V_{\infty} A_{AIP}}. \quad (3-3)$$

Through the use of these parameters computational solutions were compared with similar studies conducted by NASA.

2.3.2: Jet Modeling and Hole Geometry

CFD modeling of the jets for the flow control cases was based upon the simulation of a plenum that supplies air to all of the jets at equal pressure. As such, individual jet mass flows varied according to local backpressure values. These boundary conditions were held constant for all configurations tested. Values for the supply pressure were set to simulate compressor bleed air characteristics. Additional details of flow control jet modeling are outlined herein.

The fluidic jets were modeled using ADPAC's INLETG condition at the mesh boundary. The INLETG condition specifies flow total pressure, total temperature, and local flow angle (relative to cell orientation). In order to closely manage the size and shape of the cells in the near wall region, concentrations were established by using a polar mesh within the duct. This allowed for the most even cell spacing with the least amount of skewness. This configuration was determined to be the best meshing geometry for monitoring the secondary flows that move around the periphery of the duct, and also ensure compatibility with the AIP distortion measuring program *distortion_param* written at Techsburg. In the past, computational investigations have typically utilized either source-term modeling, or have modeled individual flow effectors at great time and computational expense.⁸ By utilizing the wall boundaries for jet modeling, significant simplification of flow control was achieved. This allowed for the examination of a multitude of different jet configurations in a short period of time. The jet modeling concept is demonstrated in Figure 2-5. Thus, the driving parameters of flow control effectiveness could be examined on a fundamental level. To facilitate jet modeling, a clustering of four cells was typically used to represent the blowing holes. (The same technique was used to model the flow suction.) This resulted in a roughly square geometry for the holes, on average having an approximate area of 0.01 in². Because the jets are oriented at a blowing angle of 30° from the wall (jet orientation is detailed in a later section), the jet diameter size is physically scaled by $\sin(30^\circ)$. Thus, the actual

jet area (from which air is blown) is equal to 0.005 in^2 . This results in a jet with an area roughly equivalent to a circular jet with a diameter of about 0.080 in .

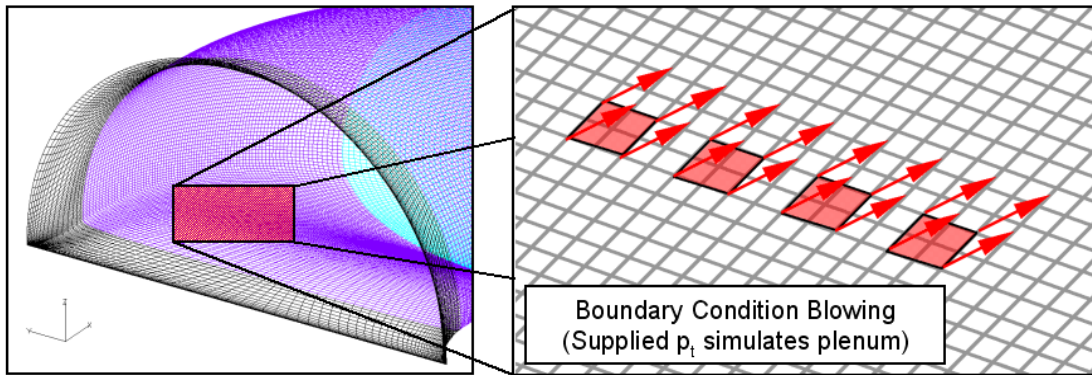


Figure 2-5: Jet Boundary Condition Modeling

2.3.3: The Spalart-Allmaras Turbulence Model

The computational analysis used the one-equation Spalart-Allmaras (S-A) turbulence model. The S-A model was chosen for the study as it is the highest fidelity working turbulence model available in ADPAC⁵, and is well established for its separated flow modeling and shock capturing ability. For a more detailed description, refer to Appendix K.

2.4: Solution Convergence

The solution convergence was based upon a relative decrease of the solution error by three orders of magnitude from the initial starting value. Duct mass flow and distortion parameters were also monitored for convergence. A representative convergence graph is shown in Figure 2-6.

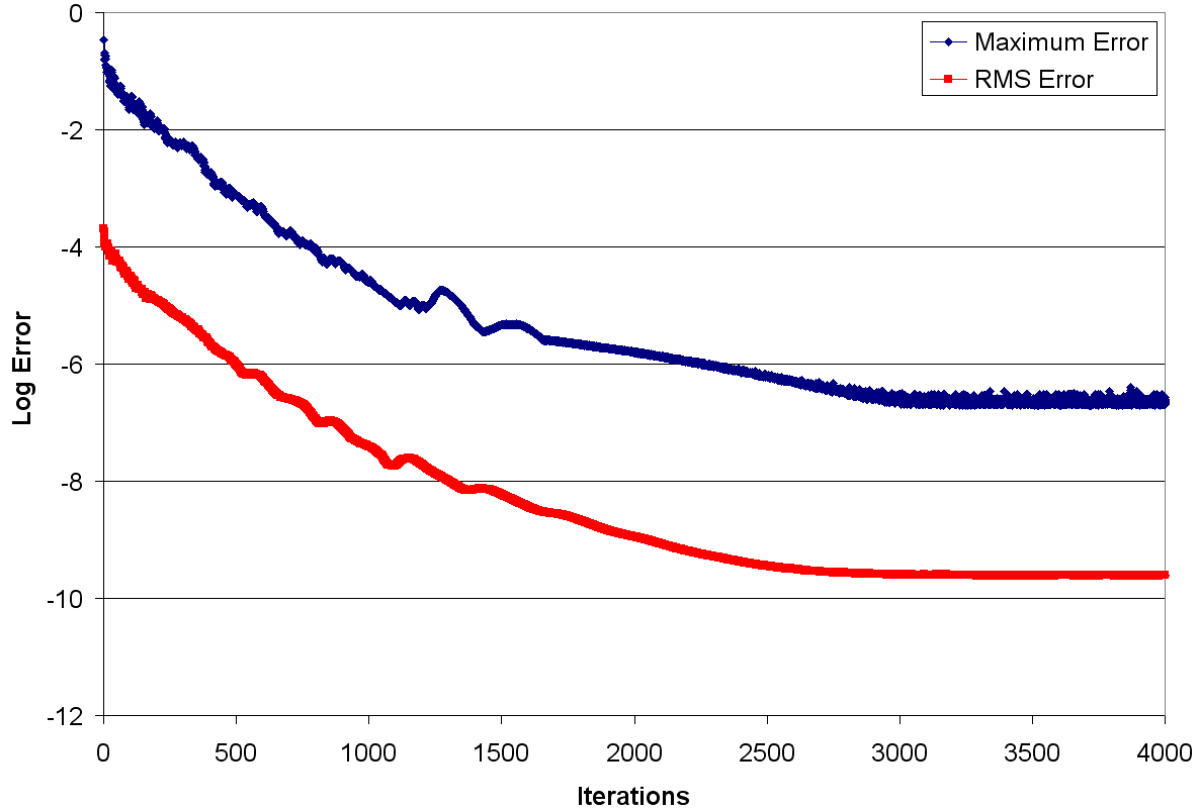


Figure 2-6: Solution Convergence

2.5: Baseline Configuration

This section summarizes the CFD results of the baseline configuration (no flow control). A grid resolution study was conducted to ensure that the mesh was of sufficient resolution to accurately capture the flow solution. For complete details of the grid resolution study, please refer to Appendix C.

2.5.1: External Boundary Layer Characteristics

Modeling the approaching boundary layer is of paramount importance when analyzing a BLI inlet. As mentioned previously, a 30% boundary layer height is desired ($\delta = 0.30$ of the inlet height, h). To determine an appropriate boundary layer growth length prior to ingestion, an approach boundary layer with an appropriate velocity profile and skin friction value was modeled using an extended “flat plate” section upstream of the inlet. This is similar to the approach used by Allan^{7,8}. The boundary layer thickness growth over this region was predicted using a turbulent flat plate boundary layer growth formulation.⁹ This method simulates the boundary layer profile according to the 1/7 power law:

$$\frac{u}{U_e} = \left(\frac{y}{\delta}\right)^{\frac{1}{7}}. \quad (3-4)$$

This assumption results in a full turbulent profile to predict the flat-plate growth. The desired boundary layer growth length was predicted according to:

$$\delta(x) = 0.375 \cdot x \cdot \text{Re}_x^{1/5} \quad (3-5)$$

The adverse pressure gradient caused by the ram effect of the inlet also results in a local boundary layer thickening. Thus, the final ingested boundary layer thickness was then determined in combination with the ram effect of the inlet capture, resulting in the boundary layer thickness as shown in Figure 2-7.

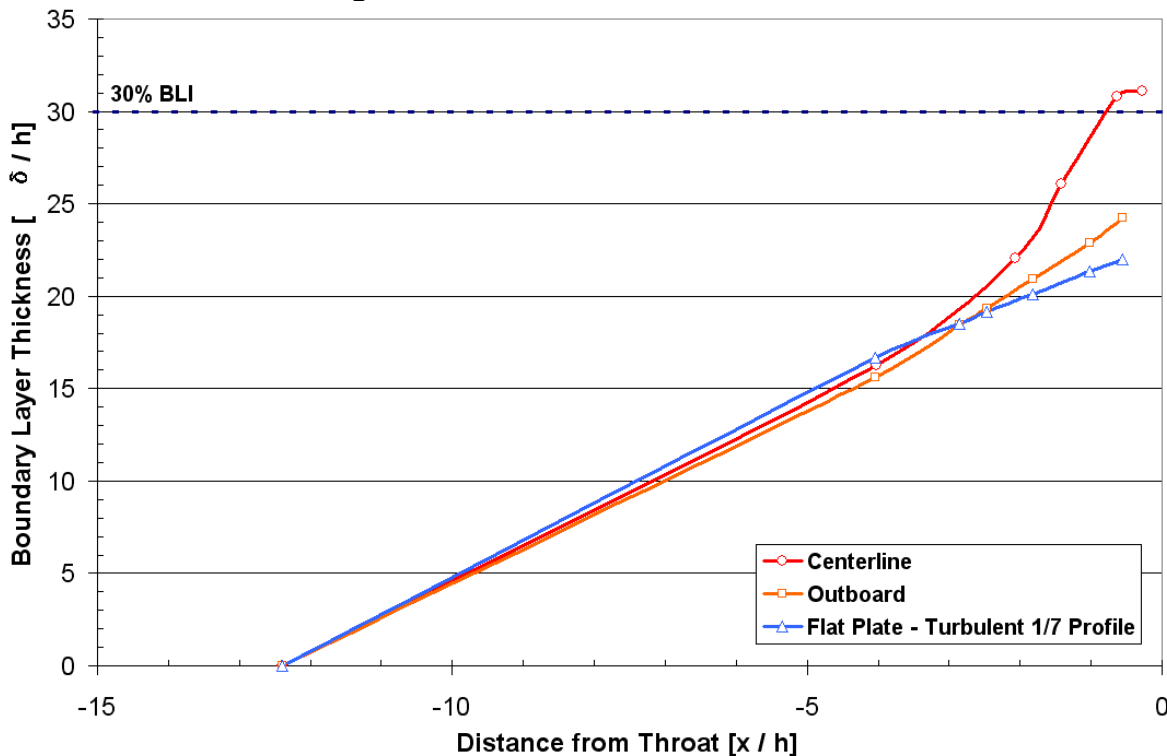


Figure 2-7: Boundary Layer Growth

The resulting velocity profile as measured at one inlet height upstream of the inlet ($x/h = -1.0$) is shown in comparison with the predicted 1/7 Power profile in Figure 2-8. These profiles were examined in order to determine the effects of engine ram on the boundary layer characteristics at the measurement location, and to ensure boundary layer uniformity between the inboard and outboard mesh blocks. The blue line (lowest) is a profile calculated according to the 1/7 power law, which was used to approximate the required boundary layer growth distance using 2D turbulent boundary layer estimates. The calculated profile shows higher skin friction versus the “natural growth” baseline profiles with significantly lower skin friction. At this location the boundary layer thickness was calculated to be $\delta/h \approx 0.29$. Additional boundary layer parameters were calculated to be:

- $\delta = 0.723$ in
- $\delta^* = 0.257$ in
- $\theta = 0.089$ in

- $H = \delta^*/\theta = 2.88$
- $C_f \sim 0.0002$ (estimated).

The result for H suggests that the flow may be separated, but no reversed flow was seen near the wall. The low estimated skin friction value also indicates incipient separation, and is significantly lower than the skin friction value obtained from the computed 1/7 velocity profile. Further computational analysis of thicker approaching boundary layers caused separation with reverse flow along the inlet centerline. Thus, capturing the correct boundary layer physics is of critical importance, as the distortion pattern and magnitude appear to be highly sensitive to the ingested boundary layer characteristics.

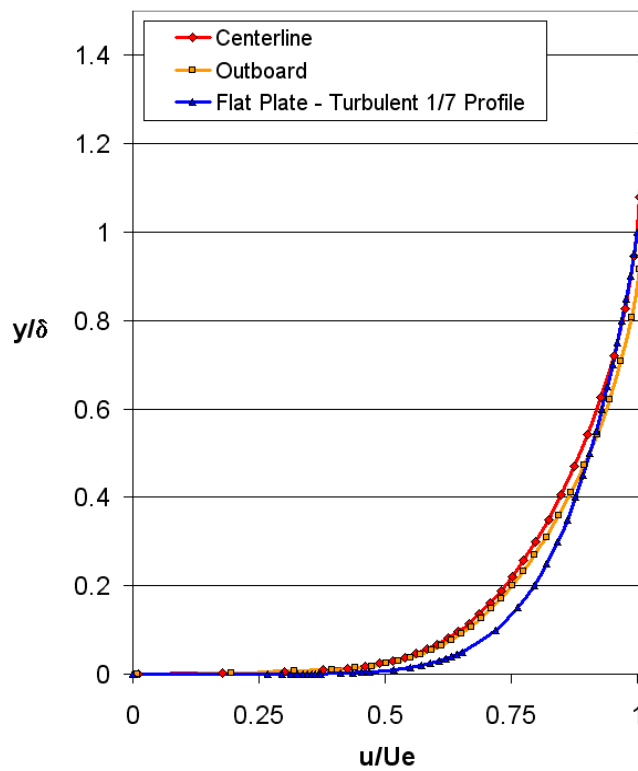


Figure 2-8: Boundary Layer Velocity Profiles (Baseline)

2.5.2: Baseline Solution Results

The CFD predictions for the baseline configuration (without flow control) will be presented in order to show the characteristics of the flow at critical locations, and to highlight the flow mechanisms that characterize the formation of flow distortion.

An isometric view of the diffuser in Figure 2-9 shows the baseline solution with several normalized total pressure contours shown for constant streamwise cross-sections. These results clearly show the initial boundary layer flow distortion generated at the nacelle entrance, followed by the influence of the circumferential pressure gradients that shape the low momentum boundary layer fluid into a central core of low total pressure fluid.

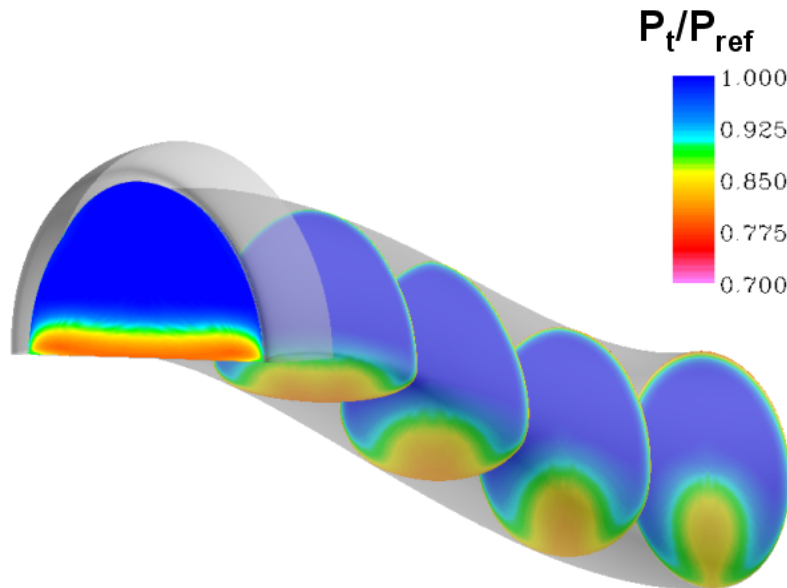


Figure 2-9: Diffuser Total Pressure Contours – Baseline

Surface static pressure contours of the diffuser are shown in Figure 2-10. As noted in section 1.2.1, the turns induce locally higher pressures on the outside of the diffuser creating the secondary flows and large pressure gradients across the diffuser.

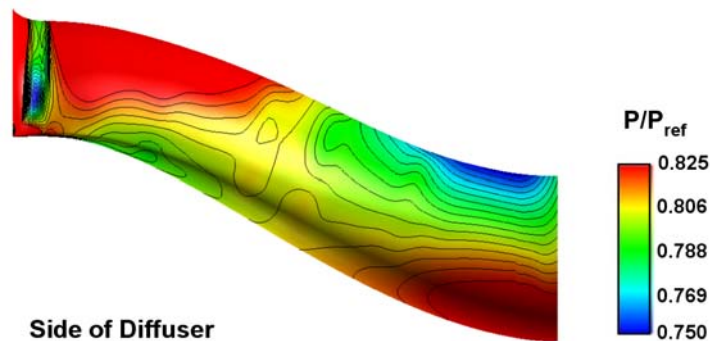


Figure 2-10: Diffuser Wall Static Pressure Contours – Baseline

Figure 2-11 shows non-dimensional velocity magnitude contours along the inlet centerline. A low speed region exists just upstream of the AIP, but this region does not appear to be separated based on boundary layer profiles inspected at the AIP. However, it is apparent that some vortex lift-off has occurred, forming the distinctive distortion pattern at the AIP. Studies examining higher inlet mass flows do not show as strong a buildup of low speed fluid ahead of the inlet throat, as discussed in Appendix D. Another distinctive flow characteristic is the formation of a “supervelocity” region just upstream of the inlet throat. This velocity profile is the result of interaction between the ingested boundary layer flow and the potential field effects of the diffuser lip. Also evident is a local thickening of the ingested boundary layer resulting from the adverse pressure gradient created by engine ram effects.

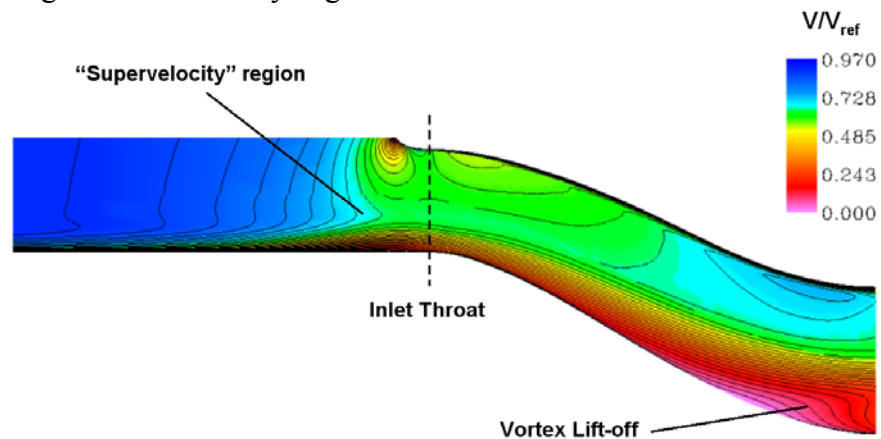


Figure 2-11: Centerline Velocity Contours – Baseline

The obtained velocity contour plots for the baseline flow can be compared to data obtained by NASA for the configuration ‘A’ inlet geometry; it should be noted however, that NASA investigations used a freestream Mach = 0.833, while Techsburg used a freestream Mach = 0.85. Figure 2-12 compares the baseline (no flow control) centerline Mach contours computed at Techsburg to those by Berrier et al.⁶ They used an overset grid topology to examine the flow using a modified Menter Shear Stress Transport (SST) turbulence model at a mass flow of 6 lbm/s. (~10% higher than for obtained results.) Despite these differences, it can be seen that the Mach contours compare favorably with the results obtained for the baseline solution. The contours show that the average Mach number of the inlet flow remains relatively unchanged in the upper half of the inlet; this is due to the small diffusion ratio ($A_{AIP}/A_{Throat} = 1.069$) of the inlet. Target Mach numbers for the inlet and AIP (0.7 and 0.55, respectively) are achieved through mass averaging at the location face. The fluid buildup upstream of the AIP and flow super-velocity region are clearly visible in both solutions.

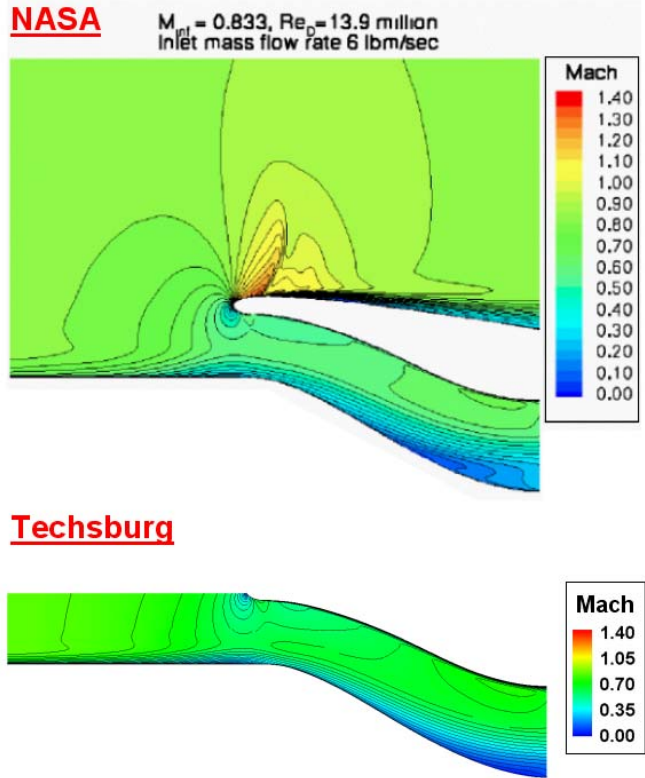


Figure 2-12: Comparative Baseline Solutions (NASA)

Shown in Figure 2-13 are the total pressure contour results at the AIP, as well as the DC(60), DPCPavg, and total pressure recovery numbers for the baseline flow solution. The total pressure contours from the current study compare well to NASA results for the same geometry also shown in Figure 2-13. It is evident that the flow mechanism present at the AIP is the same for the two cases, although the flow Mach number and modeled vortex behavior are somewhat different. This difference is the result of different turbulence models used in the analyses. The NASA solution used the Menter Shear Stress Transport turbulence model in their analysis, while Techsburg used the Spalart-Allmaras turbulence model. NASA's Allan noted that vortices embedded in boundary layers behave differently between these two models¹⁰, and thus would not model the flow identically. In particular, the strength of modeled vortices was different particularly in the vortex core; this difference then directly impacts the predicted distortion.

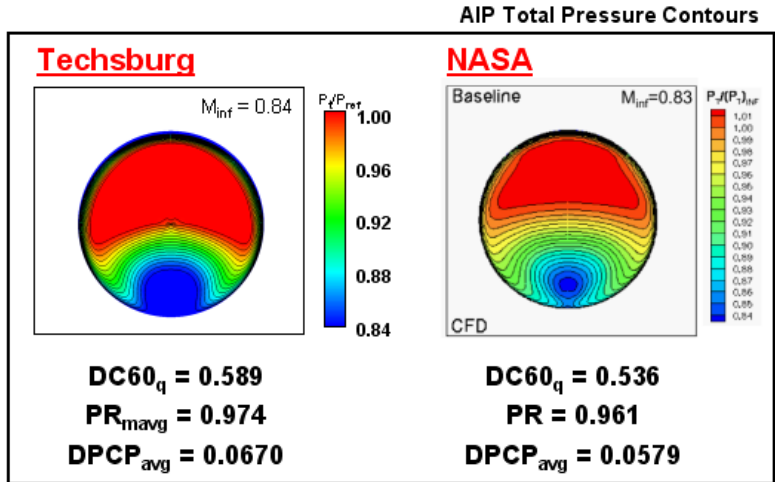


Figure 2-13: AIP Total Pressure Contours - Baseline

2.5.3: Baseline Flow Swirl

The results obtained from the baseline solution as characterized by the SC(60) swirl parameter are noted in Figure 2-14, which shows the secondary flows in terms of streamwise vorticity. It is clear that the region of highest cross-flow velocity is located at the base of the duct. In this location the flow is characterized by two large counter-rotating vortices. Additional vorticity is also present around the periphery of the duct as a result of the formation of a boundary layer.

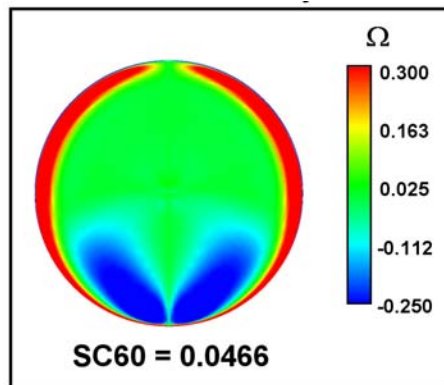


Figure 2-14: Baseline AIP Streamwise Vorticity Contours

2.5.4: Baseline Flow Distortion Mechanisms

For this inlet flow and diffuser geometry there are three distortion mechanisms at work:

- Nacelle junction vortex
- Circumferential pressure gradients
- Ingested boundary layer.

The junction vortex is the result of interaction between streamwise vorticity present within the boundary layer flow as it interacts with the geometry of the junction between the nacelle lip and the floor. The circumferential pressure gradients create secondary flows within the diffuser due to differences in flow momentum as it is forced to turn through the serpentine diffuser (as noted in section 1.2.1). The ingestion of a large boundary layer serves to enhance the effects of both of the previous mechanisms.

The combined effects of these mechanisms are shown in Figure 2-15. The boundary layer fluid at the nacelle entrance is pushed toward the center of the inlet by the ingested junction vortex legs, which have the same sense of rotation as the diffuser secondary flows. The induced rotation is highlighted by the streamlines in Figure 2-16. Once inside the diffuser, the existing circumferential pressure gradients establish the secondary flows and push the low momentum boundary layer fluid to where it collects near the bottom of the inlet in a tongue or mushroom shaped distortion pattern.

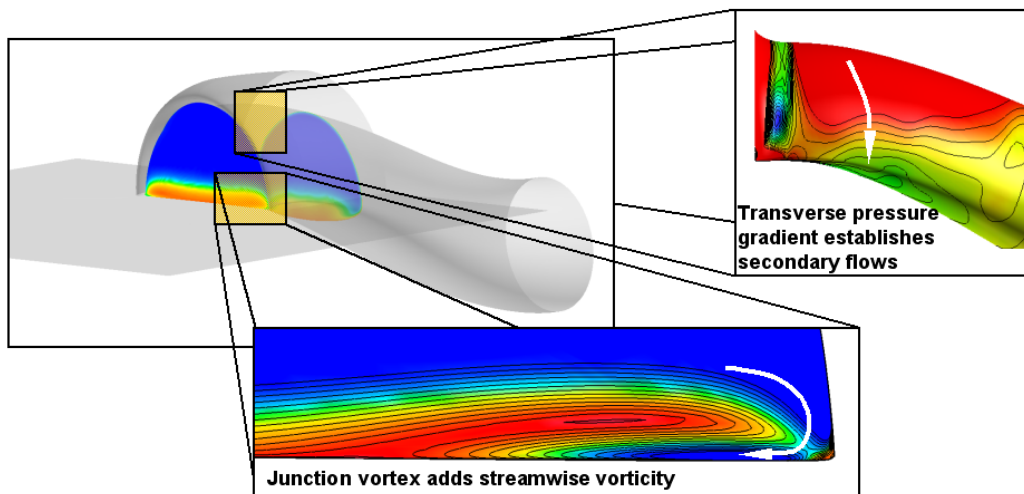


Figure 2-15: Flow distortion mechanisms

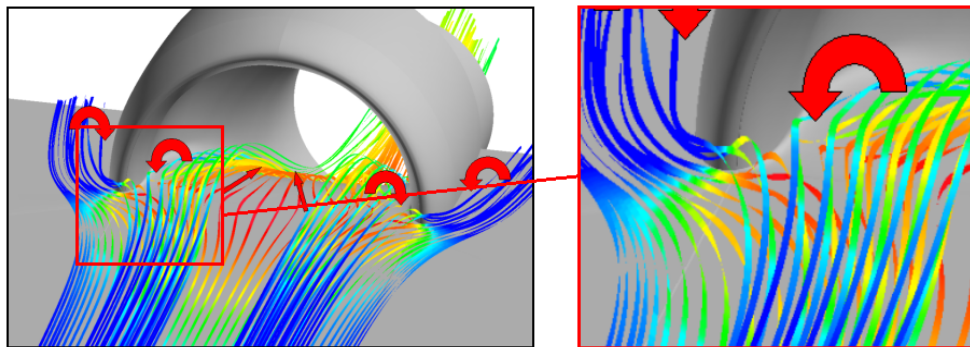


Figure 2-16: Streamlines Depicting Horseshoe/Junction Vortices

2.6: Flow Control Design Strategy

Flow control design strategies were based upon achieving a strong understanding of the driving parameters of engine face distortion. Some elements of the flow control design (i.e. jet orientation) were based on the body of previous work for serpentine inlet flow control^{8, 11} as well as previous experience at Techsburg.

In order to investigate the effectiveness of an ejector-pump based flow control device, flow control implementation was limited to combinations of suction and blowing. To make use of the existing pressure field and maximize ejector performance, suction was primarily employed in regions of high static pressure, while blowing was employed in regions of lower static pressure. To prevent secondary flows from forming, the effectors were placed slightly downstream of the duct throat. This utilized a prevention methodology as opposed to attempting to cure distortion after it has formed. Figure 2-17 shows the optimal locations for flow control based on these criteria. The left image in Figure 2-17 shows contours of pressure coefficient C_p and correspondingly locates the areas of high local static pressure suitable for the location of suction. The right image in Figure 2-17 shows diffuser surface static pressure contours and graphically depicts the optimum flow control jet location.

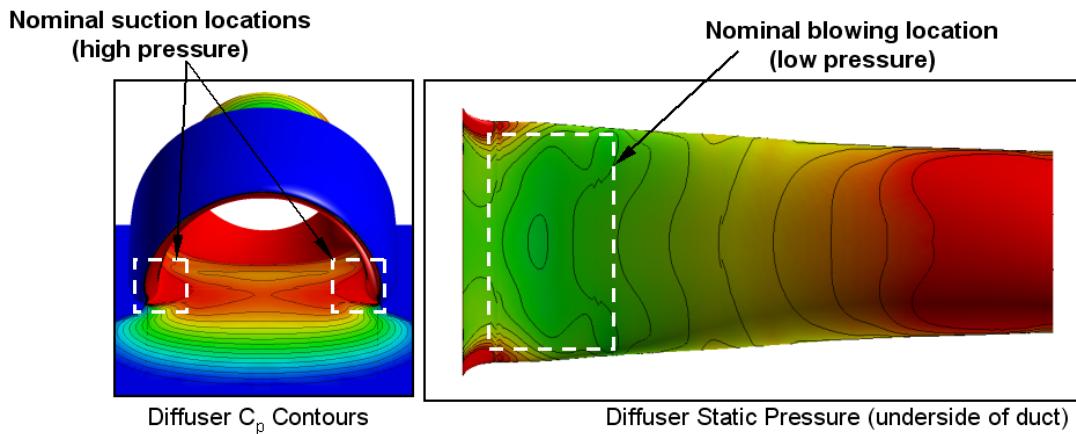


Figure 2-17: Flow Effector Location Rationale

The blowing jet orientation used for all jets in this study was based on the work of Anderson¹² and Gorton¹¹. The jets were configured to have a circumferential blowing angle of 30° from the local surface tangent (blowing outward from the centerline) with a streamwise angle of 90° . Thus, the jets were blowing perpendicular to diffuser axial direction, thereby adding no momentum in streamwise direction. In this orientation, as depicted in Figure 2-18, all the jet momentum is used to directly manage the secondary flow.

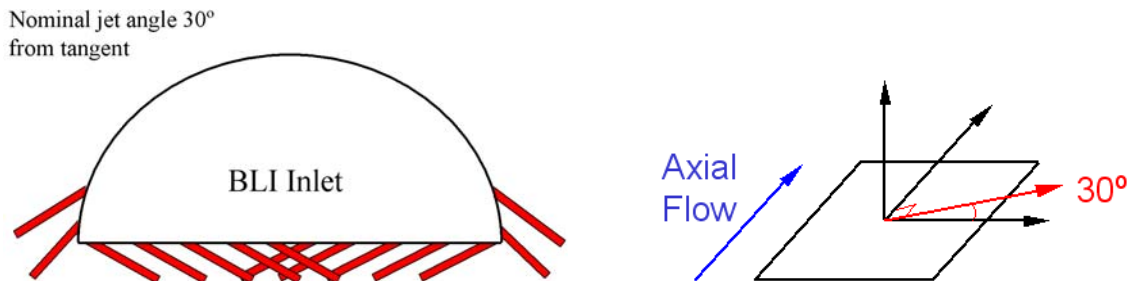


Figure 2-18: Nominal blowing jet configuration

Previous studies have examined the use of vane-type vortex generators with the goal of preventing separation or maximizing diffuser total pressure recovery. However, studies by Anderson et al.¹² have shown that using effectors to manage flow separation does not necessarily

result in the minimum flow distortion at the fan face. By using fluidic actuators to directly manage the diffuser secondary flow, the distortion can be directly managed.

2.7: Blowing Configurations

Blowing investigations covered a wide variety of parameters and geometries. In order to evaluate ejector-based performance vs. conventional blowing, two nominal mass flow rates of 1% and 2% of the inlet mass flow were examined. Cases that used 1% blowing were used to simulate the use of engine bleed for a conventional blowing scenario. The 2% blowing case would be used in combination with a 1% suction to simulate ejector-pump performance.

Different types of jet arrangements were investigated in order to determine key factors leading towards an optimum jet configuration. The general blowing schemes of Figure 2-19 - Figure 2-22 were labeled: Circumferential, Axial, Pyramid, and Reverse Pyramid. In all cases, the jet placement began at $x/L = 0.067$. The circumferential scheme placed all jets at this axial location whereas the following schemes placed only the most forward jet at this station, with successive jets being placed at a distance farther down the diffuser. The initial axial location for the jets was based upon research which showed that losses in jet performance and effectiveness at upstream locations was far less than the penalty of jets being located too close to flow disturbances.¹³ This upstream location also coincided with an area of lower static pressure, which is useful in optimizing ejector pump performance due to the necessity for a lower required motive pressure. As noted by Gorton, for an array of blowing jets there will be distinct blowing jet combinations that are optimal for the control of distortion, especially when seeking to minimize mass flow requirements¹¹. Thus, a variety of different configurations were examined.

2.7.1: Circumferential Blowing

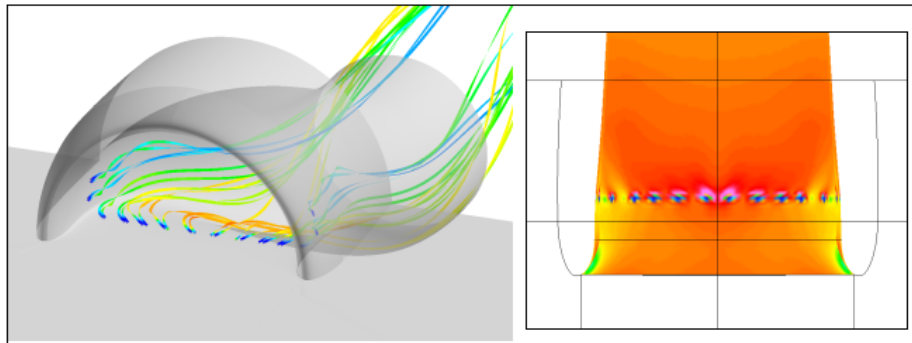


Figure 2-19: Circumferential Blowing

For the circumferential blowing configuration, the jets are spaced around the perimeter of the diffuser at a constant axial location. Five Jets are located along the diffuser “floor”, and two on the sidewall (14 total). The goal of this configuration is to spread the low momentum fluid from the near wall region around the periphery of the duct, while maintaining separation between the vortices created by the jets.

2.7.2: Axial Blowing

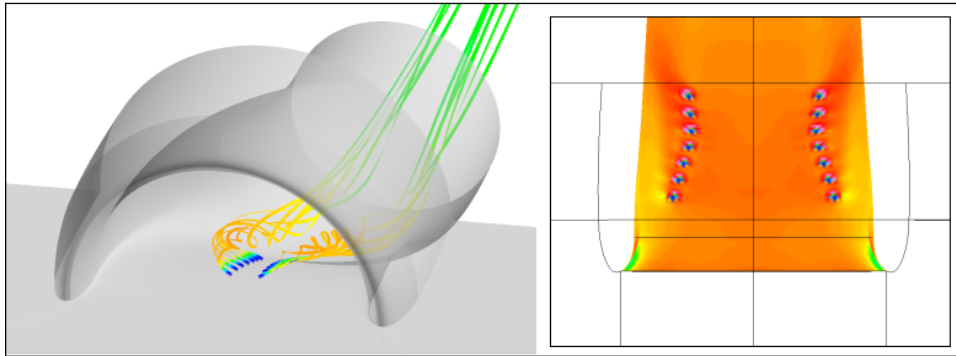


Figure 2-20: Axial Blowing

For the axial blowing configuration, the jets are located in a streamwise row, extending down the axial duct length. The goal is to continually spread the low momentum fluid from the center of the diffuser towards the outside of the duct. Two configurations were tested, one with the jets located near the outside of the diffuser, and the other with the jets located near the center of the diffuser.

2.7.3: Pyramid Blowing

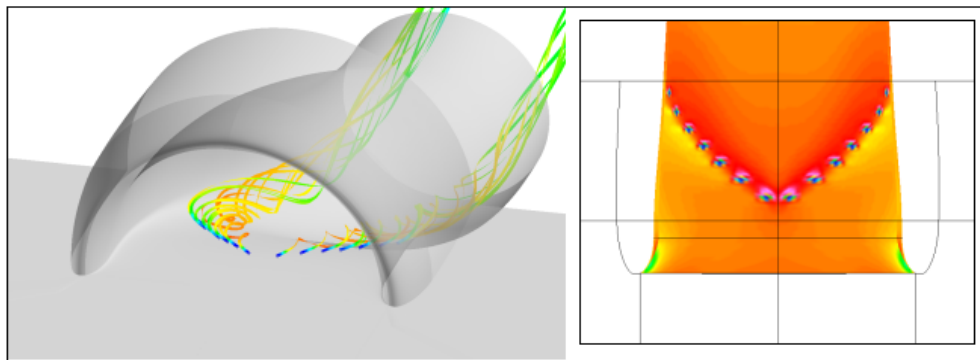


Figure 2-21: Pyramid Blowing

This configuration aims to continually manage the vortex induced by the jets by providing a more constant “push” to the secondary flows while traveling up the diffuser sidewalls. Different jet configurations were tested by progressing through a series of array skew angles. (Pyramid 1, Pyramid 2, Pyramid 3, Pyramid 4). Figure 2-21 shows the Pyramid 1 configuration.

2.7.4: Reverse Pyramid Blowing

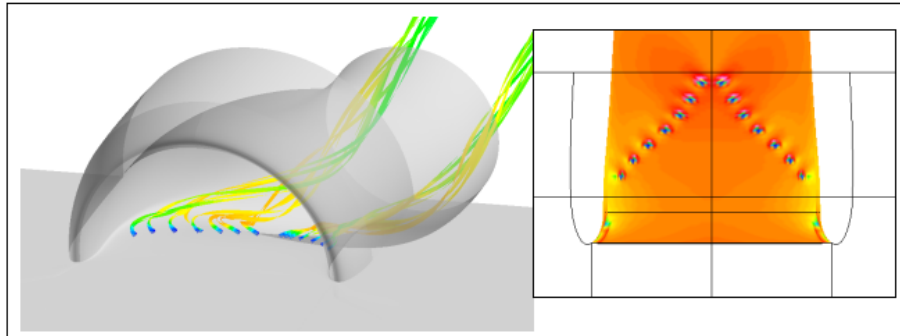


Figure 2-22: Reverse Pyramid blowing

Because the regular Pyramid often results in an additive effect creating a single large vortex on each side of the diffuser, the orientation of the jets was reversed so that the jets acted independently. This configuration aims to continually spread the low momentum fluid around the diffuser, while maintaining jet individuality.

2.8: Suction Configurations

Suction investigations focused on two different configurations – suction at the inside corner of the nacelle lip, and across the inlet entrance as shown in Figure 2-23. The desired location of the suction was determined from the floor pressure distribution. The nominal suction mass flow rate was set to 1% in order to simulate ejector performance. The pressure specified for the inflow boundary conditions was held constant in order to simulate a constant suction pressure. Thus, mass flow rates throughout the suction system are not necessarily uniform due to differences in flow conditions outside the suction ports.

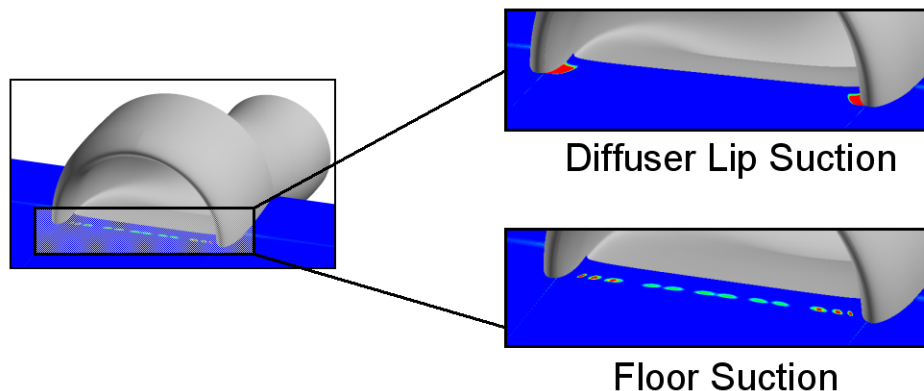


Figure 2-23: Lip and Floor Suction

The locations for the flow suction were placed based upon two basic concepts. The first approach examined the placement of suction near the inside of the diffuser inlet lip. This is an area of high pressure as it is the location of the flow stagnation streamline. As the ejector pump's performance is increased when taking advantage of existing pressure gradients, this would seem to be a promising location. In addition, there is an added benefit of ingesting part of the junction vortex which forms around the lip due to boundary layer flow interactions. This flow structure is believed to be contributing strength to the existing pressure gradients within the diffuser, in particular, reinforcing the secondary flow pattern that leads to a high flow distortion. The second

configuration investigation focused on ingesting the low momentum fluid near the wall as the flow entered the duct. In this setup, the low momentum fluid along the “floor” of the diffuser is ingested. Additional benefit arises from the placement of the suction as it nicely complements the ejector pump setup, having the suction source closer to the jets. This reduction in distance can influence ejector pump efficiency by reducing the fluidic losses as the ingested fluid moves through the pump tubing.

2.9: Modeling the Ejector Pump

2.9.1: Ejector Pump Implementation Considerations

One of the considerations for the blowing and suction configurations described to this point is their compatibility with the implementation of an ejector-pump based fluidic actuator. To implement a scheme similar to that shown in Figure 1-3, the suction and blowing locations should be relatively close together, with some space available for internal ducting to facilitate an efficient design with low frictional losses. Also, as mentioned previously, a favorable pressure gradient will help the ejector’s suction to motive flow ratio to increase. All the ejector models examined meet these criteria.

2.9.2: Blowing and Suction Configuration Selection

To select the combination of suction and blowing cases for modeling the ejector pump, the most effective blowing configurations for the four blowing types (circumferential, axial, Pyramid, or reverse Pyramid) were combined and run with both of the suction types. These combinations are shown in Figure 2-24, with a representative sample of the cases shown in Figure 2-25.

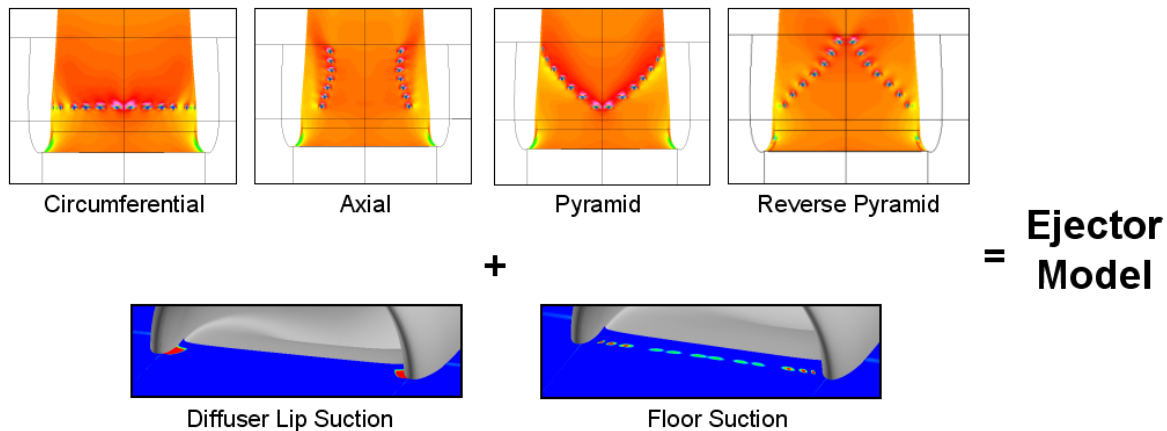


Figure 2-24: Cases Modeled Using Ejector Pump

It should be noted that when comparing the ejector model versus the conventional blowing cases, the jet velocity ratio was maintained with the same supply pressure, while the hole area was reduced. This worked to decrease the blowing jet mass by 50%, while keeping the velocity ratio constant compared to the ejector pump cases.

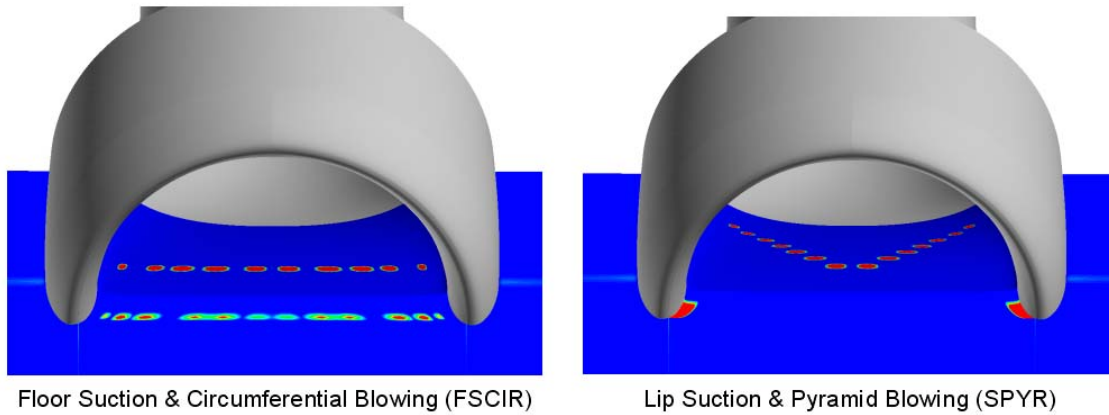


Figure 2-25: Sample Ejector Pump Models

Flow Control Results Summary

The flow control results for the most promising flow control cases are shown in Figure 2-29- Figure 2-30. The following list details the enumeration of each of the flow control cases. The better performing of these cases will be examined in detail. Complete documentation of all investigated flow control cases and their distortion values are discussed in Appendix G.

2.9.3: Flow Control Results

The flow is analyzed at the AIP for distortion using the descriptive parameters described in earlier sections.

The DC(60)pt distortion parameter examines the ‘worst’ (i.e. lowest total pressure) 60° sector of the flow non-dimensionalized by the average AIP total pressure. In addition to the DC(60)pt results, Figure 2-26 also presents the AIP total pressure contours to serve as a visual aid in showing the effects of the flow control. The DC(60)pt parameter yields a baseline value of approximately 0.12. As shown, all flow control scenarios examined reduced the total pressure distortion according to the DC(60)pt criterion. The conventional blowing scenarios (1% AIP total mass) were both successful in reducing the distortion, with the Pyramid 1 configuration yielding a 22.5% reduction, and the circumferential case yielding a 10% reduction. Significant improvement was achieved over and above these results when adopting the ejector pump model. The Pyramid and lip suction model (SP1) achieved the largest reduction in total pressure distortion by reducing it 55% below baseline distortion levels. The circumferential case also achieved a significant reduction in decreasing AIP distortion by 50% below baseline. Visual contours suggest that the boundary layer fluid has been successfully redistributed. (Further examination of pressure contours are discussed in a later section.)

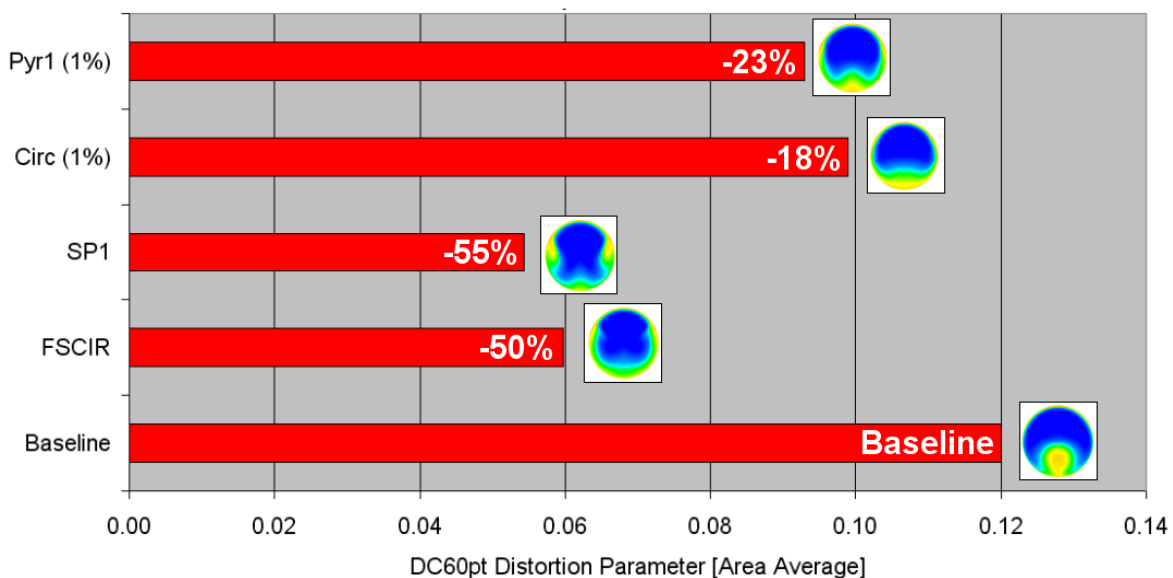


Figure 2-26: DC(60)pt Distortion Parameter Results

The distortion results of Figure 2-27 are quantified by the DC(60)q parameter, which non-dimensionalizes the total pressure distortion using the average dynamic pressure at the AIP. This parameter shows the same trends as those obtained using the DC(60)pt parameter. However, this parameter indicates a maximum reduction in distortion of 75.2% for the SP1 case. Similar to the DC(60)pt metric, this parameter indicates a larger benefit in using the ejector pump. This difference is likely the result of the higher velocities associated with the formation of

large vortices, which are more prevalent in the stronger flow control efforts. It should be noted that none of the tested models achieved the ‘acceptable’ distortion level of $DC(60)q = 0.10$. However, these systems were not optimized and additional work could likely yield a configuration that achieved the desired level of performance.

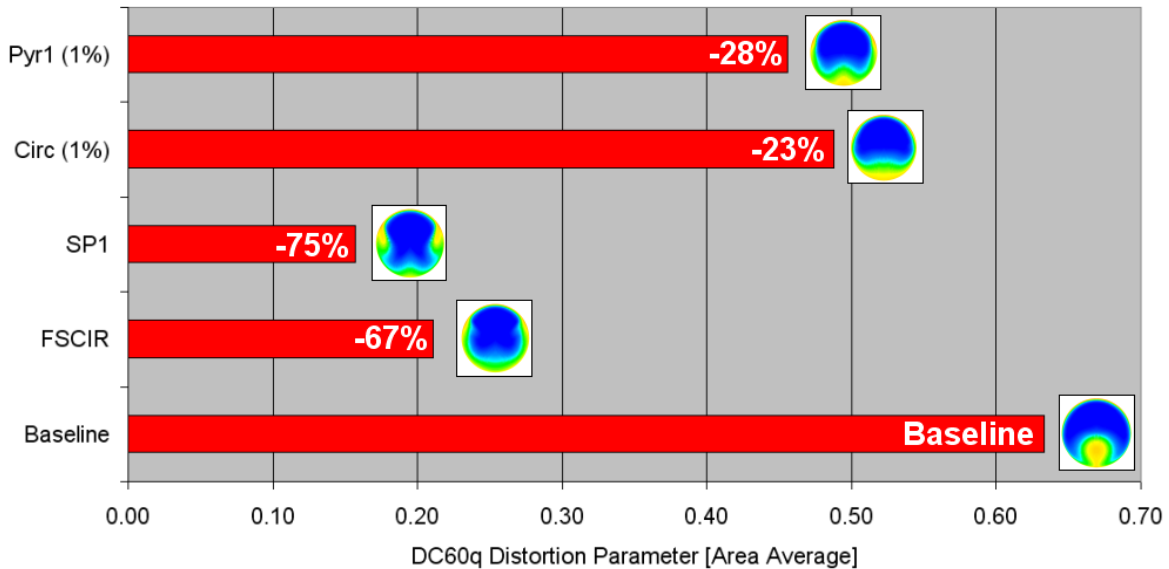


Figure 2-27: DC(60)q Distortion Parameter Results

The SAE distortion descriptor $DPCP_{avg}$ varies slightly in its perception of flow distortion at the AIP, as shown in Figure 2-28. In contrast to the $DC(60)$ descriptors, the $DPCP_{avg}$ parameter reflects an average distortion for the whole AIP, as opposed to representing only the worst 60° sector of the flow. Although the distortion is significantly reduced by all flow control schemes, the circumferential ejector configuration is quantified as being more effective than the Pyramid1 configuration. The maximum reduction in distortion is achieved by the floor suction and circumferential (FSCIR) scheme in yielding a 71.1% reduction. The control mechanism suggested by the total pressure contours suggests that although the circumferential ejector model does not have the ‘best’ 60° sectors, the distortion is more evenly distributed around the periphery of the duct. This result is consistent with the visual pressure contours shown. These results also suggest that the lowest distortion is achieved by the configurations in which the individual jets do not coalesce into a single vortex. The circumferential configuration has this feature, in contrast to the Pyramid 1 scheme that continually reinforces a single vortex that sweeps up the sides of the diffuser.

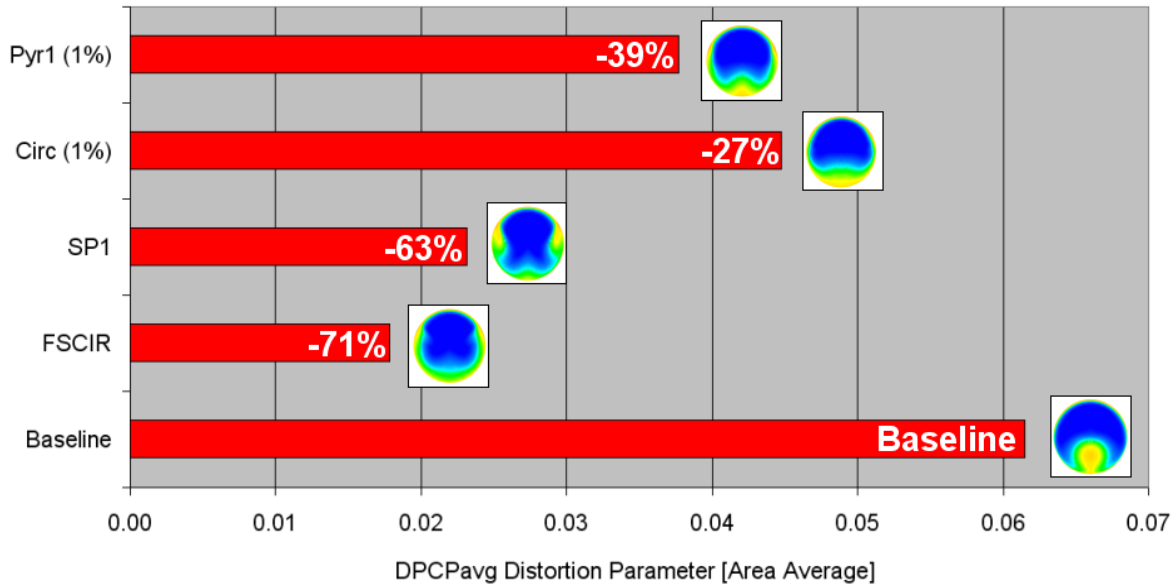


Figure 2-28: DPCPavg Distortion Parameter Results

Results from investigations using the SC(60) swirl parameter examine the relative strength of the secondary flow structures at the AIP. Values shown in Figure 2-29 represent the overall effectiveness of the flow control system to successfully counteract the formation of secondary flows within the diffuser and thus provide quality flow to the compressor. As can be seen, the circumferential schemes are by far the most effective in reducing swirl at the AIP. Due to the large-scale vortices created by the Pyramid blowing schemes, AIP swirl for Pyramid configurations is actually increased by a maximum of 64% over baseline swirl. These results again reinforce that distortion is most effectively managed with jets that do not coalesce into a single large vortex, but rather maintain their own scale and remain within the bounds of the low-momentum fluid.

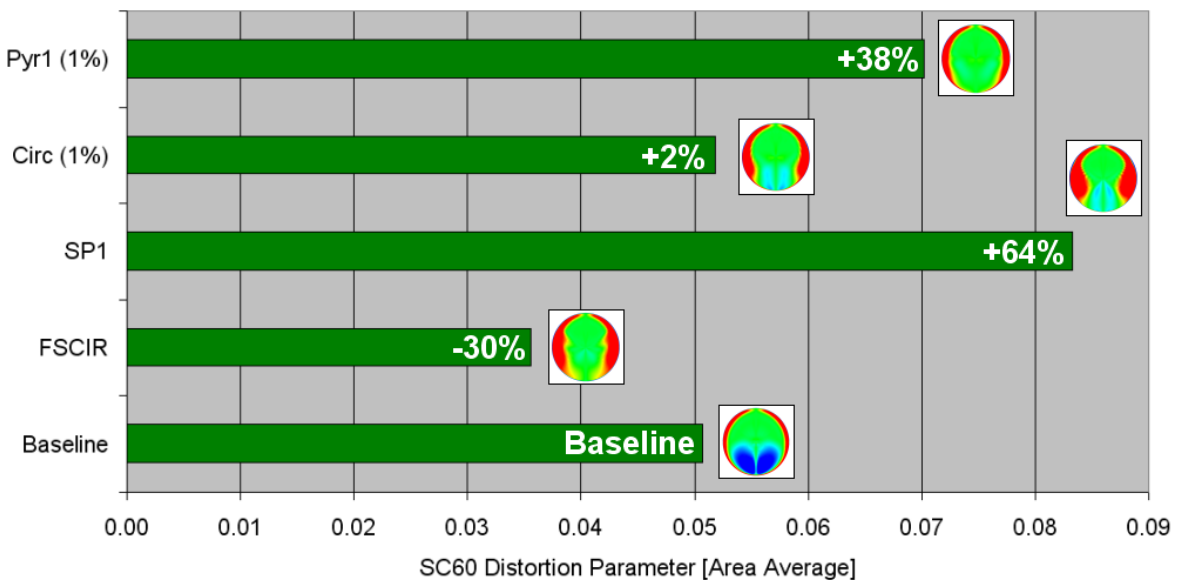


Figure 2-29: SC(60) Swirl Distortion Parameter Results with Streamwise Vorticity Contours

Investigations into the effect of flow control on diffuser total pressure recovery have shown that there is little to no benefit obtained by using fluidic actuators inside the diffuser. This is not particularly surprising since the goal of the flow control is merely to redistribute the low-momentum fluid to create a more uniform flow at the AIP. It should be noted however, that these minor effects are likely to be small in comparison to the losses typical of the large vane generators needed for high boundary layer ingestion.¹⁴

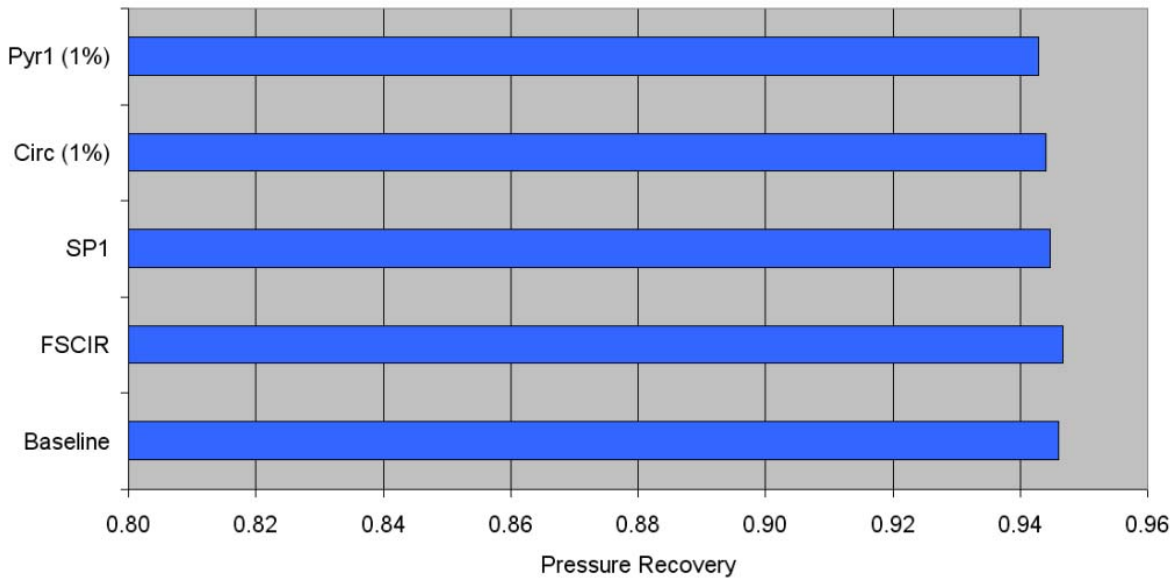


Figure 2-30: Total Pressure Recovery Results

The complete results for the ARP-1420 circumferential and radial distortion intensity descriptors are shown in Figure G.0-3.

2.10: Flow Control Visualization

Further examination of the total pressure and vorticity contours of the flow control results at the AIP, allows for better understanding of how the flow control has affected the flow distortion. Examining a few of the best ejector-based flow control results and comparing them to a conventional blowing scheme of the same type can yield an understanding of the primary mechanisms that are the most productive in flow control. The schemes that will be examined in detail will be the floor suction and circumferential blowing (FSCIR), lip suction and Pyramid 1 blowing (SP1), and the comparative conventional blowing schemes circumferential and Pyramid 1. These results will all be compared relative to the baseline case (no flow control). The total pressure contours of the aforementioned cases are shown in Figure 2-31, and their respective distortion values are listed in Table 2-1. For a complete listing of all flow control results, refer to Appendix G.

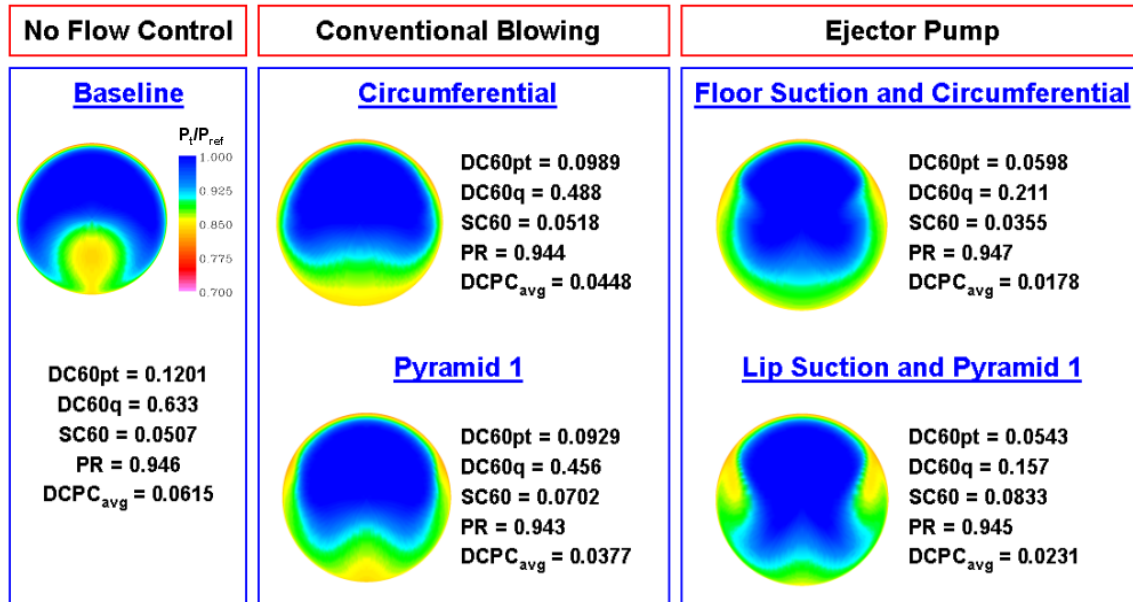


Figure 2-31: Conventional Blowing and Ejector Pump Total Pressure Contour Comparison

Table 2-1: Comparison of distortion reduction parameters for select cases.

Distortion Parameter	Distortion Parameter Value [% reduction from baseline]				
	Baseline	Circumfer.	FSCIR	Pyramid 1	SP1
DC(60)q	0.633	0.488 [23%]	0.211 [67%]	0.456 [28%]	0.157 [75%]
DC(60)pt	0.120	0.099 [18%]	0.060 [50%]	0.093 [23%]	0.054 [55%]
DPCPavg	0.062	0.045 [27%]	0.018 [71%]	0.038 [39%]	0.023 [63%]

The total pressure contours in Figure 2-31 clearly indicate the large effect flow control has had on the AIP distortion. The baseline configuration clearly shows a large region of low total pressure fluid in the lower portion of the AIP collected by the strong secondary flows within the diffuser. In first examining the total pressure contours for the conventional blowing cases (total jet mass equal to 1% of the mass through the AIP), it is evident that a large change in total pressure distortion has occurred. In both cases, the jets have significantly reduced the distortion at the AIP. As indicated in Table 2-1, the conventional circumferential blowing scheme reduced the DC(60)q distortion by 23% as compared to the baseline (no flow control) solution, and the Pyramid 1 configuration reduced the DC(60)q distortion by 28%. The contours displayed in Figure 2-31 show a redistribution of the low total pressure fluid around the periphery of the diffuser, with some residual areas of low total pressure fluid, particularly at the bottom of the AIP. As this is the original location for the “pooling” of the flow, it appears that the jets are not quite effective enough to counteract the formation of strong secondary flows within the diffuser. By implementing an ejector-based series of fluidic actuators, the relative strength of the flow control jets was increased by providing additional mass flow (and hence momentum addition) in combination with some boundary layer suction.

The ejector pump based flow control jets produced a significant improvement in the reduction of total pressure at the AIP as compared with the conventional blowing only scheme. As compared to the baseline configuration, the DC(60)q distortion parameter was reduced by 67% and 75% in

the FSCIR and SP1 configurations respectively, almost reaching the operation $DC(60)_q$ of 0.10. It should be noted that the ejector-based actuators obtained this further reduction with no additional increase in motive jet air, and thus had the same jet supply requirements. By examining the total pressure contours it is clear that the low-momentum fluid from the ingested boundary layer, along with the low momentum fluid from boundary layer growth on the diffuser have been effectively redistributed away from the lower section of the AIP. Although the ejector-based circumferential case (FSCIR) has higher $DC(60)$ distortion parameters than the Pyramid 1 ejector case (SP1), the DPC_{Pavg} calculation indicates that the average distortion in the FSCIR case is lower. This would seem to coincide with the visually more evenly distributed contours of the FSCIR case. The difference indicated by the two $DC(60)$ parameters indicates that in the “worst” 60-degree sector of the flow the SP1 case locally has a lower maximum distortion. Thus, although the parameters indicate that the SP1 case has a lower distortion in some cases, it is clear that some sensible qualification of these results must be examined at all times. There are, of course, many more types of flow distortion descriptors currently in use in both industry and academia, but they are in most cases much more complicated, and engine specific. However, by examining total pressure distortions in combination with local values of streamwise vorticity at the AIP, one can easily interpret the nuances of the flow distortions.

The secondary flow contours in Figure 2-32 show the solutions that have been examined in detail, and help to highlight the flow characteristics at the AIP. These flow patterns aid in discerning how the fluidic effectors have altered the secondary flows within the diffuser, which have been identified as one of the primary sources of engine-face flow distortion. In order to quantify the severity of the secondary flow, the flow contours can be correlated to the $SC(60)$ swirl parameter. As noted previously, the baseline flow is characterized by two large counter-rotating vortices at the base of the AIP, with a $SC(60)$ value of 0.0507. When examining the AIP secondary flow contours, the conventional blowing cases show a clear effect on secondary flow. These cases both show a net increase in flow swirl, although the circumferential case is almost at the same $SC(60)$ value as the baseline. The ejector pump cases also show a substantial change in the AIP secondary flow structure, and have eliminated the vortices created in the baseline flow. However, only the circumferential ejector case has reduced swirl below its original level. This decrease correlates well with the visual contours that suggest a symmetric distribution of secondary flows around the AIP.

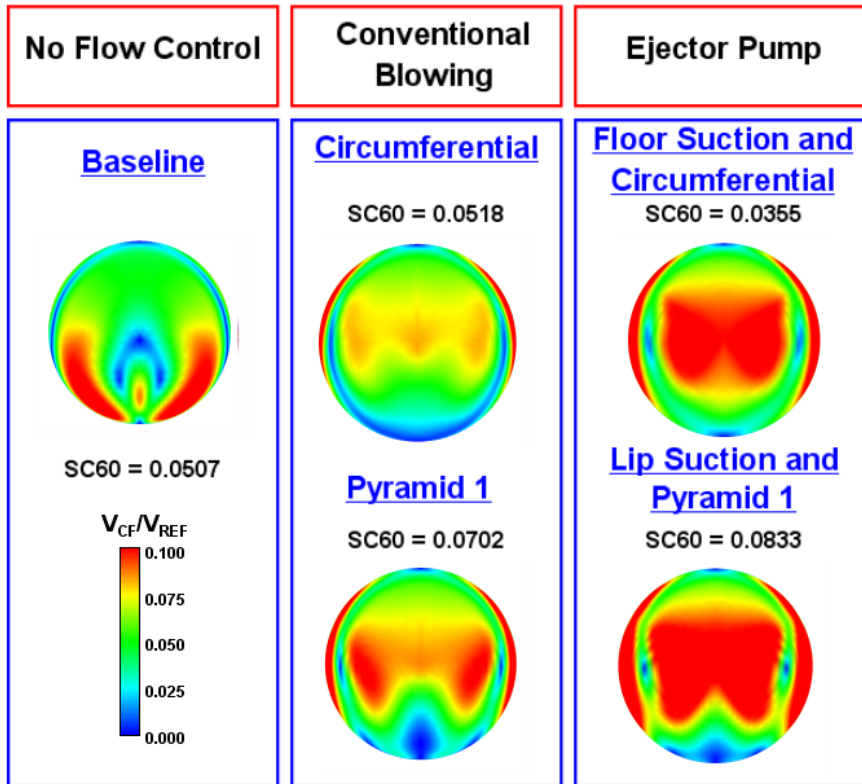


Figure 2-32: Streamwise Vorticity Contours

While both effective, the results for the circumferential blowing and Pyramid blowing cases at the AIP are quite different. In an attempt to better understand the dynamics of the flow for these cases, Figure 2-33 shows flow tracers used to track the fluid trajectories. Important elements to note are:

- The majority of the fluid in the distortion lobe at the AIP comes from the ingested boundary layer flow. This low-momentum fluid is collected into the center by the pressure gradients and resulting secondary flow.

The spanwise spacing and relative location of the jets is important, and could be optimized with increased understanding of the flow physics. While the jets in the Pyramid 1 scheme are effective, they could be more effective if they were not located such that all streams coalesce into a single vortex. Predominantly spacing the jets spanwise as opposed to axially seemed to produce “better” AIP flow patterns (but not necessarily lower DC(60) results).

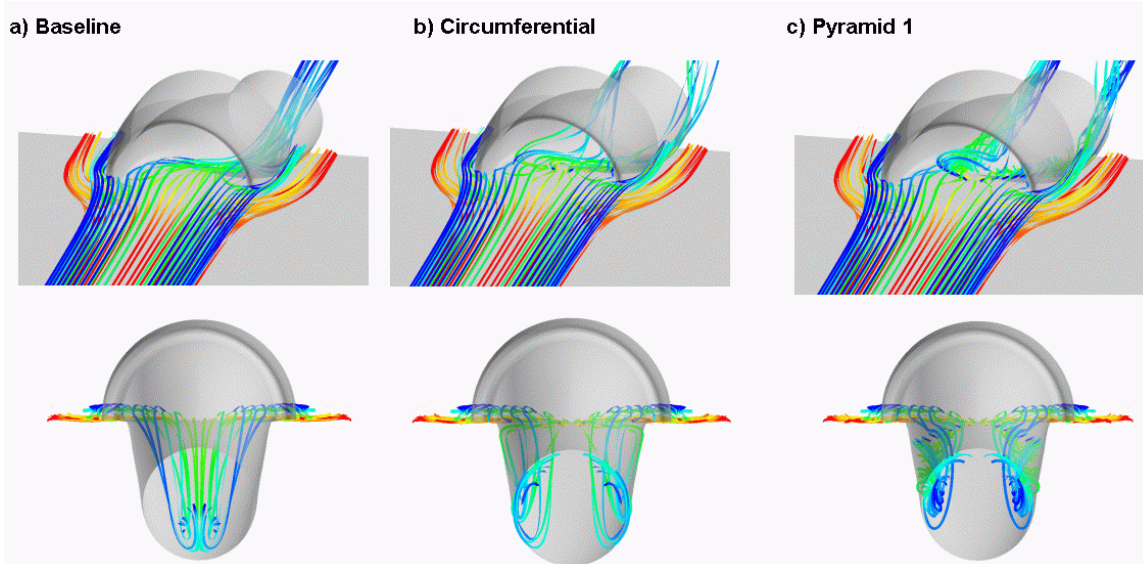


Figure 2-33: Boundary Layer Streamlines

Cross-examining the ingested boundary layer streamlines with the streamlines coming from the flow control jets also highlights the mechanisms in which the flow control was most effective. The circumferential ejector case FSCIR is depicted in Figure 2-34. In this case, the individual jets remain distinct and separate throughout most of the diffuser, and are effective in “smearing” the low-momentum fluid around the periphery of the diffuser. This is apparent when examining the total pressure contours at the AIP (Figure 2-34 - far right).

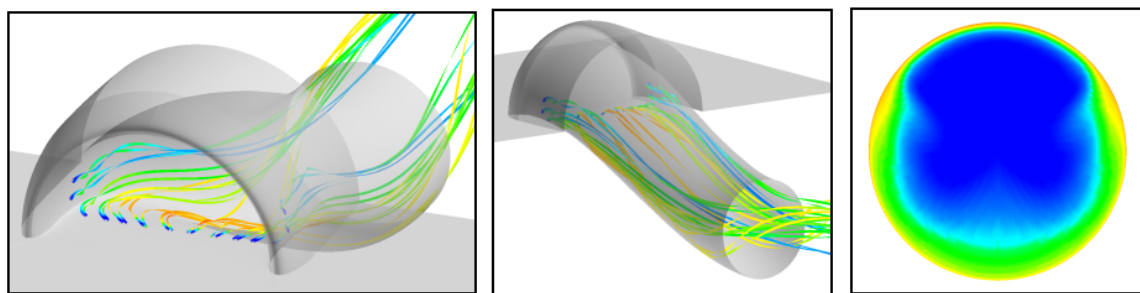


Figure 2-34: Jet Flow Streamlines – Circumferential Ejector (FSCIR)

Flow tracers for the Pyramid 1 ejector case SP1 are shown in Figure 2-35. Here it is apparent that the jets are located such that they coalesce into two counter-rotating vortices that “roll” up the sides of the diffuser, redistributing the low-momentum fluid along the way. When examining the AIP total pressure contours, (Figure 2-35 - far right) it is clear that although the DC(60) parameter indicates a lower total pressure distortion, the flow appears to be less uniform in its appearance due to the presence of these vortices.

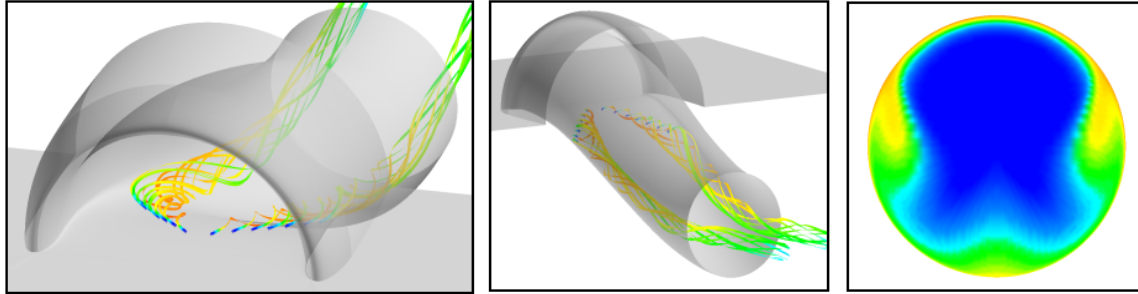


Figure 2-35: Jet Flow Streamlines - Pyramid 1 Ejector (SP1)

It is apparent that the reduction of total pressure by the current method suggests that the most effective spreading of low-momentum fluid resulted from jet configurations that kept the vortices produced by flow control separate.

2.11: Strake

One of the identified mechanisms for flow distortion in BLI diffusers is the creation of a junction vortex formed by the interaction of vorticity present in the boundary layer combined with the nacelle-wing junction. By altering the geometry of the nacelle leading edge in the boundary layer region, this flow can be virtually eliminated as a source of distortion. This allows the flow control to be more effective in managing the secondary flows created by the diffuser offset. The strake height is roughly equal to the height of the ingested boundary layer and has length-to-height ratio of $\sim 3:1$. The geometry shown in Figure 3-27 represents the geometry tested in the CFD and experimental analyses. It is believed that the strake will reduce the baseline flow distortion as well as allow the flow control to be more effective in countering flow distortion at the AIP.

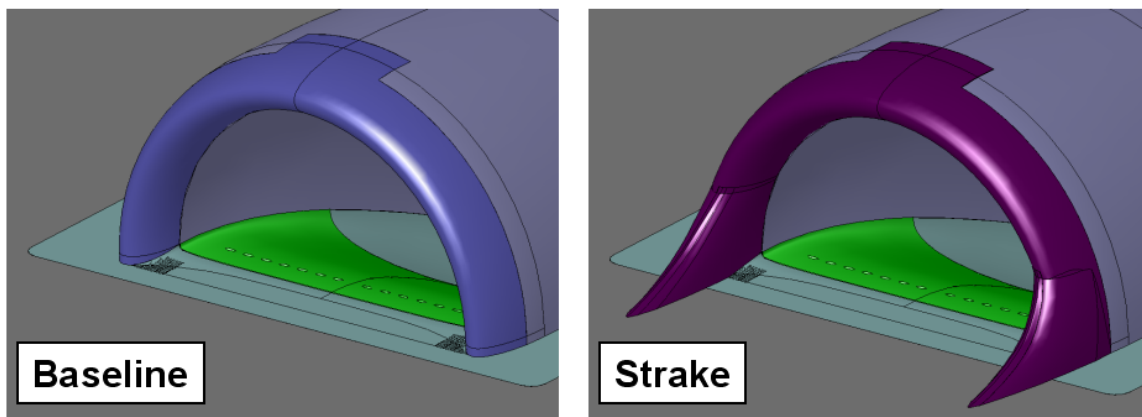


Figure 2-36: Strake Geometry

2.12: Strake Computational Results

The CFD modeling of the strake proved to be of considerable difficulty. Due to the structured nature of the mesh, the addition of the strake to the nacelle lip caused a large portion of the grid to be skewed forward. This increased the computational time required to obtain a solution. As shown in Figure 2-37, the designed strake was not highly effective in reducing the severity of the junction vortex. In order to have a large effect on this structure, it is likely that significant work would be required to create a geometry tailored for this particular nacelle geometry.

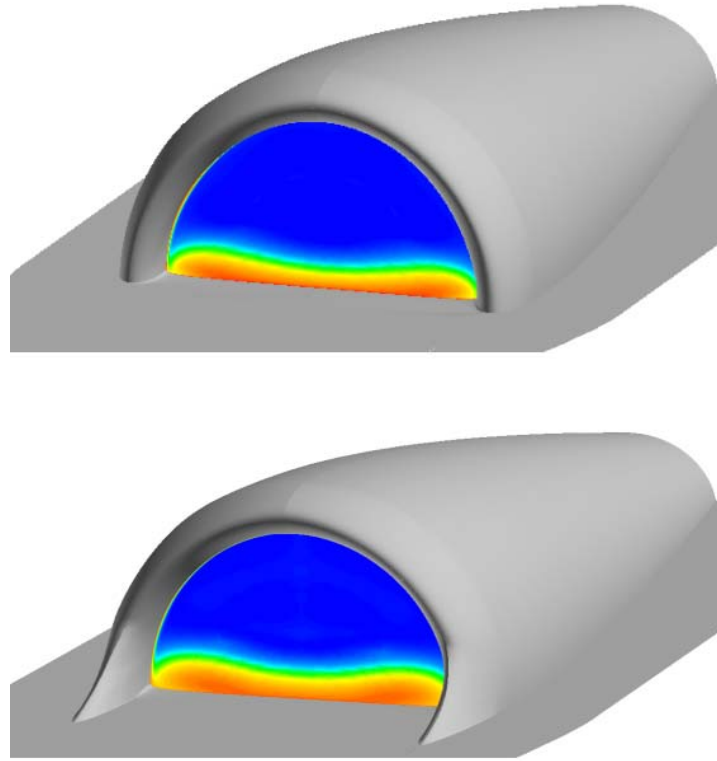


Figure 2-37: Strake Effects

Chapter 3: Experimental Validation

In order to validate the results of the CFD BLI serpentine diffuser flow control tool, an experimental investigation was undertaken. This was accomplished by designing and building a unique test section to function in combination with the Techsburg Ejector-driven wind tunnel facility. When combined, the setup was capable of matching the flight Mach number and altitude consistent with BWB cruise conditions.

3.1: Facility Overview

The tunnel operates by using an ejector-pump to serve as a suction source for the tunnel test section; air from high-pressure tanks is driven through a nozzle contained in the ejector pump. The low pressure created locally by a supersonic jet entrains air from its surroundings by drawing it through the test section. This draws high-speed, low-pressure, low temperature flow through the test section. This facility operates in contrast with conventional high-speed testing facilities. In order for conventional facilities to achieve high Mach number flows, one of several conditions typically applies: 1) small test sections not capable of simulating complex duct flows, 2) high costs associated with providing (blowing) a constant supply of air, or 3) the use of a cryogenic gas to simulate high-altitude conditions. Thus, the use of an ejector-based tunnel at Techsburg allows for the facility to provide the required test conditions at a minimum of complexity and cost associated with more conventional experimental facilities.

The tunnel configuration for this experiment is represented in Figure 3-1.

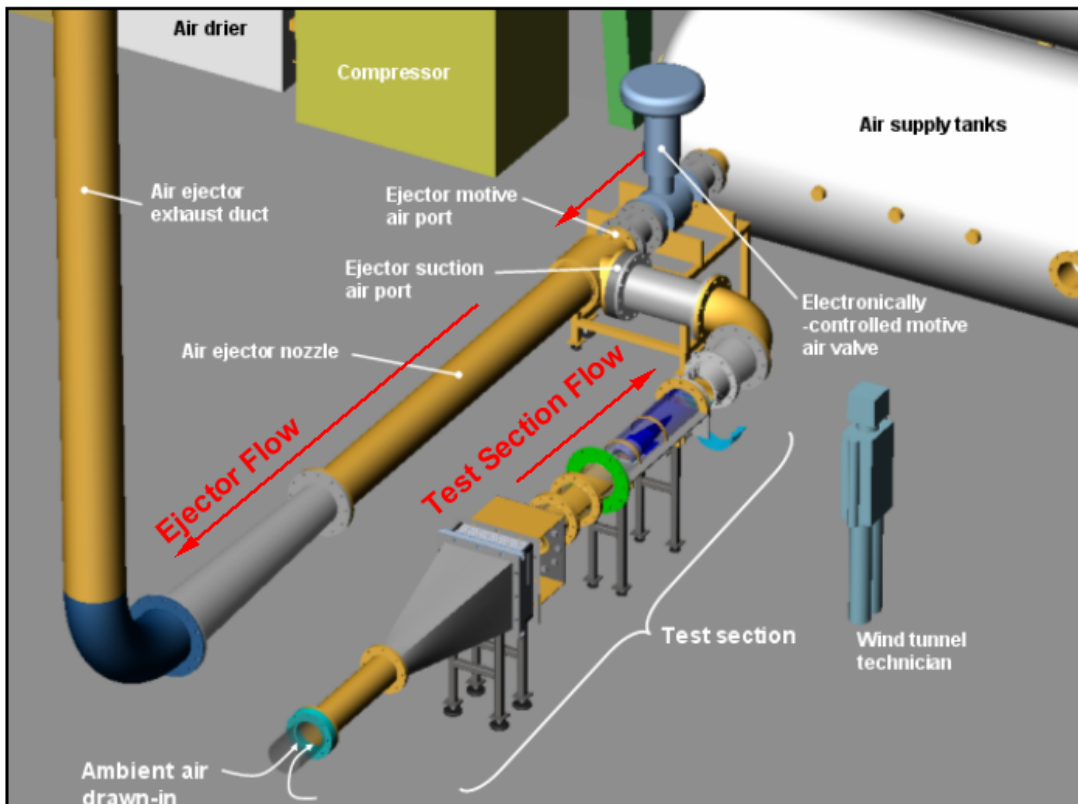


Figure 3-1: Techsburg Ejector-Pump Wind Tunnel Facility

A compartmental breakdown of the ejector-pump wind tunnel and a schematic of the operational elements are shown in Figure 3-2. As shown, the tunnel draws in ambient air through valve #1 at the lower left corner of the figure. The flow passes through a long pressure drop section designed to decrease flow total pressure to levels indicative of high altitude. The drop is achieved through friction losses in combination with the losses associated with an upstream valve and screens located in between the pipe junctions. The flow is then expanded and passes through a series of flow conditioning and honeycomb screens to facilitate flow straightening. Flow then enters a plenum chamber and is drawn into the semi-circular boundary layer growth region through a bellmouth entrance. Once in the growth region, the boundary layer is naturally ‘grown’ up to the target boundary layer thickness of 30% of the inlet height.

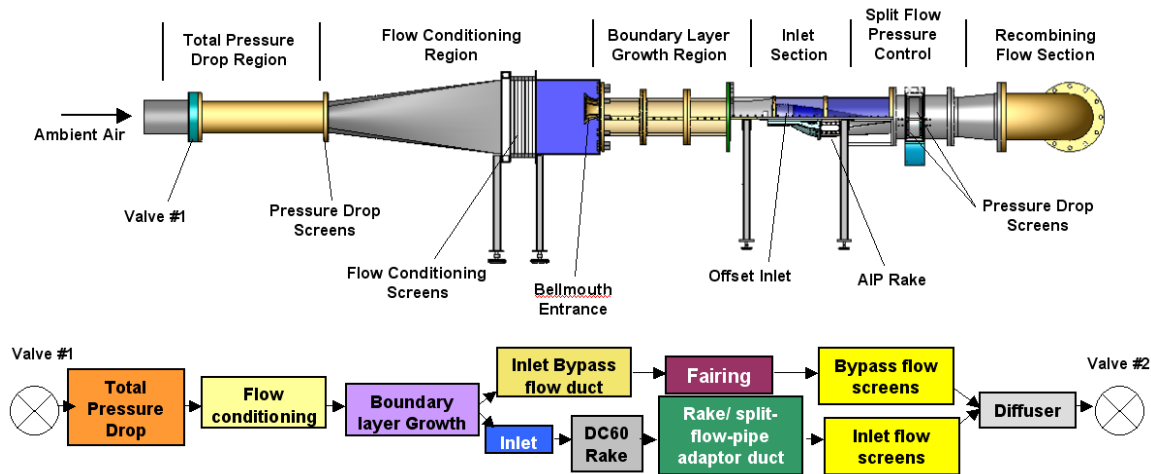


Figure 3-2: Ejector-Pump Tunnel Section

In the inlet section, the flow is split into bypass and diffuser (duct) sections. The bypass region is used to simulate external flow over the engine nacelle and also ingests corner flows that have developed over the growth region. The diffuser (duct) represents the boundary layer ingesting serpentine diffuser. Located at the aft end of the diffuser is the six-arm total pressure distortion rake. After passing through a series of variable pressure drop screens, the flow is recombined and enters the suction port of the main tunnel ejector.

A more detailed explanation and description of the key tunnel components will now be discussed. Complete details of the setup are outlined in the Techsburg Wind Tunnel Design Report.¹⁵

3.1.1: Boundary Layer Growth Region

The boundary layer growth region is composed of a series of pipes that incorporated machined aluminum plates to represent the aircraft’s upper surface, as depicted in Figure 3-3. These plates were tapered to account for boundary layer growth throughout this section. By accounting for the displacement thickness of the boundary layer, the axial pressure gradient was reduced to a minimal effect so that the flow throughout this region would remain effectively constant in velocity, and the boundary layer profile would be relatively unaffected. (The experimental measurements of this gradient are shown in Appendix J.) The bellmouth at the beginning of this section was designed to draw flow from the plenum chamber with a low level of turbulence. Prior to entering the test section, the walls near the inlet diffuse to allow for the

natural compression associated with ram effects of the inlet, and to allow smooth passage of flow streamlines into the bypass flow over the engine nacelle. The curvature of the wall was obtained by extracting the coordinates of a flow streamline obtained from CFD analysis at the design condition.

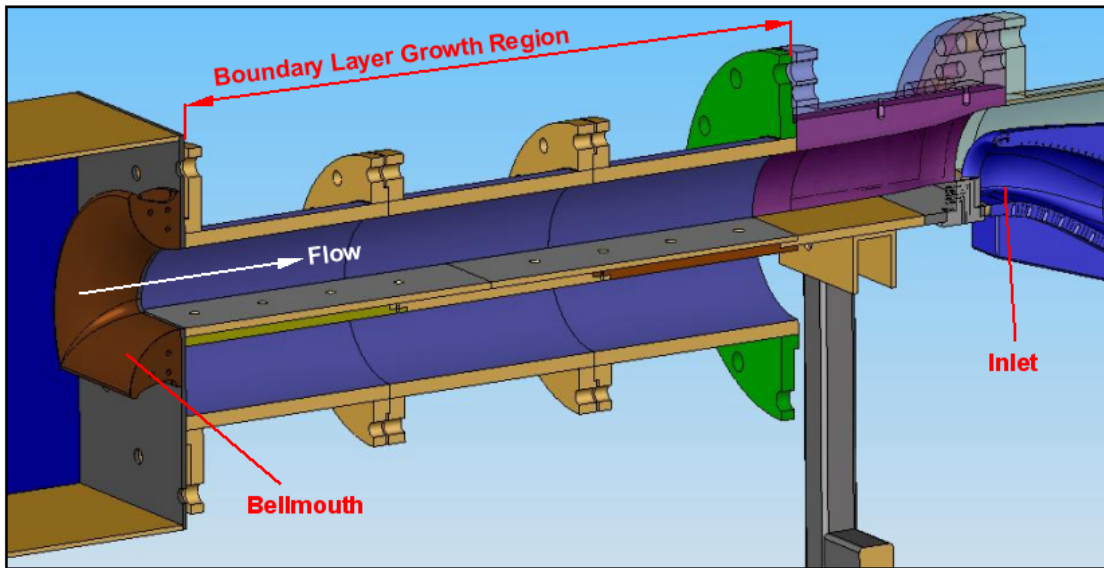


Figure 3-3: Boundary Layer Growth Region

3.1.2: Inlet test Section

Once the flow passes into the inlet test section, it is split into two separate flows. Some of the flow is ingested into the BLI diffuser, and the remainder of the flow is diverted around the outside of the inlet to simulate freestream flow around the engine nacelle. This flow division is shown in Figure 3-4.

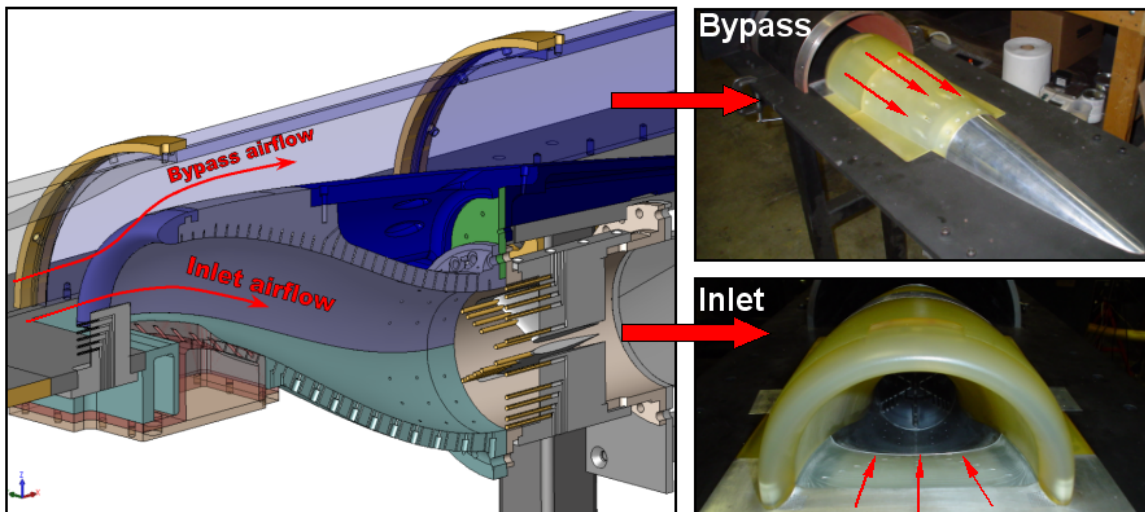


Figure 3-4: Inlet Test Section

By inserting differential screens into the flow at a downstream location, the capture area of the inlet was effectively altered. (To be discussed in further detail in a later section.) The inlet flow passes over the flow control insert and through the BLI diffuser and into a section where the distortion rake measures the effects of the flow control.

The diffuser itself is composed of several major components. The upper half of the diffuser is made using stereo-lithography (SLA) techniques. A removable cover in the bypass flow allows for access to pressure instrumentation located throughout the diffuser. For safety purposes, the lower inlet section is machined from aluminum and supports the pressure differential between operation tunnel conditions and atmosphere, a difference of approximately 10psi. A large slot is cut out of the diffuser to allow for installation of a flow control insert specific to the blowing configuration to be tested. In addition, the floor of the lower inlet has several holes drilled near the nacelle lip location to facilitate flow suction to be used in ejector pump modeling.

3.1.3: Flow Control Inserts

As flow passes into the diffuser, it passes over the test configuration flow control insert. The inserts were made using SLA, and represent variations of the circumferential and reverse Pyramid configurations studied in the CFD flow control analysis. The jet configurations are outlined in Figure 3-5. The blowing angles of the jets are the same as those examined in the CFD analysis, and draw air through a plenum incorporated into the insert. As will be noted in a later section, the motive pressure is obtained through regulated control of the pressure differential between tunnel and atmospheric conditions. The size of the flow control jet holes are scaled equivalents in cross-sectional area to those used in the CFD analysis. (The test configuration is slightly larger in size than the CFD solutions.) In contrast to the jets modeled in CFD using cell boundary conditions, these jets have a round cross-section and incorporate a significant length to diameter ratio (~10:1) to facilitate a developed jet flow.

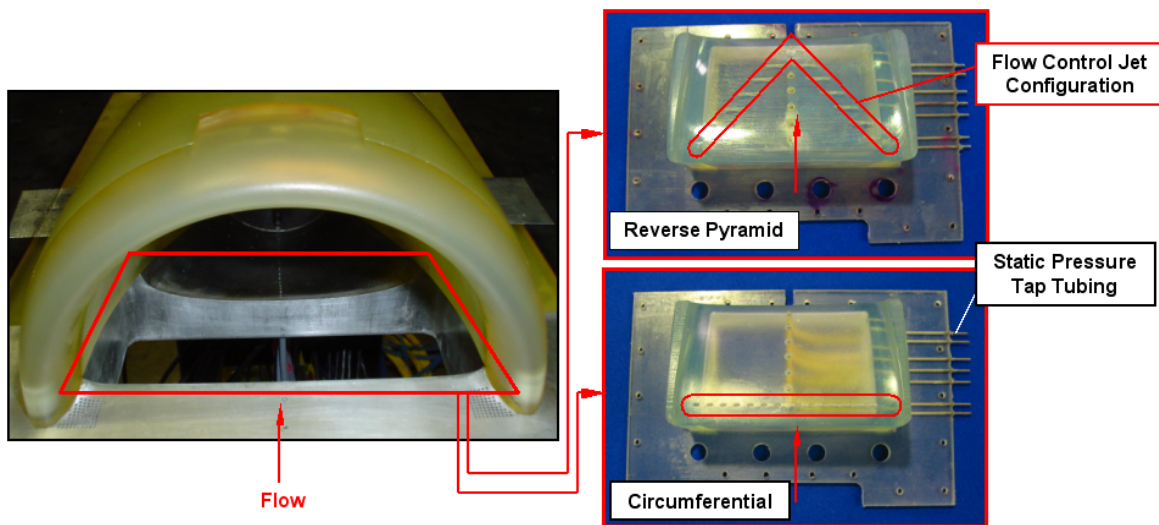


Figure 3-5: Flow Control Inserts

3.1.4: Distortion Rake

The distortion rake is a standard six-arm design that measures inlet face (AIP) total pressure, and correlates the data according to the DC(60) distortion parameters. A cross-section and photo of the rake are shown in Figure 3-6. The pressure probes are located such that all measurements represent an equal area-averaged segment of the AIP total pressure. The total pressure probe tips are located directly at the AIP in order to measure the flow at the virtual engine face. The probes extend 1.25" upstream from the airfoil-shaped struts on which they are mounted as an attempt to minimize the potential effects of the struts. In addition, the probe tips have a 40° internal conically tapered head in order to accept flow vectors that are not aligned with the axial flow direction by as much as 28°. The rake airfoils use a NACA 0010 airfoil section and are designed to create a minimum flow blockage of approximately 20% in terms of frontal area. The curvature of the rake walls also incorporates a slight area increase in order to offset flow blockage effects due to the airfoils and associated boundary layer growth. In addition to the 30 total pressure probes, 6 static pressure measurements are located on the wall between the rake blades, and allow for the approximate calculation of dynamic pressure at the AIP.

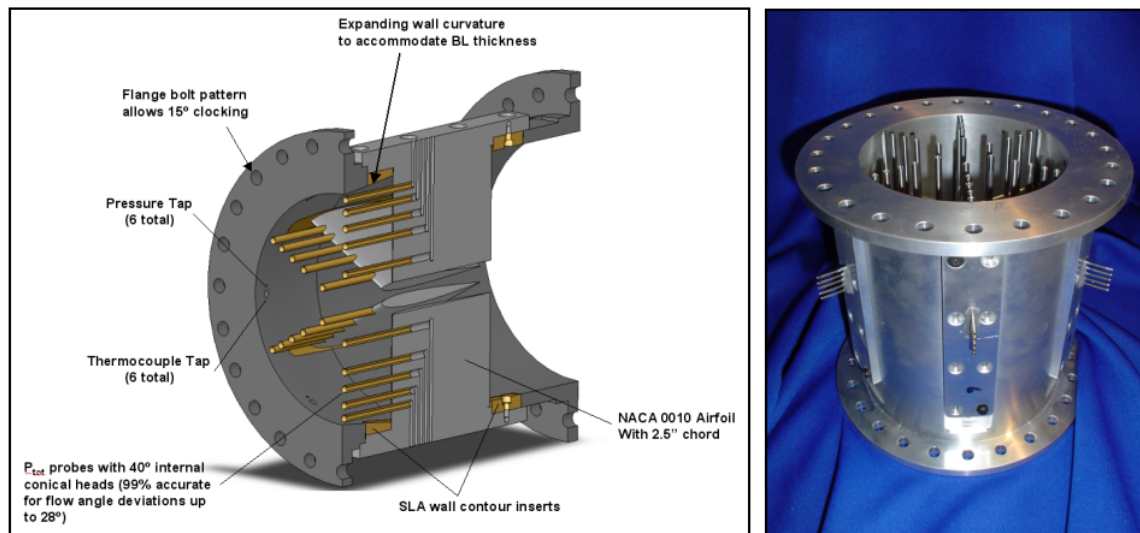


Figure 3-6: Six-Arm Total Pressure Distortion Rake

3.1.5: Pressure Drop Screens

As previously noted, the inlet capture area is controlled through the use of screens at a location downstream of the test section. At this location, the inlet and bypass flows are still separate. The pressure drop section is shown in Figure 3-7. A differential blockage is achieved through the installation or removal of a series of screens in the upper and lower flows. The pressure loss associated with an installed screen was used to create a pressure differential between the upper (bypass) and lower (inlet) sections. A total of four upper and four lower screens could be installed by opening an access hatch in the side of the tunnel. Fine-tuning of desired mass flows could be achieved through the installation of duct tape on top of the screens. At the aft end of this component, the upper and lower flows are slightly diffused and recombined prior to entering the suction port of the ejector.

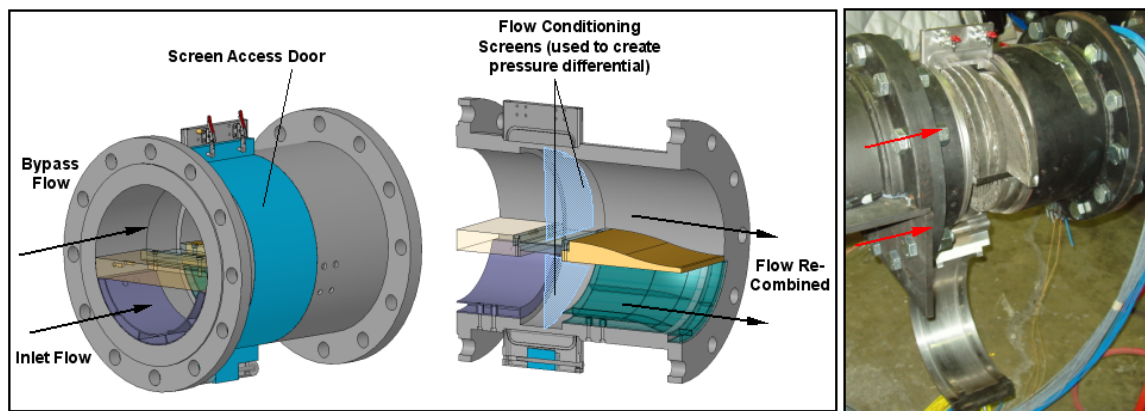


Figure 3-7: Pressure Drop Section

3.1.6: Flow Control: Blowing

As depicted in the schematic and photo shown in Figure 3-8, the blowing element of the flow control was achieved through valve control of atmospheric air into the test section. By adjusting the valve position, the plenum pressure of the flow control insert was adjusted, thereby altering the mass flow through the flow control jets. The total mass flow of the jets was measured through the use of an orifice plate.

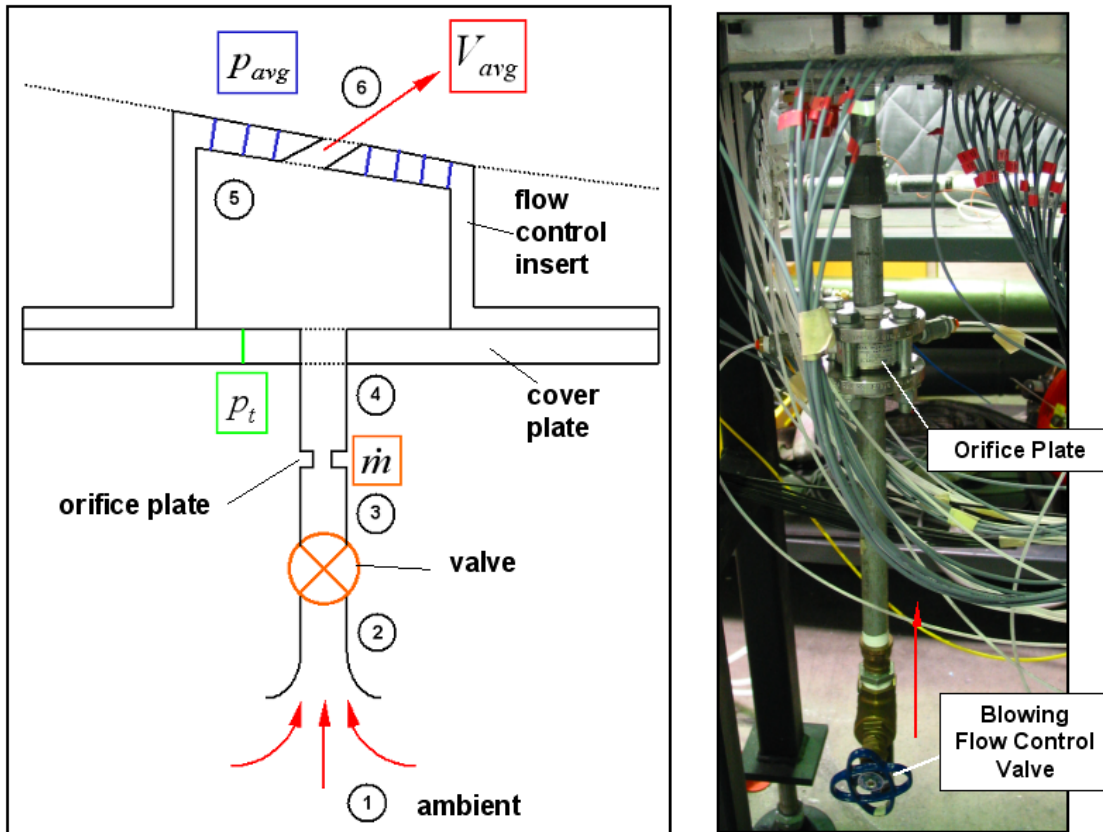


Figure 3-8: Flow Control - Blowing Apparatus

3.1.7: Flow Control – Suction

In order to achieve the required suction rates to simulate an ejector-pump based flow control system, a Vaccon VDF-550 ejector pump was used in conjunction with a laminar flow element (LFE). The Vaccon ejector-pump used the 210 psi motive air from the main tunnel ejector to draw air through the suction holes located in the lower inlet section. The suction schematic and system are shown in Figure 3-9. The suction mass flow rate was measured using the LFE, which incorporated a low pressure-drop measurement. The motive and suction flows were recombined inside the Vaccon ejector and drawn into the tunnel flow upstream of the main tunnel ejector suction port. The Vaccon ejector could also be adjusted to entrain different suction mass flows, thereby adjusting the amount of suction used in the tunnel model.

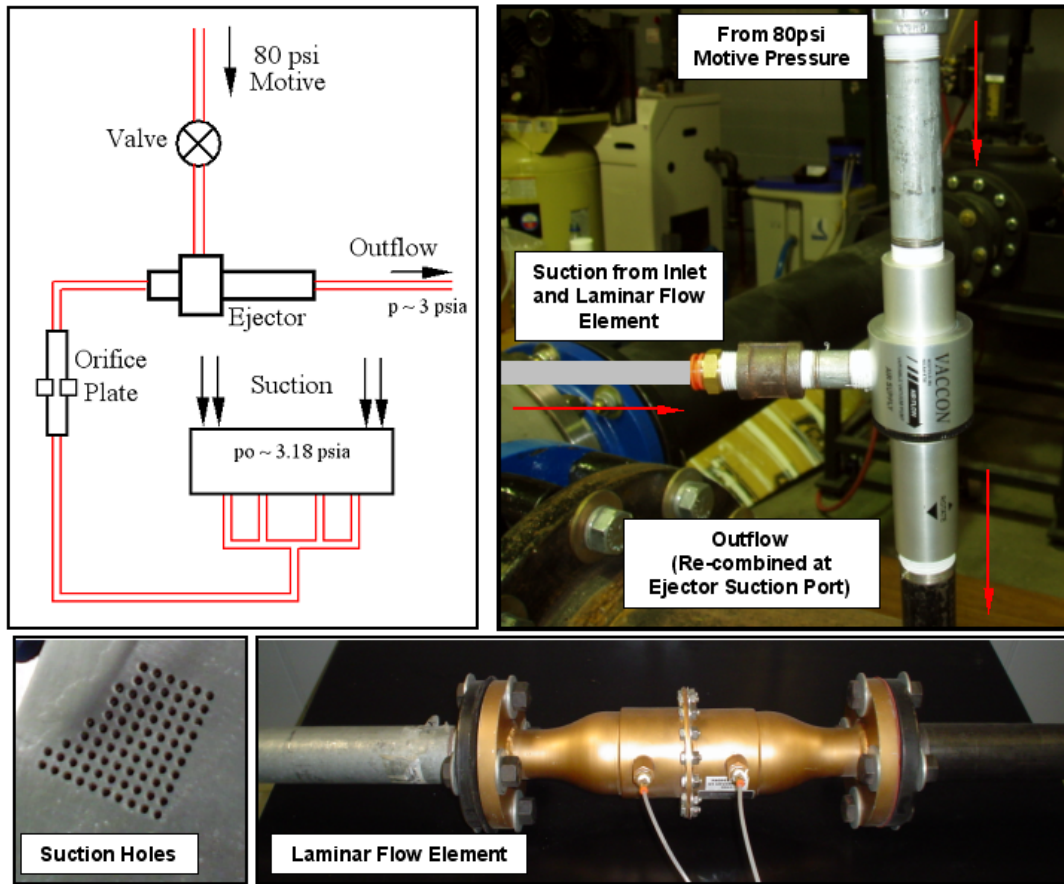


Figure 3-9: Flow Control - Suction Apparatus

3.2: Wind Tunnel Instrumentation

The wind tunnel setup was heavily instrumented with a variety of pressure measurements. Static pressure measurements were located axially throughout the boundary layer growth region and also in a transverse direction immediately in front of the inlet. Freestream total pressure was measured using two 1/8" diameter keel probes located immediately upstream of the flow diffusion in front of the inlet. The boundary layer velocity profile was measured using a six-probe boundary layer rake located 2" upstream of the inlet throat, as shown in Figure 3-10.

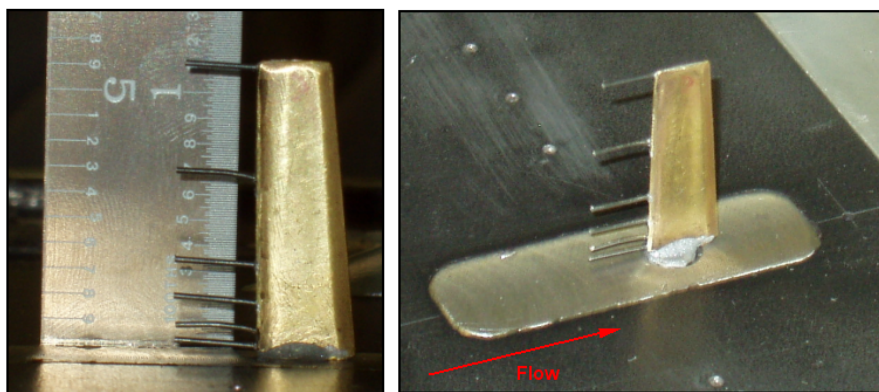


Figure 3-10: Boundary Layer Rake

The inlet itself is heavily instrumented on both the upper and lower sections. The upper and lower inlets each house 30 static pressure taps along the inlet centerline. The setup is shown in Figure 3-11 with the access cover removed from the upper inlet section. All AIP instrumentation is installed in the distortion rake, which incorporates 30 total pressure measurements and six static pressure measurements.

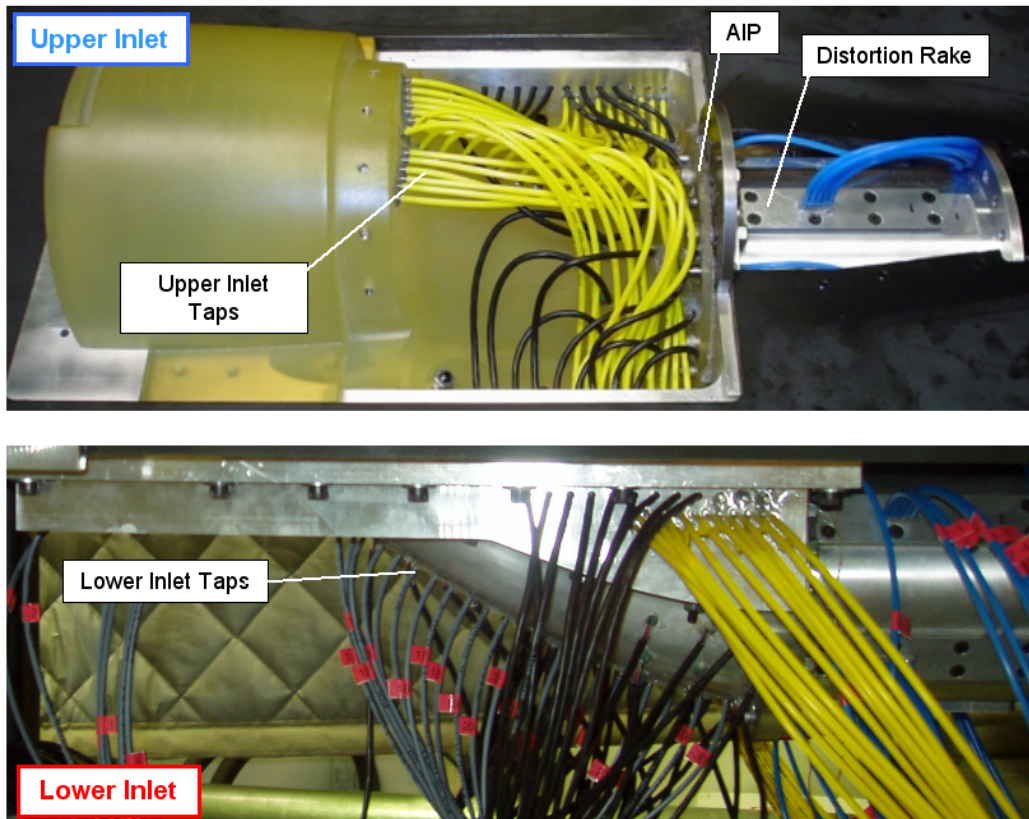


Figure 3-11: Inlet Instrumentation

3.2.1: Pressure Transducers and Data Acquisition

Tunnel data was collected using a variety of analog and digital pressure transducers:

- Scanivalve DSA Pressure Modules:
 - 8 channels, 0-30 psid
 - 24 channels, 0-5 psid
- PSI System Digitizer
 - 32 channels, 0-15 psid
- Scanivalve ZOC Pressure Modules
 - 8 channels, 0-15 psid
 - 40 channels, 0-5 psid.

All data acquisition was collected through the use of National Instruments Lab View software. The data acquisition system is shown in Figure 3-12.

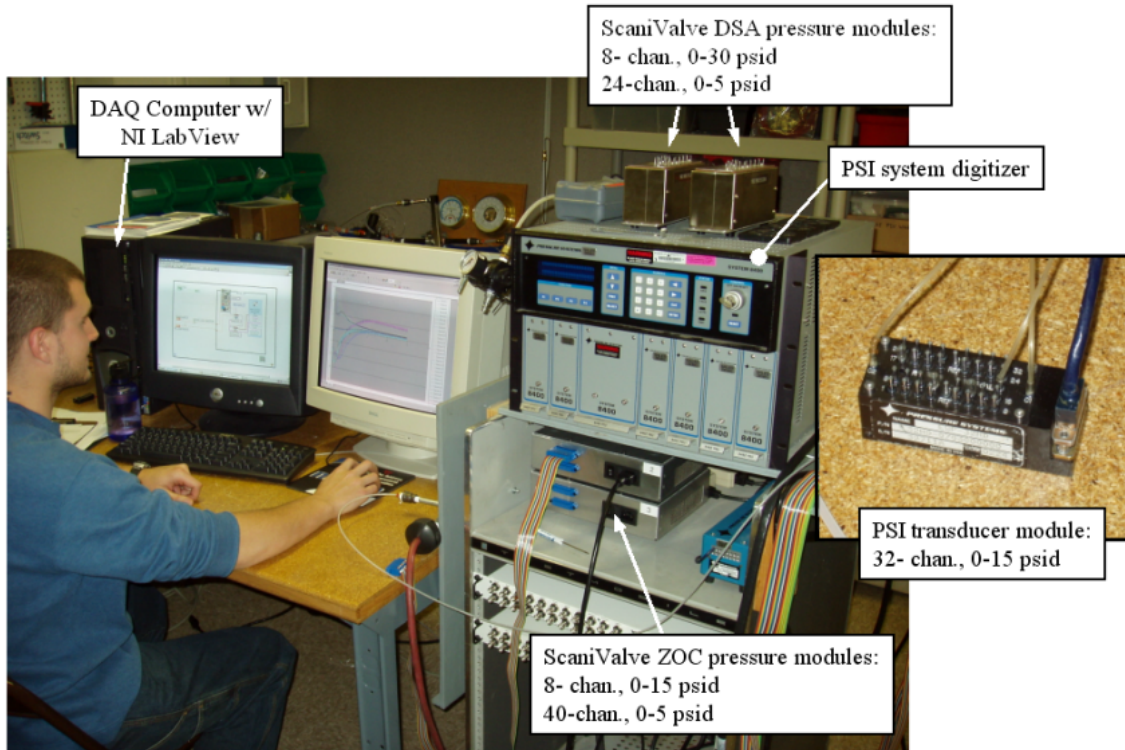


Figure 3-12: Data Acquisition System

3.3: Wind Tunnel CFD

As a predictive measure, the wind tunnel configuration was modeled to determine any possible undesirable flow qualities resulting from the test configuration. Results obtained from wind tunnel modeling suggest that the boundary layer from the outer tunnel walls will not be ingested into the inlet at the desired operational flow conditions, and thus will not effect the diffuser flow. Figure 3-13 shows the centerline Mach number contours of the modified wind tunnel design. Also, the corner flows that extend along the length of the boundary layer growth section are sufficiently diverted around the inlet into the bypass flow section. The boundary layer growth section of the wind tunnel is designed to increase in area to account for boundary layer growth through this section. The aim of this area expansion will ideally eliminate or at least reduce the magnitude of any axial pressure gradients that may affect boundary layer growth. In addition, the AIP distortion pattern remained essentially unaltered for the test configuration. Investigations of engine mass flow and the effect on distortion are noted in Appendix D.

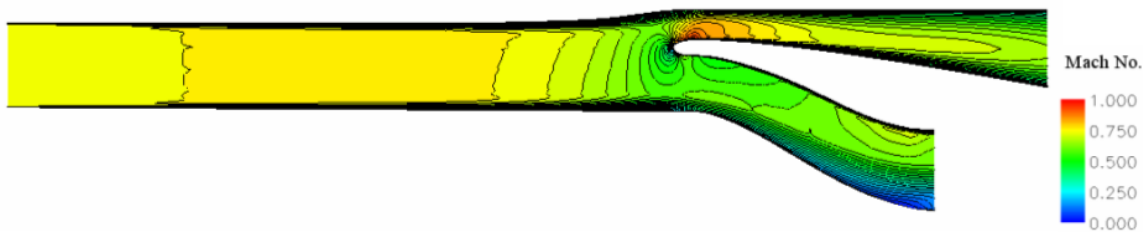


Figure 3-13: Wind Tunnel Mach Number Contours

3.4: Experimental Results

During a period of tunnel shakedown procedures, the relative flow quality and characteristics were investigated. Perhaps the most important flow characteristic to be determined was the boundary layer thickness and velocity profile, as CFD predictions showed that inlet performance was very sensitive to changes in the boundary layer profile. A complete discussion of the tunnel flow quality investigations may be found in Appendix J. Evaluation of experimental uncertainties for all results are based upon the Kline-McClintock relation¹⁷, with further discussion in Section 4.4.5, and detailed calculations shown in Appendix H.

3.4.1: Ingested Boundary Layer Profile

The tunnel boundary layer profile was measured using the boundary layer rake described in Section 4.2 which was positioned approximately two inches upstream of the inlet throat. The obtained profile was then compared with CFD predictions of the tunnel behavior, as shown in Figure 3-14. From the obtained profile, the experimental points collected by the rake match very closely with the predicted profile. As the experimental points appear to match, it is believed that the ingested boundary layer is of appropriate thickness. The boundary layer profile was calculated by obtaining the flow Mach number in the boundary layer from measured total pressures (rake), and local wall static pressure and using the local total temperature to calculate the freestream velocity. Both the CFD and experimental velocities were non-dimensionalized by the freestream velocity (U_{ref}) from the location of an upstream keel probe. The upstream velocity (calculated from total pressure, local static pressure and temperature) was used since determination of the precise local freestream velocity was not an easily defined quantity. As noted in Appendix H, the uncertainty in experimental velocity values was ± 1.47 m/s.

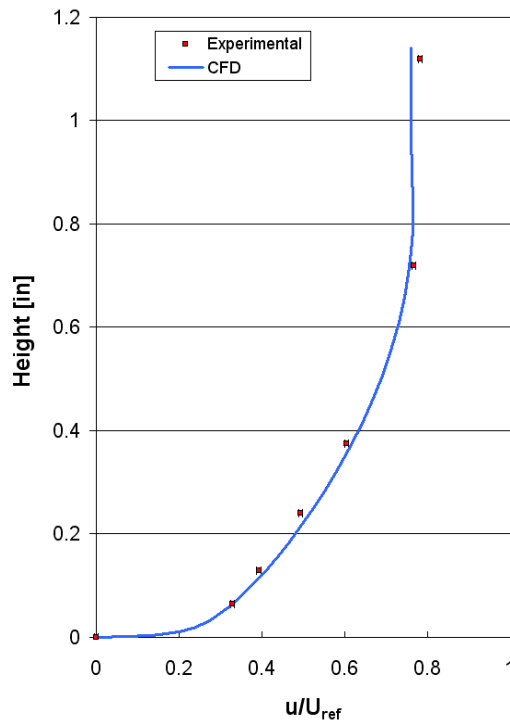


Figure 3-14: Wind Tunnel Ingested Boundary Layer Velocity Profile

3.4.2: Diffuser Wall Centerline Pressures

As an additional assessment of the CFD solver capability, the inlet wall pressures predicted by CFD were compared to the actual measured pressures from the experiments for the baseline configuration (i.e., no flow control). This comparison was performed using the non-dimensional pressure coefficient defined as

$$C_p = \frac{(P_\infty - P_{wall})}{\frac{1}{2} \rho_\infty V_\infty^2} .$$

The comparisons of the pressure coefficient for the upper and lower surfaces of the diffuser are shown in Figure 3-15, which shows how well the CFD predictions agree with the actual measurements.

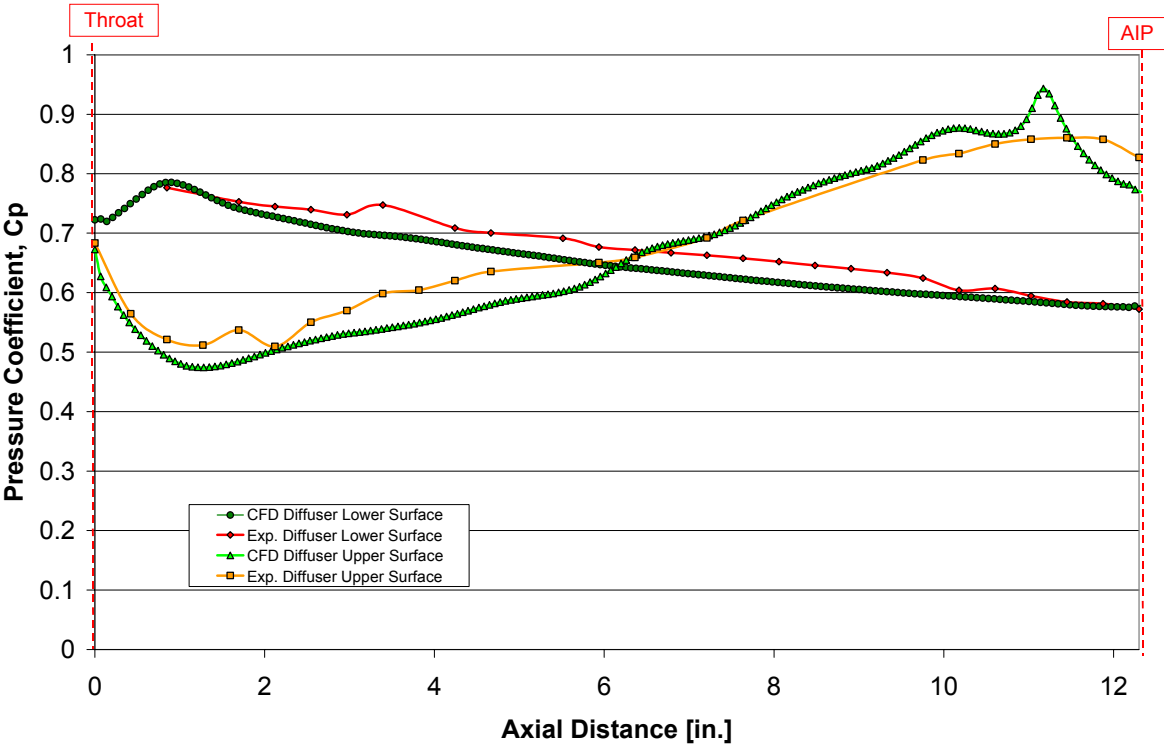


Figure 3-15: Comparison of CFD and measured Pressure Coefficients for upper and lower surfaces of diffuser on the axial center line

3.4.3: Baseline Distortion Contours

Prior to application of flow control to the inlet, baseline flow measurements were performed as a means for comparison with the CFD results. In order to validate the CFD flow control design tool, the baseline CFD flow predictions needed to match well with the experimentally measured quantities. Because the distortion rake takes finite area-averaged measurements, CFD values were interpolated onto a ‘virtual rake’ to simulate how the contours would appear if obtained by

the experimental rake. The baseline contours are shown in Figure 3-16. As shown, the baseline distortion contours are captured well during the experiment. Slight variations are apparent between the reverse Pyramid and circumferential inserts due to the physical nature of the jet holes. CFD contours are based upon a freestream Mach number of $M = 0.85$. However, freestream values achieved during experimental work were slightly lower. ($M \approx 0.82$) In addition, the achieved altitude conditions achieved during testing were also lower than computationally modeled. Actual modeled altitude during tunnel testing was approximately 36,500 ft. The reduction in Mach number combined with the altitude difference accounts for some of the disparity in distortion intensity between the experimental and CFD cases.

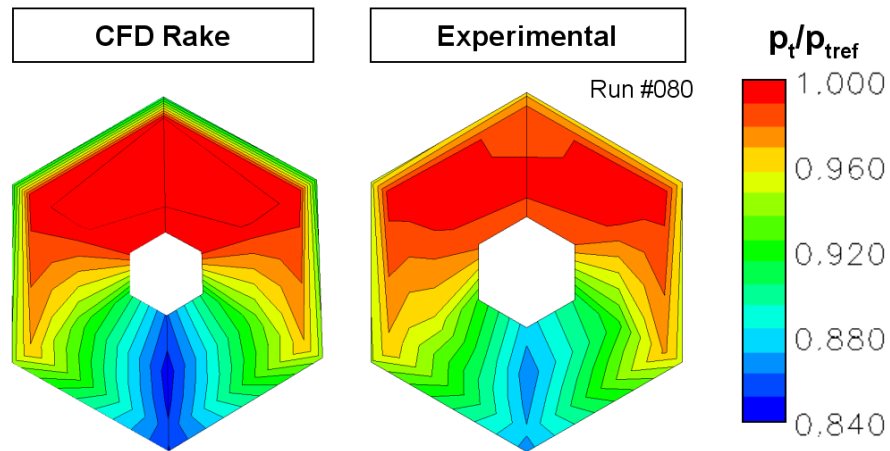


Figure 3-16: Baseline Solution distortion Contours (No flow control)

3.4.4: Shortcomings of DC(60)

Due to the physical and financial constraints of wind tunnel modeling, it was not possible to create a rake of higher fidelity. Time constraints during testing also prevented clocking the rake to increase fidelity. Thus, the pressure contours at the AIP must be carefully interpreted. Computational and rake measurements are shown in Figure 3-17 to show how distortion is captured by the rake. The case shown represents Reverse Pyramid results obtained by experiment. The far left contour is the analysis from CFD, and uses almost 10,000 points over the AIP area. The center image utilizes data from CFD and simulates what a standard DC(60) distortion rake (30 finite measurement locations) would interpret from this data. The far right image was measured experimentally. DC(60) distortion numbers for all cases are presented. Most apparent in the qualitative comparison of the CFD contours is that the distortion rake does not capture the lowest total pressure region due to the rake's finite nature. As such, this highlights the fact that taking finite measurements can provide both accurate and poor results based upon where the primary flow distortion lies. For this reason, a variety of flow distortion descriptors should be used, with as much resolution of measurements as possible. The experimental contour image does highlight the fact that the experimental rake does capture the same flow physics as captured by the CFD rake. DC(60)pt Distortion descriptors show good comparison, and justify that reasonable results were obtained with the rake configuration tested.

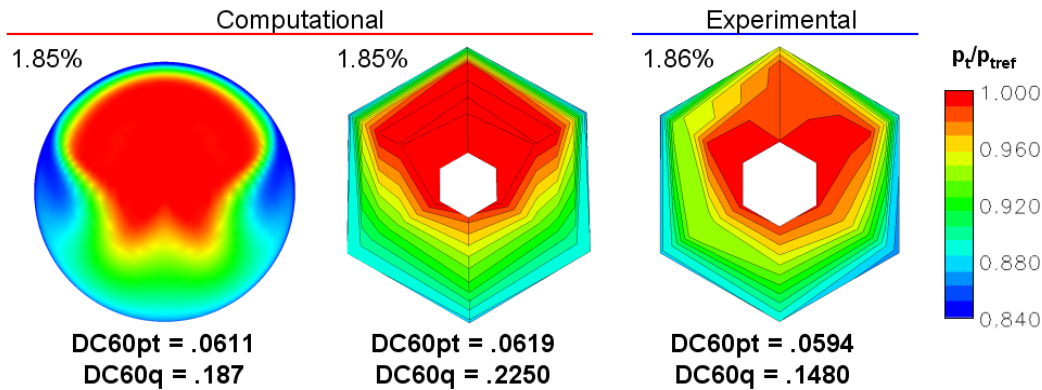


Figure 3-17: Effect of Rake on Distortion

However, variation in the DC(60)q parameter highlights the difficulty in accurately determining values based upon the AIP dynamic pressure (q_{AIP}) during experimental investigations. This is primarily due to the need to estimate both AIP average static and total pressures based on finite measurements. The average total pressure is computed using the 30 rake measurements from within the flow field at the AIP. However, the average static pressure is calculated from wall measurements at select locations around the AIP. This can lead to a substantial error in estimation of the face dynamic pressure, and thus filters down into the DC(60)q metric. By examining the CFD interpolated results and comparing to the CFD finite measurements used in this experiment by way of a “simulated” rake, this estimation can result in a DC(60)q uncertainty of ± 0.038 . (As determined in Appendix H.) The reason for this variation is apparent when examining the AIP static pressure contours of Figure 3-18, and the significant variation in static pressure across the engine face.

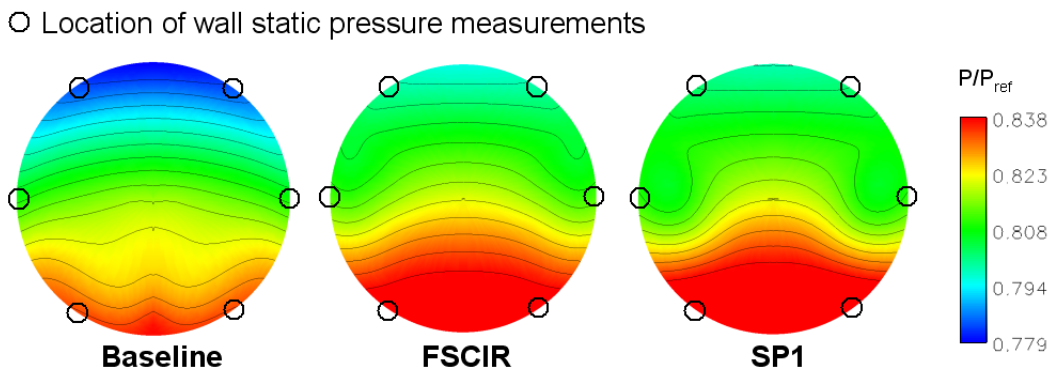


Figure 3-18: AIP Static Pressure Contours

Because of these inaccuracies, any calculation based upon the face dynamic pressure will inherently have high error. For this reason, it seems much more practical to use the DC(60)pt parameter to describe results. Results obtained in this study also highlight an increased accuracy when comparing to predicted DC(60)pt values, in addition to being a more robust parameter capable of collapsing results for different flow rates and duct sizes.¹ Ultimately, engine companies have distortion descriptors that are more complicated, more costly, and tailored to the specific performance characteristics of their particular engine capabilities.

DC(60) Distortion Results – Reverse Pyramid Flow Control

The first tested configuration utilized the reverse flow control scheme. Due to the small confines of the scaled-down test inlet and complexity constraints, it was not possible to create a working ejector pump model. Thus, the ejector concept was simulated using separate blowing and suction mechanisms as described earlier. Experimental investigations examined both blowing only and the simulated ejector.

The experimental results in Figure 3-19 show distortion investigations of the reverse Pyramid flow control configuration as characterized by the DC(60)q parameter. From this figure it is apparent that the experimental investigations were successful in predicting the trends associated with the application of flow control. (It should be noted that CFD investigations used for comparison to experimental data examined only changes in blowing rate, and thus are comparable to the experimental ‘blowing only’ series.) The addition of suction to the system further reduced the distortion when coupled with flow blowing. Predictions for lower rates of flow control were less accurate as compared with computational values, although the presence of jet holes may have had a small effect on the flow, particularly for low (or zero) flow control efforts.

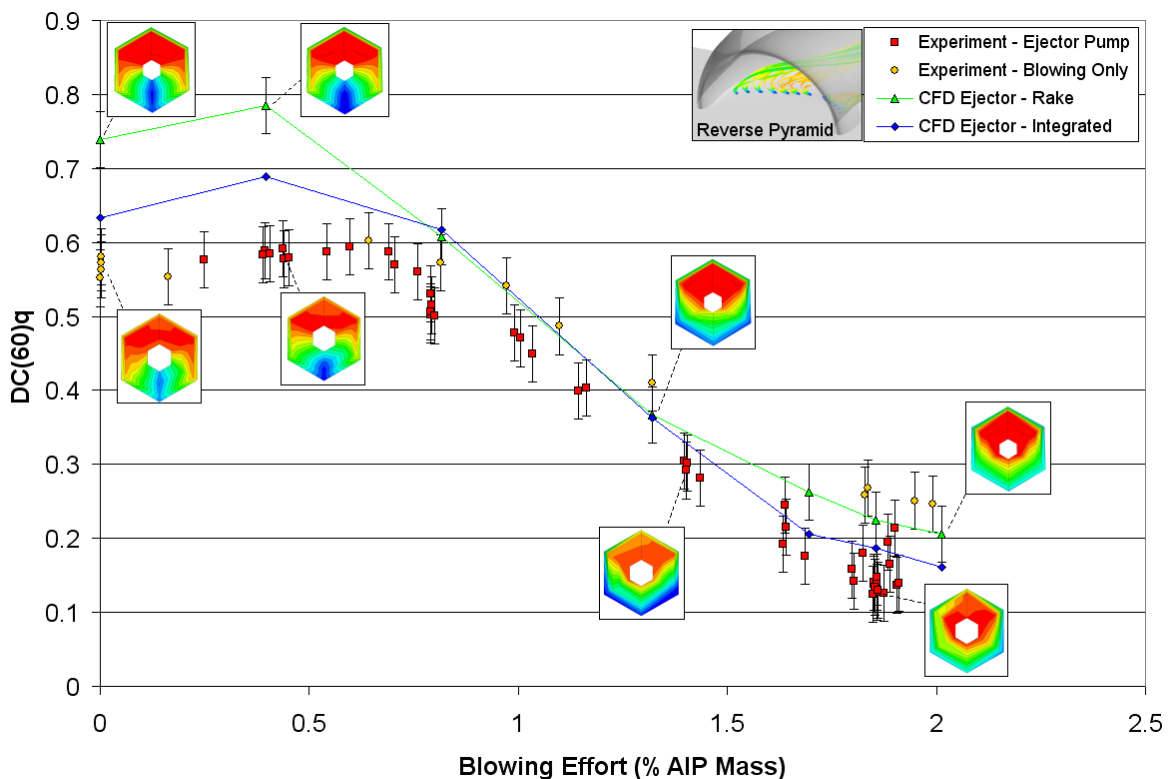


Figure 3-19: DC(60)q Experimental Distortion Results - Reverse Pyramid Blowing

Overall, the visual flow contours agree very well in form between experimental and computational depictions. All data sets obtained show a small rise in distortion for low flow control efforts. This behavior is not uncommon when using jets to control distortion; the addition of fluid with less total pressure than freestream values increases the flow distortion at first when

the jets are not effective in countering the secondary flows present within the flow. However, once the jets begin to become more effective, the distortion begins to decrease. Using this configuration, for blowing efforts of greater than 1.5% AIP mass there are diminishing returns for flow control, although the distortion continues to decrease. However, the commercially ‘acceptable’ DC(60)q distortion value of 0.1 is not quite achieved. It seems realistic that a more thorough system optimization could result in values at or below this mark.

Computational DC(60)pt values are closer in their prediction to experimental values, as shown in Figure 3-20. The trends for this parameter are very similar to those seen in the DC(60)q parameter, showing the same initial rise in distortion as well as a slight decrease in effectiveness for blowing mass flows of greater than 1.5% AIP mass. This figure also shows a slight over-prediction in distortion as measured by a simulated CFD rake. This difference is the most likely the result of a discrepancy in the severity of the distortion at the AIP due to the CFD turbulence model. This discrepancy is accentuated by the difference in freestream Mach number between experimental and computational investigations.

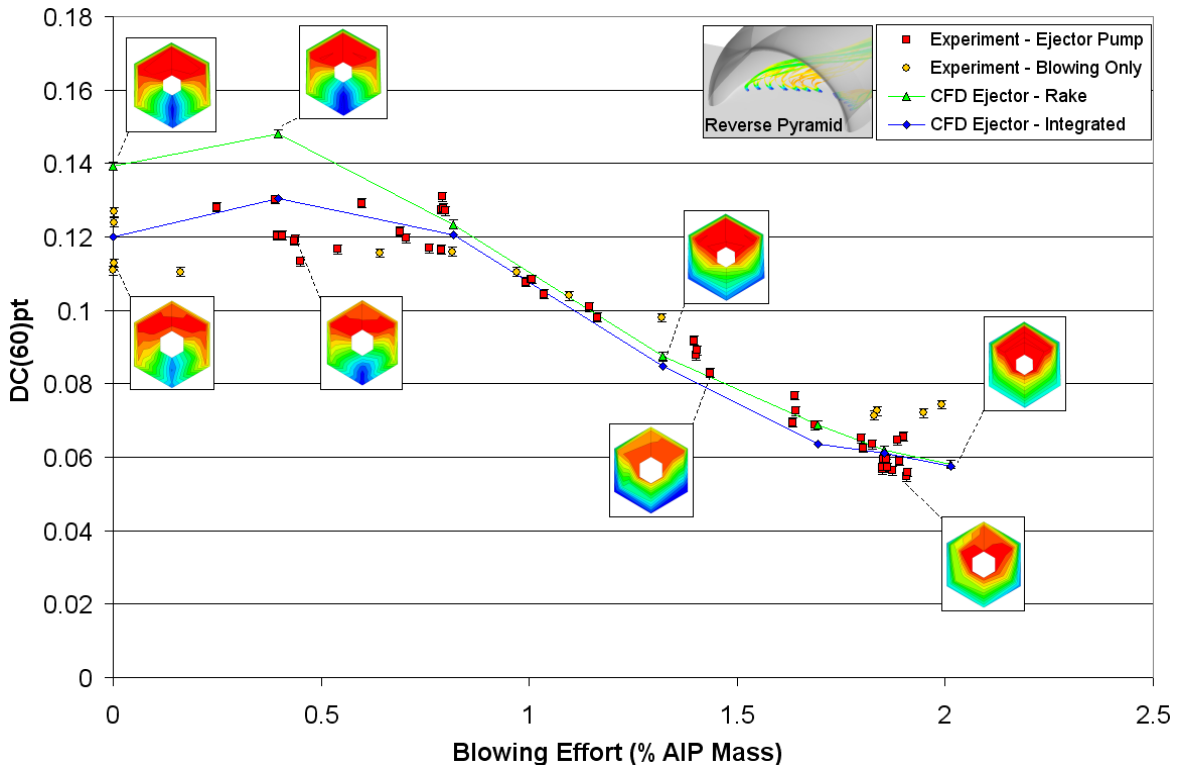


Figure 3-20: DC(60)pt Experimental Distortion Results - Reverse Pyramid Blowing

The AIP total pressure recovery values as referenced to freestream total pressure are shown in Figure 3-21. The spread in the results shown is strongly influenced by slight differences in freestream Mach number from run to run. In addition, the referenced total pressure does not represent the average total pressure of all flow ingested into the inlet as it does not account for the presence of the boundary layer, which biases the experimental estimates of the inlet pressure recovery towards lower values.

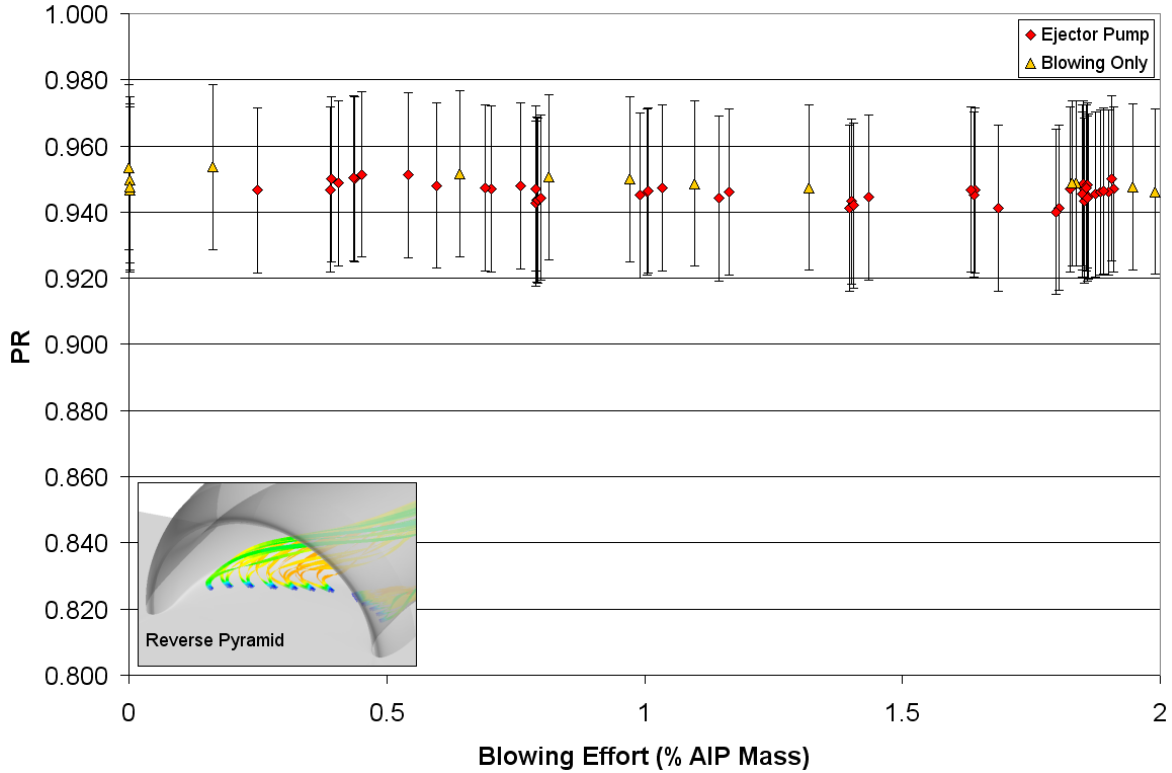


Figure 3-21: Pressure Recovery Experimental Results - Reverse Pyramid Blowing

Further insight can be gained by examining the AIP total pressure contours of the experimental values and comparing them to values predicted by. The CFD simulated rake data is compared to experimental data for similar blowing rates in Figure 3-22. Distortion values are also shown. The three cases represent small, medium, and large blowing efforts. Qualitatively, the pressure contours show that the experimental and computational rake values capture the same flow structures. Small magnitude differences are apparent due to variation in flow Mach number. Experimental flow contours show a high degree of symmetry. In general it is apparent that CFD tends to over-predict distortion for low blowing efforts. This is consistent with observations by Allan¹⁴, and is likely the result of a lower predicted minimum total pressure value, and a total pressure maximum that can at times exceed unity. Quantitatively the distortion results match very closely, with CFD distortion values slightly higher than obtained in experiment.

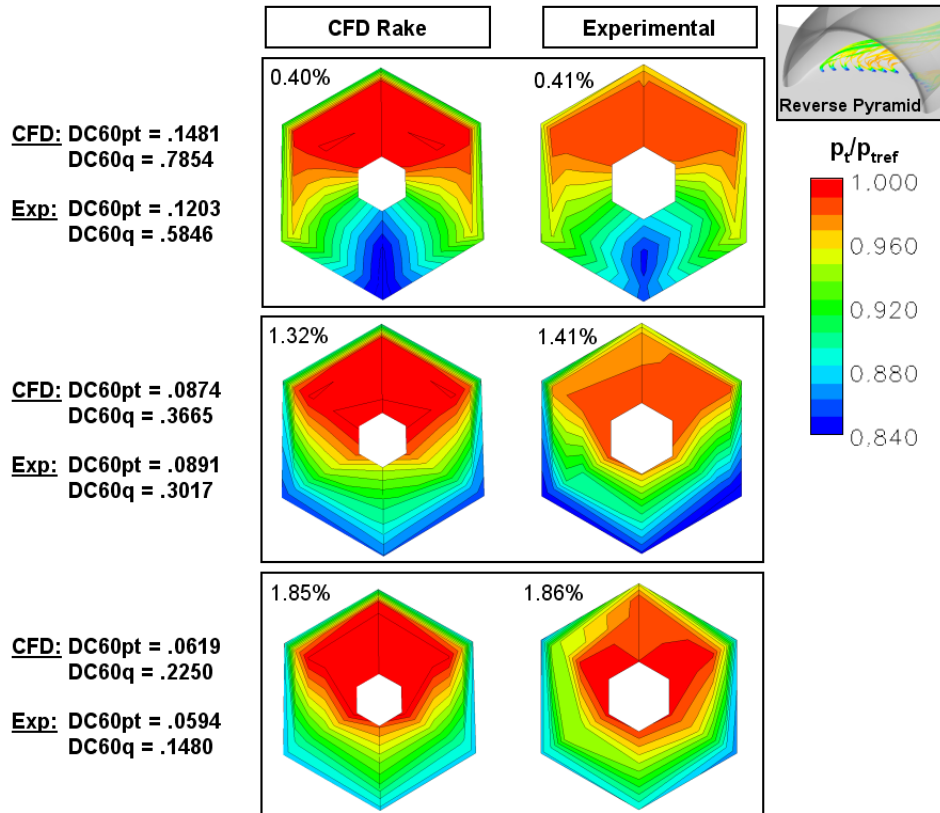


Figure 3-22: Reverse Pyramid Blowing Total Pressure Contours

3.4.5: DC(60) Distortion Results – Circumferential Flow Control

The circumferential blowing scheme was investigated also by examining blowing alone, and a simulated ejector pump blowing system. Due to the physical constraints associated with the wind tunnel setup, the circumferential blowing case selected was not identical to the configuration tested in initial flow control CFD investigations. The primary difference was that in the experimental setup no jets could be placed on the diffuser sidewall. Thus, all jets in this configuration are mounted on the floor. This limitation is only a result of the small scale associated with the test, and could easily be replicated in larger scale tests. However, CFD predictions of the experimental setup were conducted with only a reasonably small variation in jet configuration. These predictions are compared to the obtained experimental DC(60)q values in Figure 3-23.

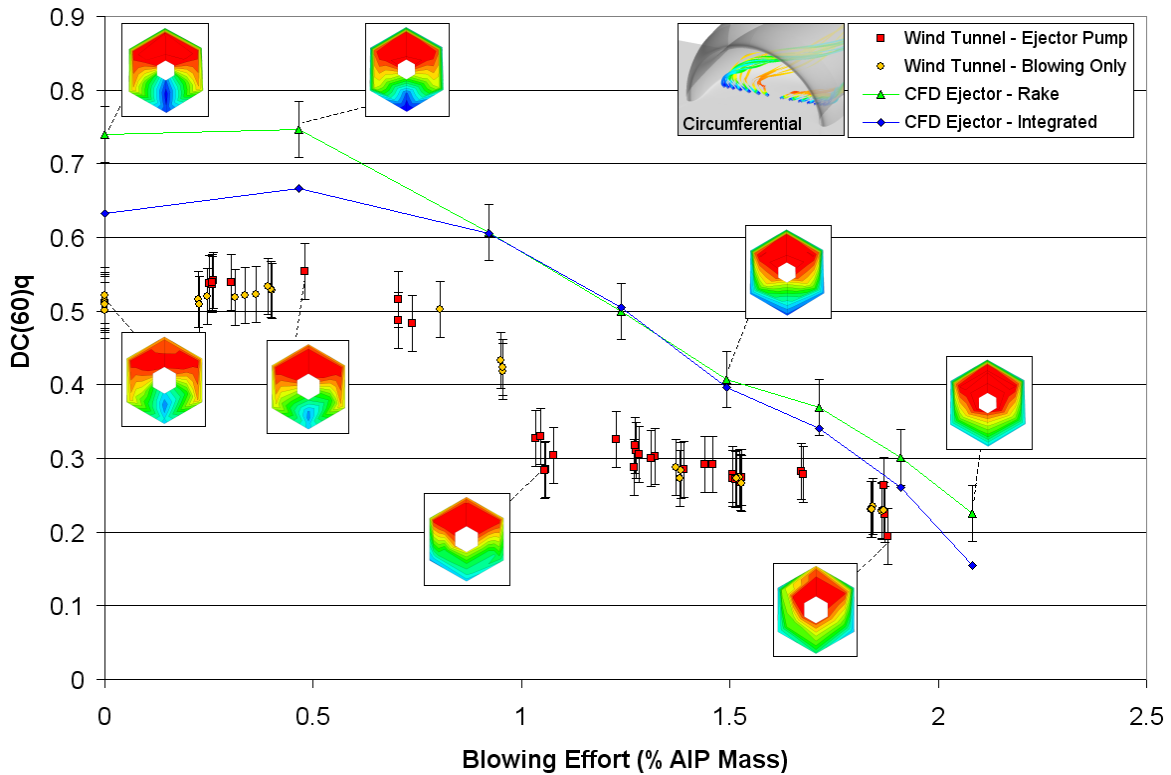


Figure 3-23: DC(60)q Experimental Distortion Results - Circumferential Blowing

Investigations of the circumferential insert yielded similar trends to those obtained in the reverse Pyramid blowing investigation. As before, the distortion shows a slight rise for little (or no) blowing effort. Experimental baseline (no flow control) values for the circumferential insert are also lower than previous values. This is likely the result of the flow control jets being located in a less sensitive (upstream) location, along with the possibility of a slightly different flow control insert fit.

The DC(60)pt results for the circumferential flow insert are shown in Figure 3-24. As before, the DC(60)pt computational results compare much more closely with the obtained data. A similar trend is observed in the experimental data with a slight initial rise in distortion coupled with a rate of ‘diminishing returns’. CFD also predicts a sudden increase in jet effectiveness for blowing mass flows greater than 2% AIP mass. However, the experimental facility did not prove capable of achieving these mass flows. CFD analysis shows that for mass flows slightly over 2% AIP mass the jets become choked. However, altering the plenum supply pressure should still result in an increase in jet mass, and thus an increase in jet momentum.

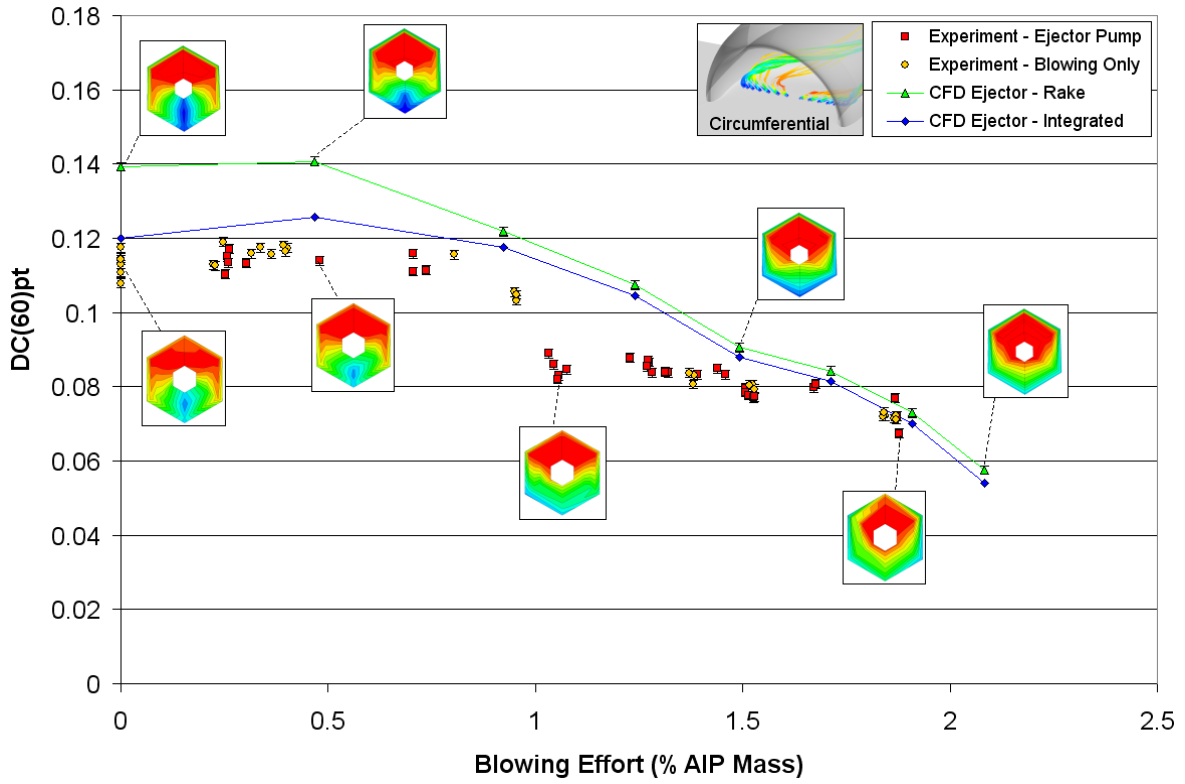


Figure 3-24: DC(60)pt Experimental Distortion Results - Circumferential Blowing

The circumferential insert pressure recovery values are shown in Figure 3-25. As can be seen, there is not a large impact on inlet pressure recovery resulting from the application of flow control.

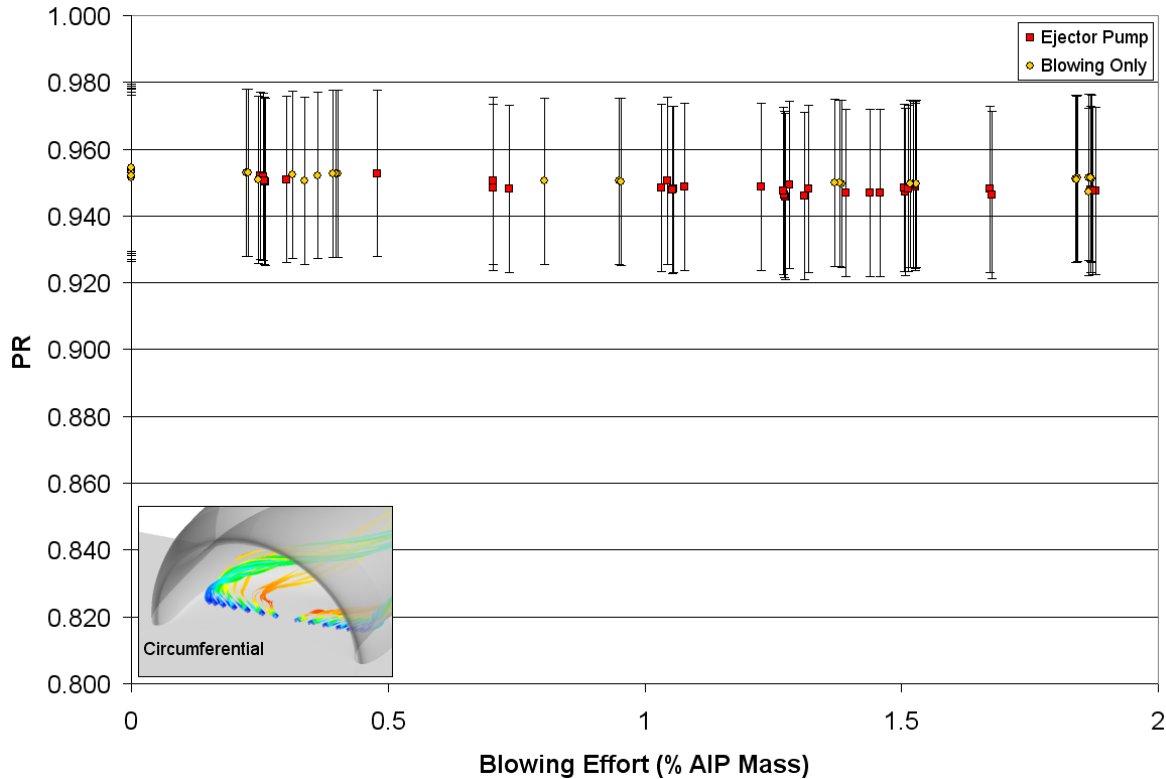


Figure 3-25: Inlet Pressure Recovery Experimental Results - Circumferential Blowing

The total pressure contours from CFD and experiment for the circumferential blowing case are compared in Figure 3-26. Contours are non-dimensionalized by the freestream total pressure, with the blowing effort expressed as a percentage of total AIP mass.

As noted in previous sections, CFD tends to over-predict the flow distortion for small flow control efforts. This over-prediction decreases as the blowing effort increases. As noted before, this is likely the result of the turbulence modeling of the vortex behavior; as the scale of the large disturbance is decreased, predictions become more accurate. Over-prediction of distortion is also the result of a variation in freestream Mach number. (Experiment 0.3 Mach lower.)

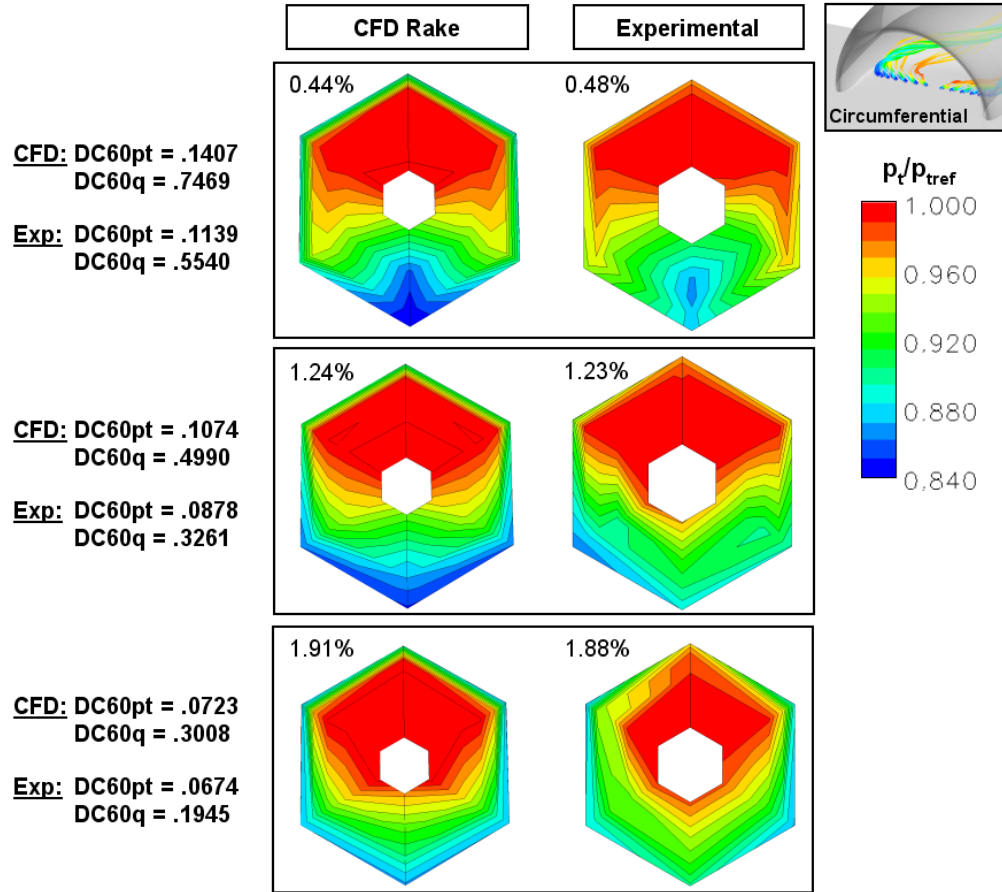


Figure 3-26: Circumferential Blowing Total Pressure Contours

3.4.6: Strake

The addition of the strake to the baseline configuration had some effect on the AIP flow distortion, as shown in Figure 3-27. The severity of the total pressure distortion has decreased by 9.5% for the DC60pt parameter, and 10.8% for the DC60q parameter. The pressure recovery of the system remained essentially constant. This result shows that by geometrically reducing the effect of the junction vortex the distortion can be reduced, possibly allowing for the flow control to be more effective.

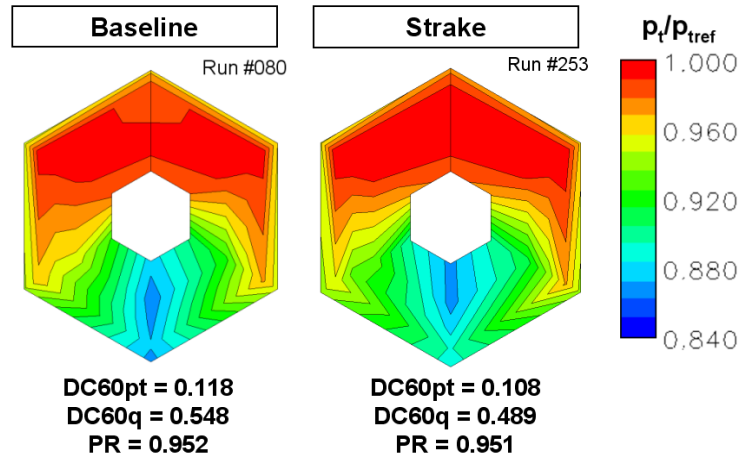


Figure 3-27: Experimental Results – Effect of Strake

3.4.7: Effect of Strake on Flow Control

The strake was then tested using different flow control efforts in order to ascertain whether the addition of the strake could reduced the amount of necessary flow control. To reduce the complexity of the investigation, only blowing was used. The distortion results for the addition of the strake are shown in Figure 3-28 and Figure 3-29.

From the results it is apparent that the addition of a strake can have a strong effect on the AIP distortion. The baseline (no flow control) distortion has been decreased as noted in the above section. However, as the flow control effort increased, the strake appeared to reduce the effectiveness of the flow control.

It is likely that as the flow control effort changes, the flow structure upstream of the effectors is altered such that the strake does not behave as designed. The significant benefit at the baseline level suggests that a variable geometry lip may provide a significant benefit to the reduction of distortion.

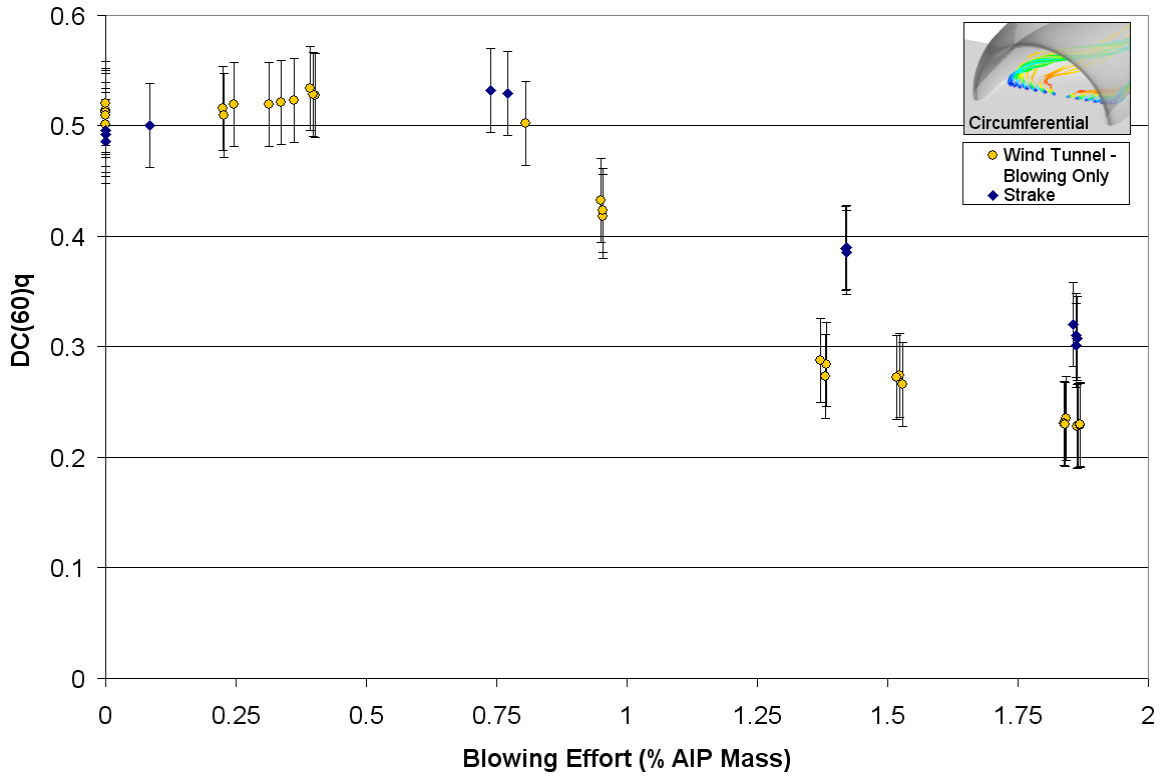


Figure 3-28: DC(60)q Experimental Distortion Results with Strake

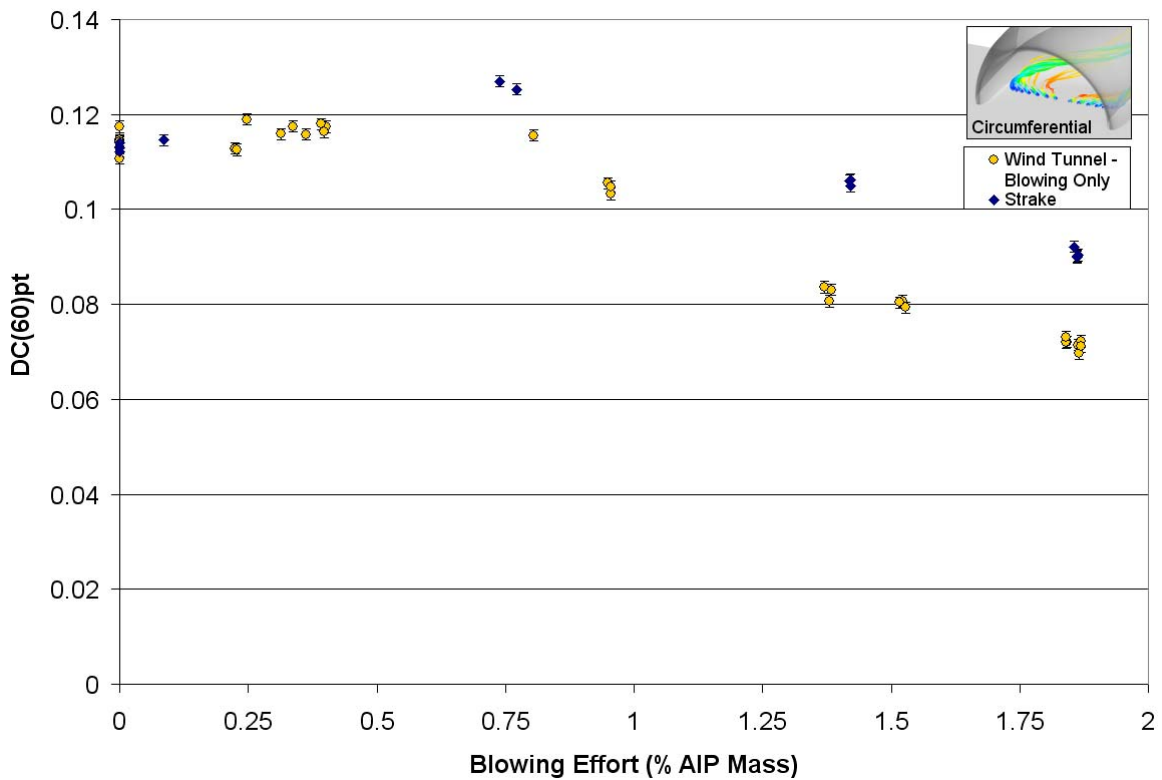


Figure 3-29: DC(60)pt Experimental Distortion Results with Strake

Chapter 4: Non-intrusive Flow Distortion Sensor Development

The novel concept of using jet-type vortex generator (VG) arrays to manage the secondary flows, and therefore to reduce total pressure distortion, in BLI serpentine inlets has been proven to be quite effective in this research as well as in previous research by Gorton *et al.* Use of the jet-type VG's for flow control in BLI serpentine inlets offers two main advantages over their traditional vane-type counterparts, non-intrusiveness and adjustability of flow control effort. The non-intrusive nature of the jet-type VG's allows for fewer fluidic losses than would be incurred in a vane-type VG installation. Then the ability to adjust the flow control effort allows by increasing or decreasing the momentum from the jets allows for the possibility of achieving optimal flow control in the BLI serpentine inlet.

The aforementioned benefits of active flow control in BLI serpentine inlets using jet-type VG's cannot be optimally attained without the use of an automated system to control the flow control jet momentum. Unfortunately, no such closed-loop control system can be achieved without the development of a sensing approach that can non-intrusively detect and feed back the distortion levels. Traditionally, flow distortion is quantified using total pressure rakes at the AIP, which obstruct the flow path as it enters into the gas turbine engine's compression system. As an alternative to this intrusive sensing approach, Techsburg proposed to develop a method of using wall-pressure fluctuation measurements from non-intrusive, wall-imbedded microphones in order to estimate the levels of flow distortion at the AIP of a BLI serpentine inlet.

4.1: Technical Objectives of Sensing Approach

As previously stated, a non-intrusive method of detecting flow distortion in BLI serpentine inlets is proposed for the future purpose of feedback in an automated flow control system. Specifically, it was proposed that the sensing for such a hypothetical control system would be achieved via wall-pressure fluctuation measurements within the duct. The sensing approach was to be developed using a mixture of first principles from fluid mechanics as well as an empirical development from pressure measurements recorded from a microphone array distributed throughout the duct. The primary goal is to develop a microphone-based signal that can accurately estimate the total pressure distortion metric DC(60) that is normally measured using an intrusive total pressure rake at the AIP.

4.2: Theory of Wall-Pressure Fluctuations

Many researchers over the past 40 years have been interested in developing the velocity – wall-pressure fluctuation relationships. This research has been primarily motivated by the desire to measure, or at least estimate, the internal flow quantities using only surface measurements at the boundary of the flow. Researchers began this investigation with theoretical approaches due to the lack of high fidelity experimental apparatus available to perform the desired measurements.

The most prominent relationship between flow velocity within a flow field and a pressure measurement at another point within or on the boundary of the flow field is attributed to Poisson. In his development one first considers the Navier-Stokes equation,

$$\frac{D\vec{V}}{Dt} = -\frac{1}{\rho}\nabla p + \nu\nabla^2\vec{V} . \quad (4.1)$$

Before proceeding to manipulate Eq. (4.1), we must realize that a predominance of the unsteady pressure detected at the wall derives from the near-wall, turbulent fluid in the boundary layer. Additionally, turbulence is an incompressible flow phenomenon because the turbulent velocity perturbations occur at Mach numbers much less than 1. Further, the pressure is not linked thermodynamically to density for incompressible flows. To this end, the divergence of Eq. (4.1) takes the form

$$\nabla \cdot \frac{D\vec{V}}{Dt} = \nabla \cdot \left(-\frac{1}{\rho}\nabla p + \nu\nabla^2\vec{V} \right). \quad (4.2)$$

With some algebraic manipulation, the first term of the divergence of Eq. (4.1) can be written as

$$\nabla \cdot \frac{D\vec{V}}{Dt} = \frac{D(\nabla \cdot \vec{V})}{Dt} + \frac{\partial V_i}{\partial x_j} \frac{\partial V_j}{\partial x_i}, \quad (4.3)$$

and now Eq. (4.2) can be written as an inhomogeneous equation in terms of the dilation, $\Delta = \nabla \cdot \vec{V}$, to yield

$$\left(\frac{D}{Dt} - \nu\nabla^2 \right) \Delta = R, \quad (4.4)$$

where

$$R \equiv -\frac{1}{\rho}\nabla^2 p - \frac{\partial V_i}{\partial x_j} \frac{\partial V_j}{\partial x_i}. \quad (4.5)$$

At this point it is advantageous to consider solving Eq. (4.4) in a fluid where $\Delta = 0$ initially and at the boundaries for all time. In this scenario, R must equal zero at all space and time, which from Eq. (4.5) leaves the fact that the pressure must satisfy Poisson's equation:

$$\nabla^2 p = -\rho \frac{\partial V_i}{\partial x_j} \frac{\partial V_j}{\partial x_i}. \quad (4.6)$$

Applying a Green's function formulation to Equation (4.6), leads to

$$p(\bar{x}, t) = p^{(h)}(\bar{x}, t) + \frac{\rho}{4\pi} \iiint_{\bar{y}} \left(\frac{\partial V_i}{\partial x_i} \frac{\partial V_j}{\partial x_j} \right)_{y,t} \frac{d\bar{y}}{|\bar{x} - \bar{y}|}, \quad (4.7)$$

which describes the pressure observed at location \bar{x} due to flow disturbances at locations \bar{y} . In Eq. (4.7), the term $p^{(h)}(\bar{x}, t)$ is a harmonic function (i.e., $\nabla^2 p^{(h)} = 0$) that is dependent upon the boundary conditions. Finally, since we desire an expression for the fluctuating pressures that are to be measured at the wall of the inlet duct, a Reynolds decomposition of the velocities into time-averaged components and fluctuating components can be performed according to

$$V_i = \langle V \rangle + v_i, \quad (4.8)$$

where $\langle \rangle$ represents a time average at a single point in space. Applying the Reynolds decomposition of Eq. (4.10) to Eq. (4.7) and keeping only those terms that contain fluctuating terms leads to

$$p'(\bar{x}, t) = p^{(h)}(\bar{x}, t) + \frac{\rho}{2\pi} \iiint_{\bar{y}} \left(\underbrace{\frac{\partial \langle V_i \rangle}{\partial x_j} \frac{\partial v_j}{\partial x_i}}_{\text{Rapid pressure source}} + \underbrace{\frac{\partial^2}{\partial x_i \partial x_j} (v_i v_j - \langle v_i v_j \rangle)}_{\text{Slow pressure source}} \right) \frac{d\bar{y}}{|\bar{x} - \bar{y}|}, \quad (4.9)$$

which is an expression for the fluctuating pressure $p'(\bar{x}, t)$ measured at the wall due to the source terms located within the flow at location \bar{y} . There are two source terms in Eq. (4.9), the rapid pressure source and the slow pressure source, which are named according to the speed with which they invoke a pressure response to the time-averaged velocity gradients within the flow.

4.3: Microphone Installation and Calibration

4.3.1: Sensor Specifications

A Panasonic series WM-60A omni-directional back electret condenser microphone has been chosen to serve as the non-intrusive sensor for this research program. This sensor has the advantage of being compact in size with only a 6-mm diameter sensing surface, which is ideal for fitting the microphones around the small test inlet that has a 4-inch diameter AIP. The WM-60A microphones have flat frequency responses out to 20 kHz, and have demonstrated consistency in a phased-array at Virginia Tech having only a maximum of 1 dB relative difference in magnitude response between the 32 microphones. Of equal importance to their

small dimensions, these microphones are low cost (approximately \$2 each), which makes full instrumentation of the entire inlet economical.

4.3.2: Sensor Installation

Due to the extreme curvatures throughout the scaled-down test inlet the microphones will not be flush-mounted to the inner surfaces of the inlet duct. As an alternative, the microphones will be recessed into the inlet wall, and small pinholes in the inlet wall will allow the microphone access to the internal flow. A schematic of this recessed microphone installation is shown in Figure 4-1. The two key parameters shown in the microphone installation schematic of Figure 4-1 are the diameter of the pinhole d and the length of the pinhole cavity h .

Decreasing the pinhole diameter d has the effect of improving the sensor spatial resolution because the microphone's pressure sensing surface is now the cross-sectional area of the pinhole. Since microphones essentially sense the integrated pressure across the sensing surface, it is imperative to choose a sensor diameter that is smaller than the smallest turbulent structure to be sensed. In light of the large boundary layers in this offset diffuser, and therefore, the relatively large turbulent structures that are to be found, a pinhole diameter of 2-mm has been chosen. As previously mentioned, the length of the pinhole cavity has significant bearing on the microphone measurements. In particular, the cavity will act as a quarter-wave resonator, whereby, acoustic axial resonances will occur within the tube at every harmonic of the frequency $\frac{c}{4h}$. In sizing the dimension h it was decided that the measurement bandwidth for this experiment will be 20 k Hz. Thus, the dimension h was set at 0.167-inches in order to prevent cavity acoustic resonances from biasing the measurements.

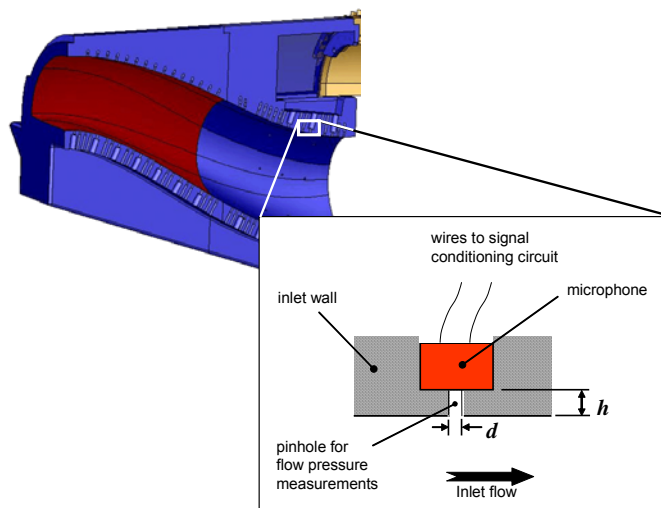


Figure 4-1: Wall-imbedded microphone installation technique

4.3.3: Sensor Locations

A single wall-mounted microphone detects pressure disturbances that originate over a wide region of the flow field within the inlet as described by Eq. (4. 7). However, a single pressure measurement is insufficient for resolving the source locations or characteristics. Thus, the inlet for this research work was instrumented with 46 wall-imbedded microphones spanning the entire inlet, which is illustrated in Figure 4-2. This sensor layout consists of a linear, stream-wise array of wall-imbedded microphones down the centerline of the bottom half of the inlet*, which was used to monitor the stream-wise development of the ingested boundary layer, and also consists of three circumferential microphone arrays located near the AIP†, which was used to monitor the airflow circumferential uniformity at the AIP.

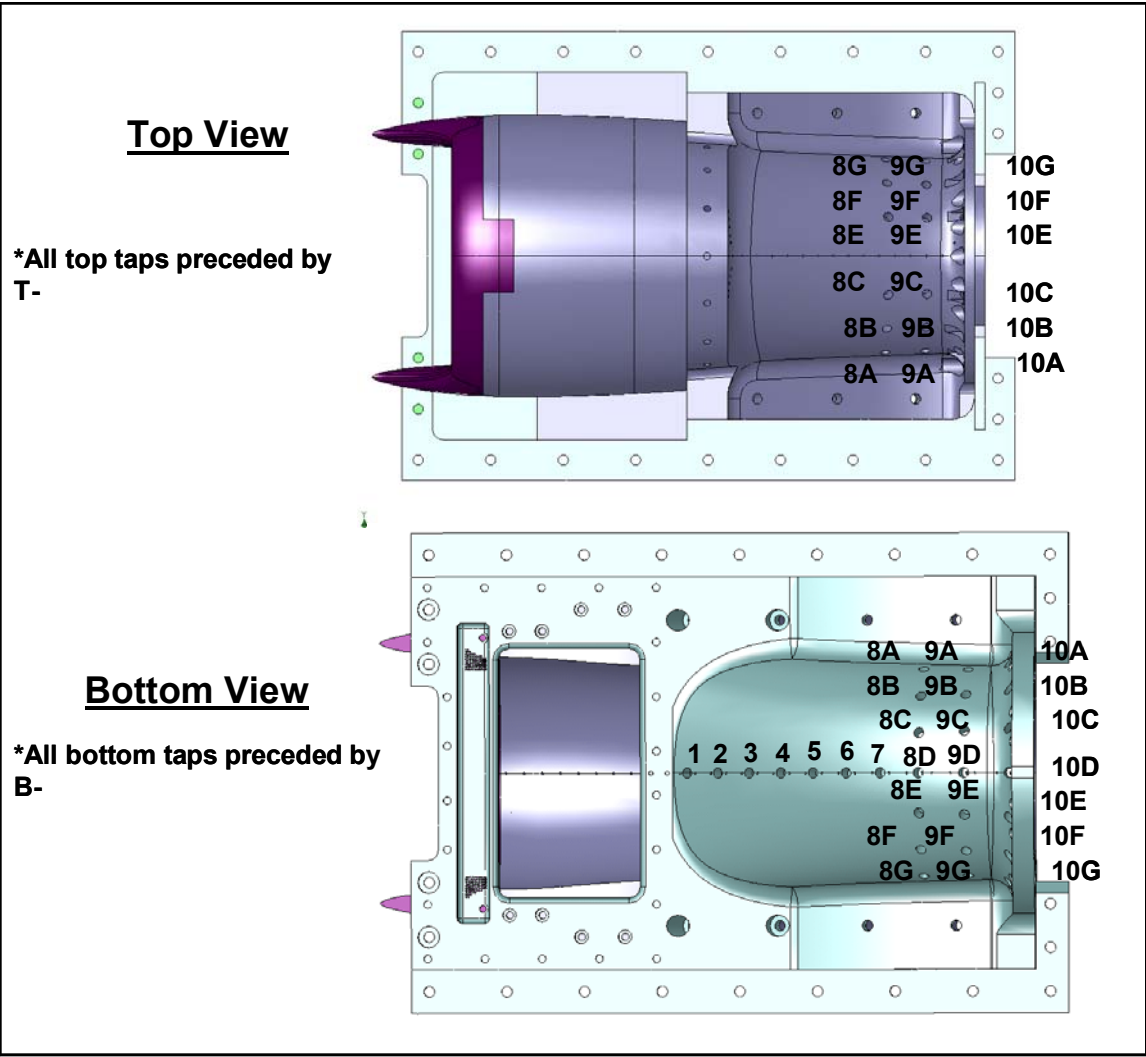


Figure 4-2: Wall-imbedded microphone installation locations in the test inlet

* bottom centerline array consists of microphones: B1, B2, B3, B4, B5, B6, B7, B8-D, B9-D, and B10-D
 † AIP circumferential arrays consist of all microphones excluding: B1, B2, B3, B4, B5, B6, and B7

4.3.4: Sensor Calibration

Because these microphones were installed into the inlet wall such that the wall-pressure fluctuations were measured via a pinhole drilled into the wall of the duct (refer to Figure 4-1 for the installation technique), the microphones did not operate simply according to the specifications given in Appendix H. First, the pinhole cross-sectional area was smaller than the face of the microphone's flexible membrane, which produced a less sensitive transducer in terms of measured pressure per volt. Second, the finite dimensions, d and h (refer to Figure 4-1), of the pinhole produce a compound wave propagation wave field inside the pinhole due to reflections off of the microphone membrane, which result in standing waves and altered pressure readings as indicated in Figure 4-3.

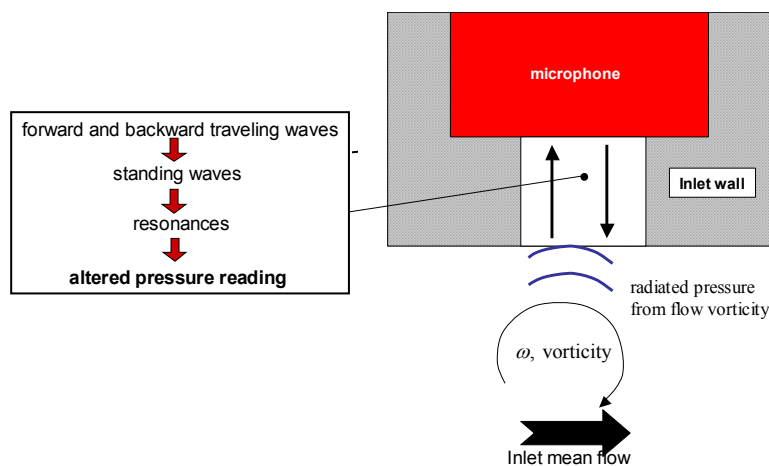


Figure 4-3: Dynamics that affect microphone pressure measurement

A calibration technique was devised in order to remove the dynamics associated with the microphone installation, whereby all of the inlet microphones were calibrated with respect to a single reference microphone. In this calibration technique, an acoustic waveguide was equipped with a reference microphone mounted into the wall of the waveguide with a pinhole orifice with the same diameter as those found in the inlet microphone installation. At the same axial station directly across from where the reference microphone was located, a conically tapered tube was tapped into the waveguide for the purpose of inserting it into the inlet microphone taps. This waveguide was inserted into the entrance of the duct as depicted by the schematic in Figure 4-4 with an acoustic driver connected to one end, while the other end of the waveguide terminated with an open-end approximately one foot past the reference microphone axial station. The waveguide was designed with an internal cross-sectional diameter of 0.5 inches in order to yield a cut-on frequency of approximately 13.4 kHz, which meant that only plane-wave modes would propagate down the waveguide. Thus, calibration pressure waves measured by the inlet and the reference microphone would be in-phase allowing for a simple frequency response function analysis to be performed between the inlet and the reference microphone. The acoustic driver was driven with white noise in order to provide pressures at all the frequencies of interest.

A three signal frequency response function (FRF) estimation technique developed by Goyder¹⁸ was utilized in order to obtain an unbiased measurement of the pressure tubing dynamics. This FRF estimator is denoted as $H_c(f)$ since it is a ratio of complex numbers, and is defined as

$$H_c(f) \equiv \frac{\overline{S(f)} * X(f)}{S(f) * Y(f)} = \frac{G_{SX}(f)}{G_{SY}(f)} \quad (4.10)$$

where, $X(f) \equiv$ reference microphone signal
 $Y(f) \equiv$ test microphone signal
 $S(f) \equiv$ white noise source signal
 $\overline{} \equiv$ complex conjugate

All 46 of the test microphones were calibrated against the same reference microphone. The microphone measurements from the actual experiment were simply convolved with their respective FRF $H_c(f)$, which yielded test measurements that were all calibrated with respect to the single reference microphone.

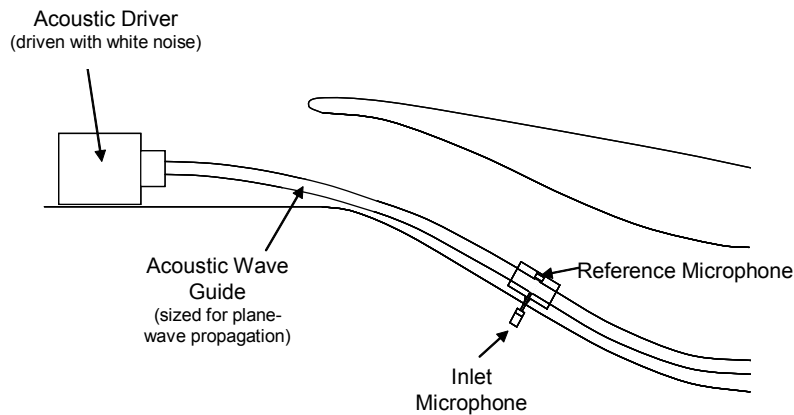


Figure 4-4: Microphone calibration technique

4.4: Test Matrix and Data Acquisition

An Agilent® 16-channel data acquisition system (DAS) was used to simultaneously acquire signals from portions of the 46-microphone array at a 51.2 kHz sampling rate, and the data was streamed to a computer via IEEE 1394 “fire wire”. Ten- second time histories were recorded for each wind tunnel run. Because the high speed DAS only contained 16 channels and the sensor array contained 46 microphones, the microphones were grouped into three different sets of 16 as listed in Table 4-1. Refer to Figure 4-2 for the location of each microphone number. The wind

tunnel test run variables were repeated in order to perform measurements using all three microphone sets for each test point. Microphone Set #1 was configured to capture wall-pressure fluctuations around the circumference of the AIP. Microphone Set #2 focused the measurement attention toward the 6 O'clock position (looking downstream) near the AIP, which is where the majority of the spoiled flow is located in this inlet. Finally, microphone Set #3 provided a mix between an axial centerline array and a circumferential array around the bottom half of the AIP region of the inlet.

Table 4-1: Microphone data set configurations

Channel	Set #1 Microphone #	Set #2 Microphone #	Set #3 Microphone #
1	B10-A	B10-A	B1
2	B10-B	B10-B	B2
3	B10-C	B10-C	B3
4	B10-D	B10-D	B4
5	B10-E	B10-E	B5
6	B10-F	B10-F	B8-D
7	B10-G	B10-G	B9-D
8	T10-G	B9-A	B10-D
9	T10-F	B9-B	B10-A
10	T10-E	B9-C	B10-B
11	T10-B	B9-D	B10-C
12	T10-A	B9-E	B10-E
13	B4	B9-F	B10-F
14	B5	B9-G	B10-G
15	B8-D	B8-C	B9-C
16	B9-D	B8-E	B9-E

4.5: Experimental Distortion Estimator Development

As a first step in experimentally developing a microphone array signal to estimate the inlet total pressure distortion metric DC(60), a time-averaged estimator of DC(60) was explored using frequency domain techniques. Fourier transforms were performed on the 10-second time histories using 1-second data windows, thus providing 10 spectrums with a frequency resolution of 1 Hz with which to perform averaging.

4.5.1: Preliminary Data and Observations

The power spectral signal content of the wall-pressure fluctuation measurements was analyzed as a first-cut effort toward understanding the unsteady flow field at the AIP of the test BLI serpentine inlet for the situations of different flow control efforts. The power spectra provide

scalar information pertaining to the energy of the turbulence convecting through the AIP, which would be impinging upon the fan of an aero engine in a real application.

Referring back to the Green's function formulation that relates fluctuating pressures measured at a certain location to the rapid and slow source terms at all points within the flow (Eq. (4. 9)), it is apparent that the pressure-velocity relationship is not unique. Specifically, the velocity field cannot be recreated directly from a given pressure measurement. However, with some experimental investigation it can be expected that a qualitative description of the flow field can be achieved with an array of pressure measurements. To this end, the circumferential microphone array at the AIP was analyzed to gain an understanding of the AIP flow field.

The AIP array data was first analyzed in the frequency domain using the carpet plot of the AIP circumferential microphone array power spectra shown in Figure 4-5 (a). In looking at the spectra in Figure 4-5 (a), three salient 'hot spots', high amplitude pressure fluctuations from specific microphone locations at specific frequency bands, are quickly noticed, which are labeled as ①, ②, and ③. The hot spot at location #1 refers to high amplitude pressure fluctuations measured from microphone B10-D, which is located at the 6 O'clock position at the AIP cross-section of the inlet (refer to Figure 4-5 (b)), at the high frequency band between 2000 to 4500 Hz. This wall-pressure signal indicates the detection of the energetic, mid-to-small-scale turbulence that is generated by the collision of the large-scale secondary flow that is created by the curvature of the duct and the ingested BL. Then at location #2, the microphone at location B10-A detects high amplitude fluctuations from 2000 to 3000 Hz, which are indicative of the large velocity gradients at the edge of the large momentum defect region centered at the 6 O'clock position of the AIP. Finally at the 'hot spot' referred to as location #3, microphone T10-G detected moderately high level pressure fluctuations in the frequency band between 1000 and 2000 Hz. This is an indication of modest velocity gradients coupled with relatively larger-scaled turbulence near the 9 O'clock AIP location.

The sensitivity of the measured pressure fluctuation amplitudes to the magnitudes of the mean velocity gradients at locations #1, #2, and #3 suggest that the rapid pressure source term from Eq. (4.9) is dominating the wall-pressure fluctuation signature. Given this observation, we can approximate the wall-pressure fluctuations as

$$p'(\bar{x}, t) \approx \frac{\rho}{\pi} \iiint_V \underbrace{\left(\frac{\partial \langle V_i \rangle}{\partial x_j} \frac{\partial v_j}{\partial x_i} \right)}_{\text{Rapid pressure source}} \frac{d\bar{y}}{|\bar{x} - \bar{y}|}, \quad (4. 11)$$

where the harmonic source term equals the Rapid Pressure Source term at the wall because the wall is assumed to be perfectly rigid. The Rapid Pressure source term in Eq. (4.11) is a scalar field that contains the summation of nine terms, which yields the following approximation for the fluctuating wall pressure in longhand notation:

$$p'(\bar{x}, t) \approx \frac{\rho}{\pi} \iiint_{\neq} \left(\begin{array}{l} \frac{\partial \langle V_1 \rangle}{\partial x_1} \frac{\partial v_1}{\partial x_1} + \frac{\partial \langle V_1 \rangle}{\partial x_2} \frac{\partial v_2}{\partial x_1} + \frac{\partial \langle V_1 \rangle}{\partial x_3} \frac{\partial v_3}{\partial x_1} \\ + \frac{\partial \langle V_2 \rangle}{\partial x_1} \frac{\partial v_1}{\partial x_2} + \frac{\partial \langle V_2 \rangle}{\partial x_2} \frac{\partial v_2}{\partial x_2} + \frac{\partial \langle V_2 \rangle}{\partial x_3} \frac{\partial v_3}{\partial x_2} \\ + \frac{\partial \langle V_3 \rangle}{\partial x_1} \frac{\partial v_1}{\partial x_3} + \frac{\partial \langle V_3 \rangle}{\partial x_2} \frac{\partial v_2}{\partial x_3} + \frac{\partial \langle V_3 \rangle}{\partial x_3} \frac{\partial v_3}{\partial x_3} \end{array} \right) \frac{d\bar{y}}{|\bar{x} - \bar{y}|}. \quad (4.12)$$

In working with Eq. (4.12), a right-hand coordinate system will be used where the 1-direction is in the duct streamwise direction and the 2-direction is normal to the wall. Since the primary sources for the wall-pressure fluctuations are concentrated in the boundary layer near the duct wall, a direct interchangability between Cartesian and polar cylindrical coordinates can be used here, thus allowing $(x_1, x_2, x_3) \approx (x_1, x_r, x_\theta)$.

Due to the strong mean secondary flow in the duct, which is a primary agent in creating the flow distortion, it is intuitive that we focus on the mean velocity gradients in the circumferential and radial directions denoted by the subscripts θ and r , respectively. Also, the effects of the nearby wall boundary layer must be accounted. Considering these effects, the leading order terms of Eq. (4.12) for the flow near the AIP pertain to vorticity terms ω_1 and ω_θ , which yields the following reduced-order model for the wall-pressure fluctuation expression:

$$p'(\bar{x}, t) \approx \frac{\rho}{\pi} \iiint_{\neq} \left(\frac{\partial \langle V_1 \rangle}{\partial x_r} \frac{\partial v_r}{\partial x_1} + \frac{\partial \langle V_r \rangle}{\partial x_1} \frac{\partial v_1}{\partial x_r} + \frac{\partial \langle V_r \rangle}{\partial x_\theta} \frac{\partial v_\theta}{\partial x_r} + \frac{\partial \langle V_\theta \rangle}{\partial x_r} \frac{\partial v_r}{\partial x_\theta} \right) \frac{d\bar{y}}{|\bar{x} - \bar{y}|}. \quad (4.13)$$

From our reduced order model in Eq. (4.13), it is clear that the wall-pressure fluctuations should be sensitive to the coupling of the mean and unsteady components of the swirl at the AIP, which appears to be true from the experimental results shown in Figure 4-5. Further, it can be assumed that the mean velocity gradients will be greater than the unsteady velocity gradients in Eq. (4.13),

or in mathematical form this can be stated as $\frac{\partial \langle V_r \rangle}{\partial x_\theta} > \frac{\partial v_\theta}{\partial x_r}$, $\frac{\partial \langle V_\theta \rangle}{\partial x_r} > \frac{\partial v_r}{\partial x_\theta}$, etcetera. Also, these mean velocity gradients will have an effect on the turbulent structures size or length scales. For example, the mean velocity gradient of $\frac{\partial \langle V_r \rangle}{\partial x_\theta}$ will stretch the size of the coherent turbulent

structure in the r -direction thereby decreasing the frequency of the unsteady component $\frac{\partial v_\theta}{\partial x_r}$.

The same phenomenon occurs for the remaining coupled velocity gradients of Eq. (4.13). This phenomenon is commonly seen in turbulent boundary layer theory whereupon the coherent structures are elongated in the spanwise direction near flow separations (i.e., large pressure gradients)¹⁹. Finally, a few conclusions from this reduced order analysis can be made:

Wall-pressure fluctuation amplitudes are most sensitive to the gradients of the swirl components of the inlet mean velocity,
Large turbulent integral length scales will be associated with large mean swirl velocity gradients.

Moving on with further observations of the wall-pressure spectra measured by the AIP microphone array, the conclusions from the reduced order model of Eq. (4.13) can be verified with data collected for the case where 0.98% flow control effort was implemented. This analysis is aided by the carpet plot presenting spectra of the RMS microphone voltage reduction versus the baseline case shown in Figure 4-6. These changes in the RMS microphone responses versus the baseline case are compared to the changes in the normalized total pressures measured for these two flow control cases. The major highlights to be seen from Figure 4-6 are that the reductions in the swirl velocity gradients with the addition of 0.98 flow control effort at locations #1, #2, and #3, which can be speculated from the total pressure contours, are correctly measured by reductions in the pressure fluctuation amplitudes in the corresponding highlighted areas in the spectra carpet plot of Figure 4-6. In addition, the microphones measured increases in the high-frequency band pressure fluctuations at locations #4 (located along the top side of the AIP sector, refer to Figure 4-6), which correctly indicate increases in the near-wall swirl velocity gradients (i.e., streamwise vorticity associated with the boundary layer). Then the ability of the AIP microphone array to detect further flow field changes due to an increase in flow control to 1.87% is described in Figure 4-7. The same trends previously seen for the 0.98% flow control case are seen for the 1.87% case.

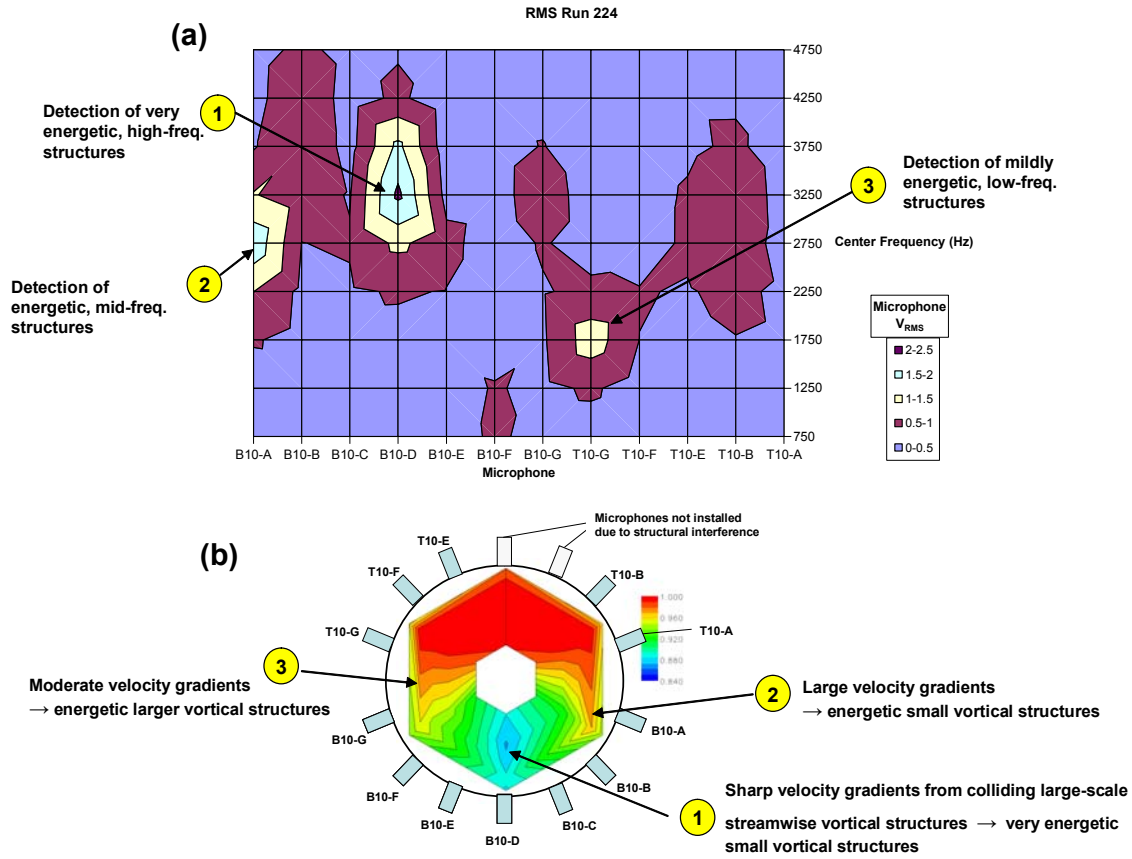


Figure 4-5: AIP flow field characteristics indicated by the AIP circumferential microphone array measurements

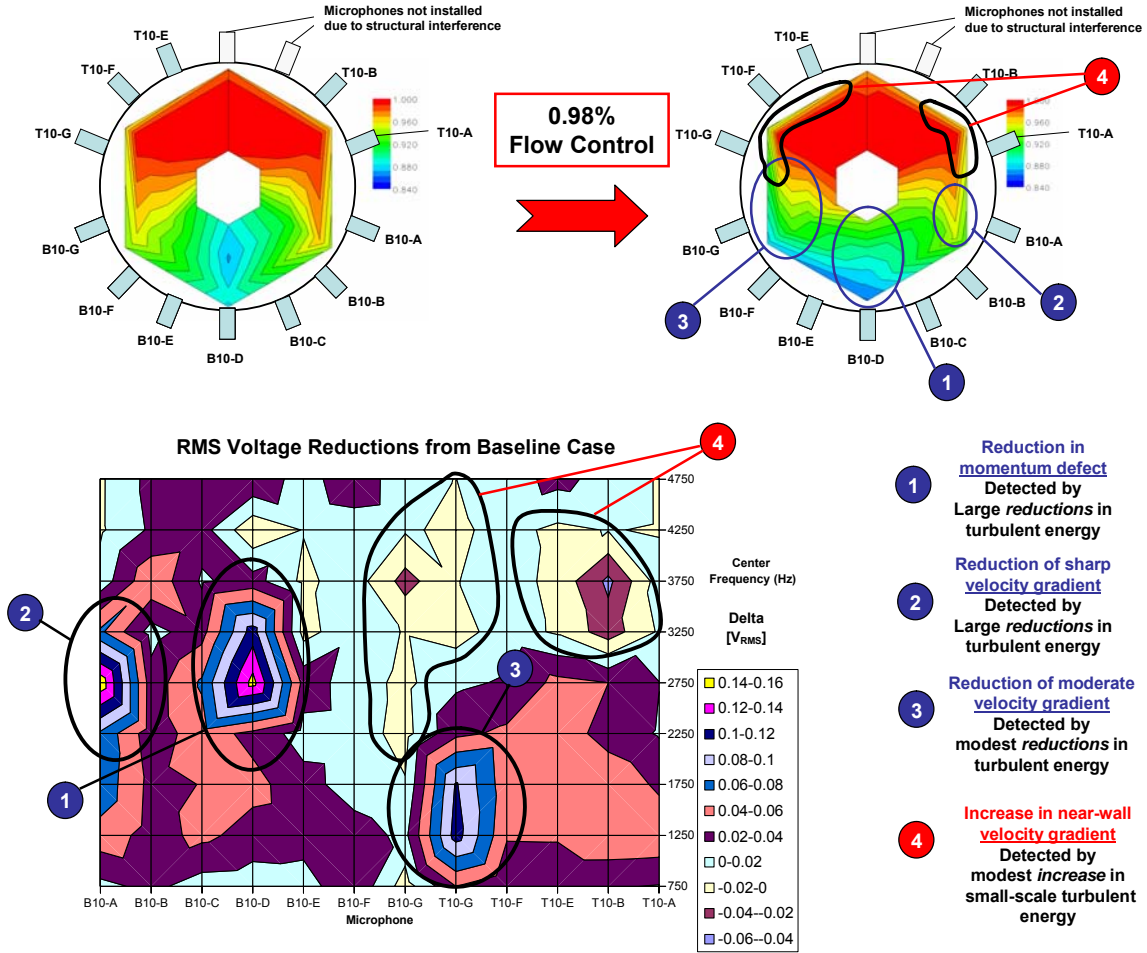


Figure 4-6: Detection of flow field changes by AIP circumferential microphone array due to 0.98% flow control

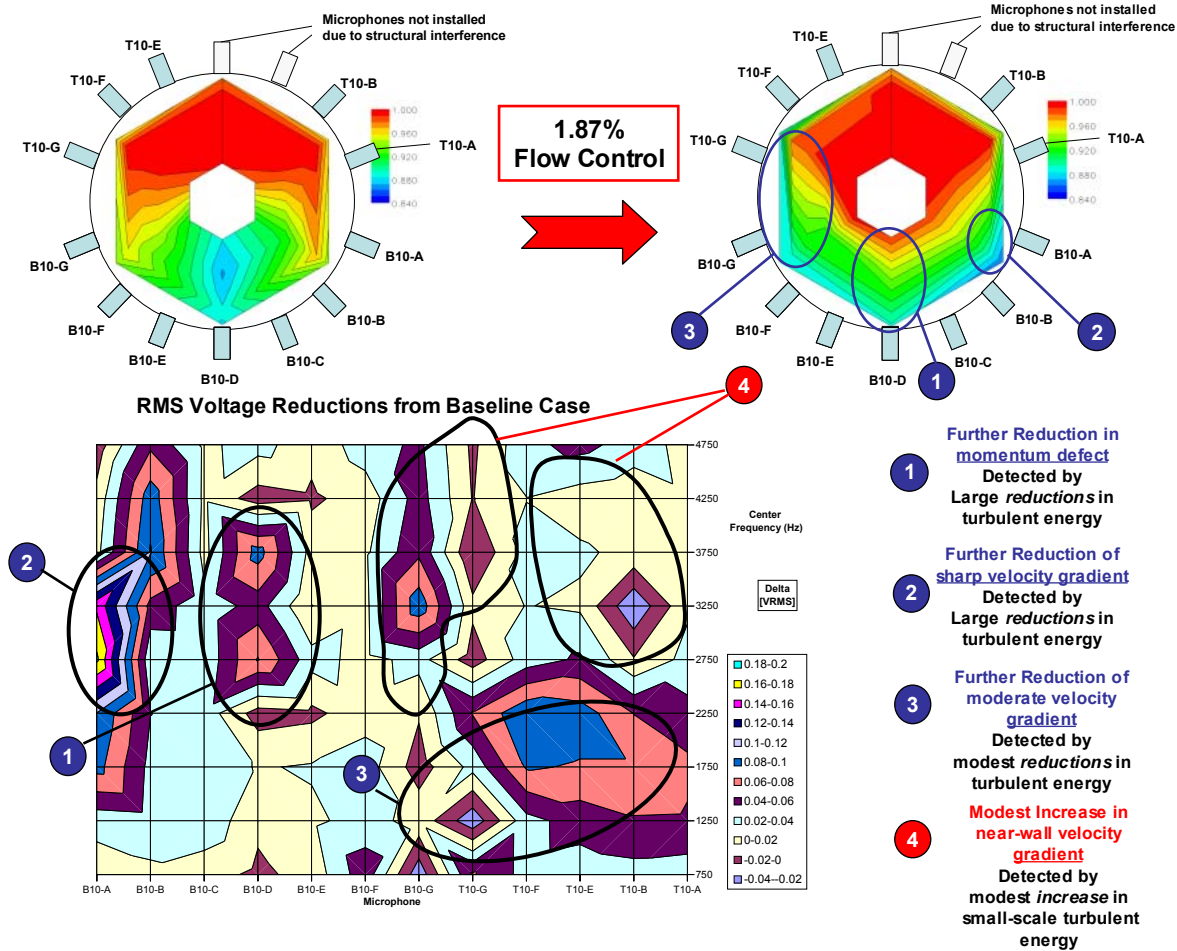


Figure 4-7: Detection of further flow field changes by AIP circumferential microphone array due to 1.87% flow control

4.5.2: Circumferential Array Correlation Approach

A new, more intelligent microphone-based technique to estimate the total pressure distortion descriptor DC(60) for BLI serpentine inlets has been developed that utilizes two circumferential microphone arrays located near the AIP. This technique has been named the Circumferential Array Correlation (CAC) approach. The hypothesis of the CAC approach is that the turbulent integral length scales are related to the flow distortion created in BLI serpentine inlets. The means to this end are based on the conclusions drawn from the reduced order model of Eq. (4.13) that describes the relationship between pressure fluctuation measurements at a location \bar{x} due to the coupling of steady and unsteady streamwise vorticity within the flow field at locations \bar{y} , say near the AIP. This reduced order model that considers the streamwise vorticity is appropriate in this application because the streamwise vorticity is directly related to the secondary flow field in the serpentine BLI inlet that is a primary contributor to the creation of flow distortion. In fact, the flow control approach developed in this research, which was described in §2 and §3, is based

on this very premise that distortion can be reduced via secondary flow management; a notion that has also been realized by Gorton et al. ¹¹ and others in the field.

The two primary conclusions from the reduced order model of Eq. (4.13) were that:

- ❑ the wall-pressure fluctuation amplitudes will be proportional to the mean swirl gradients, and
- ❑ the integral length scales will be larger for flows with large swirl structures in the outer part of the boundary layer and free stream.

Using these two premises, it is expected that the integral turbulent length scales will decrease as the flow control rids the BLI serpentine inlet of the large velocity gradients and, by definition, the flow distortion at the AIP. In this research program, the turbulent length scales were estimated from the correlated content between microphones oriented in two circumferential arrays located on the bottom half of the inlet near the AIP as indicated in Figure 4-8.

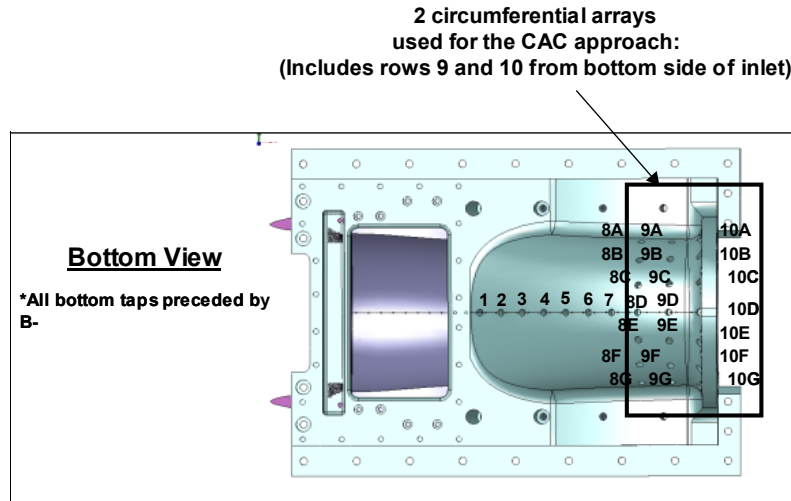


Figure 4-8: CAC approach microphone approach

The estimated length scales from the wall-pressure fluctuation measurements were determined in the frequency domain utilizing the coherence functions, $\gamma_{\alpha,\beta}^2$, between signals from microphones α and β according to

$$\gamma_{\alpha,\beta}^2(f) = \frac{G_{\alpha,\beta}(f)G_{\beta,\alpha}(f)}{G_{\alpha,\alpha}(f)G_{\beta,\beta}(f)}, \quad (4.14)$$

where $G_{\alpha,\alpha}(f)$ denotes the auto spectrum for microphone α , $G_{\alpha,\beta}(f)$ denotes the cross spectrum between microphones α and β , and so forth. The average coherence was then determined for five different frequency bands between 0 and 5000 Hz, which were then denoted as $\gamma_{\alpha,\beta}^2(f_n)$ where $(n=1,2,3,4,5)$ for each of the five frequency bands. In general, the length

scales in the streamwise direction (denoted by the subscript x) at a microphone location α according to

$${}_x L_\alpha = \sum_n \int_0^\infty \gamma_{\alpha, \alpha+d\zeta}^2(f_n) d\zeta \quad , \quad (4.15)$$

where ζ is a spatial dummy variable in the streamwise direction. For example, the streamwise length scale at location B10-A was estimated according to

$$\begin{aligned} {}_x L_{10A} &= \sum_n \int_0^\infty \gamma_{10A, 10A+d\zeta}^2(f_n) d\zeta \approx \sum_n \sum_{i=0}^1 \gamma_{10A, 10A+i\Delta x}^2(f_n) \Delta x \\ &= \sum_n [\gamma_{10A, 10A}^2(f_n) + \gamma_{10A, 9A}^2(f_n)] \Delta x \end{aligned} \quad (4.16)$$

The spatial summation of the coherence function in the streamwise direction only involves two terms because the array consists of only two circumferential arrays in the streamwise direction. A similar approach can be applied to compute the length scales in the circumferential direction (denoted by the subscript θ) in general at a location α according to

$${}_\theta L_\alpha = \sum_n \int_0^\infty \gamma_{\alpha, \alpha+d\lambda}^2(f_n) d\lambda \quad , \quad (4.17)$$

where λ is a spatial dummy variable in the streamwise direction. Now as an example, the circumferential length scale can be estimated at location B10-A according to

$$\begin{aligned} {}_\theta L_{10A} &= \sum_n \int_0^\infty \gamma_{10A, 10A+d\lambda}^2(f_n) d\lambda \approx \sum_n \sum_{i=0}^3 \gamma_{10A, 10A+i\Delta\theta}^2(f_n) \Delta\theta \\ &= \sum_n [\gamma_{10A, 10A}^2(f_n) + \gamma_{10A, 10B}^2(f_n) + \gamma_{10A, 10C}^2(f_n) + \gamma_{10A, 10D}^2(f_n)] \Delta\theta \end{aligned} \quad (4.18)$$

Now that the length scales can be computed in the streamwise and circumferential directions at each microphone location, the overall length scale at these locations is computed by determining the resultant vector magnitude according to

$$L_\alpha = \sqrt{({}_x L_\alpha)^2 + ({}_\theta L_\alpha)^2} \quad . \quad (4.19)$$

It should be noted that only the resultant length scales for those microphones located in row 10 on the bottom right-hand side of the AIP looking downstream (i.e., microphones B10-A, B10-B, B10-C, and B10-D) were computed toward the end goal of developing the DC(60) estimator.

Before diving into computed length scales for each of the four microphone locations, coherence plots between microphone B10-B and all of the other microphones in the array on the right hand side of the duct were analyzed in order to check which frequency bands were most

sensitive to the flow changes brought on by flow control. These coherence plots are presented in for three levels of flow control, baseline, 0.98%, and 1.87%. From these coherence plots it seemed that the frequency band between 1000 to 2000 Hz was most sensitive in detecting the reduced length scales of the turbulent structures in both the streamwise and circumferential directions. The next most sensitive band was 2000 – 3000 Hz. As can be seen from Figure 4-9, the low frequency correlations are low in value and do not change much with the addition of flow control, which indicates that the turbulent structures are small in size and do not contribute toward the flow distortion. This conclusion is in conjunction with the power spectra plot of Figure 4-5 that shows low energy levels for low frequencies at location B10-B; in addition, the RMS voltage difference plots of Figure 4-6 and Figure 4-7 show small changes in the low frequency amplitudes from microphone B10-B with the addition of flow control. At location B10-B, it is the reduction of the mid-frequency structures associated with the sharp velocity that originally existed for the baseline case at this location. In light of the high sensitivity of the two-point correlations with microphone B10-B to flow control in the frequency band between 1000 and 2000 Hz, this band was first chosen for the length scale calculations.

In this first attempt in calculating the wall-pressure-based length scale estimators, L_w , only the frequency band of 1000 to 2000 Hz was studied due to the two-point correlation analysis discussed in the previous paragraph. The estimated length scales computed for the four microphone locations B10-A, B10-B, B10-C, and B10-D considering only the 1000-2000 Hz frequency band are plotted in Figure 4-10 versus the respective traditionally measured DC(60) values for each wind tunnel run. Based on the correlation analysis that was preliminarily performed using only microphone B10-B, it is no surprise that the length scales for microphone B10-B are the most sensitive and the largest in this frequency range. Length scales at B10-A are also sensitive to flow control in this frequency band because the flow structures at B10-A are affected in a fashion similar to B10-B. The major trends for the length scales at all four locations do follow a physically understandable trend. First, flow control reduces all four length scales eventually. The length scales all increase at low levels of flow control, which follows the same trend as the DC(60) metric. Also, the length scales at location B10-C increase over a broad range of moderate flow control efforts as the main momentum defect region is moved past this microphone location.

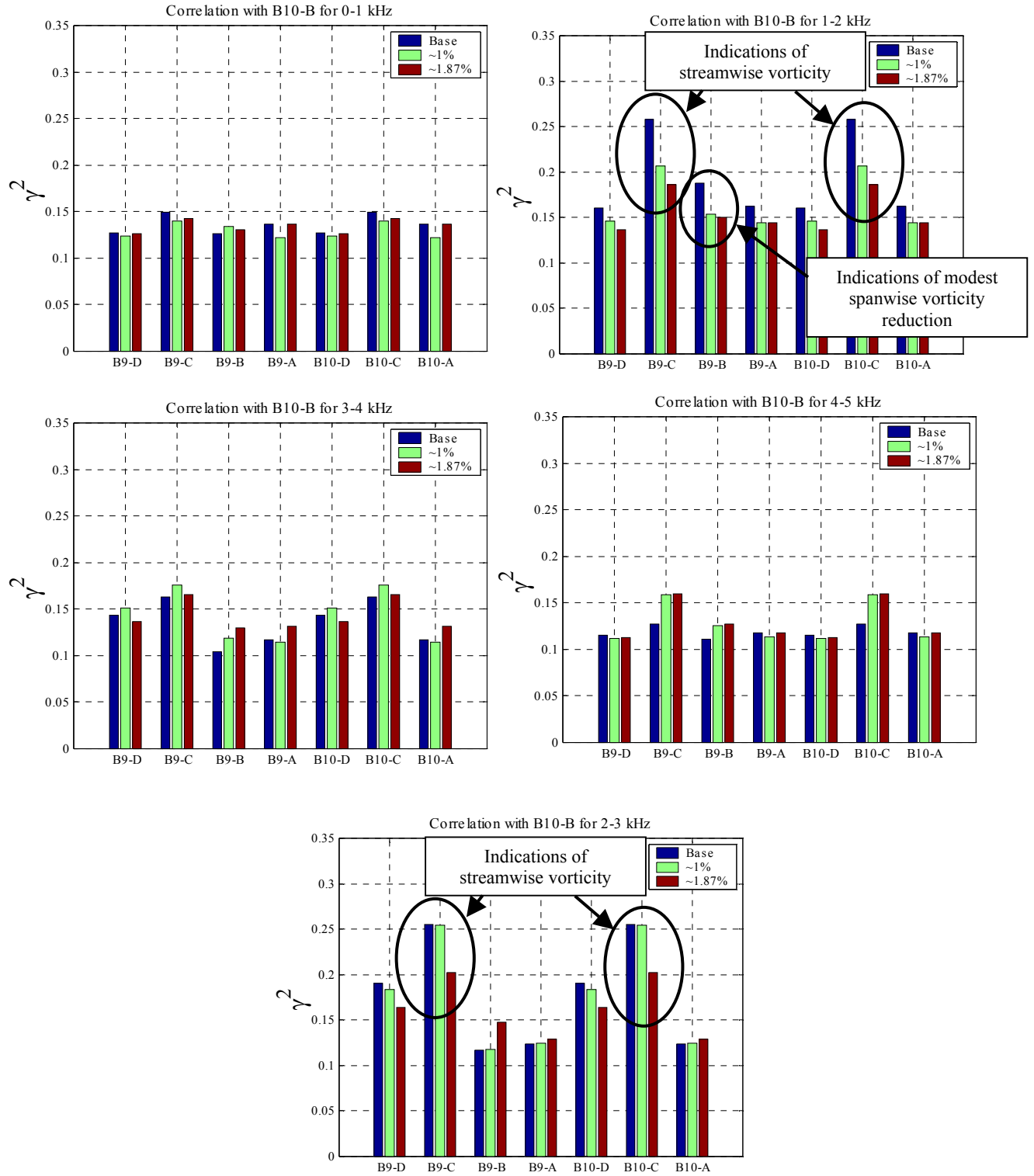


Figure 4-9: Two-point coherence with the microphone at location B10-B

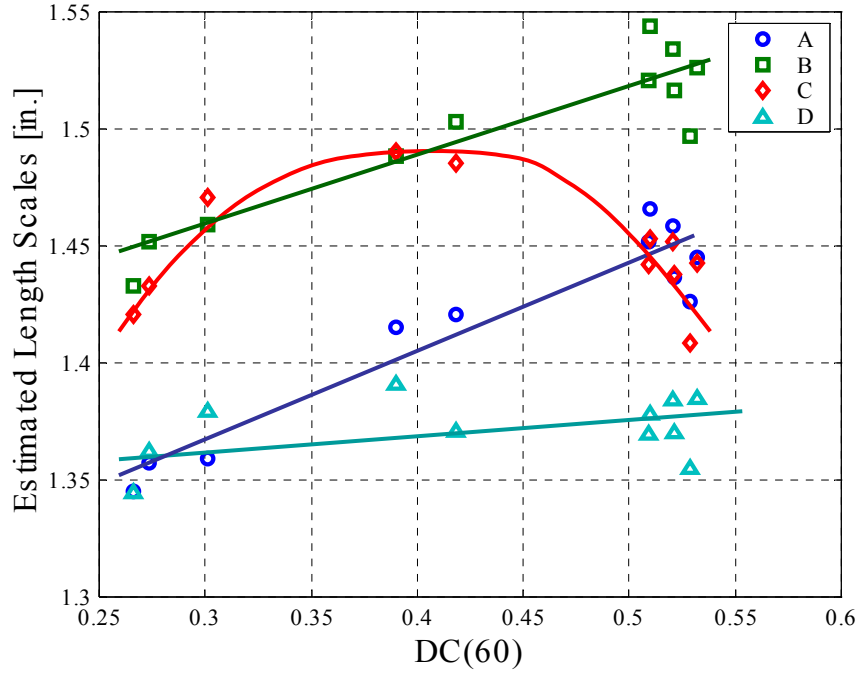


Figure 4-10: Estimated length scales versus DC(60) considering only the frequency band of 1000-2000 Hz

At this point it is of interest to combine the four length scale estimates from each flow control case into a single value to estimate the DC(60) parameter. The preliminary DC(60) estimator model, denoted as the signal D , was proposed to be a linear summation of the four length scale estimates from each wind tunnel run, which takes the form

$$D = [L_\alpha]^T \bar{c} = [L_A \ L_B \ L_C \ L_D] [a \ b \ c \ d]^T, \quad (4.20)$$

where \bar{c} is simply a vector of constants. An optimal set of constants for \bar{c} is determined using a least-squared approach, where the error is defined as $e = DC(60) - D$. The minimization of the squared error leads to a solution for the optimal constant vector, \hat{c} , written as

$$\hat{c} = M^{-1} \begin{Bmatrix} \sum L_A DC(60) \\ \sum L_B DC(60) \\ \sum L_C DC(60) \\ \sum L_D DC(60) \end{Bmatrix}, \quad \text{where} \quad (4.21)$$

$$M = \begin{bmatrix} \sum L_A L_A & \sum L_A L_B & \sum L_A L_C & \sum L_A L_D \\ \sum L_B L_A & \sum L_B L_B & \sum L_B L_C & \sum L_B L_D \\ \sum L_C L_A & \sum L_C L_B & \sum L_C L_C & \sum L_C L_D \\ \sum L_D L_A & \sum L_D L_B & \sum L_D L_C & \sum L_D L_D \end{bmatrix}.$$

For this case where only the frequency band between 1000-2000 Hz was considered, the resulting optimal constant vector is

$$\hat{c} = [2.84 \quad -0.40 \quad -0.79 \quad -1.35]^T, \quad (4.22)$$

which when used in the proposed preliminary DC(60) estimator model (Eq. (4.20)) yields a nearly linear trend with respect to the actual DC(60) values as shown in Figure 4-11. Despite the near linear agreement between DC(60) and the computed values of D , there would still be a moderate error in predicting DC(60) directly from D as can be seen in the slight scatter in the data. This error in predicting DC(60) directly from D can be proclaimed moderate due to the high quality of linear fit suggested by the R^2 value of 0.916 that resulted from a linear least-squared error regression for an estimate of DC(60) of the form

$$\overline{DC(60)} = mD + b. \quad (4.23)$$

The regression analysis of the linear model for the DC(60) estimate, $\overline{DC(60)}$ (Eq. (4.23)), yielded values of $m = 1.0069$ and $b = -0.0031$. Since the slope of the linear distortion estimator $\overline{DC(60)}$ is so close to 1, $\overline{DC(60)}$ itself could serve as an excellent estimator of the traditionally measured distortion metric DC(60). Thus, the proposed estimate of DC(60) using microphone two-point correlations from the frequency band between 1-2 kHz is

$$\overline{DC(60)}\Big|_{1-2kHz} = 1.0069D\Big|_{1-2kHz} - 0.0031. \quad (4.24)$$

In looking back at the predicted length scales in Figure 4-10, it is clear that the 1-2 kHz frequency band created possibly high estimates of the integral length scales for the B10-B microphone location. At the same time, the energy-containing turbulent structures near the B10-D location as seen in Figure 4-5 occurred at frequencies higher than 2000 Hz. Therefore, the length scales would be underestimated for the structures near the B10-D location when considering only this frequency band. As a result, length scales were then estimated from the two-point microphone correlations considering this time frequencies spanning from 1000 to 5000 Hz. The signal processing procedures explained by Eq.'s (4.13) – (4.23) were used to create a DC(60) estimator considering the larger frequency band between 1000 – 5000 Hz, $\overline{DC(60)}\Big|_{1-5kHz}$. The microphone-based estimations of the length scales considering frequencies between 1000-5000 Hz are shown in Figure 4-12, and now the length scales seem to be more appropriately ordered. This data then led to the comparison of the $D\Big|_{1-5kHz}$ data with the actual DC(60) values, which is shown in Figure 4-13. The most salient feature of the updated distortion estimator model is the increase in accuracy. The equation for $\overline{DC(60)}\Big|_{1-5kHz}$ that resulted from this analysis is written as

$$\overline{DC(60)}\Big|_{1-5kHz} = 0.9984D\Big|_{1-5kHz} - 0.0007, \quad (4.25)$$

which yields an estimator that has a 97% agreement of linear fit to the traditionally measured DC(60) values. Given its high level of linear fit with the traditionally measured distortion, Techsburg recommends that $\overline{DC(60)}\Big|_{1-5kHz}$ be used to non-intrusively estimate the distortion metric DC(60) in BLI serpentine inlets that may be potentially used on future BWB aircraft.

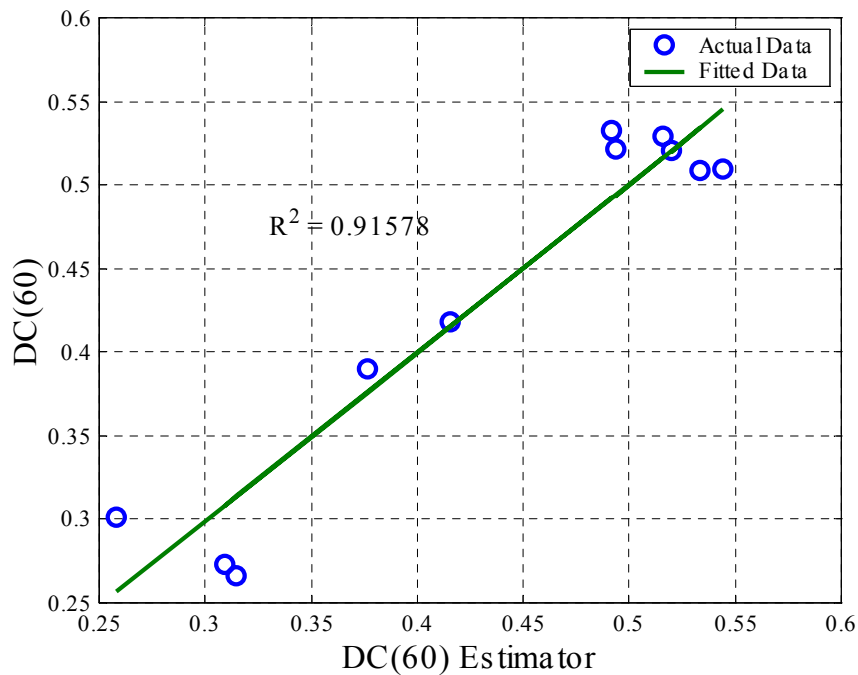


Figure 4-11: DC(60) versus the DC(60) estimator determined from the correlations from only the 1000-2000 Hz bandwidth

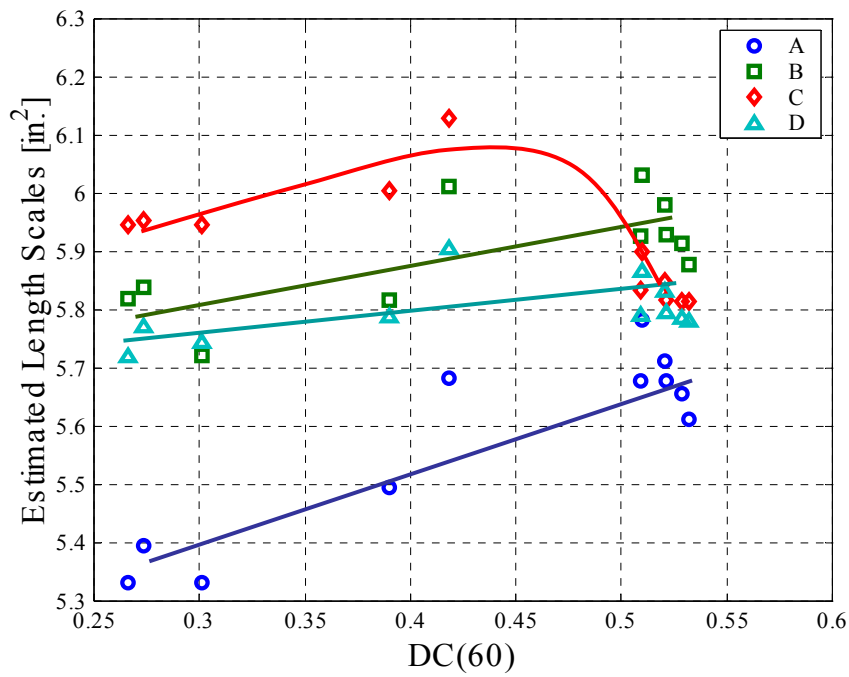


Figure 4-12: Estimated length scales versus DC(60) considering only the frequency band of 1000-5000 Hz

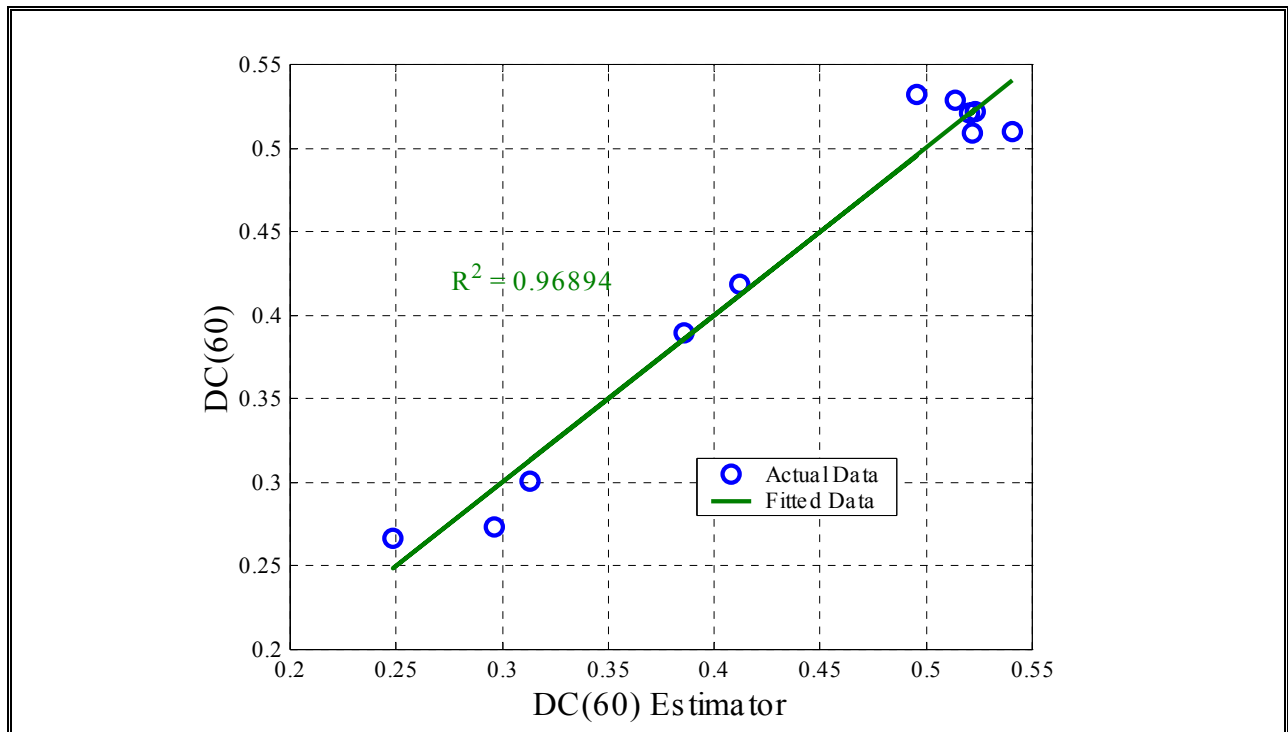


Figure 4-13: DC(60) versus the DC(60) estimator determined from the correlations from only the 1000-5000 Hz bandwidth

4.6: Proposed Closed-Loop Implementation

While not performed under the current contract, Techsburg proposes that the distortion estimator $\overline{DC(60)}|_{1-5kHz}$ that was described in the previous section be used as a non-intrusive distortion sensor as part of the feedback loop in an automated system to control total pressure distortion in BLI serpentine inlets. A proposed PID-compensated, feedback distortion control system architecture is shown in Figure 4-14. As shown in Figure 4-14, the distortion observer will include the mathematical operations described by Eq.'s (4.13) – (4.18) of this report culminating with Eq. (4.24) as the final calculation of the estimated DC(60) value. The primary caveat in performing Techsburg's non-intrusive distortion sensing strategy is the need to use least mean squared (LMS) error adaptive filters in order to compute the two-point correlations between the microphones of the array. The basic block diagram of the adaptive filter network to extract a signal representing the correlated content, $p'_{\text{correlated}}$, between two wall-imbedded microphone signals p'_1 and p'_2 . This technique has been previously used by Anderson²⁰ to remove the correlated content between two widely spaced microphones that was related to background acoustic disturbances. The key in designing the LMS adaptive filter will be to maintain a proper balance between the accuracy of the filter and the response time of the filter. The final required information for the PID controller design will be the actuator dynamics, as it has been discovered in past feedback inlet flow control demonstrations that the valve's dynamics serve as the dominant poles. In other words, the high-pressure valves used in the past were slow, and served as the bottleneck in system response time.

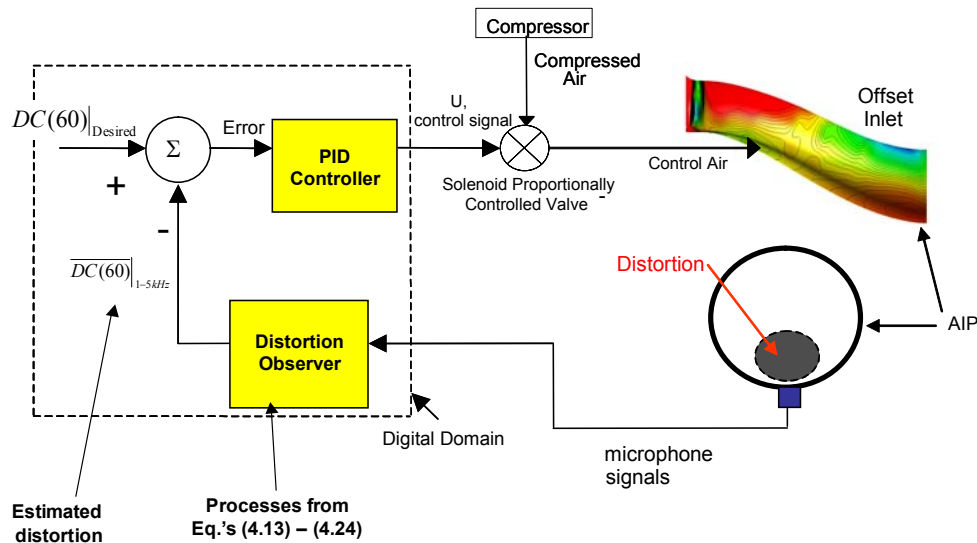


Figure 4-14: Proposed flow distortion control system with microphone feedback sensors

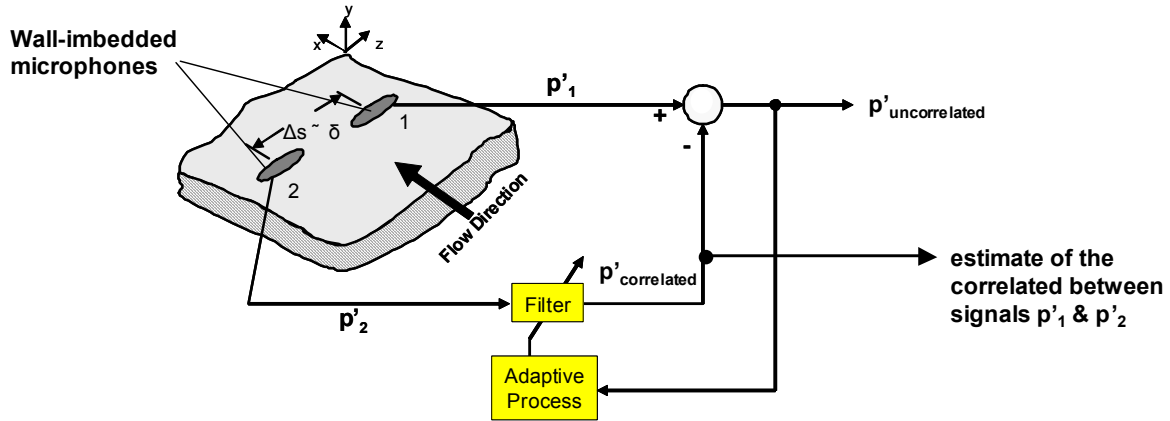


Figure 4-15: Illustration of LMS adaptive filter technique to determine the correlated content between two microphone signals in real-time

4.7: Non-Intrusive Distortion Sensor Conclusions

A novel technique to estimate the inlet total pressure distortion metric $DC(60)$ has been developed that utilizes a small array of wall-imbedded microphone sensors near the AIP. This distortion sensing approach offers a non-intrusive alternative to using the traditional total pressure probe rake, which would be unacceptable to place in front of an aero gas turbine engine for an extended amount of time. This particular microphone distortion observer is based on a reduced order model derived from the Green's function solution to the Poisson equation for pressure. From this reduced order model, it was determined that a signal that emulates the calculation of turbulent length scales using an integration of the different permutations of the two-point correlations between the microphones in the array would indicate the distortion at the AIP. A model for estimating the metric $DC(60)$ from a linear summation of the estimated integral length scales measured by the microphone array was proposed, and optimized using a least-squared error regression approach. This process resulted in the $DC(60)$ observer referred to as $\overline{DC(60)}_{1-5kHz}$ in Eq. (4.24), which proved to be 97% accurate in predicting the $DC(60)$ values measured by the traditional total pressure rake at the AIP.

Chapter 5: Future Potential Commercial Applications

The implementation of an active flow control system can be an enabling technology for the practical application of boundary-layer-ingesting serpentine diffusers. These systems are of the most practical use for flying wing configurations such as the NASA/Boeing blended wing-body and UAV applications. Techsburg feels that the market for flying wing configurations will prosper in the coming years as airframers, such as Boeing, decide to reap the benefits of offering airliners a more efficient aircraft in terms of both payload capacity and life cycle cost. Through the implementation of flow control, engine-face flow distortion can be decreased to levels acceptable to aircraft engines, enabling substantial gains in aircraft performance. When the flow control system is coupled with Techsburg's acoustic distortion-measuring system, an adaptive flow control system is created that is capable of tailoring the flow control effectors to variable distortion conditions. Further preliminary testing of this enabling technology can be performed economically at the Techsburg Ejector-driven wind tunnel facility, which has the capability to match the high altitude, high subsonic Mach number freestream conditions representative of modern aircraft cruise conditions.

Chapter 6: Conclusions

In order to realize the substantial performance benefits of serpentine BLI diffusers, this study investigated the use of enabling active flow control methods to reduce engine-face distortion. An ejector-pump based system of fluidic actuators was used to directly manage the diffuser secondary flows. This system was modeled computationally using a novel flow control technique, and then tested in the Techsburg ejector-driven wind tunnel facility.

The tunnel test section used for this experiment was designed, built, and tested as a validation tool for the computational methods. This process resulted in the creation of an efficient system capable of investigating and testing the fundamental mechanisms of flow control in BLI serpentine diffusers at a fraction of the time and expense required by previous investigations.

Active flow control offers substantial performance benefits by providing a wide range of flexible, and adaptable control methods. This control system can achieve significant reductions in engine-face distortion while virtually eliminating the viscous losses created by vane-type vortex generators. Because active flow control systems typically draw motive pressure from the engine compressor, the performance penalties of using compressor bleed air for flow control purposes can limit the amount of air available. Thus, it is necessary to augment jet performance as much as possible.

This augmentation was accomplished by employing the use of an ejector-pump based system of fluidic actuators that effectively increased jet mass flow with no net increase in required motive air. The performance of these jets was then evaluated to identify some of the driving parameters that govern the effectiveness of active flow control methods in serpentine BLI diffusers. This was investigated through computational and experimental means by designing a process capable of identifying key performance parameters while simultaneously reducing unnecessary time and cost.

The computational methods and novel flow control modeling techniques used herein allowed for rapid, accurate analysis of flow control geometries. By utilizing mesh boundary conditions to model the fluidic actuators, extensive gains were made in terms of the number of configurations tested, as well as the accompanying grid construction and computational processing time. These methods contrast with previous studies that have often focused on individual actuator modeling (whether vane or jet-type), or the introduction of vorticity source-terms to the flow field in order to simulate the physical effects of vortex generators: processes that are both time-consuming and cost prohibitive.

Computational results were validated by designing and testing a representative BWB BLI diffuser test section for the Techsburg ejector-based wind tunnel. This facility simulated the high-altitude, high subsonic Mach number conditions representative of BWB cruise conditions, while substantially reducing the cost and complexity associated with cryogenic or blow-down tunnel configurations.

Results of computational and wind tunnel analysis confirmed the large potential benefit of adopting fluidic actuators to control flow distortion in serpentine BLI inlets. Computational analysis showed a maximum 71% reduction in flow distortion at the AIP through the use of the Pyramid 1 (SP1) ejector scheme, and a 68% reduction using the Circumferential ejector (FSCIR) scheme. The experimental results showed that the computational analysis slightly over-predicts the flow distortion. However, the trends are accurately predicted despite slight variances in freestream Mach number between runs and a slightly lower tested altitude. Although these

configurations have not been optimized, with additional work they could likely achieve the ‘acceptable’ performance level of $DC(60)_q = 0.01$.

The effects of fluidic flow control actuators can, however, be deceptive. While configurations that produce large-scale vortices can have a tremendous impact on reducing AIP total pressure distortion, careful simultaneous observation of AIP flow swirl is warranted. Strong vortices, although a powerful mechanism for flow mixing, can induce high flow swirl that can result in local stalling of compressor blades. This can lead to reduced engine performance and the increased possibility of engine surge or stall. Computational analyses have highlighted the importance of maintaining jet separation and individuality, because the coalescence of multiple jets can result in low total pressure distortion at the expense of increased flow swirl.

Finally, a novel technique to estimate the $DC(60)$ total pressure distortion descriptor non-intrusively via wall-pressure fluctuation measurements from an array of wall-imbedded microphones. A simple reduced order model was developed to gain insight into the relationship between the vorticity within the inlet duct and the pressure fluctuations measured at the inlet wall. This simple model facilitated the development of a microphone array signal that involved the estimation of integral turbulent length scales using the permutations of two-point correlations between the microphone measurements within the array. A linear summation of the estimated integral turbulence length scales led to a single microphone-based signal, $\overline{DC(60)}\big|_{1-5kHz}$, that

estimated the traditionally measured $DC(60)$ with a 97% accuracy. As a last offering, the architecture for an automatic closed-loop system to control inlet distortion using Techsburg’s non-intrusive distortion observer $\overline{DC(60)}\big|_{1-5kHz}$ is proposed for future potential application in

BLI serpentine inlets on BWB aircraft.

Bibliography

- ¹ Seddon, J., Goldsmith, E. L.. *Intake Aerodynamics*. 2nd Edition. AIAA Education Series. Reston, VA. 1999.
- ² Der, Jr., J.. *Improved Methods of Characterizing Ejector Pumping Performance*. AIAA 1998-0008. 27th Aerospace Sciences Meeting, Reno, NV, January 8-10, 1989.
- ³ Guo R. W., Seddon, J.. *Swirl Characteristics of an S-shaped Air Intake with both Horizontal and Vertical Offsets*. Aeronautical Quarterly, May 1983.
- ⁴ Anon. SAE-ARP-1420 Revision B. *Gas Turbine Engine Inlet Flow Distortion Guidelines*. January 11, 2001.
- ⁵ Hall, E., Heidegger, N., Delaney, R.. *ADPAC v.1.0 – User’s Manual*. Allison Engine Company, Indianapolis, IN. NASA/CR-1999-206600. February 1999.
- ⁶ Berrier, B., Allan, B.. *Experimental and Computational Evaluation of Flush-Mounted, S-Duct Inlets*. AIAA 2004-0764. 42nd Aerospace Sciences Meeting and Exhibit. January 5-8, 2004. Reno, NV.
- ⁷ Allan, B., Owens, L., Berrier, B.. *Numerical Modeling of Active Flow Control in a Boundary Layer Ingesting Offset Inlet*. AIAA 2004-2318. AIAA 2nd Flow Control Conference. June 28, 2004. Portland, Oregon.
- ⁸ Anderson, B., Huang, P., Paschal, W., Cavatorta, E.. *A Study on Vortex Flow Control of Inlet Distortion on the Re-Engined 727-100 Center Inlet Duct Using Computational Fluid Dynamics*. AIAA 1992-0152. 30th Aerospace Sciences Meeting and Exhibit. Reno, NV. January 6-9, 1992.
- ⁹ Schetz, J.. *Boundary Layer Analysis*. Prentice Hall Inc., Englewood Cliffs, New Jersey, 1993.
- ¹⁰ Allan, B., Yao, C., Lin, J.. *Numerical Simulations of Vortex Generator Vanes and Jets on a Flat Plate*. AIAA 2002-3160. AIAA 1st Flow Control Conference. June 24-26, 2002. St. Louis, Missouri.
- ¹¹ Gorton, S., Owens, L., Jenkins, L., Allan, B., Schuster, E... *Active Flow Control on a Boundary-Layer-Ingesting Inlet*. AIAA 2004-1203. 42nd AIAA Aerospace Sciences Meeting and Exhibit. January 5-8, 2004. Reno, NV.
- ¹² Anderson, B., Gibb, J.. *Study on Vortex Generating Flow Control for the Management of Inlet Distortion*. Journal of Propulsion and Power. Vol. 9, No. 3. May-June 1993.
- ¹³ Reichert, B., Wendt, B.. *An Experimental Investigation of S-Duct Flow Control Using Arrays of Low-Profile Vortex Generators*. AIAA 1993-0018. AIAA 31nd Aerospace Sciences Meeting and Exhibit. Reno, NV. January 1993.
- ¹⁴ Anabtawi, A., Blackwelder, R., Lissaman, P., Liebeck, R.. *An Experimental Study of Vortex Generators in Boundary Layer Ingesting Diffusers with a Centerline Offset*. AIAA 1999-2110. 35th AIAA Joint Propulsion Conference and Exhibit. June 20-24, 1999. Los Angeles, CA.
- ¹⁵ Fleming, J.. *Wind Tunnel Design Report*. Techsburg, Inc. Interim Report, NASA Contract NAS1-03066, April 2005.
- ¹⁶ Gracey, W.. *Wind Tunnel Investigation of a Number of Total-Pressure Tubes at High Angles of Attack Subsonic, Transonic, and Supersonic Speeds*. Report 1303 – National Advisory Committee for Aeronautics, Langley Field, Virginia., January 17, 1956.
- ¹⁷ Figliola, R., Beasley, D.. *Theory and Design for Mechanical Measurements, 3rd Edition*. John Wiley and Sons, Inc. New York, 1991.

¹⁸ Goyder, H.G.D., "Foolproof Methods for Frequency Response Measurements," Proc. 2nd Int. Conf. on Recent Advances in Structural Dynamics, **II**, eds. M. Petyt and H.F. Wolfe, Inst. of Sound and Vibration Research University of Southampton, England, 437-446 (1984).

¹⁹ Simpson, R. L., Ghodbane, M., and McGrath, B.E., "Surface pressure fluctuations in a separating turbulent boundary layer," *J. Fluid Mech.*, vol. 177, pp. 167-186, 1987.

²⁰ Anderson, J. M., "Non-Intrusive Sensing and Feedback Control of Serpentine Inlet Flow Distortion," Ph.D. Dissertation, Mechanical Engr., Virginia Polytechnic Institute and State University, 2003.

Appendix A: Distortion Descriptors

There are several distortion descriptors that are common throughout the aircraft industry. Many of these descriptors have been in use for several decades and were created long before computational methods were commonplace. Thus, these descriptors were created based on experimental methods. Both of the methods described herein are based upon a standard six arm 30 probe distortion rake, which uses pressure transducers located on arms at various radii corresponding to area-averaged flow sections.

DC(60) and SC(60)

The DC(60) distortion parameters use total pressure data from the rake to calculate a maximum distortion value for a given flow condition. Each rake arm represents a 60° sector of the flow at the AIP. Additional distortion descriptors exist that use both smaller and large angles at which to place rake arms, such as the DC(45), DC(90), and DC(120) parameters. However, in experimental work, each rake arm also represents a blockage in the flow area. Thus, the angle selected is often based upon acceptable resolution at a minimum of flow blockage. In most cases, the DC(60) and DC(45) parameters are adopted.

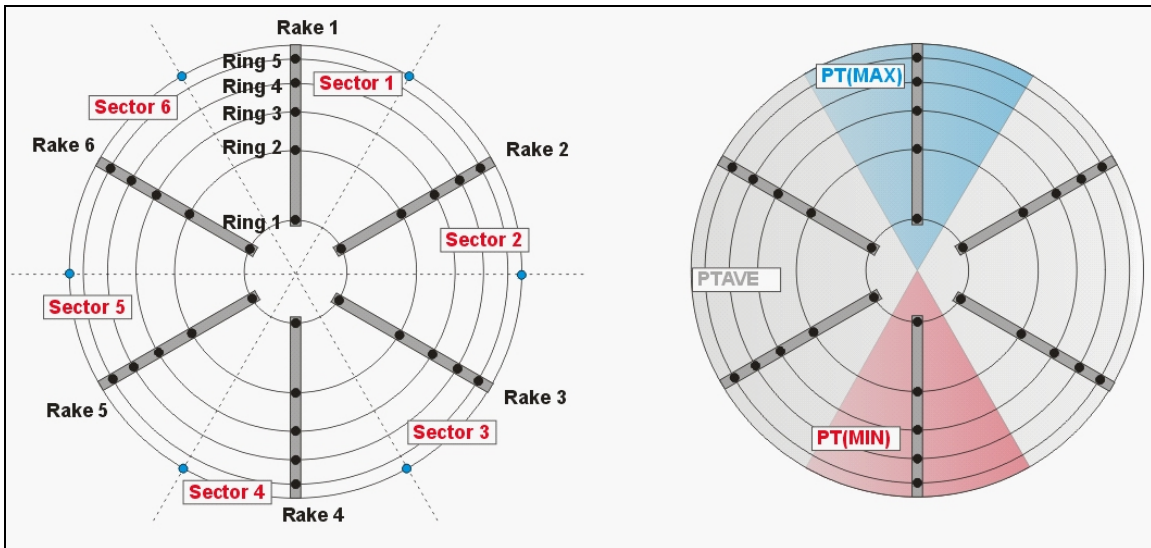


Figure A.0-1: DC(60) Distortion Rake

For total pressure distortions, the rake is used to obtain the average total pressure for each sector, and is then compared to the maximum and minimum sector values. This yields a maximum total pressure distortion that a blade of the compressor would be

subjected to during a complete revolution. However, some variation exists in these descriptors; some groups prefer to non-dimensionalize the pressure difference by the average total pressure at the AIP, and some prefer to non-dimensionalize by the average dynamic pressure. There are advantages and disadvantages to each formulation. By using the AIP average total pressure, the descriptor is less sensitive to changes in flow rate and duct area. However, by using the average AIP dynamic pressure, the distortion values examine an average deficit of flow energy. In this study, both values are calculated.

$$DC(60)_{PT} = \frac{PT_{MAX} - PT_{MIN}}{PT_{AVE}} \quad (A-1)$$

$$DC(60)_q = \frac{PT_{AVE} - PT_{MIN}}{q_{AVE}} \quad (A-2)$$

Where PT_{AVE} is the average total pressure at the AIP, PT_{MAX} is the maximum average total pressure over a 60° sector, PT_{MIN} is the minimum average total pressure over a 60° -degree sector, and q_{AVE} is the average flow dynamic pressure at the AIP.

The swirl counterpart for the $DC(60)$ distortion coefficient is the $SC(60)$ swirl coefficient. The relationship between total pressure and flow swirl was quantified by Guo who formulated a descriptor in order to correlate the two distortion values. This factor evaluates the severity of the cross-flow velocities at the AIP. These velocities are equivalent to the secondary flows developed within the duct. The $SC(60)$ swirl coefficient is calculated according to:

$$SC(60) = \frac{V_{CF_MAX} - V_{CF_MIN}}{V_{AVE}} \quad (A-3)$$

where V_{CF_MAX} represents the maximum average secondary flow over a 60° sector, V_{CF_MIN} represents the minimum average secondary flow over a 60° sector, and V_{AVE} represents the average flow velocity at the AIP. This parameter can be used to highlight the possible severity of local non-axial flow vectors, and thereby highlight the possibility of compressor blade stall.

SAE-ARP1420

The ARP1420 distortion descriptor was originally designed to minimize the risk of inlet and engine compatibility problems arising from total pressure distortion. The standard examines both circumferential and radial distortion and is used to characterize the type of flow distortion, including distortion extent and intensity.

Circumferential Distortion Extent

The circumferential distortion extent (θ_i^-) is defined by the sector of flow (in degrees) that has a total pressure less than the ring average total pressure. Extent is calculated by:

$$Extent = \theta_i^- = \theta_{2i} - \theta_{1i} \quad (A-4)$$

as referenced in Figure A.0-2. Where $(PAV)_i$ is the ring averaged total pressure, $(PAVLOW)_i$ is the ring average total pressure of the low-pressure extent, and $\theta_{2i,1i}$ are the circumferential location in degrees.

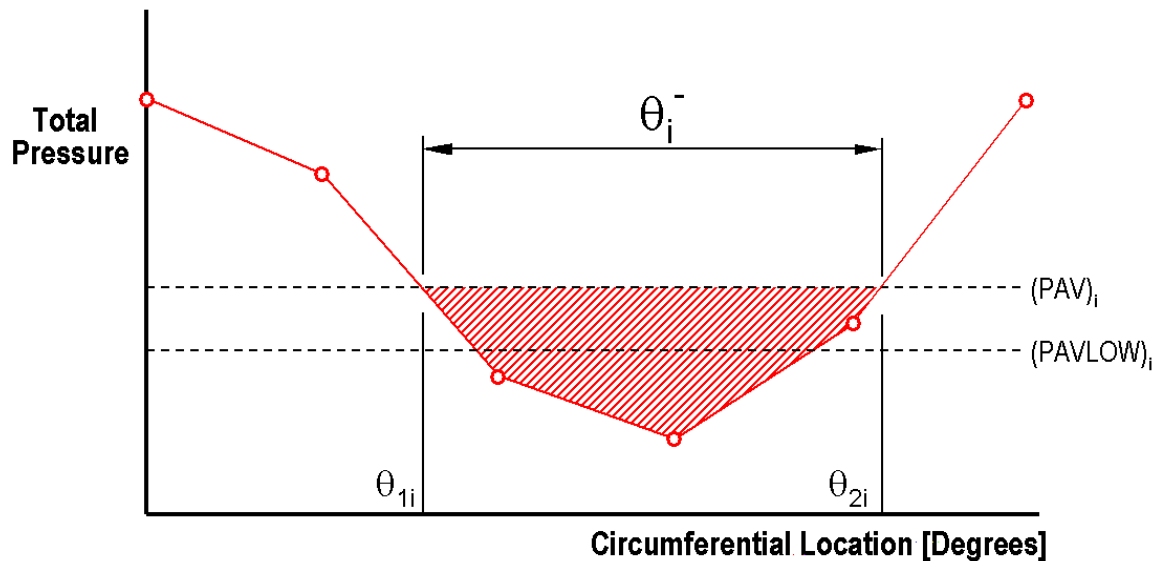


Figure A.0-2: Ring Circumferential Distortion Extent (One-per-Revolution)

Circumferential Distortion Intensity

The circumferential distortion intensity represents the average total pressure difference of each individual ring non-dimensionalized by the ring averaged total pressure. It also gives an indication of the radial location at which the distortion is a maximum.

$$Intensity = \left(\frac{\Delta PC}{P} \right)_{Ring\ i} = \frac{PAV_{Ring\ i} - PAVLOW_{Ring\ i}}{PAV_{Ring\ i}} \quad (A-5)$$

Circumferential Distortion Extent: Multiple per Revolution

In many cases, flow distortion is not confined to a singular disturbance within the duct. A typical military configuration utilizes twin serpentine inlets mounted on either side of the fuselage. In such situations it is not uncommon for multiple low energy regions to form.

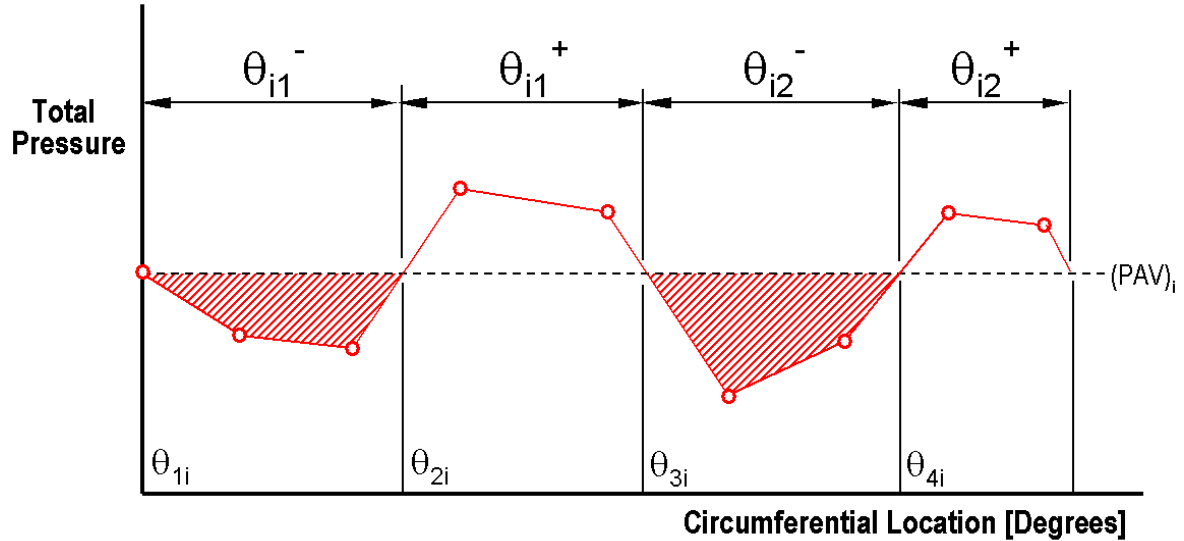


Figure A.0-3: Ring Circumferential Distortion Extent (Multiple-per-Revolution)

The analytical expressions are thus altered to account for the k^{th} low-pressure region for Q low-pressure regions per ring, yielding:

$$Extent = \theta_i^- = \sum_{k=1}^Q \theta_{ik}^- \quad (\text{A-6})$$

$$Intensity = \left(\frac{\Delta PC}{P} \right)_{Ring\ i} = \frac{\sum_{k=1}^Q \left[\left(\frac{\Delta PC}{P} \right)_{ik} \theta_{ik}^- \right]}{\sum_{k=1}^Q \theta_{ik}^-} \quad (\text{A-7})$$

It should be noted however, that if the low-pressure regions are not separated by more than 25 degrees, they should be treated as a one-per-revolution distortion.

Radial Distortion Intensity

The radial distortion intensity represents the total pressure distortion in a direction aligned with the spanwise length of a compressor blade. A typical distribution is shown in Figure A.0-4, and is calculated from:

$$Intensity = \left(\frac{\Delta PR}{P} \right)_{Ring\ i} = \frac{PFAV - PAV_{Ring\ i}}{PFAV} \quad (\text{A-8})$$

Where $PAV_{Ring\ i}$ is the ring-averaged total pressure, and PFAV is the area-weighted face-average total pressure.

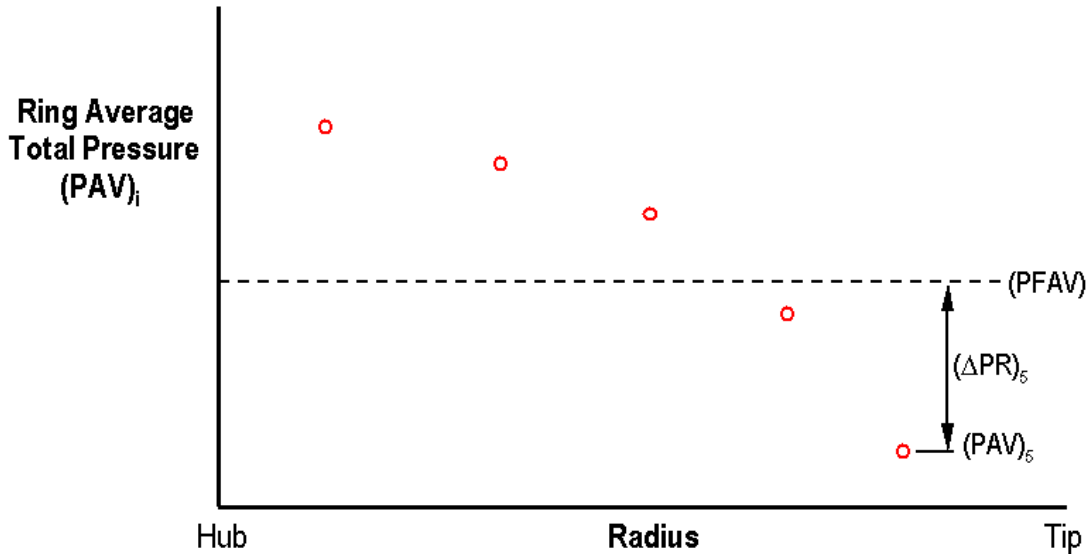


Figure A.0-4: Radial Distortion

Average Distortion Intensity: DPCP

Average distortion intensity ($DPCP_{avg}$) can be defined by averaging the ARP1420 circumferential distortion results according to:

$$DPCP_{avg} = Intensity_{avg} = \sum_{i=1}^5 \frac{PAV_{Ring\ i} - PAV_{LOW\ Ring\ i}}{PAV_{Ring\ i}} \quad (A-9)$$

This gives an overall area-weighted value for the AIP circumferential distortion intensity that can then be compared to other engine or duct configurations.

Inlet Pressure Recovery

The inlet diffuser represents an integral part of the engine system design. Because the engine needs to accept relatively low velocity, high-pressure flow, the efficiency of the diffuser has a profound impact on overall propulsive efficiency. Inlet pressure recovery is generally considered to represent the efficiency of the diffuser in providing flow to the AIP by accounting for losses incurred from the freestream condition.¹

$$PR = \frac{AIP\ Total\ pressure}{Freestream\ Total\ pressure} \quad (A-10)$$

The implication of increasingly complex serpentine diffusers has had an impact on diffuser pressure recovery. Since stealth observability has come to the forefront of the

design process, there has been a corresponding decrease in the importance of diffuser pressure recovery. Although it is important to maintain high-pressure recovery, the necessity of hiding the aircraft from detection is generally considered more important as it has a substantial impact on aircraft survivability as well as operational life-cycle cost. Although the effect of flow control on diffuser pressure recovery will be examined, it does not represent the focus of this study.

Appendix B: Geometry

The diffuser geometry used throughout this study was defined through joint NASA/Boeing investigations. A standard model was chosen by NASA and Boeing from several generic geometries in order to represent a typical boundary layer ingesting serpentine inlet that exhibited the characteristic flow feature, namely, a high flow distortion. This model would then be used as a generic representation in all subsequent flow analyses. The configuration chosen was inlet configuration ‘A’, represented in Figure B.0-1.

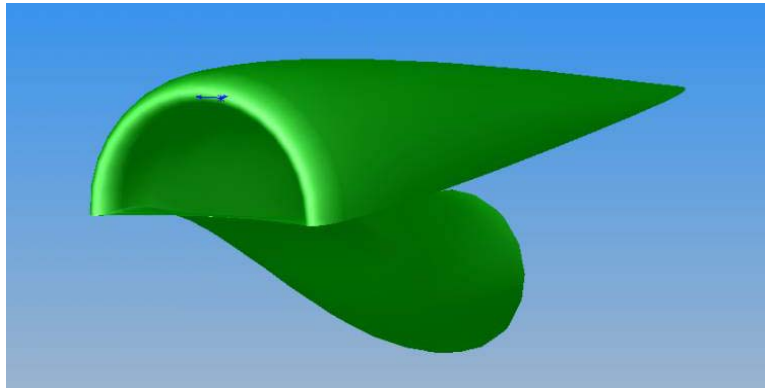
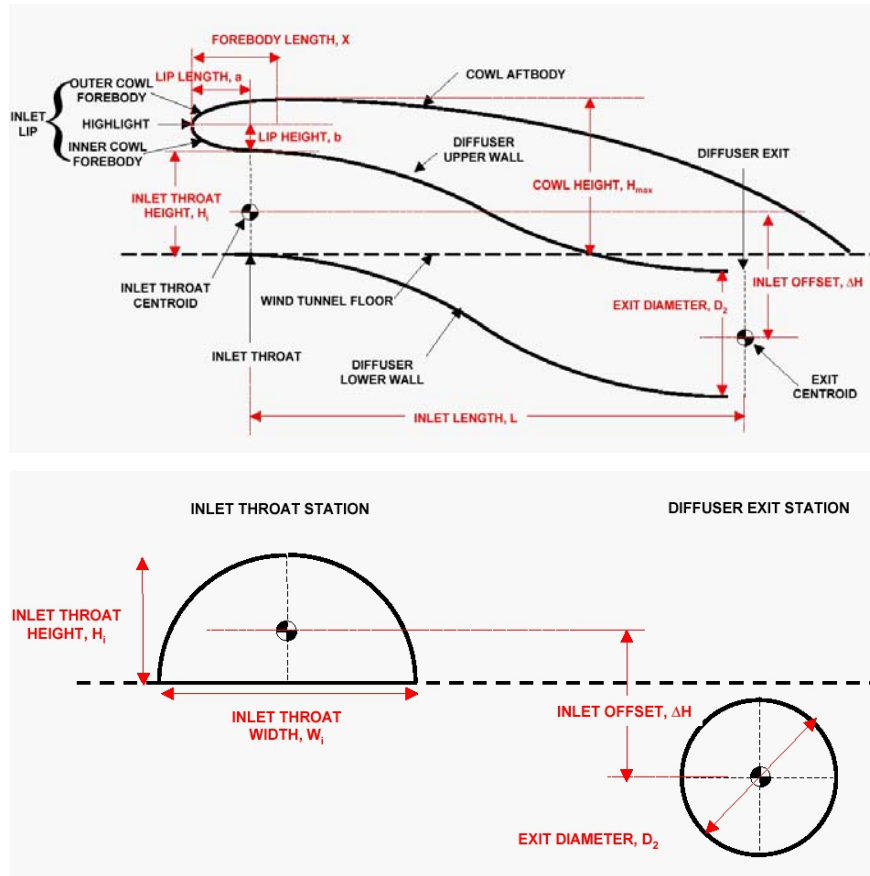


Figure B.0-1: NASA/Boeing BLI Inlet Configuration 'A'

The geometry of the chosen configuration, dimensions, and the critical design parameters of the inlet are outlined in Figure B.0-2 and Figure B.0-3.

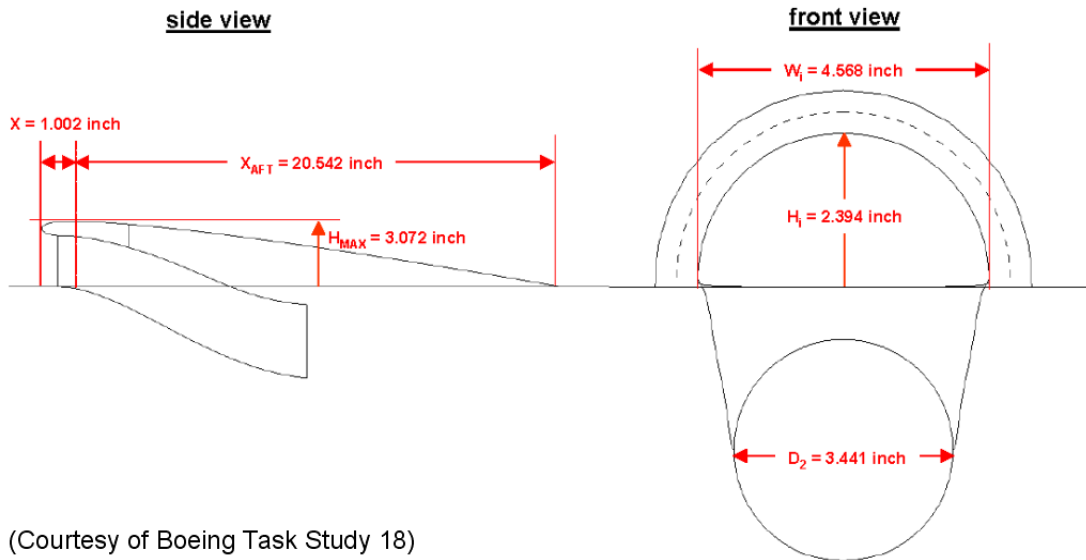


NASA Inlet “A” geometry:

- Diffuser Exit to Inlet Area $A_2/A_1 = 1.069$
- Diffuser Length to Exit Diameter Ratio $L/D_2 = 5.97$
- Rounded nacelle lip (length/thickness = 2)

Figure B.0-2: NASA Configuration 'A' Diffuser Geometry

As can be seen above, the diffuser has an aggressive inlet offset height, which will cause strong transverse pressure gradients across the duct’s cross section, and thus strong secondary flows to form. The severity of the diffuser curvature will also lead to a boundary layer that could be prone to separation in regions of strong adverse pressure gradients. The diffuser also has a low exit to inlet area ratio due to the decreased necessity for diffusion as a result of a large amount of ingested low-energy fluid.



(Courtesy of Boeing Task Study 18)

Figure B.0-3: NASA/Boeing Configuration 'A' Dimensions

The above dimensions represent the size and configuration of the nacelle used in a NASA cryogenic wind tunnel test at the Basic Aerodynamics Research Facility (BART) at NASA Langley.¹¹ All subsequent representations of the diffuser are in accordance with the above geometry.

Appendix C: Grid Resolution Study

A grid resolution study was conducted on the baseline CFD solution by examining the solution dependency on the mesh size. Three different mesh densities: fine, medium, and coarse were generated. Each successive coarsening resulted in a reduction of the number of cells by $\frac{1}{2}$ in each direction. Therefore, the number of cells for the fine, medium, and coarse meshes span roughly two orders of magnitude (1, 1/8, and 1/64). The distortion parameters were monitored for all three cases and compared for a measure of the grid independence.

Agreement was seen for most flow data between the medium and fine grids, indicating that some measure of grid independence had been achieved. The values for the calculated quantities (DC(60) values, etc.) agreed very closely between the medium and fine mesh cases, as did the total pressure contour results. Sample results for the average total pressure along the inlet for the different mesh densities are given in Figure C.0-1, again displaying very good agreement between the medium and fine grid cases.

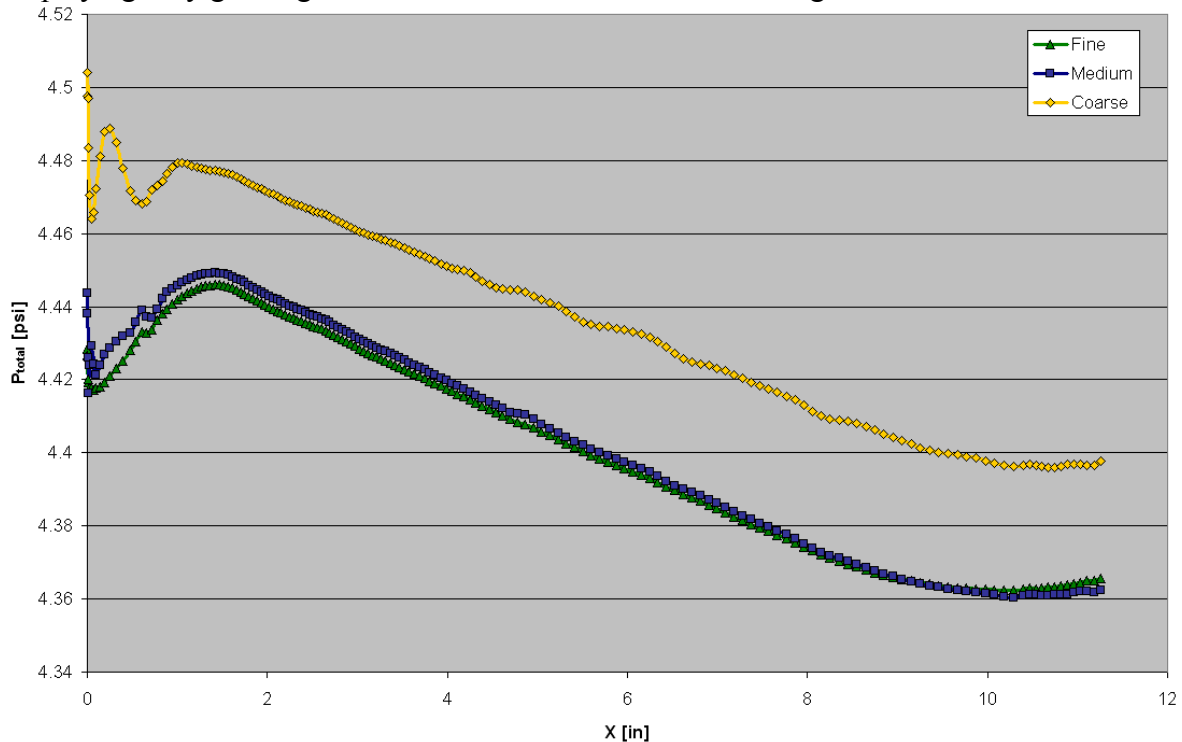


Figure C.0-1: Grid Resolution Study - Baseline Total Pressure Distribution

Figure C.0-2 and Figure C.0-3 show convergence results for the DC(60) and DPCPavg parameters respectively. These parameters are correlated according to the inverse of the number of cells. Thus, it was possible to project what the distortion result would be for an infinite number of cells. As seen in these figures, an increase in the number of cells is not likely to create a large difference in solution accuracy. The leveling

out of the distortion numbers also suggests that the possible increase in accuracy will be very small compared to the large increase in required computational time associated with an increase in mesh resolution.

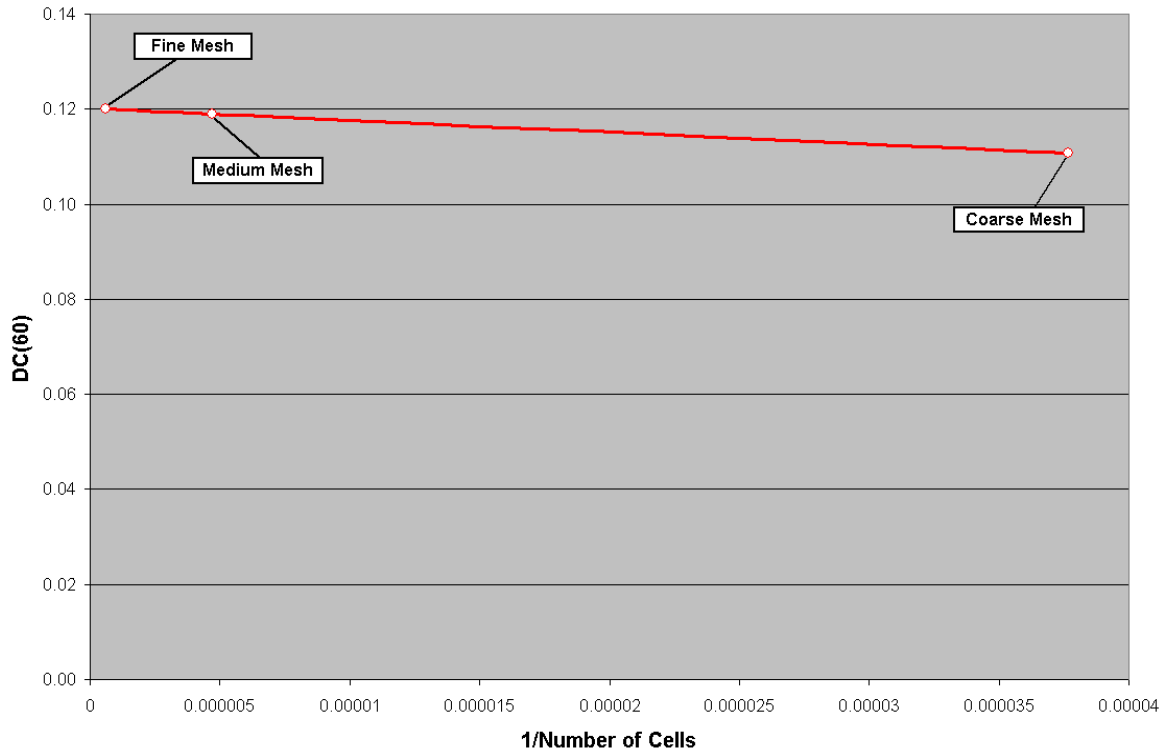


Figure C.0-2: Grid Resolution Study - Baseline DC(60) Convergence

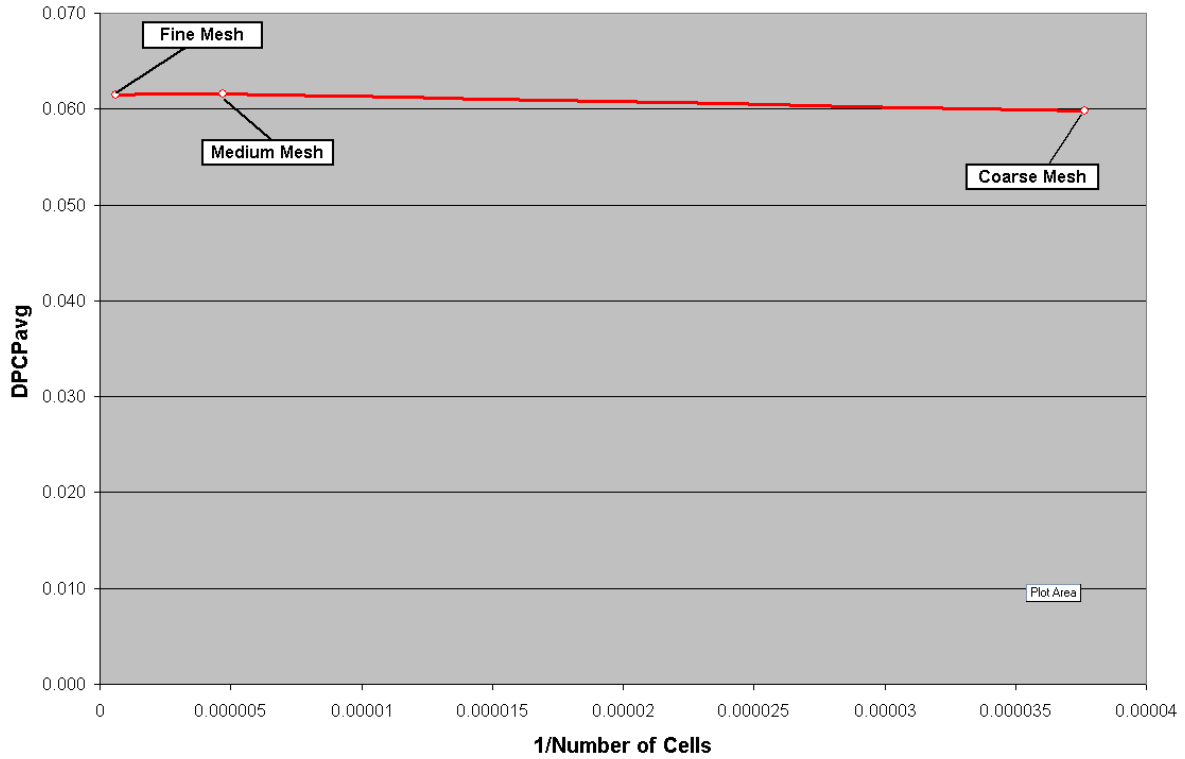


Figure C.0-3: Grid Resolution Study - Baseline DPCavg Convergence

Figure C.0-4 and Figure C.0-5 examine the grid resolution study results based upon the ARP1420 circumferential and radial intensity distortion results. Results of these studies indicate a significant difference between the fine and coarse results. The medium and fine densities show reasonable agreement and predict the same trends. Results from the DPCavg, which are based upon the circumferential distortion intensities shows good converge as noted in Figure C.0-3. Results therefore suggest that little benefit will be gained by adopting a finer mesh density.

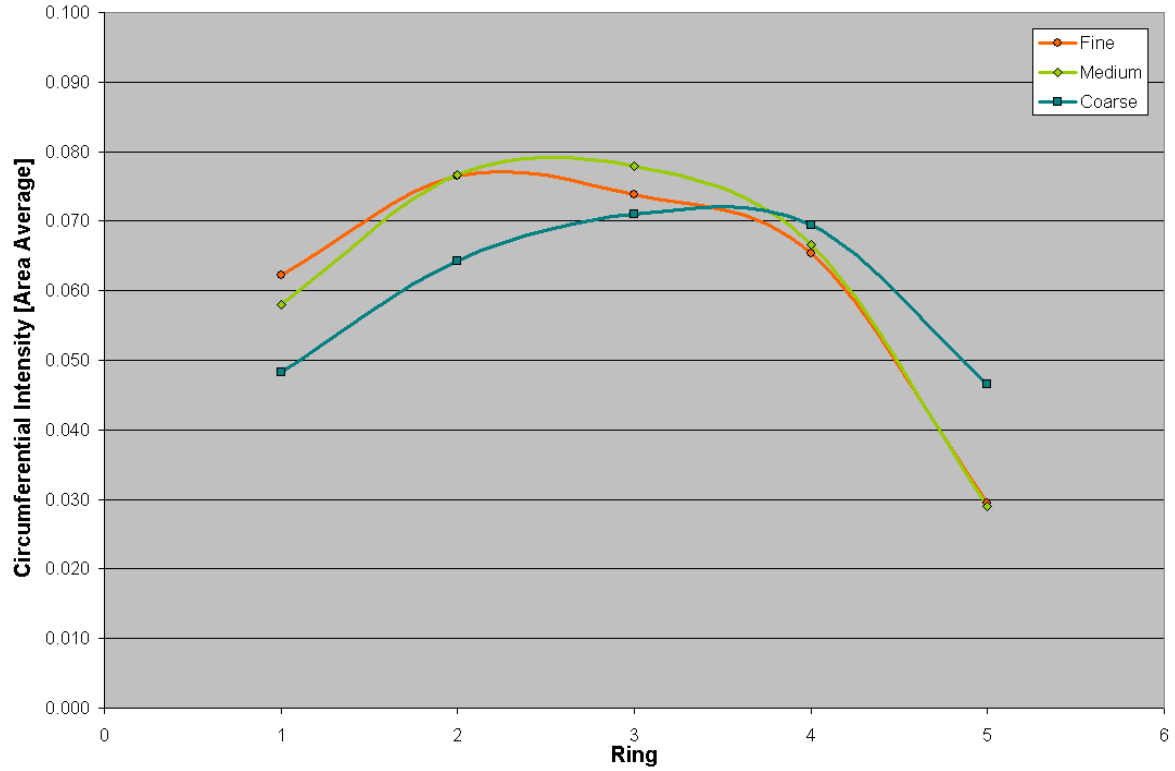


Figure C.0-4: Grid Resolution Study - Baseline Circumferential Distortion Intensity

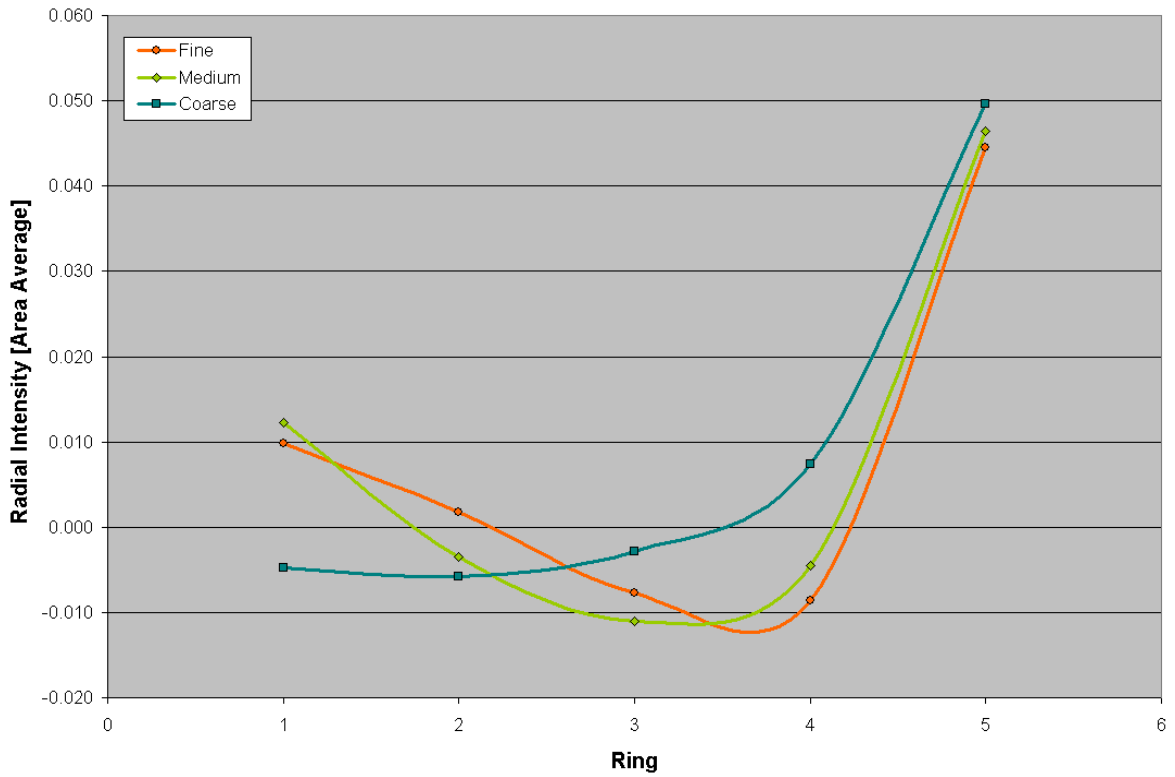


Figure C.0-5: Grid Resolution Study - Baseline Radial Distortion Intensity

Appendix D: Impact of Diffuser Mass Flow on AIP Distortion

In order to facilitate better comparison with results provided by NASA, computational models were run for various engine mass flows. Since the dimensions of the diffuser may vary from test to test, a non-dimensional mass flow value $C\dot{m}$ was used to compare the solutions. This value can be roughly correlated to diffuser capture area, and represents the percentage of freestream air that enters the inlet. The value of the non-dimensional mass flow is calculated by dividing the AIP mass flow by the freestream mass flow through an area equal to the AIP total area:

$$C\dot{m} = \frac{\dot{m}}{\rho_{\infty} A_{AIP} V_{\infty}} \quad (D-1)$$

The evaluated CFD cases examined six $C\dot{m}$ values ranging from 0.524 to 0.796. The results for these tests are shown below:

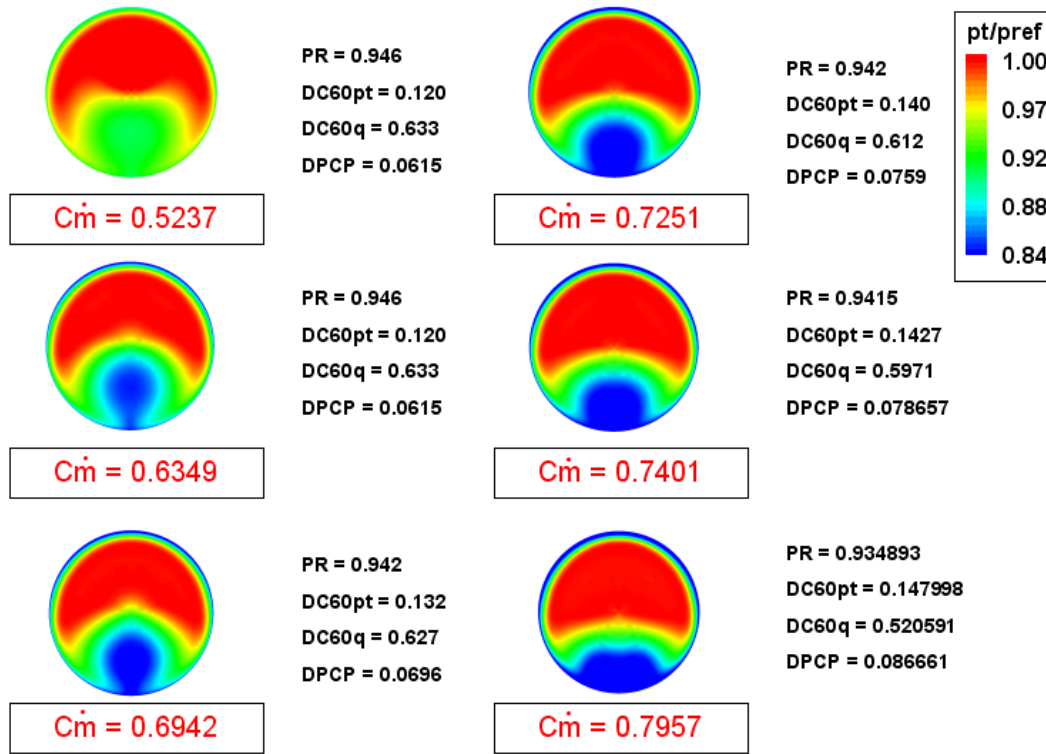


Figure D.0-1: Effect of Variation in AIP Mass Flow

It can be seen that as the mass flow increases (and hence inlet Mach number), the severity of the total pressure distortion also increases. This is demonstrated by the continual increase in DC(60) with increasing mass flow. The total pressure contours show a continually growing region of low momentum fluid buildup along the bottom of the diffuser. As the AIP mass flow increases, the severity of the total pressure distortion also increases, leading to a greater differential between the high and low momentum fluid

regions. In addition, as the engine mass flow increases, the total pressure recovery of the engine decreases.

Results from NASA compare reasonably well with the Techsburg results. Results deviate slightly as expected due to the use of different turbulence models in the CFD analysis. Techsburg solutions used the 1-equation Spalart-Allmaras (S-A) turbulence model while NASA computations used the 2-equation Menter Shear Stress Transport (SST) model. In addition, the NASA mesh used an overset grid topology and over 8 million nodes to model the flow field. Techsburg does not currently have the computational resources to replicate this approach, and thus used a traditional structured grid with no more than 2.6 million nodes. The overall goal of the study was to predict the flow's behavioral trends, and the effect of varying mass flow in the unaltered diffuser. The trends obtained in this study are believed to be accurate in predicting the overall flow behavior. The total pressure contours match well for similar $C\dot{m}$ values as highlighted in Figure D.0-2.

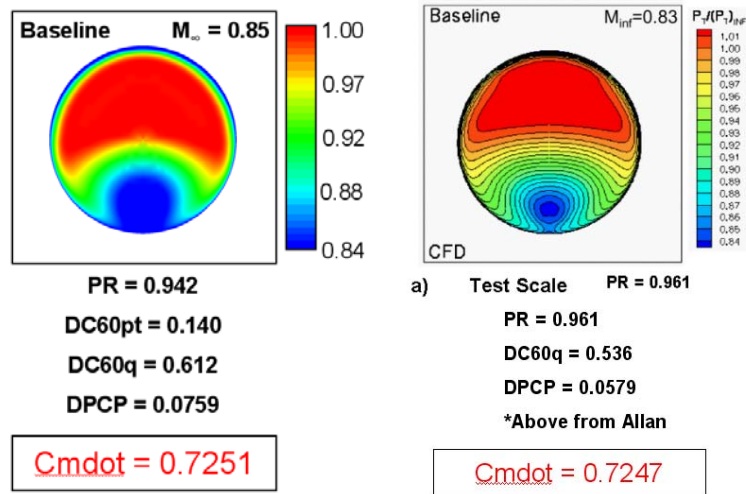


Figure D.0-2: Baseline Comparative Mass Flow Solutions

Appendix E: Flow Control Axial Location

In order to better understand the driving parameters of flow control effectiveness, the flow control array was located in a variety of axial locations. This was accomplished by varying the streamwise (axial) location of the circumferential jet configuration. Jet arrays were located at axial stations of $x/L = 0.010, 0.126, 0.170, 0.177, 0.292$ as shown in Figure E.0-1.

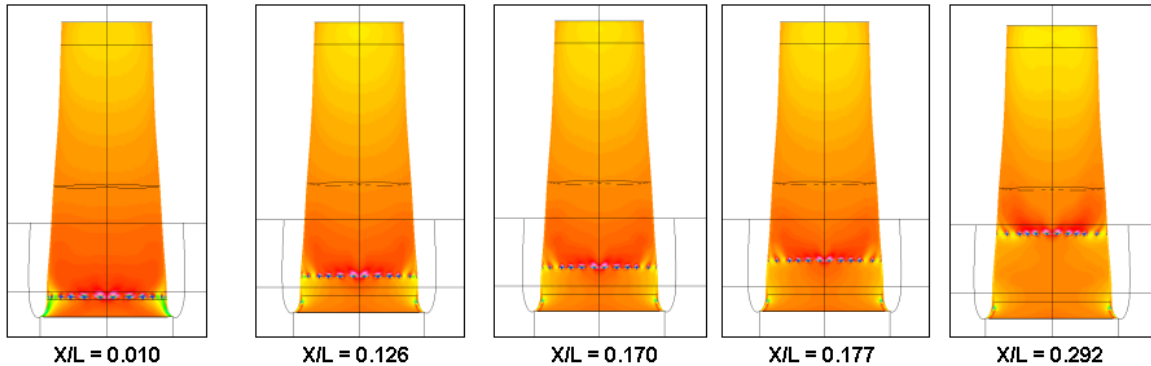


Figure E.0-1: Flow Control Axial Location

At upstream locations, the boundary layer is thinner and the secondary flows are not yet established within the diffuser. As the flow progresses down the diffuser, the centrifugal forces establish a pressure gradient across the flow due to differences in the momentum of the boundary layer and flow of near freestream velocity. These gradients set up the secondary flow patterns commonly associated with offset diffusers. In the case of boundary layer ingesting inlets, the strength of the counter-rotating vortices is further enhanced by the addition of a junction vortex formed by the interaction of the boundary layer with the engine nacelle. Because these vortices have the same sense of rotation as the established secondary flows, the severity of the flow distortion is increased.

Several considerations should be weighed when locating flow control effectors. Logic would dictate that locating flow control at an upstream location would allow the effectors to combat secondary flows before they are established with a minimum of effort. However, studies by Reichert et al. have shown that locating effectors at upstream locations incurs a slight performance penalty, but this penalty is comparatively smaller than the penalty associated with locating effectors too close to flow disturbances. If the effectors are too close to flow disturbances (such as flow separation), they become almost completely ineffective. It should be noted that the specific goal of Reichert's study was to prevent flow separation in serpentine diffusers, and although the methodology differs from that adopted in this study, the reasoning may still be applicable. In consideration of the ejector pump model, it should be noted that maximum performance of the effectors will be gained if the suction is located in a region of comparatively high pressure and the jets in a region of low pressure. This pressure differential is essential in establishing the maximum benefit of the flow effectors. By placing the suction source at the stagnation point of the nacelle highlight, the maximum benefit may be gained. Also, considerable benefit is gained by locating the jets as near to the suction source as possible, as excessive distances result in high-pressure drop associated with pipe friction losses.

Through judicious placement of the flow control effectors, the overall effectiveness of the jets was investigated. Results shown in Figure E.0-2 suggest that

there is an optimum axial location near $x/L = 0.17$. It is likely the locations farther upstream of this point are not effective due to their proximity to the inlet throat, while downstream locations appear to be less effective due to the increasing strength of secondary flow patterns. These results confirm the findings of Reichert et al., and reinforce the design strategy of managing secondary flows early in the diffuser for maximum effectiveness.

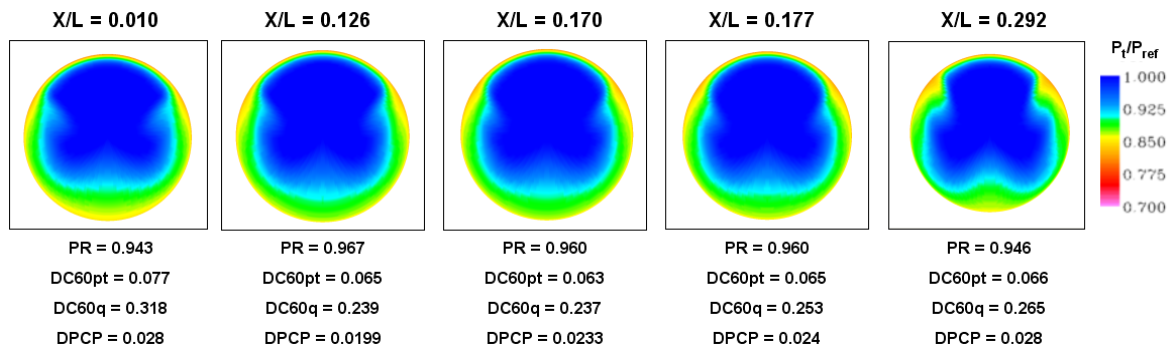


Figure E.0-2: Effect of Axial Jet Location - Total Pressure Contours

Appendix F: Flow Control Spanwise Spacing

Results from the original flow control study showed a performance variation between the circumferential and Pyramid 4 case, which had very similar jet configurations. The major variation between these cases was the spanwise jet spacing. The variation in the resulting distortion highlighted the importance of jet interaction, and implied that the circumferential jet spacing had a profound effect on overall configuration performance. Thus, variations in spanwise jet spacing and its effect on AIP distortion was further investigated.

Configurations examined ranged from a very tightly spaced configuration to a well-dispersed configuration. The configuration with the smallest spanwise spacing was located on the diffuser “floor” starting near the duct centerline. (Narrow) The most dispersed configuration had jets spanning a large portion of the diffuser circumference (Wide). In all cases, the total jet array mass was held constant, as was the jet supply pressure; this allowed for a reasonable comparison between obtained results. The examined configurations are shown in Figure F.0-1 with the jet locations indicated.

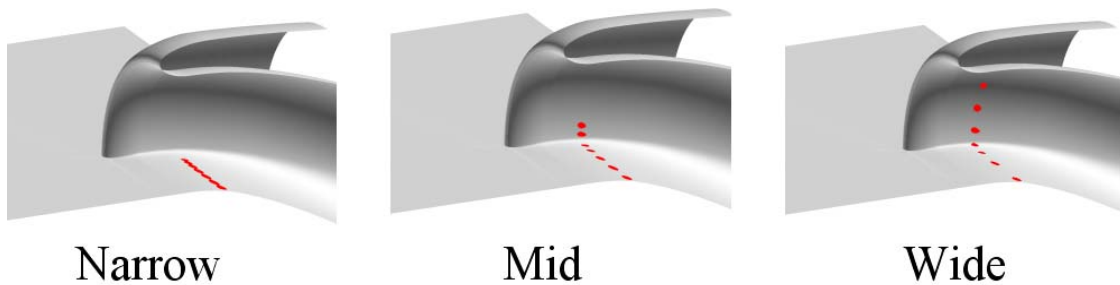


Figure F.0-1: Spanwise Jet Configurations

As seen in Figure F.0-2, altering the spanwise spacing has a strong effect on the management of total pressure distortion at the AIP. For both of the examined DC(60) parameters, the distortion decreased with each subsequent reduction in spanwise jet separation. Thus, the “Narrow” configuration produced the best results in terms of a reduction in the maximum “worst-case” sector distortion.

The DPCPavg parameter suggests that the average distortion intensity is relatively constant until the jets are no longer effect in counteracting the secondary flows. The difference between values from the Mid and Wide configurations is much greater than differences between the Narrow and Mid configurations. However, the general trend is the same as predicted by the DC(60) parameters.

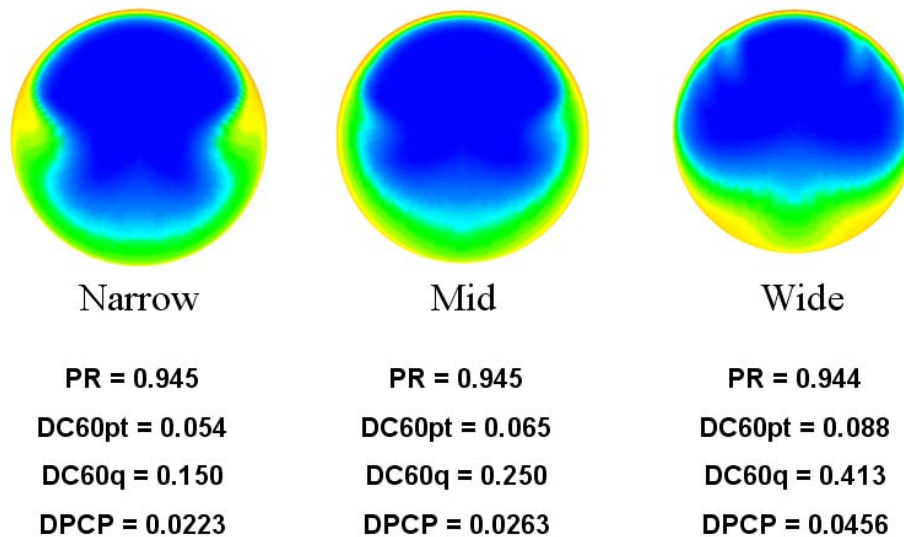


Figure F.0-2: Effect of Jet Circumferential Spacing

Figure F.0-3 shows the streamwise vorticity contours at the AIP for the investigated spanwise spacing flows. Here it can be seen that for the most closely spaced jet configurations, the resultant vorticity at the AIP is much more concentrated than for the most dispersed jet cases. Visual contours suggest that the jets in the Narrow configuration produced a single vortex of higher strength, while more spaced configurations produced several vortices of lower magnitude. (Vortices resulting from the upper wall jets can be seen in the Wide configuration.) Trends suggested by visual contours are confirmed by the SC(60) swirl parameter, which suggests an increase in AIP swirl proportional to a decrease in jet spacing. The induced swirl can be highly detrimental to engine performance as it can lead to local stalling of compressor blades and eventually to engine surge. Thus, selection of an appropriate flow control solution for each specific case should be based upon engine performance requirements; engines that can tolerate a larger swirl velocity can obtain increased benefit from a further decrease in total pressure distortion. In reality, the increased vorticity is likely to result in the acceptance of a slight penalty in total pressure distortion in order to obtain acceptable levels of swirl. Thus, for an individual engine, an optimal configuration can be determined for a given jet total pressure.

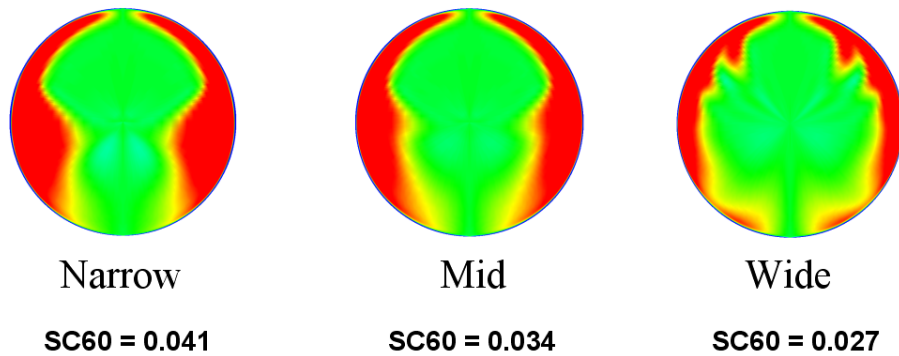


Figure F.0-3: AIP Streamwise Vorticity - Effect of Spanwise Jet Spacing

Appendix G: Complete CFD Results

The section details the results for all investigated flow control cases, and presents AIP total pressure contours and distortion parameters for obtained solutions.

Baseline ARP1420 Distortion Parameter Results

In examining the AIP distortion descriptors, it was seen that the regions with the highest circumferential distortion intensities were rings 2 and 3, located near the hub of the engine (Figure G.0-1). These center circumferential rings encapsulate both the center of the vortex formed by secondary flows and a section of the undisrupted high momentum core flow. The maximum intensity is due to the large difference in total pressure between the upper duct “core” flow and the low momentum region at the bottom half of the duct.

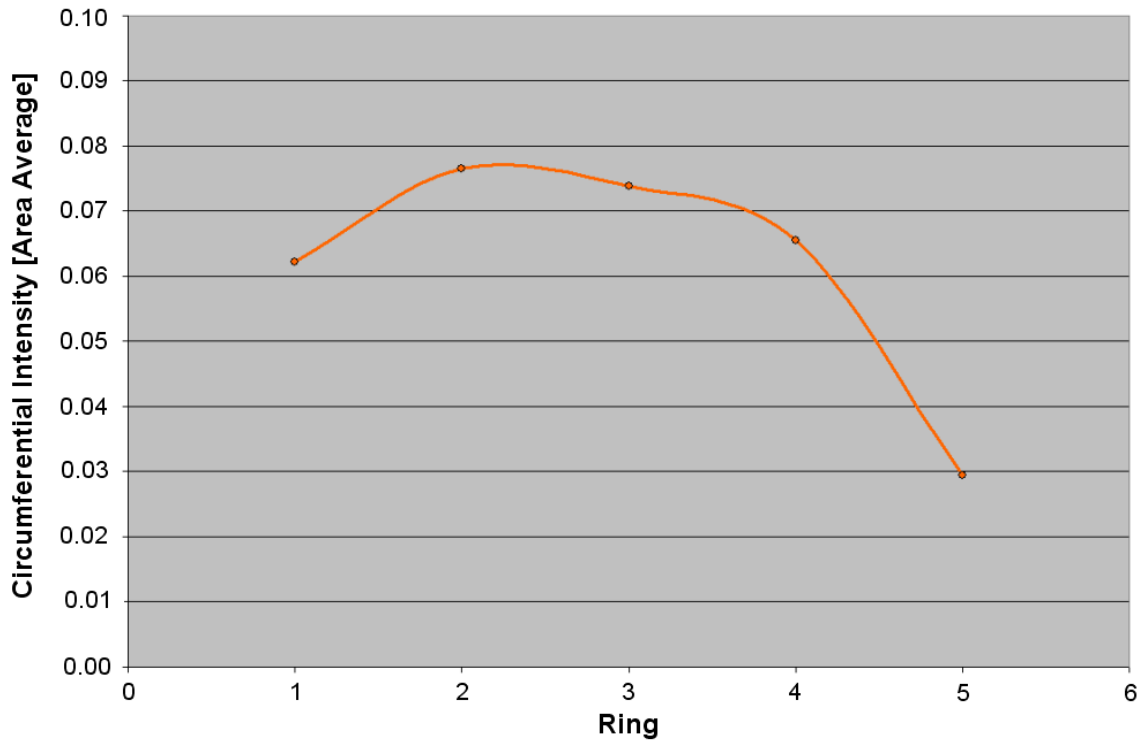


Figure G.0-1: Circumferential Distortion Intensity – Baseline

The largest radial distortion results were for ring 5, at the outer edge of the AIP (Figure G.0-2). This is expected due to the inlet wall boundary layer growth at the AIP.

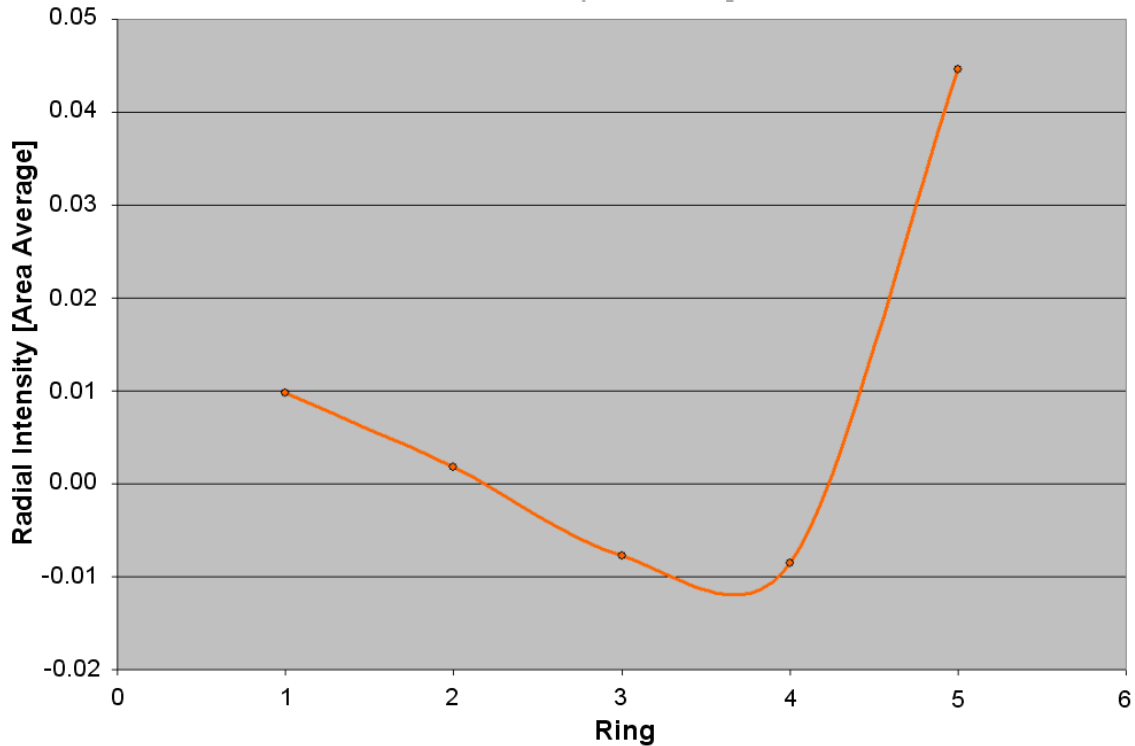


Figure G.0-2: Radial Distortion Intensity – Baseline

Flow Control Case Descriptions

Baseline: Baseline Solution - no flow control

Blowing Only ('Traditional' Configuration, Jet mass flow ~1% AIP total):

Cir (1%): Circumferential Blowing Scheme

Pyr1 (1%): Pyramid 1 Blowing Scheme

Blowing Only (Jet mass flow ~2% AIP total):

Circ. Blow: Circumferential jet arrangement

Axial 1: Jets arranged in an axial (streamwise) line near outer edge of diffuser 'floor'

Axial 2: Jets arranged in an axial line (streamwise) near center of diffuser 'floor'

Pyramid 1: Jets arranged in a row at an angle to the oncoming flow (most acute angle)

Pyramid 2: Jets arranged in a row at an angle to the oncoming flow (intermediate angle)

Pyramid 3: Jets arranged in a row at an angle to the oncoming flow (intermediate angle)

Pyramid 4: Jets arranged in a row at an angle to the oncoming flow (almost perpendicular)

Suction Only (Suction mass flow ~1% AIP total):

Suction: 'Lip' suction - suction located at stagnation point on inlet lip and diffuser 'floor'

Suction2: 'floor' suction - located along diffuser floor in line with diffuser highlight

Ejector Pump Models (Jet mass flow ~2%, suction mass flow ~1% AIP total):

FSCIR: Floor suction combined with circumferential blowing scheme

FSA2: Floor suction combined with axial 2 blowing scheme

FSP1: Floor suction combined with Pyramid 1 blowing scheme

FSRP: Floor Suction combined with the 'reversed' Pyramid 1

SRP: Lip Suction combined with a 'reversed' Pyramid 1 arrangement

SCIR: Lip Suction combined with circumferential blowing scheme
SP1: Lip Suction combined with Pyramid 1 blowing scheme
SA2: Lip Suction combined with Axial 2 blowing scheme

Flow Control ARP1420 Distortion Results

As can be seen in Figure G.0-3, the baseline case (no flow control) has the highest circumferential distortion for each ring of the distortion rake as compared to all examined cases. The conventional blowing schemes show a clear reduction in circumferential distortion, with the Pyramid1 case showing the largest reduction. However, it should be noted that although the values for the Pyramid 1 case are lower than the circumferential case, the relative change in distortion between circumferential locations is more localized along the blade radius. The circumferential case, although displaying a higher distortion, is more even in its distribution for different rings, which is more likely to produce a more uniform distortion distribution.

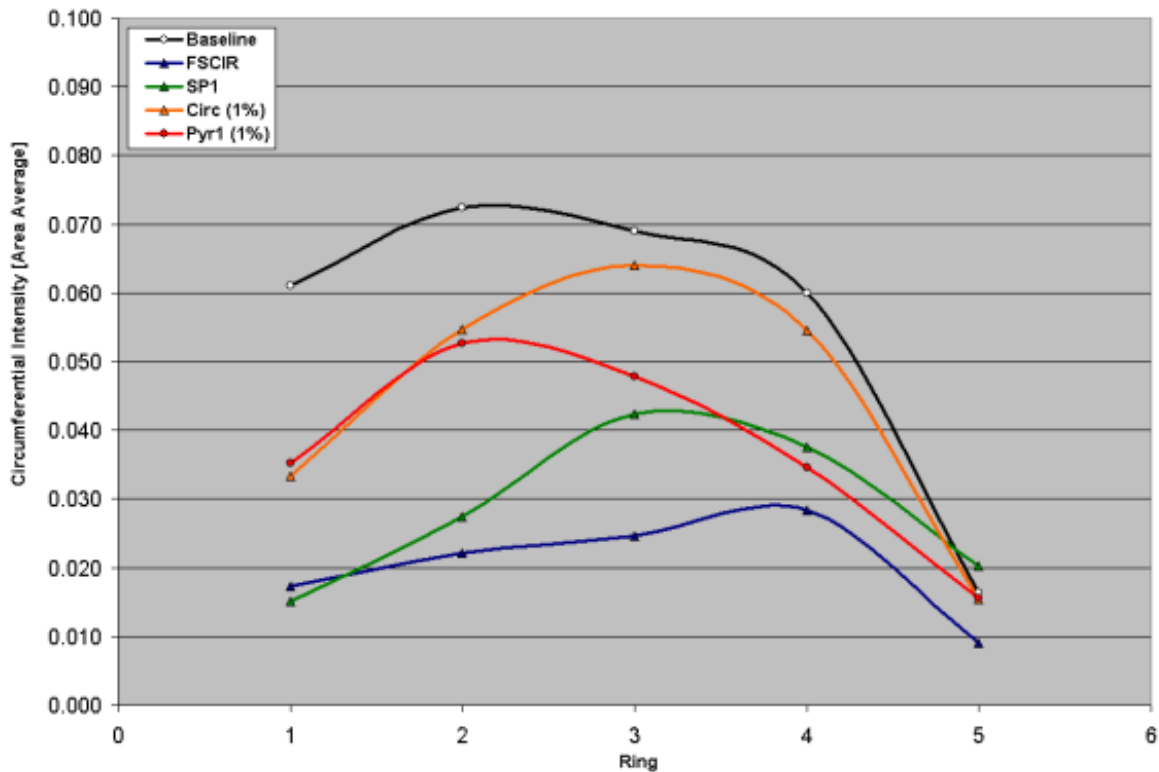


Figure G.0-3: ARP1420 Circumferential Distortion Intensity (Selected Cases)

The radial distortion plot shows a baseline with a very large distortion that changes quickly in the radial direction. All other cases in Figure G.0-4 show a much more gradual distortion profile in the radial direction. This gradual change is a good indicator that the flow distortion has been distributed, and is likely to produce more steady engine operation. However, note that the conventional blowing cases (Circ (1%) and Pyri (1%))

are not as even in their distribution of the distortion; the ejector based models (FSCIR and SP1) show a near-linear distribution in the radial direction.

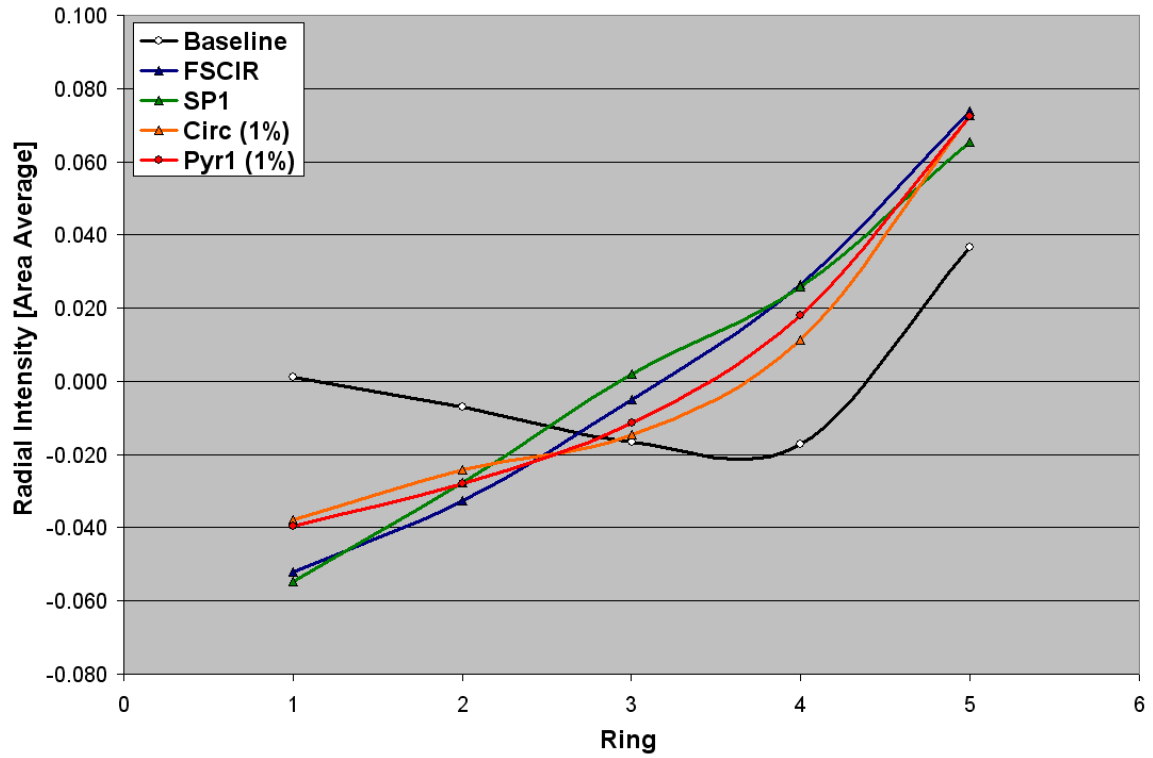
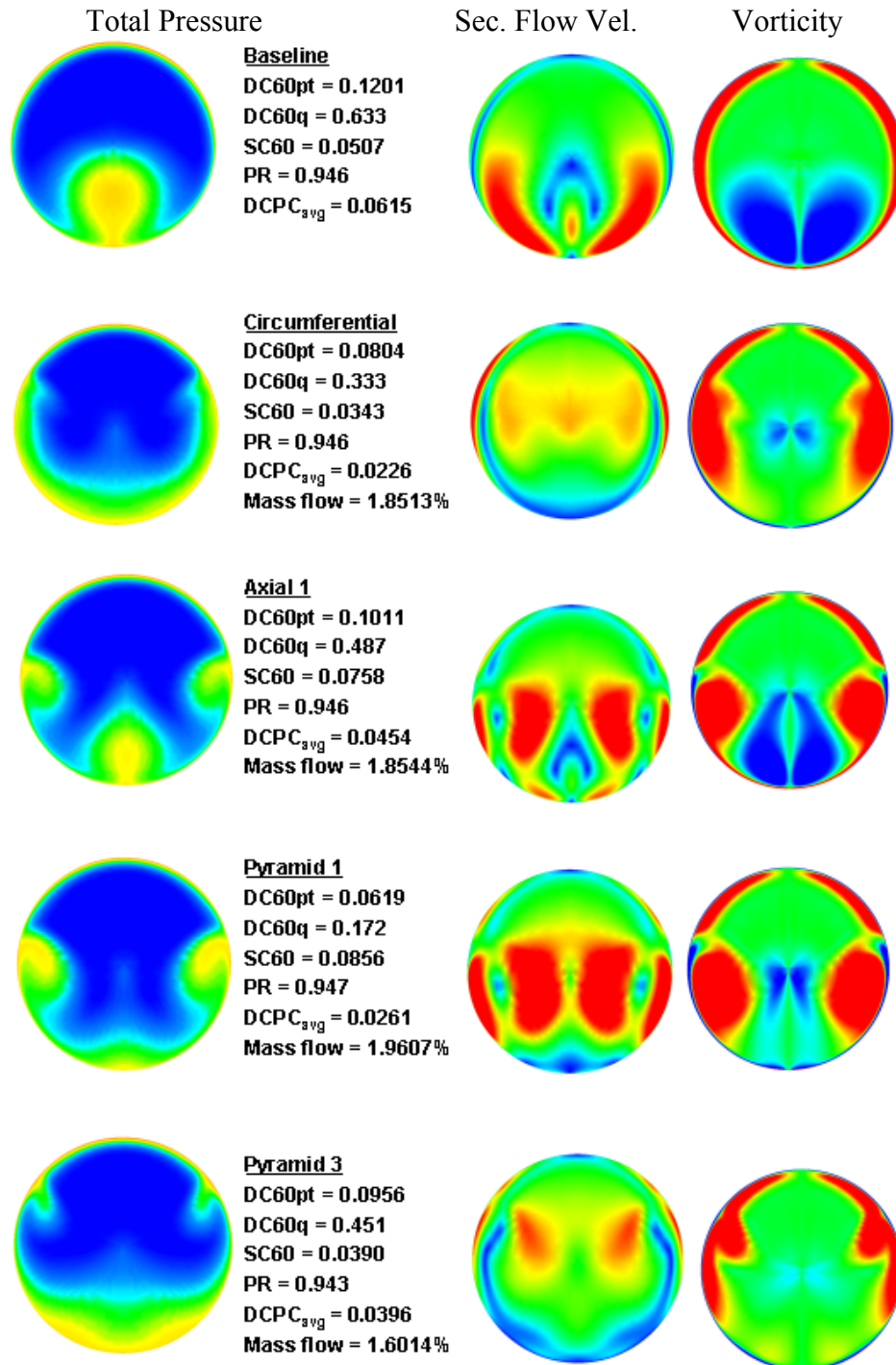


Figure G.0-4: ARP1420 Radial Distortion Intensity

Flow Control Solution Contours

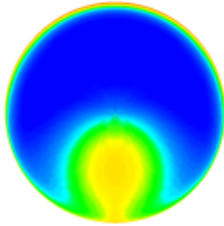
This section shows contour plots for all obtained flow control solutions. Contours from left to right are AIP total pressure, secondary flow magnitude, and streamwise vorticity.



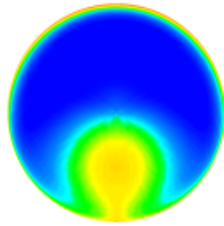
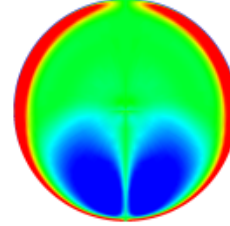
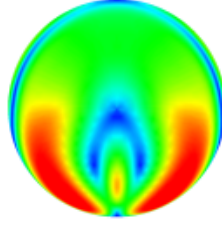
Total Pressure

Sec. Flow Vel.

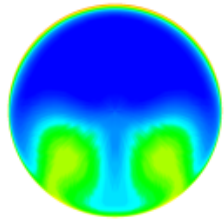
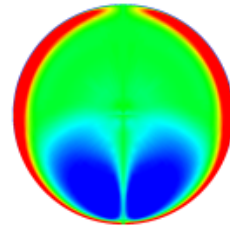
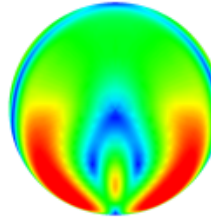
Vorticity



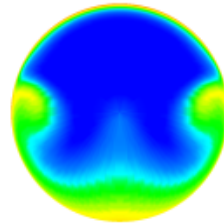
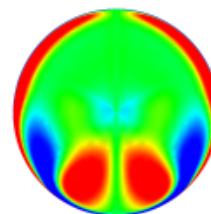
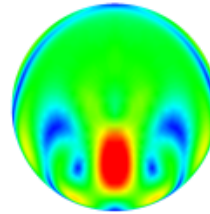
Suction
DC60pt = 0.1187
DC60q = 0.631
SC60 = 0.0506
PR = 0.947
DCPC_{avg} = 0.0613
Mass flow = 1.0175%



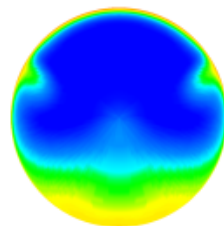
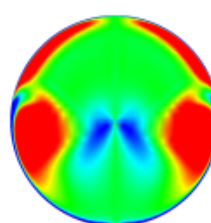
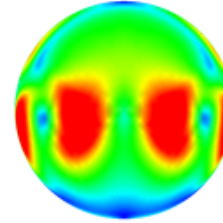
Floor Suction
DC60pt = 0.1189
DC60q = 0.632
SC60 = 0.0506
PR = 0.947
DCPC_{avg} = 0.0622
Mass flow = 0.25%



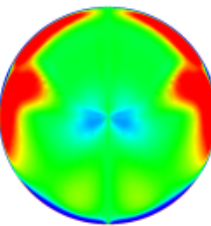
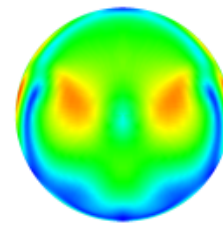
Axial 2
DC60pt = 0.0860
DC60q = 0.342
SC60 = 0.0600
PR = 0.945
DCPC_{avg} = 0.0368
Mass flow = 2.0374%



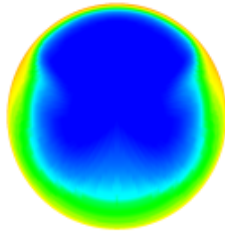
Pyramid 2
DC60pt = 0.0862
DC60q = 0.375
SC60 = 0.0761
PR = 0.947
DCPC_{avg} = 0.0325
Mass flow = 1.6612%



Pyramid 4
DC60pt = 0.1017
DC60q = 0.494
SC60 = 0.0378
PR = 0.946
DCPC_{avg} = 0.0440
Mass flow = 1.4774%

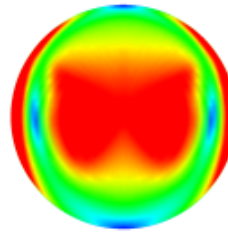


Total Pressure

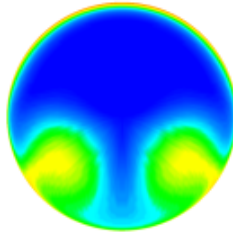
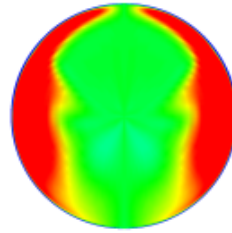


SCIR
DC60pt = 0.0651
DC60q = 0.239
SC60 = 0.0398
PR = 0.947
DCPC_{avg} = 0.0199
Mass flow = 1.8559%

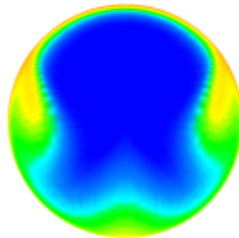
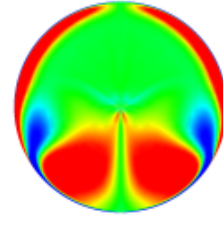
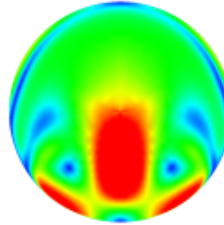
Sec. Flow Vel.



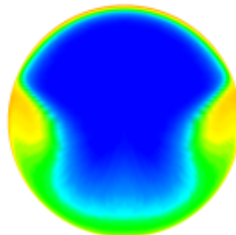
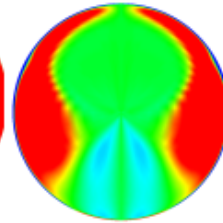
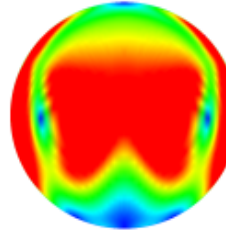
Vorticity



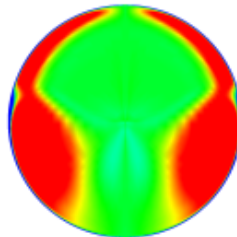
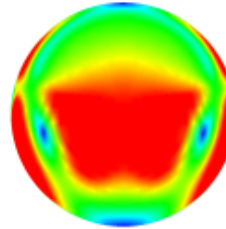
SA2
DC60pt = 0.0871
DC60q = 0.377
SC60 = 0.0101
PR = 0.941
DCPC_{avg} = 0.0343
Mass flow = 2.0470%



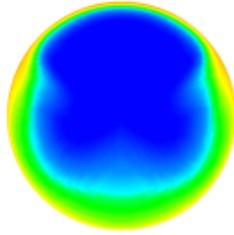
SP1
DC60pt = 0.0543
DC60q = 0.157
SC60 = 0.0833
PR = 0.945
DCPC_{avg} = 0.0231
Mass flow = 1.9671%



SRP
DC60pt = 0.0625
DC60q = 0.211
SC60 = 0.0696
PR = 0.945
DCPC_{avg} = 0.0205
Mass flow = 1.7615%

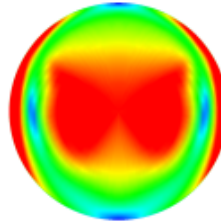


Total Pressure

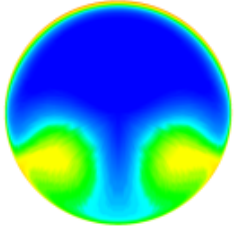
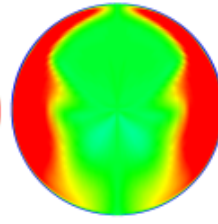


FSCIR
DC60pt = 0.0598
DC60q = 0.211
SC60 = 0.0355
PR = 0.947
DCPC_{avg} = 0.0178
Mass flow = 1.8555%

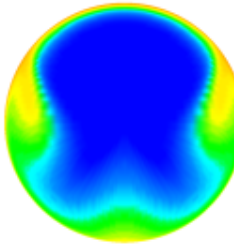
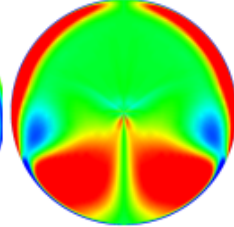
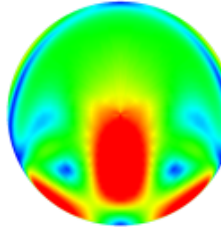
Sec. Flow Vel.



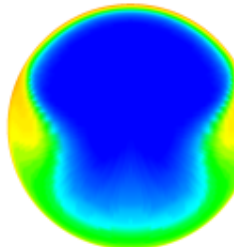
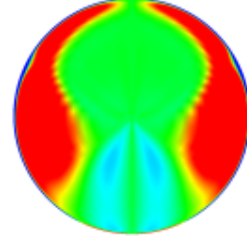
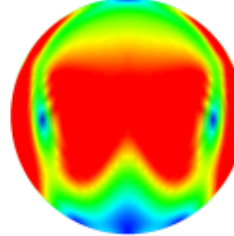
Vorticity



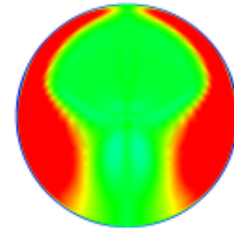
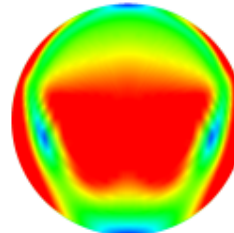
FSA2
DC60pt = 0.0896
DC60q = 0.383
SC60 = 0.0965
PR = 0.942
DCPC_{avg} = 0.0358
Mass flow = 2.0418%

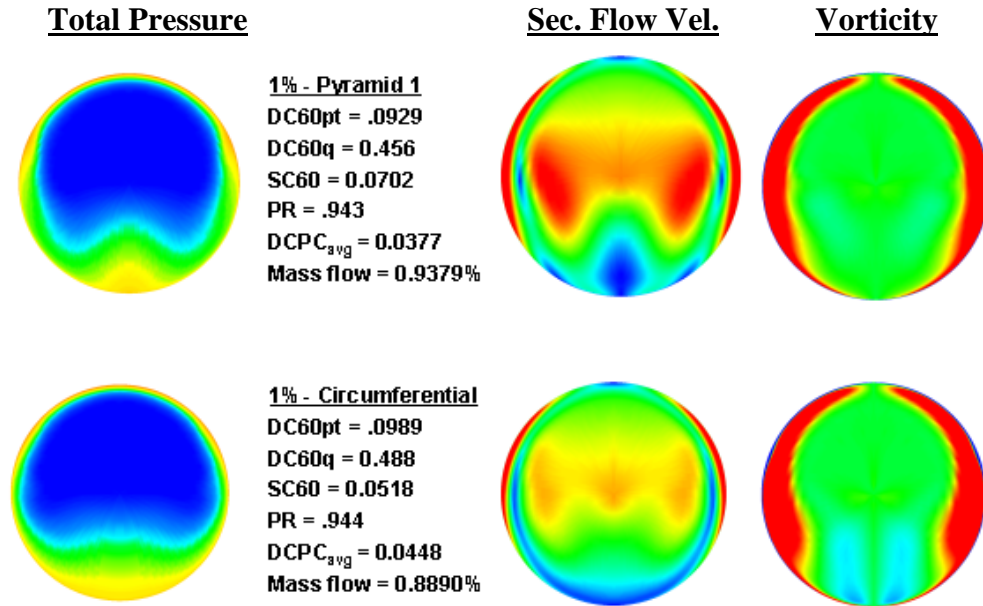


FSP1
DC60pt = 0.0586
DC60q = 0.180
SC60 = 0.0845
PR = 0.946
DCPC_{avg} = 0.0240
Mass flow = 1.9643



FSRP
DC60pt = 0.0595
DC60q = 0.192
SC60 = 0.0596
PR = 0.946
DCPC_{avg} = 0.0264
Mass flow = %





Flow Control Distortion Results

In this section, a brief description of all results obtained in the flow control analyses will be presented.

Figure G.0-5 and Figure G.0-6 show the obtained DC(60) distortion results for all flow control configurations tested. As compared to the baseline solution, all flow control cases reduced the AIP distortion to some extent. The application of 1% AIP mass suction alone did not appear to have any significant impact on the flow distortion. ‘Conventional’ flow control cases that utilized 1% of the AIP mass appeared to have varying degrees of effectiveness. The most successful of these cases were the circumferential and Pyramid 1 blowing schemes. Examinations of the 2% blowing only Pyramid blowing schemes suggest that the jet array angle has a significant impact on overall system effectiveness. The 2% axial blowing schemes did not substantially reduce distortion, although the axial 2 configuration showed improved performance over the axial 1 configuration when blowing fluid up the diffuser sidewall.

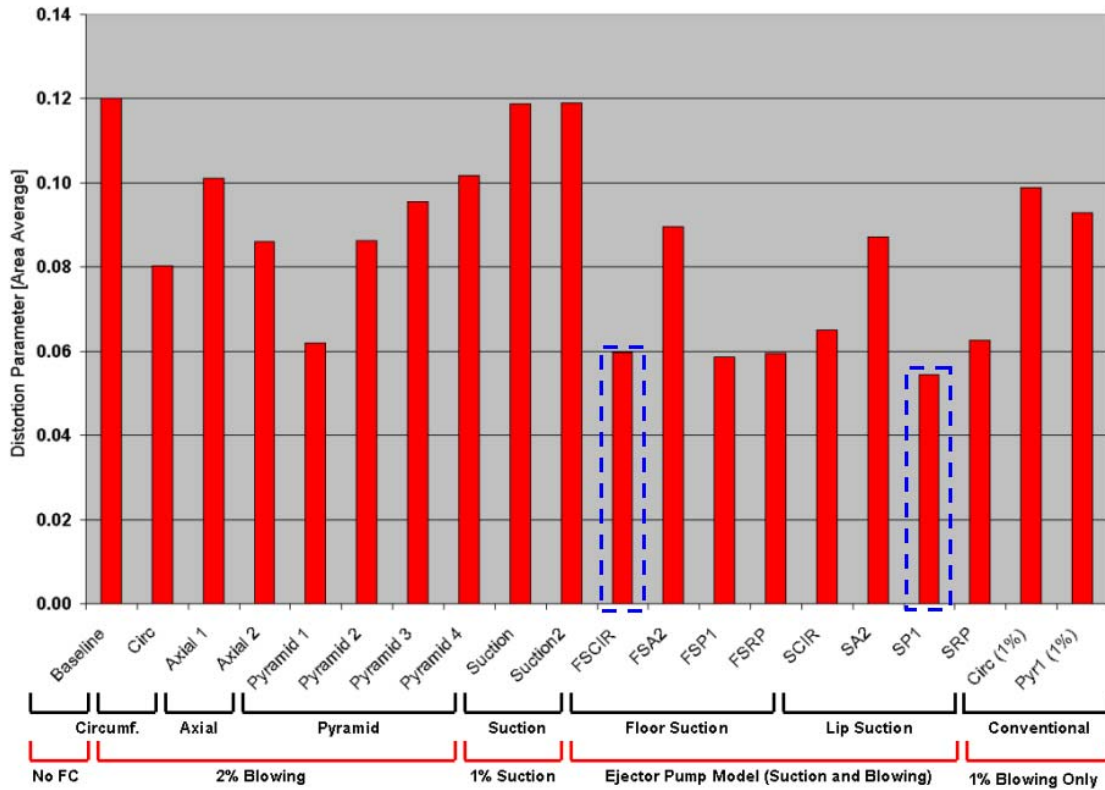


Figure G.0-5: DC(60)pt Distortion Parameter Results

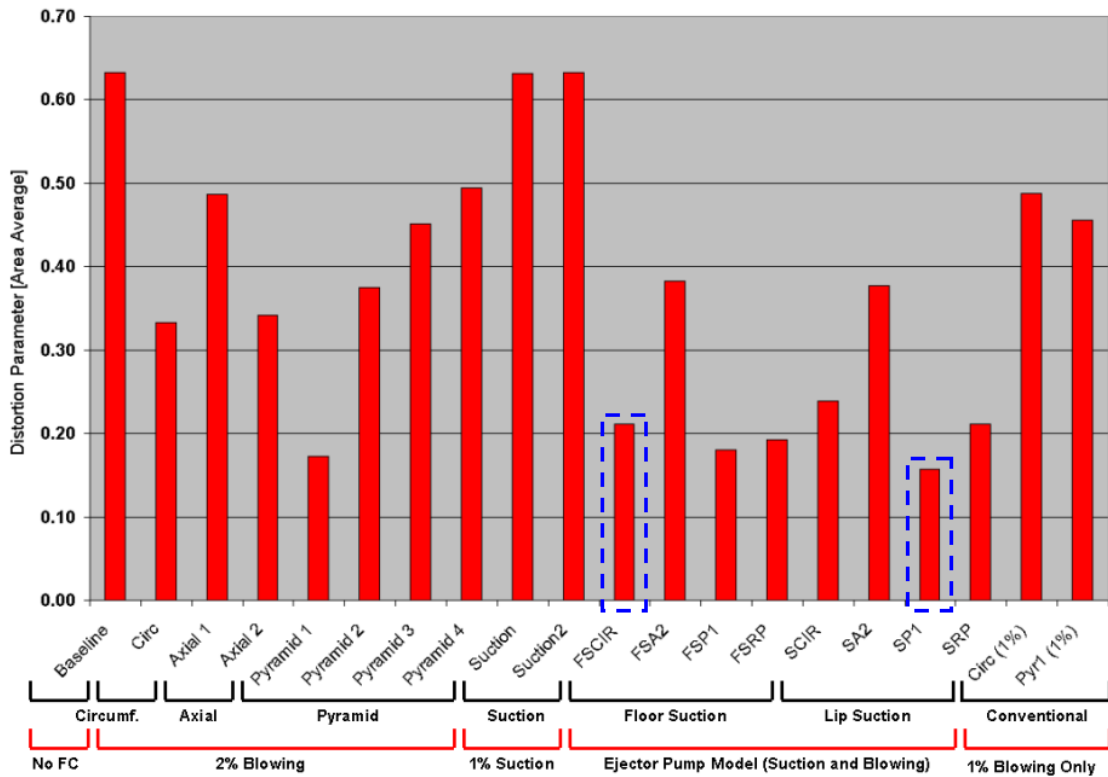


Figure G.0-6: DC(60)q Distortion Parameter Results

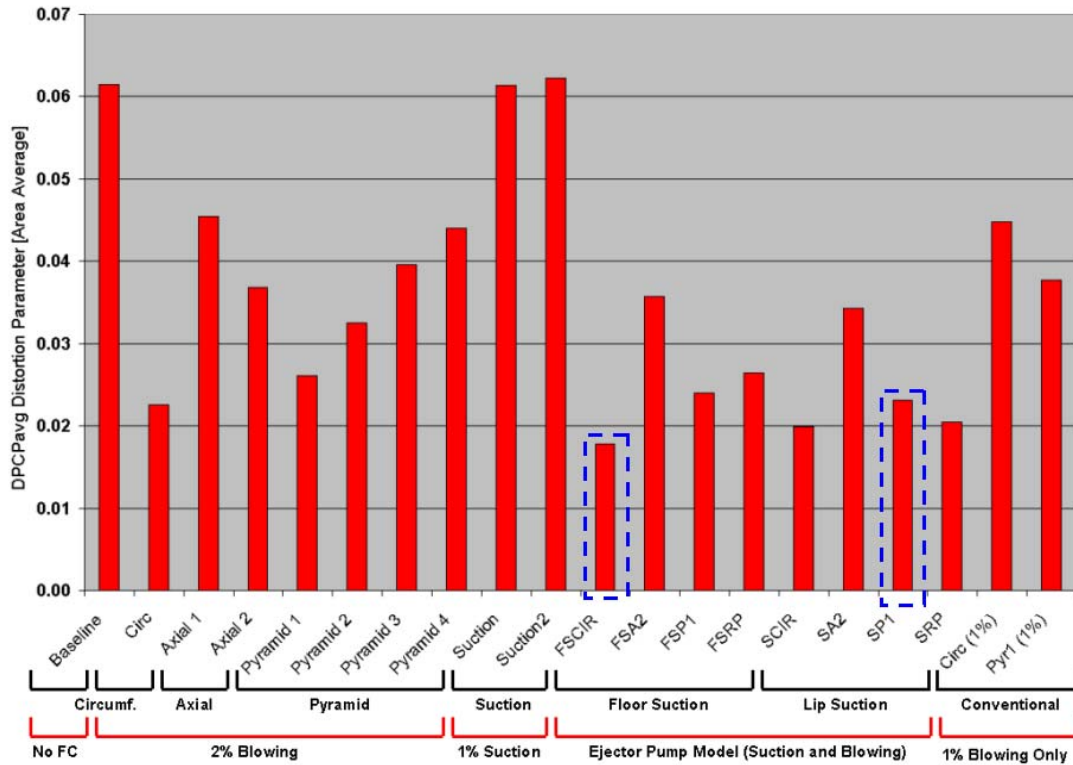


Figure G.0-7: DPCPavg Distortion Parameter Results

The SAE distortion descriptor DPCPavg, however, varies slightly in its perception of flow distortion at the AIP. (Figure G.0-7) In contrast to the DC(60) descriptors, the DPCPavg parameter reflects an average distortion for the whole AIP, as opposed to representing only the worst 60° sector of the flow. Although the distortion is significantly reduced by all flow control schemes, the circumferential and reverse Pyramid configurations are quantified as being more effective than the Pyramid1 configurations. The maximum reduction in distortion is achieved by the FSCIR scheme (71.1% reduction), which utilizes floor suction in combination with a circumferential blowing configuration. The reverse Pyramid configuration is also more effective than the Pyramid1 configuration. These results suggest that the lowest distortion is achieved by the configurations in which the individual jets do not coalesce into a single vortex. Both the circumferential and reverse Pyramid configurations have this feature, in contrast to the Pyramid 1 and axial schemes that continually reinforce a single vortex that sweeps up the sides of the diffuser.

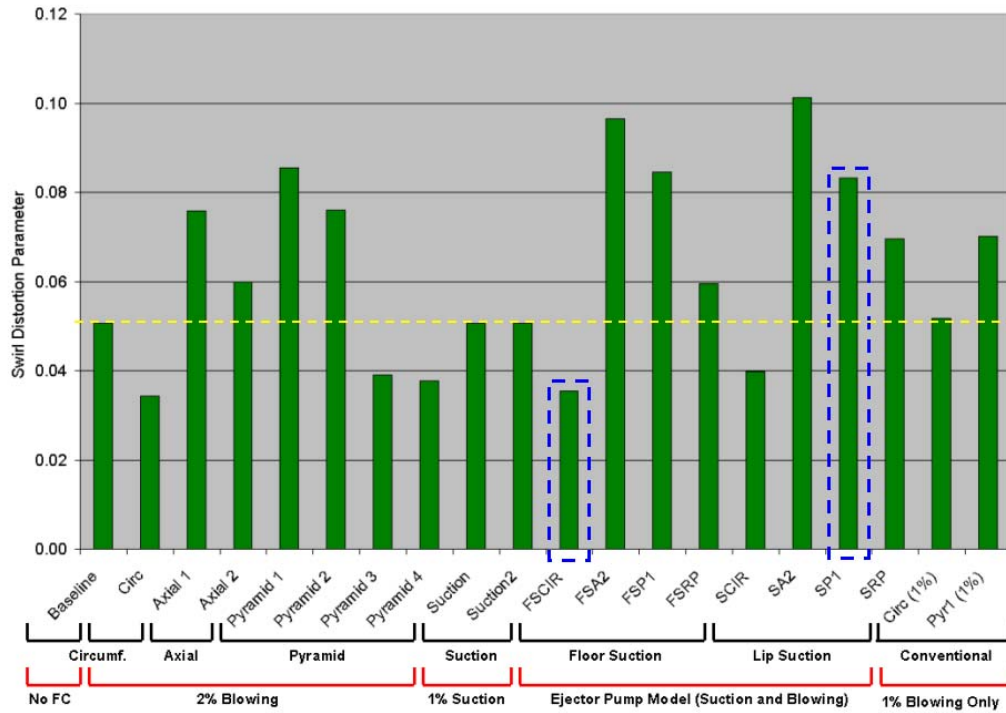


Figure G.0-8: SC(60) Swirl Distortion Parameter Results

Investigations of AIP flow swirl highlighted the impact of the flow control configurations on compressor flow quality. The DC(60) results suggested that in order to minimize flow distortion a significant blowing effort was required, and the ‘conventional’ 1% blowing cases did not have enough momentum to successfully counteract the diffuser secondary flows. However, the stronger ejector-driven jets needed to be carefully arranged so that they did not increase flow swirl at the AIP. With the exception of the reverse Pyramid configuration, the circumferential ejector case was the only ejector scheme to show a net reduction in swirl at the AIP. The larger angle Pyramid cases (3&4) show little increase in swirl, although these cases are closely related in configuration to the circumferential cases. In some cases it is also evident that the addition of flow suction had a negative impact on swirl at the AIP. When selecting a flow control configuration, it is important to realize that although some configurations can yield substantial improvements in total pressure distortion, the reduction is sometimes accomplished at the expense of an increase in swirl at the AIP. If of sufficient magnitude, swirl entering the compressor can lead to rotating stall and engine surge, thus trading one type of distortion for another.

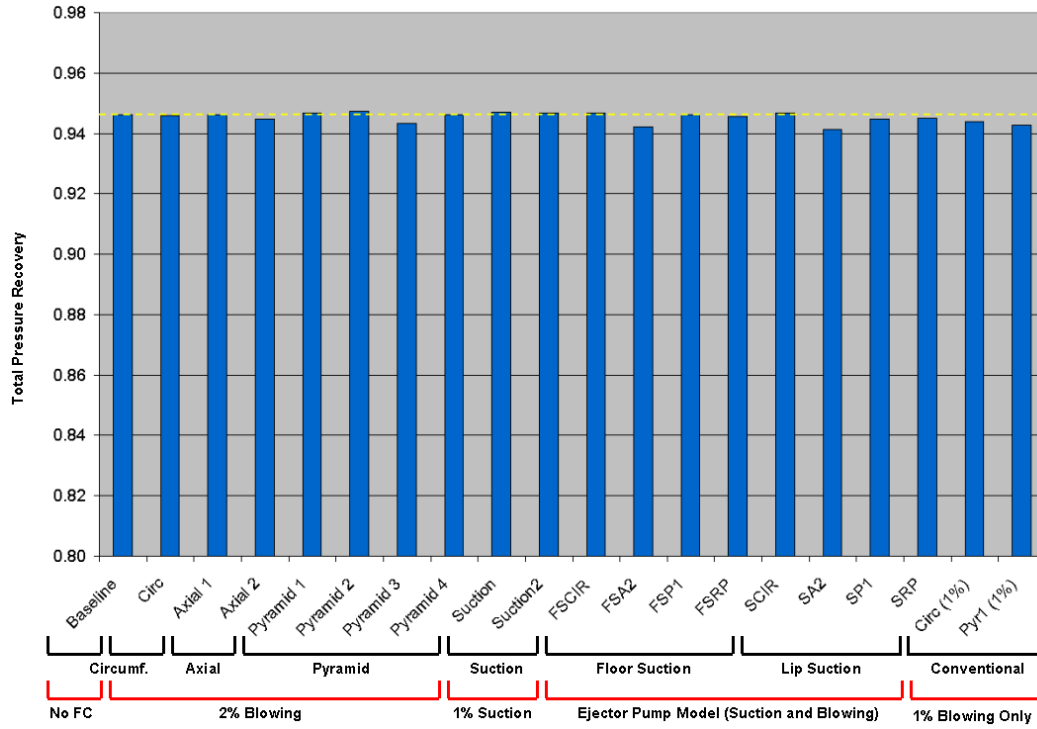


Figure G.0-9: Total Pressure Recovery Results

All configurations tested did not appear to have a strong impact on duct pressure recovery with no clear increase or decrease from the baseline value.

Appendix H: Calculations and Uncertainty

During the course of the experimental work, several flow quantities had to be calculated from measured temperature and pressure data. This section outlines those calculations and provides error estimates on all obtained data and the resulting calculations.

Experimental Calculations

The current experimental setup measures 111 time-averaged pressures and 6 time-averaged temperatures for each flow control condition at the desired simulated flight condition. An overview of these measurements is shown in the schematic of Figure H.0-1, and a summary of the transducers and data acquisition is shown in

Table H.0-1.

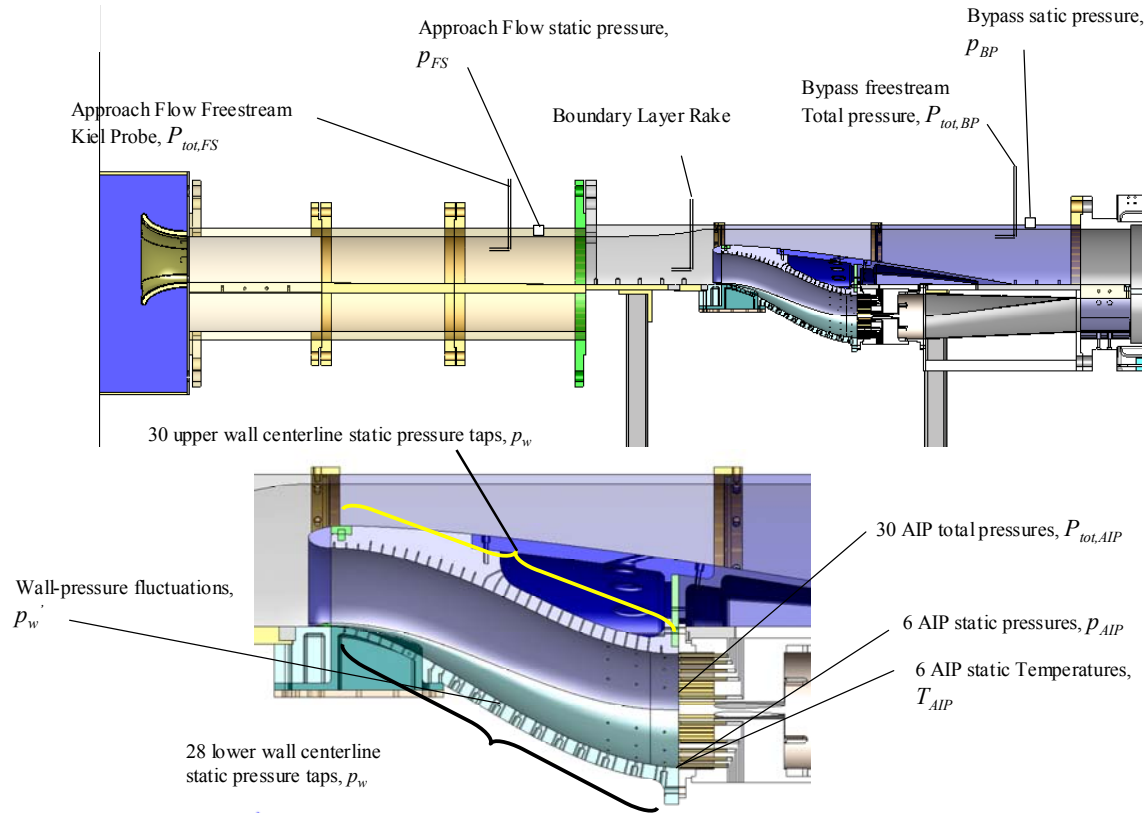


Figure H.0-1: Overview of measurements

Table H.0-1: Summary of Transducers and Data Acquisition

Parameter	Quantity	Transducer	DAQ System
P_{FS}	2	ZOC, 0-15 psid	
p_{FS}	1	ZOC, 0-5 psid	
P_{BL}	7	ZOC, 0-5 psid	National
p_w	60	ZOC, 0-5 psid and DSA	Instruments, 64-ch. Card
P_{AIP}	30	PSI	+ GPIB card for PSI
p_{AIP}	6	ZOC, 0-5 psid	system
T_{AIP}	6	K-type Thermocouple	+ Ethernet connection for DSA
P_{motive}	1	Transmitter	system
$p_{suction}$	1	ZOC, 0-5 psid	
$P_{massflow}$	4	ZOC, 0-5 psid	

In order to perform these pressure measurements, Techsburg has compiled three different pressure transducer systems: a 32-channel ScaniValve DSA pressure module system, a 32-channel PSI pressure measurement system, and a modular 48-channel ScaniValve ZOC pressure transducer system. The DSA and PSI pressure transducer systems both send digitized signals to a host computer via an Ethernet cable and a GPIB connection, respectively. The ZOC system sends analog signals to a National Instruments 64-channel A/D card in the host computer. A National Instruments Lab View program has been composed to simultaneously acquire the electrical signals from all three transducer systems and compute the necessary performance metrics of the experiment, which will be subsequently explained in this section of the report.

As seen in Figure H.0-1, the freestream inlet approach flow will be characterized by the freestream total pressure P_{FS} , the freestream static pressure p_{FS} , and the freestream total temperature $T_{tot,FS}$, which will assumed to be equal to the room ambient temperature T_{amb} . With the aforementioned freestream approach flow parameters, the freestream Mach number M_{FS} will be calculated:

$$M_{FS} = \sqrt{\frac{2}{\gamma-1} \left(\left(\frac{P_{FS}}{p_{FS}} \right)^{\frac{\gamma-1}{\gamma}} - 1 \right)}.$$

The static temperature of the freestream approach flow will be determined according to the isentropic relation:

$$T_{FS} = \frac{T_{amb}}{1 + \frac{\gamma-1}{2} M_{FS}^2}.$$

The freestream velocity will then be determined according to:

$$V_{FS} = M_{FS} \sqrt{\gamma R T_{FS}}.$$

These equations will be used in conjunction with the measured inlet mass flow rate to compute the corrected mass flow ratio c_{in} , which is a measure of the inlet capture.

Moving further downstream in the B.L. Development Region, the next parameter to be determined is the boundary layer thickness just upstream of the inlet entrance. A

boundary layer rake will be used to measure the boundary layer total pressures P_{BL} , which in combination with local static pressure will be used to determine the velocity profile. This profile will then be used to determine the boundary layer thickness δ .

By far, most of the measurements to be performed in this experiment are concentrated inside the offset BLI inlet. There will be 60 duct centerline locations (30 along the top and 30 along the bottom) where time-averaged, wall-pressures p_w will be measured.

At the exit plane (AIP) of the offset BLI inlet a 30 total pressure probe rake is stationed in order to measure total pressure distortion. Each total pressure probe is positioned at the centroid of equal area sectors, which allows for area-weighted averages of the AIP total pressures P_{AIP} to be computed by the arithmetic mean of all 30 measurements. Also at the AIP, there will be 6 time-averaged wall-pressure p_{AIP} and 6 wall temperature T_{AIP} measurements made at locations indicated in Figure H.0-2.

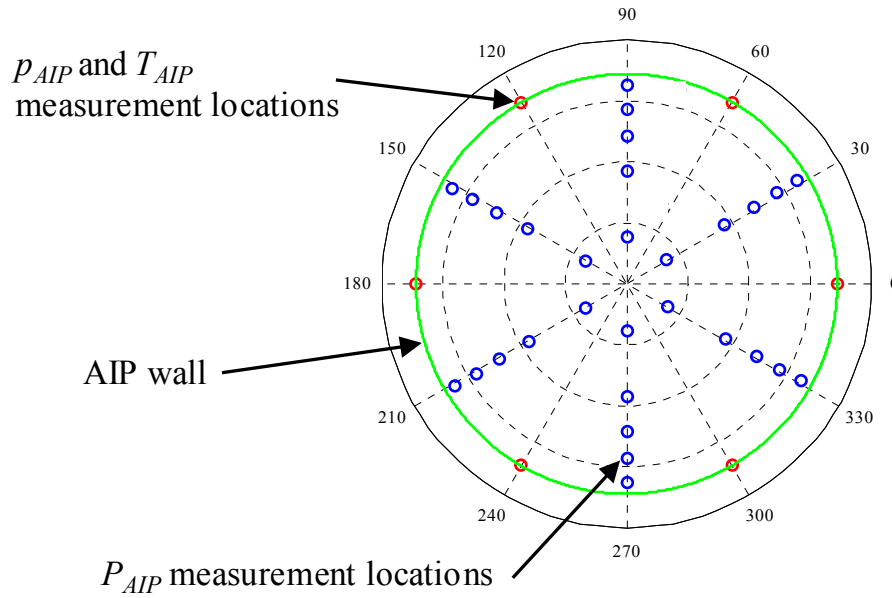


Figure H.0-2: AIP measurement locations

The inlet mass flow rate is then computed with the AIP measurements according to:

$$\dot{m}_{inlet} = \langle p_{AIP} \rangle \sqrt{\left(\frac{2\gamma}{R(\gamma-1)\langle T_{AIP} \rangle} \right) \left[\left(\frac{\langle P_{AIP} \rangle}{\langle p_{AIP} \rangle} \right)^{\gamma-1/\gamma} - 1 \right]}$$

where $\langle p_{AIP} \rangle \equiv$ arithmetic mean of 6 wall pressure measurements,

$\langle T_{AIP} \rangle \equiv$ arithmetic mean of 6 wall temperature measurements,

and $\langle P_{AIP} \rangle \equiv$ arithmetic mean of 30 AIP total pressure measurements.

Once the inlet mass flow rate is determined, the non-dimensional mass flow ratio c_m can be computed according to:

$$c_{\dot{m}} = \frac{\dot{m}_{inlet} R T_{FS}}{P_{FS} V_{FS} A_{AIP}}$$

This calculation serves as an indication of the amount of freestream flow captured by the inlet; NASA simulations use the design condition of $c_{\dot{m}} \approx 0.72$.

The next set of calculations are concerned with computing the total pressure distortion metrics DC(60). The DC(60) distortion metrics are defined as:

$$DC60q = \frac{\langle P_{AIP} \rangle - \langle P_{\theta} \rangle}{q_{AIP}}$$

$$DC60pt = \frac{\langle P_{MAX} \rangle - \langle P_{\theta} \rangle}{\langle P_{AIP} \rangle}$$

Where $\langle P_{\theta} \rangle$ is defined as the mean total pressure in the ‘worst’ sector (of angle θ) of the AIP, and $\langle P_{MAX} \rangle$ is the sector of ‘best’ total pressure. The dynamic pressure q_{AIP} will be estimated using the same nomenclature as above according to:

$$q_{AIP} = \frac{\gamma \langle P_{AIP} \rangle}{(\gamma - 1)} \left[\left(\frac{\langle P_{AIP} \rangle}{\langle P_{AIP} \rangle} \right)^{\gamma-1/\gamma} - 1 \right].$$

Uncertainty Calculations

Calculations of uncertainty are based primarily on the uncertainty of individual transducers and the propagation of errors calculated according to the Kline-McClintock method.¹⁷ This method utilizes a linear approximation between the dependent and measured variables. When the uncertainty in a measurement is dependent on more than one variable, the total uncertainty is correlated to the partial derivative of each dependent variable. Thus, if the function

$$F = f(a,b,c,d)$$

Then the uncertainty in F (u_F) is determined according to:

$$u_F = \pm \sqrt{\left(\left(\frac{\partial F}{\partial a} \right) \cdot \delta a \right)^2 + \left(\left(\frac{\partial F}{\partial b} \right) \cdot \delta b \right)^2 + \left(\left(\frac{\partial F}{\partial c} \right) \cdot \delta c \right)^2 + \left(\left(\frac{\partial F}{\partial d} \right) \cdot \delta d \right)^2}$$

Where $\left(\frac{\partial F}{\partial x} \right)$ represents the linear dependence of each variable and $\delta(x)$ represents the transducer errors represented in Table H.0-2.

Table H.0-2: Transducer Uncertainties ($\delta(x)$)

Transducer	Range	Uncertainty
ZOC	0-15 psid	± 0.00975 psi
ZOC	0-5 psid	± 0.00325 psi
DSA	0-30 psid	± 0.015 psi
DSA	0-5 psid	± 0.0025 psi
PSI	0-15 psid	± 0.0075 psi

These values can then be combined with the equations used to determine the uncertainty in each calculated flow parameter. Results obtained from this analysis yielded the uncertainty values listed in Table H.0-3.

Table H.0-3: System Metric Uncertainty Based on Transducer Error

Parameter	Uncertainty
M_{FS}	± 0.00355 psi
T_{FS}	± 1.7702 K
V_{FS}	± 1.4732 m/s
q_{AIP}	± 0.00167 psi
DC(60)pt	± 0.0010
DC(60)q	± 0.0051

The obtained transducer uncertainty results may then be plotted on the obtained data as error bars. The uncertainty results show a relatively small variation in the critical distortion parameters, and are likely less important than some of the basic assumptions inherent in the distortion equations. Of the most particular note is the assumption that the six static pressure measurements located around the AIP are sufficient to determine the face average pressure value. This assumption can be investigated through a brief examination of the CFD results.

By comparing the integrated CFD solutions with simulated wind tunnel calculation methods additional uncertainty values could be calculated. These uncertainties are based on the maximum deviation of tunnel calculation methods from interpolated CFD results. Values obtained from this analysis are listed in Table H.0-4.

Table H.0-4: Distortion Uncertainty Based on Assumption Error

Parameter	Uncertainty
DC(60)pt	± 0.0012
DC(60)q	± 0.0385

Based on experimental results, the uncertainty due to flow approximations can range from 5.6%-27.2% for the DC(60)q parameter, and 0.9%-2.2% for obtained DC(60)pt values. Experimentally calculated DC(60)q values are considerably affected by the flow assumptions. This increase in distortion uncertainty is largely the result of uncertainty in the calculation in AIP average dynamic pressure.

Appendix I: Wind Tunnel Adaptation of CFD Grid

In order to predict the basic wind tunnel performance, the flow control grid was modified to model the boundaries of the experimental setup. Far-field boundaries were replaced with the wind tunnel walls as represented in Figure I.0-1.

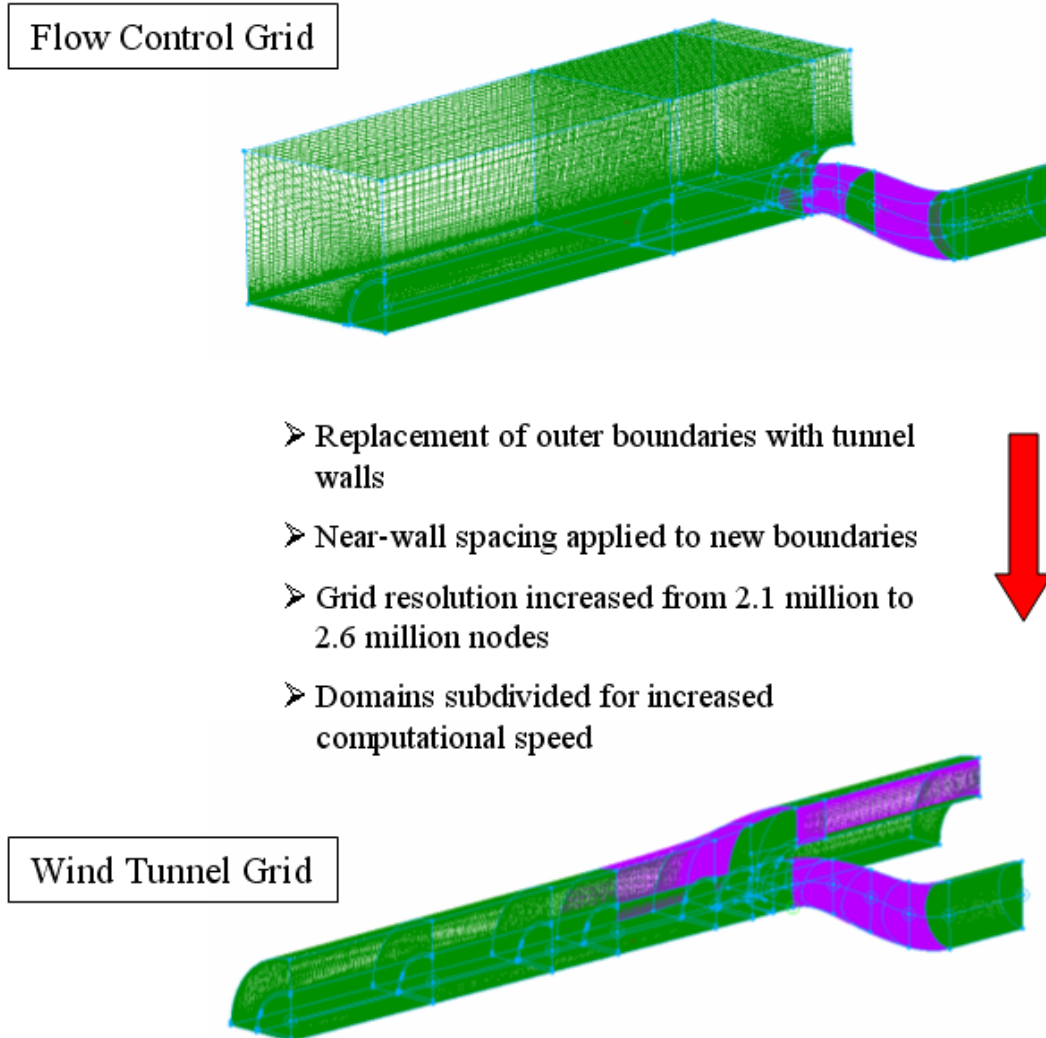


Figure I.0-1: Wind Tunnel Grid Modification

Due to this adaptation, the number of points within the grid increased in order to capture the boundary growth along the inside of the added tunnel walls. These calculations were critical as it was necessary to determine if the inlet would ingest the flow from the interior walls. In order to reduce this possibility, the tunnel walls expanded near the inlet. The wall curvature was based upon a streamline obtained from the CFD baseline solution.

The mesh was also adapted to remove the polar point from the mesh, by incorporating a center block and wrapping the internal duct surface mesh around it. (Refer to Figure I.0-2) This allowed for a quicker convergence due to the increased local time-step, but prohibited the use of the *distortion_param* program.

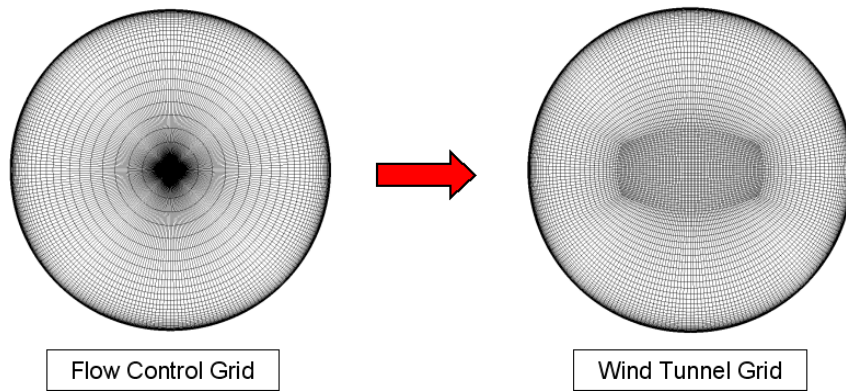


Figure I.0-2: AIP Grid Modification

Appendix J: Wind Tunnel Flow Quality

Axial Pressure Gradient

Investigations into the quality of flow within the wind tunnel were conducted during experiments. Data was collected to characterize the axial and transverse pressure gradients due to their ability to affect as well as diagnose boundary layer quality. In addition, the ingested boundary layer velocity profile was compared to computational predictions. Figure J.0-1 shows the static pressure gradient along the length of the boundary layer growth region. The pressure gradient along the growth region is relatively constant, although it is evident that the area expansion along the length was not sufficient to entirely prevent flow acceleration due to boundary layer displacement thickness growth. Significant change begins to occur at the onset of the tunnel area expansion. This expansion causes a drop in static pressure as the flow that is not ingested into the inlet is forced to accelerate into the flow bypass. A sharp pressure increase is evident when the ram effect of the inlet begins to impinge on the flow. This positive pressure gradient is characteristic of isentropic compression occurring as a result of engine inlet capture, and results in a local thickening of the boundary layer. (Shown in a previous section.)

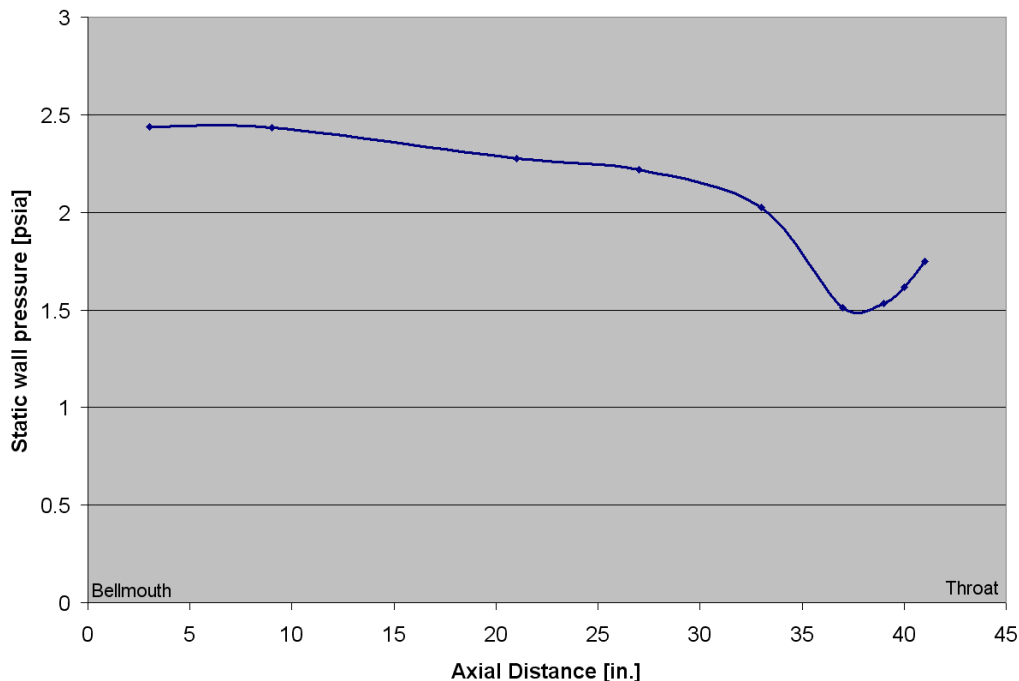


Figure J.0-1: Wind Tunnel Axial Pressure Gradient

Spanwise Pressure Gradient

Figure J.0-2 shows the transverse static pressure gradient ~2” upstream of the inlet. This gradient was measured in order to diagnose the quality of flow being ingested into the inlet. The relatively constant profile suggests that there are no large-scale flow perturbations being ingested. When coupled with the measured boundary layer velocity profile it was determined that the general boundary layer flow quality was reasonable and not likely to cause any large-scale deviations from predicted results. The slight drop in pressure at the outermost points may be flow that is being accelerated as it is diverted around the inlet lip; this outer flow was not likely ingested.

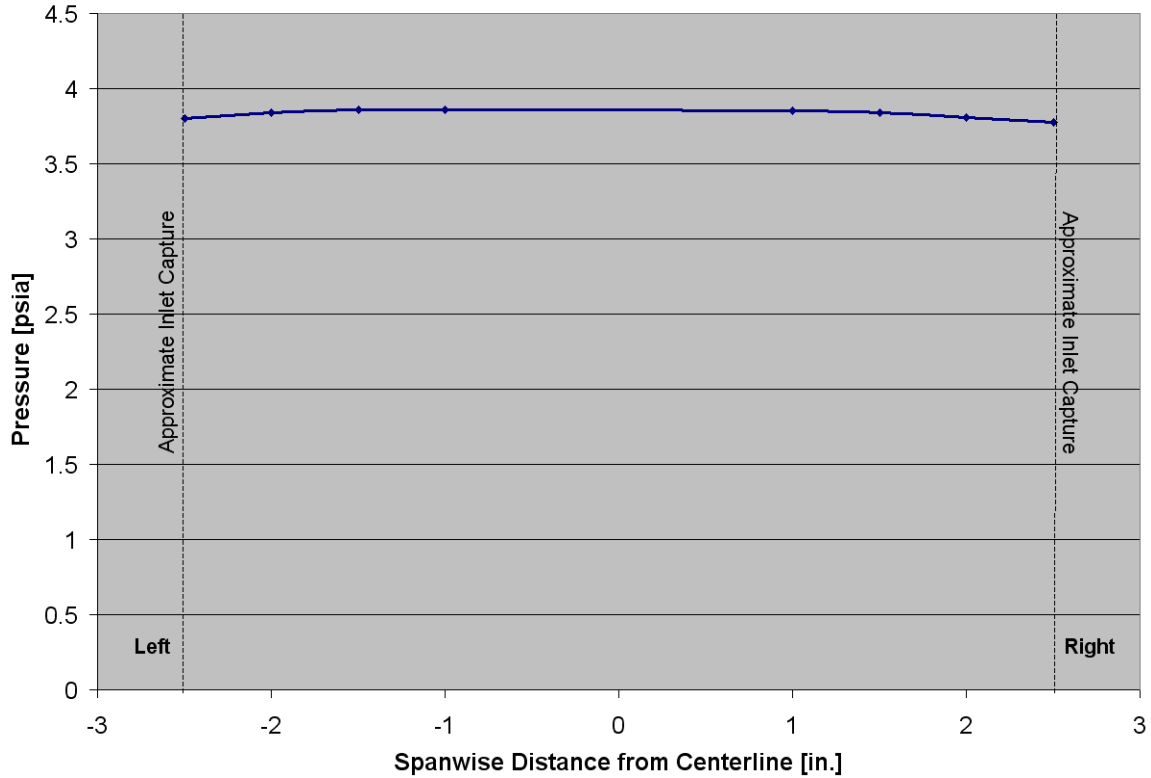


Figure J.0-2: Wind Tunnel Transverse Pressure Gradient

Diffuser Static Pressure Profile

Wind tunnel static pressure measurements of the upper and lower diffuser surfaces are shown in Figure J.0-3. The pressure profiles shown for the upper and lower surfaces compare well between the CFD and experimental results. The vertical offset is consistent with the variation in freestream Mach number; experimental data was not collected at as high a Mach number as analyzed in CFD. Upper surface contours show the initial pressure rise associated with the first diffuser turn. This pressure then decreases throughout the length of the duct and begins to climb again briefly near the AIP at the onset of the second turn. Lower contours shown the effect of the area diffusion as the pressure gradually rises along the length of the duct. The pressure offset between the upper and lower walls at the AIP indicate a difference in the flow Mach number resulting from the presence of distortion on the lower diffuser surface.

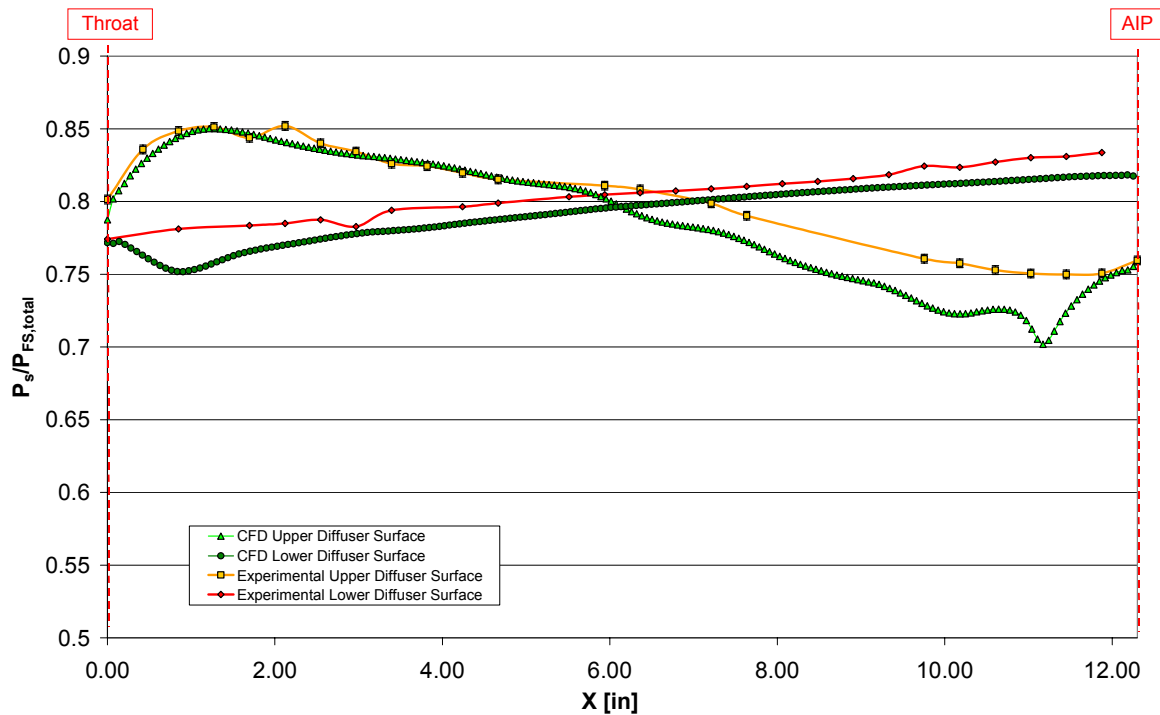


Figure J.0-3: Baseline Diffuser Centerline Static Pressure Normalized by Free Stream Total Pressure

Appendix K: ADPAC

ADPAC (Advanced Ducted Propfan Analysis Code) was created by the Allison Engine Company under funding by NASA.⁵ It utilizes a finite-volume, multi-grid, Runge-Kutta time-marching solution algorithm to solve a time dependent form of the 3D Reynolds-Averaged Navier-Stokes (RANS) equations. The code provides a multiple block mesh discretization to allow for flexibility when meshing complex geometries. The Reynolds stresses (representing the time-averaged turbulence values) are modeled via the Boussinesq approximation. This simplifies the Reynolds shear-stress terms by eliminating them in favor of a modified effective viscosity:

$$\mu_{\text{effective}} = \mu_{\text{laminar}} + \mu_t$$

Where μ_t represents the eddy viscosity – a term used to relate the turbulent stresses to the flow mean strain rate.

The Spalart-Allmaras Turbulence Model

The Spalart-Allmaras (S-A) turbulence model is the highest-fidelity working turbulence model available for use in ADPAC. According to the Boussinesq approximation, the turbulent (eddy) viscosity is modeled, in this case by one equation that evaluates the kinematic viscosity (ν) in the transport equation:

$$\frac{D\tilde{\nu}}{Dt} = \text{Production} + \text{Diffusion} - \text{Destruction} + \text{Trip}$$

REPORT DOCUMENTATION PAGE

*Form Approved
OMB No. 0704-0188*

The public reporting burden for this collection of information is estimated to average 1 hour per response, including the time for reviewing instructions, searching existing data sources, gathering and maintaining the data needed, and completing and reviewing the collection of information. Send comments regarding this burden estimate or any other aspect of this collection of information, including suggestions for reducing this burden, to Department of Defense, Washington Headquarters Services, Directorate for Information Operations and Reports (0704-0188), 1215 Jefferson Davis Highway, Suite 1204, Arlington, VA 22202-4302. Respondents should be aware that notwithstanding any other provision of law, no person shall be subject to any penalty for failing to comply with a collection of information if it does not display a currently valid OMB control number.
PLEASE DO NOT RETURN YOUR FORM TO THE ABOVE ADDRESS.

1. REPORT DATE (DD-MM-YYYY) 01- 09 - 2005		2. REPORT TYPE Contractor Report		3. DATES COVERED (From - To)	
4. TITLE AND SUBTITLE Sensing and Active Flow Control for Advanced BWB Propulsion-Airframe Integration Concepts			5a. CONTRACT NUMBER NAS1-03066		
			5b. GRANT NUMBER		
			5c. PROGRAM ELEMENT NUMBER		
6. AUTHOR(S) Fleming, John; Anderson, Jason; Ng, Wing; and Harrison, Neal			5d. PROJECT NUMBER		
			5e. TASK NUMBER		
			5f. WORK UNIT NUMBER 23-714-80-VC		
7. PERFORMING ORGANIZATION NAME(S) AND ADDRESS(ES) NASA Langley Research Center Hampton, VA 23681-2199			8. PERFORMING ORGANIZATION REPORT NUMBER		
9. SPONSORING/MONITORING AGENCY NAME(S) AND ADDRESS(ES) National Aeronautics and Space Administration Washington, DC 20546-0001			10. SPONSOR/MONITOR'S ACRONYM(S) NASA		
			11. SPONSOR/MONITOR'S REPORT NUMBER(S) NASA/CR-2005-213919		
12. DISTRIBUTION/AVAILABILITY STATEMENT Unclassified - Unlimited Subject Category 02 Availability: NASA CASI (301) 621-0390					
13. SUPPLEMENTARY NOTES Langley Technical Monitor: Susan A. Gorton An electronic version can be found at http://ntrs.nasa.gov					
14. ABSTRACT In order to realize the substantial performance benefits of serpentine boundary layer ingesting diffusers, this study investigated the use of enabling flow control methods to reduce engine-face flow distortion. Computational methods and novel flow control modeling techniques were utilized that allowed for rapid, accurate analysis of flow control geometries. Results were validated experimentally using the Techsburg Ejector-based wind tunnel facility; this facility is capable of simulating the high-altitude, high subsonic Mach number conditions representative of BWB cruise conditions.					
15. SUBJECT TERMS BLI; Active flow control; Boundary layer ingesting; Diffuser; Distortion; Inlet; Wind tunnel					
16. SECURITY CLASSIFICATION OF:			17. LIMITATION OF ABSTRACT	18. NUMBER OF PAGES	19a. NAME OF RESPONSIBLE PERSON
a. REPORT	b. ABSTRACT	c. THIS PAGE			STI Help Desk (email: help@sti.nasa.gov)
U	U	U	UU	146	19b. TELEPHONE NUMBER (Include area code) (301) 621-0390